Catalytic Conversion of Carbon Dioxide to Formate Using Novel Metal Organic Frameworks

PIWAI TSHUMA

Thesis presented for the degree of

DOCTOR OF PHILOSOPHY IN CHEMISTRY

In the Department of Chemical Technology

Midlands State University

June 2020

Supervisor: Dr G. Mehlana

Co-Supervisor: Dr B. C. E. Makhubela

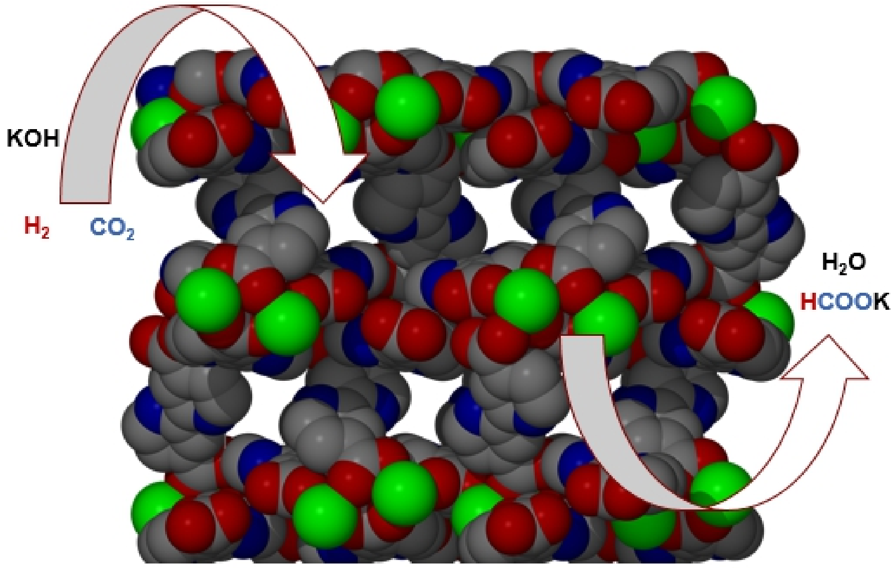

Acknowledgements

I owe my deepest thanks to:

- Dr G. Mehlana and Dr B. C. E. Makhubela for their priceless supervision and support during my doctoral studies.
- Centre of Synthesis and Catalysis, Department of Chemical Sciences, the University of Johannesburg for availing their facilities.
- Dr Hong Su, University of Cape Town, Department of Chemistry, for her assistance in single crystal X-ray data collection.
- Professor Lars Ohrstrom, Chalmers University of Technology, Department of Chemistry and Chemical Engineering for his assistance with work related to topological analysis.
- Prof. S. Bourne, Dr C.L. Oliver, Dr N. Chatterjee and Mr C. A. Ndamyabera, University of Cape Town, Department of Chemistry for their assistance in gas sorption studies.
- Dr N. Bingwa, Centre of Synthesis and Catalysis, Department of Chemical Sciences, the University of Johannesburg for his assistance in BET surface area, SEM-EDX and HR-TEM analysis.
- Prof. J. Dakwa and Dr I. Beas, Botswana Institute of Technology, Research and Innovation for their assistance in X-ray Photoelectron Spectroscopy analysis.
- The Organometallic Group, University of Johannesburg, Department of Chemical Sciences for their support, help and constructive criticism. Your efforts and inspiration did not go unnoticed.
- The Department of Chemical Technology, Midlands State University did a great job. Thank you for asking me all insightful questions, helpful suggestions and invaluable training throughout my doctoral studies.
- The organisation of Woman in Science for the Developing World, Green Chemistry for Life Program (PhosAgro/UNESCO/IUPAC), The Royal Society, and the African Academy of Sciences (AAS) Future Leaders African Independent Research (FLAIR) for funding this project.
- Finally, to my husband Collet Tshuma and children Blessing, Graca and Ruth, I dedicate this thesis.

Publications

Parts of this thesis have been published:

1. **Piwai Tshuma**, Banothile C. E. Makhubela, Ndzondelelo Bingwa and Gift Mehlana, Palladium(II) Immobilised on metal organic frameworks for catalytic hydrogenation of CO_2 to formate, *Inorganic Chemistry*, 2020,59, 6717-6728
2. **Piwai Tshuma**, B. C. E. Makhubela, Lars Ohrstrom, Susan A. Bourne, Nabanita Chatterjje, Issac N. Beas, James Dakwa and Gift Mehlana, Cyclometalation of a Lanthanum(III) based MOF for catalytic hydrogenation of carbon dioxide to formate, *RSC Advances*, 2020, 10, 3593-3605
3. **Piwai Tshuma,** Christophe A. Ndamyabera, Banothile C. Makhubela, Susan A. Bourne, and Gift Mehlana, Synthesis and Characterisation of 2D Metal-Organic Frameworks for Adsorption of Carbon Dioxide and Hydrogen, *Frontiers in Chemistry*, 2020, doi: 10.3389/fchem.2020.581226

Abstract

The combustion of fossil fuels has significantly increased the concentration of carbon dioxide (CO_2) in the atmosphere. CO_2 is a greenhouse gas and a major contributor to global warming. To rectify the CO_2 problem, its capture and conversion have been proposed. Metal-organic framework (MOF) based materials, a relatively new class of porous materials, with unique structural features, high surface area, chemical tenability and stability, have been extensively studied for various applications. Advances in the design of these materials, including functionalisation of the linker with catalytically active species, add to the variation in the structures, providing a further means of tailoring MOF properties.

In this thesis, a series of MOFs, prepared from 2,2'-bipyridine-4,4'-dicarboxylate linker with La^{III}, Mn^{II}, Mg^{II}, Cd^{II} and Zn^{II} are presented. The choice of the linker was to allow MOF formation through the carboxylate moiety while the bipyridyl units act as anchoring sites for catalytically active metals such as Ru^{II} and Pd^{II}. Structural elucidation of the compounds was performed by single crystal X-ray diffraction. The topological analysis was performed on the networks to get a better understanding of network connectivity. Bulk material was characterised using thermogravimetric analysis (TGA), Fourier transform infrared spectroscopy (FTIR), powder X-ray diffraction (PXRD), scanning electron microscopy energy dispersive spectroscopy (SEM-EDS), X-ray photoelectron spectroscopy, high resolution transmission electron microscopy (HR-TEM) and nuclear magnetic resonance spectroscopy (NMR). The topological analysis revealed that the MOF constructed using La^{III}, **JMS-1** (Johannesburg and Midlands State) had a new network topology, zaz (South Africa and Zimbabwe).

The porosity of the activated phases was tested using CO_2 (298, 273, 195 K), nitrogen (77 K) and hydrogen (77 K) sorption experiments. CO_2 sorption experiments on **JMS-1a**, **Ru(II)@JMS-1a**, **JMS-3a** and **JMS-4a** showed a Type I isotherm, which is typical of microporous materials. The hydrogenation of CO_2 to formate was performed under various conditions (solvent, base, temperature, pressure, time and catalyst loading) to establish the optimum conditions. The formate product was detected and quantified by ^1H NMR spectroscopy, with acetone as an internal standard. The functionalised MOFs, **Ru(II)@JMS-1a**, **Pd@Mn: JMS-2a** and **Pd@Mg:**

JMS-2a displayed excellent catalytic hydrogenation of CO_2 under mild conditions. On the contrary, the native MOF, **JMS-1a** required harsh conditions to produce significant yields of formate. This work demonstrates that the catalytic activity of homogeneous systems can be enhanced under heterogeneous conditions by incorporating them in the MOFs.

Abbreviations

MOF	Metal organic framework
ppm	Parts per million
TON	Turnover number
TOF	Turnover Frequency
MPa	Mega Pascal
SBU	Secondary building unit
dbip	5-(3,5-dicarboxybenzyloxy)isophthalic acid
PSM	Post-synthetic modification
H_3TCPB	1,3,5-tri (4-carboxyphenoxy) benzene
dmb	4,4′-dimethyl-2,2′bipyridine
BNAH	1-benzyl-1,4-dihydronicotinamide
1D	One dimensional
2D	Two dimensional
3D	Three dimensional
IRMOF	Isoreticular metal organic framework
MIL	Matériaux de l'Institut Lavoisier
ZIFs	Zeolitic imidazolate framework
IUPAC	International Union of Pure and Applied Chemistry
PXRD	Powder X-ray Diffraction
SCXRD	Single Crystal X-ray Diffraction
FTIR	Fourier Transform Infrared
NMR	Nuclear Magnetic Resonance

TGA	Thermogravimetric Analysis
ICP-OES	Inductively Coupled Plasma-Optical Emission Spectroscopy
HR-TEM	High Resolution Transmission Electron
XPS	X-ray Photoelectron Spectroscopy
BET	Brunauer-Emmett-Teller
BTB	Benzenetribenzoate
Bpy	Bipyridine
LMCT	Ligand to metal charge transfer
LUCO	Lowest unoccupied crystal orbital
HOMO	Highest occupied molecular orbital
LUMO	Lowest unoccupied molecular orbital
CR-MOF	Rubeanate metal organic framework
OMS	Open metal site
DFT	Density functional theory
H_2bpdc	2,2’-bipyridine-4,4’ dicarboxylic acid
RCSR	Reticular Chemistry Structural Resource
CCDC	Cambridge Crystallographic Data Centre
SEM-EDS	Scanning Electron microscopy- Energy Dispersive Spectroscopy
JMS	Johannesburg and Midlands State (code used for MOFs)
zaz	Topology symbol (za, South Africa and z, Zimbabwe)

Table of contents

Acknowledgements i

Publications ii

Abstract iii

Abbreviations v

Chapter 1 Introduction 1

1.1 Climate change and CO_2 emission 2
1.2 Catalytic hydrogenation of CO_2 2
  1.2.1 Methanol from CO_2 3
  1.2.2 CO_2 methanation 4
  1.2.3 Formic acid from CO_2 4
1.3 Metal Organic Frameworks (MOFs) 9
  1.3.1 The design and synthesis of MOFs 9
  1.3.2 Gas sorption behaviour in MOFs 11
  1.3.3 Strategies to enhance adsorption of CO_2 and H_2 in MOFs 14
  1.3.4 Designing MOFs for heterogeneous catalysis 19
  1.3.5 MOF supported catalysts for photocatalytic reduction of CO_2 22
  1.3.6 MOF supported catalysts for electrocatalytic reduction of CO_2 26
  1.3.7 MOF supported catalysts for hydrogenation of CO_2 29
1.4 Organic linkers 34
1.5 Metal ions 36
1.6 Motivation and objectives of the study 37
  1.6.1 Motivation 37
  1.6.2 Objectives 38
1.7 References 39

Chapter 2 Experimental 50

2.1 Starting materials 51
2.2 General synthetic procedure 51
2.3 X-Ray Diffraction 51
    2.3.1 Single Crystal X-ray Diffraction (SCXRD) 51
    2.3.2 Powder X-ray Diffraction (PXRD) 52
2.3 Topological analysis 53
2.4 Spectroscopic analysis 53
    2.4.1 Fourier Transform Infrared Spectroscopy (FTIR) 53
    2.4.2 Nuclear Magnetic Resonance Spectroscopy (NMR) 54
2.5 Elemental analysis 54
    2.5.1 Inductively Coupled Plasma Optical Emission Spectroscopy 54
    2.5.2 CHN-analysis 54
2.6 Thermogravimetric analysis (TGA) 55
2.7 Gas sorption studies 55
2.8 High Resolution Transmission Electron Microscopy (HR-TEM) analysis 55
2.9 Scanning Electron Microscopy Energy Dispersive (SEM-EDX) analysis 55
2.10 X-ray Photoelectron Spectroscopy (XPS) 56
2.11 Chemical stability tests 56
2.12 Catalytic hydrogenation of CO_2 to formate 56
2.13 References 57

Chapter 3 Hydrogenation of CO_2 to Formate Using Novel Lanthanum(III) Based Metal Organic Frameworks. 58

3.1 Synthesis of JMS-1 and Ru(II)@JMS-1a 59
3.2 Single Crystal X-ray Diffraction 59
3.3 Structural description 60
3.4 Thermal analysis 62
3.5 FTIR analysis 64
3.6 PXRD analysis 65
3.7 Topological analysis 65
3.8 Functionalisation of JMS-1a 69
3.9 Gas sorption measurements 74

3.10 Catalytic hydrogenation of CO_2 to formate 78
3.11 Leaching, heterogeneity and recyclability studies 87
3.12 Reaction mechanism 91
3.13 Summary 92
3.14 References 93

Chapter 4 Palladium(II) Functionalised Metal Organic Frameworks for CO_2 Hydrogenation to Formate 97

4.1 Synthesis of C1 98
4.2 1H NMR and 13C {H} NMR of C1 98
4.3 Synthesis of Pd@Mg: JMS-2 and Pd@Mn: JMS-2 99
4.4 Single Crystal X-ray Diffraction 100
4.5 Structural description 102
4.6 FTIR analysis 104
4.7 Thermal analysis 105
4.8 PXRD analysis 106
4.9 Chemical stability tests 107
4.10 Nitrogen sorption studies 110
4.11 Catalysis studies 111
4.12 Poisoning studies 116
4.13 Leaching, heterogeneity and recyclability studies 118
4.14 Reaction kinetics 126
4.15 Reaction mechanism 127
4.16 Summary 129
4.17 References 130

Chapter 5 Synthesis of Cd, Zn and Mg Based Metal Organic Frameworks for CO_2 and H_2 Adsorption 132

5.1 Synthesis of JMS-3, JMS-4 and JMS-5 133
5.2 Single crystal X-ray diffraction 134

5.3 Structural description of JMS-3 134
5.4 Topological analysis of JMS-3 140
5.5 Structural description of JMS-4 140
5.6 Topological analysis of JMS-4 145
5.7 Structural description of JMS-5 145
5.8 Topological analysis of JMS-5 150
5.9 Chemical stability studies 151
5.10 Gas sorption studies 156
5.11 Summary 160
5.12 References 161

Chapter 6 Conclusion 163
6.1 Summary 164
  6.1.1 Hydrogenation of CO_2 to Formate Using Novel Lanthanum(III) Based Metal Organic Frameworks. 165
  6.1.2 Palladium(II) functionalised Metal-Organic Frameworks for Carbon Dioxide Hydrogenation to Formate 168
  6.1.3 Synthesis of Cd, Zn and Mg Based Metal Organic Frameworks for CO_2 and H_2 Adsorption 170
6.2 Final Remarks and future works 172
6.3 References 174

Appendices 176

CHAPTER 1

Introduction

This chapter gives an overview of several aspects such as climate change and carbon dioxide emissions, catalytic hydrogenation of CO_2 to value-added chemicals and the design and synthesis of metal organic frameworks for H_2 and CO_2 storage, with subsequent conversion to formate. The various strategies that are used to enhance CO_2 capture and conversion in MOFs are also discussed.

1.1 Climate change and CO_2 emission

The concentration of carbon dioxide (CO_2) in the atmosphere has reached unprecedented levels and already exceeds 400 ppm. It is further predicted this will reach ~570 ppm by the end of the twenty-first century, mainly due to the utilisation of carbon-rich fossil fuels such as coal, natural gas and oil.[1–3] The increase in CO_2 emissions arguably contributes to the increase in global temperatures and climate change due to the 'greenhouse effect'.[4–7] Global warming and climate change have a wide range of potential ecological, physical and health impacts, including extreme weather events (such as floods, droughts, storms and heatwaves), sea-level rise, altered crop growth and disrupted water systems.[8,9] As a result, there has been increasing pressure on the scientific and technological community to curb CO_2 emissions and to develop efficient CO_2 capture and utilisation systems.

In essence, there are three possible strategies concerning reducing CO_2 emissions namely; a reduction of the amount of CO_2 produced, storage, and usage.[10] The first approach requires energy-efficient improvements and diverting from fossil fuels to less carbon intensive energy sources such as hydrogen and renewable energy. The storage of CO_2, which involves the development of new technologies for capture and sequestration of CO_2, is a relatively well-established process.[10,11] The utilisation of CO_2 as an increasingly attractive C1 building block, not only contributes to alleviating global climate change induced by increasing CO_2 emissions in the atmosphere but also opens new sustainable routes for synthesising useful feedstock chemicals and fuels. [5,9,11–16] On the other hand, the use of CO_2 as a chemical feedstock is limited to a few industrial processes due to its chemical inertness and thermodynamic stability, [8,17–19] which in turn requires highly active catalysts,[20] electrical reductive[21] or photocatalytic methods[22] to promote CO_2 transformation into other chemicals.

1.2 Catalytic hydrogenation of CO_2

Catalytic hydrogenation is among the most important conversion pathways for CO_2, leading to a wide range of fuels and chemicals such as methanol, methane, formic acid and higher hydrocarbons (Scheme 1.1), depending on the reaction conditions and catalyst used. [1,19, 23]

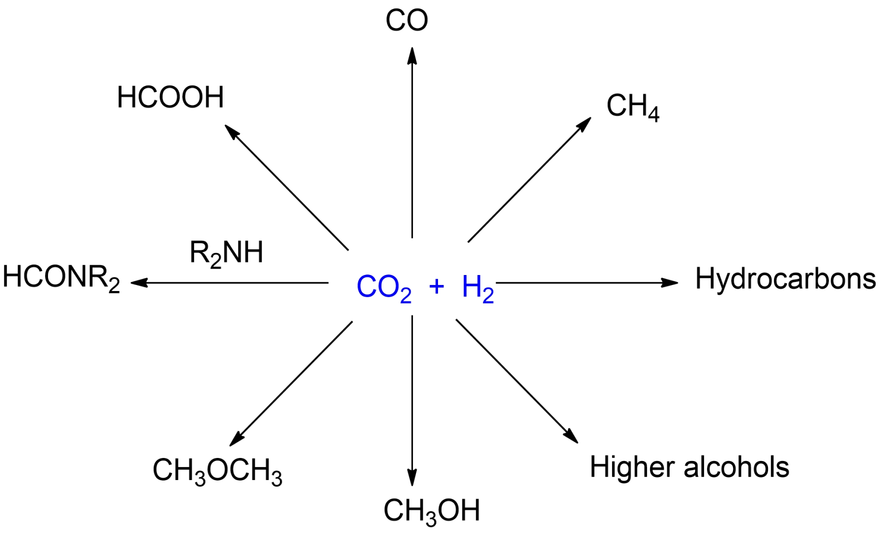

Scheme 1.1: Products from CO_2 hydrogenation.[19]

1.2.1 Methanol from CO_2

Methanol (CH_3OH) represents a particularly attractive product as it can be directly used as fuel in internal combustion engines, gas turbines, direct methanol fuel cells, as a C1 source in organic transformations and as a solvent or a chemical precursor for the production of higher hydrocarbons.[24] Industrially, CH_3OH is produced from syngas (CO, H_2 and CO_2) at high temperatures and pressure over $Cu/ZnO/Al_2O_3$ based heterogeneous catalysts.[25] CO_2 has replaced CO and is considered an effective, and relatively safer, input molecule for methanol production.

$$CO_2 + 3H_2 \longrightarrow CH_3OH + H_2O \quad \Delta H_{298\ K} = -49.5\ kJmol^{-1}$$

From a thermodynamic point of view, a decrease in reaction temperature or an increase in reaction pressure could favour the synthesis of methanol. Indeed, enhanced reaction temperature (e.g., higher than 513 K) facilitate CO_2 activation and subsequent methanol formation.[26] Furthermore, other by-products are formed during the hydrogenation of CO_2 such as hydrocarbons, and higher alcohols. Therefore, a highly selective catalyst is required to avoid the formation of undesired by-products during methanol synthesis. In the past six years, homogeneous catalysts mainly based on noble metals like ruthenium and iridium, have also been reported for direct or indirect CO_2 reduction to CH_3OH with molecular H_2 at much lower temperatures and pressure. [27–29]

Methanol is not just a fuel and base chemical used to produce other commodity chemicals; it is also relevant as a hydrogen carrier. Hydrogen is regarded as a low carbon energy technology and its widespread application, in this capacity, has been precluded by technical complications around its storage and transportation. Methanol can carry up to 12.5 wt.% H_2 reversibly, in a liquid form that is easy to drop into existing high carbon liquid fuels infrastructure.[30] As a result of this methanol is expected to play a profound role in the hydrogen economy.

1.2.2 CO_2 methanation

Considering the importance of methane (CH_4) as a potential solar fuel and that CO_2 is a good feedstock from the environmental point of view in terms of availability, supported noble metals or nickel have been known to catalyse the methanation of CO_2. Catalysts, reaction conditions, and mechanistic concepts are thoroughly reviewed by Wang *et al*. covering the literature up to 2010. Among the metals tested, ruthenium exhibits superior activity and selectivity.[31] Since the conversion of CO_2 to CH_4 is exothermic, it is highly desired to develop catalysts for low-temperature operation favouring high degrees of CO_2 conversion. Low temperatures are also favourable for suppressing the undesired reverse water-gas shift (RWGS) reaction, which is endothermic.

1.2.3 Formic acid from CO_2

The production or synthesis of formic acid (FA) is very important as it plays a major role in synthetic chemistry as an acid, reductant and precursor for synthesis.[32] Formic acid is a starting material for the production of formate esters, which allows access to a range of useful organic derivatives such as aldehydes, ketones, carboxylic acids and amides.[19] Formate esters can be used in a variety of industries such as perfumes and fragrances, in paints and dyeing agents as well as in mordant and auxiliary agents. Formate salt readily made from formic acid is a preferred de-icing agent on aeroplane runways because it is less corrosive than chloride salts. [17] Moreover, FA has emerged as a promising fuel source in direct liquid fuel cell systems due to its excellent oxidation kinetics, high cell potential and fewer crossover problems.[33]

The hydrogen economy requires renewable methods for producing hydrogen, safe and reversible methods for storing it and efficient fuel cells for using hydrogen and water to produce electricity. FA has lately emerged as a promising hydrogen storage material because of its relatively high H_2 content (4.4 wt.%), low toxicity and liquid state under ambient conditions, making it easy to store and transport. [34,35] FA also has the added advantage of the facile release of its H_2 content under ambient conditions.[36] Tsang and colleagues have shown that hydrogen stored in formic acid can be released under ambient conditions by using core-shell silver-palladium nanoparticles as catalyst (Scheme 1.2).[37] Thus, the myriad applications of FA, as well as CO_2 utilisation, attracts the hydrogenation of CO_2 to FA/ formate in the scientific community to a greater extent.

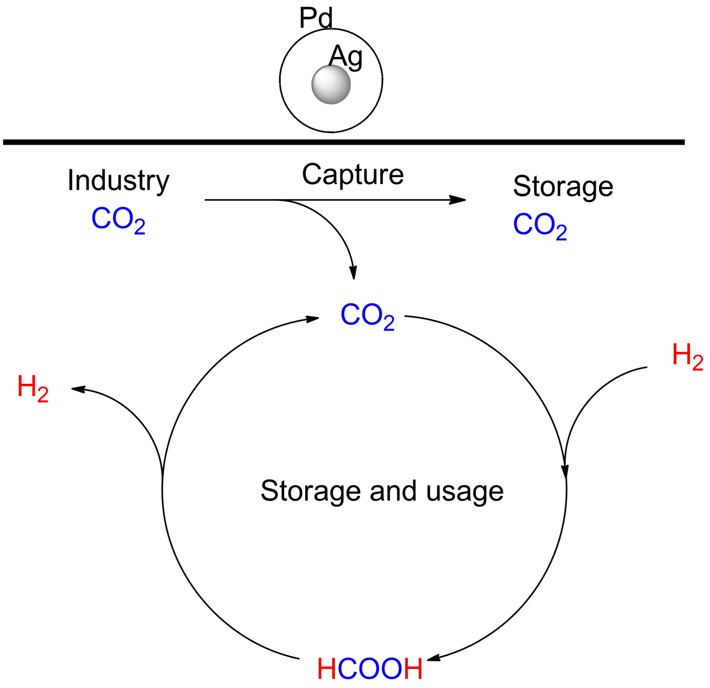

Scheme 1.2: Hydrogen storage cycle established using formic acid as a hydrogen source. [36,37]

CO_2 hydrogenation to FA has been extensively studied using both homogeneous[17,38] and heterogeneous[3,39] catalysts. Since the discovery of phosphine-based ruthenium complexes by Inoue and co-workers,[40] excellent progress has been achieved in the development of homogenous catalysts for the hydrogenation of CO_2 to formate. In particular, extensive studies focusing on homogeneous Ir[13,34], Ru[28,41,42] and Rh[38] complexes have been reported due to their high activities. Recently, a half-sandwich iridium pincer complex has shown tremendous catalytic activity, with a maximum turnover number (TON) of 3 500 000 and maximum turnover frequency (TOF) of 1 100 000 hr^{-1} in aqueous KOH generating potassium formate (HCOOK).[43]

The possible reaction mechanism for the hydrogenation of CO_2 using the complex is illustrated in Scheme 1.3. The catalytic cycle consists of iridium trihydride **1**, iridium formate **2** and imidoiridium dihydride **3**. Exposure of trihydride complex **1** to 1 atm CO_2 led to immediate equilibrium between 1 and dihydridoiridium(III) formate **2** at 25 °C, as observed by 1H and 13C NMR spectroscopy. The two distinct hydride signals of **2** indicated that the formato ligand was located *cis* to the nitrogen atom of the pyridine moiety. The next step involved the elimination of formate from **2**, accompanied by deprotonation from Ar-CH_2-P and subsequent dearomatisation of the pyridine ring, gave amidoiridium dihydride complex **3**. The cycle is completed by the hydrogenation of **3** to regenerate the trihydride complex **1**.

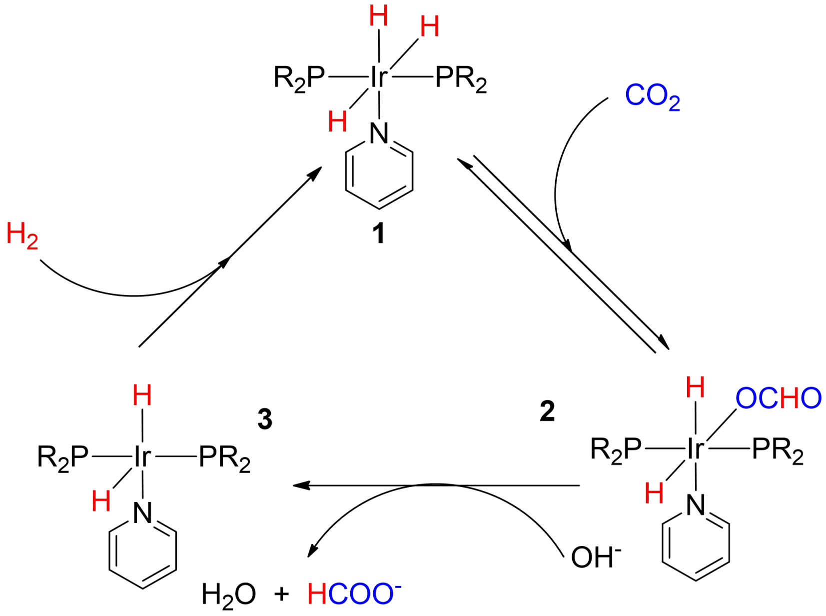

Scheme 1.3: The plausible mechanism for the hydrogenation of CO_2 using iridium trihydrate complex. Reprinted with permission from ref 43. Copyright (2009) American Chemical

Society.

Although the reported homogeneous complexes exhibit excellent catalytic efficiency for the hydrogenation of CO_2 to formate, industries are still reluctant to use them for large-scale production owing to the difficulty in catalyst separation from the final reaction mixture.[44] These homogeneous catalysts also promote the decomposition of the generated formate back to CO_2 and H_2 during product separation steps.[45,46] Because of such limitations, diverse heterogeneous catalysts which have strong merit in separation have been investigated.

The heterogeneous route is preferable in terms of stability, simplicity of separation, recyclability and reusability of the catalysts, handling as well as reactor design, which reflects in lower costs for large-scale industrial productions.[39,38,] Heterogeneous hydrogenation of CO_2 can be accomplished on metal surfaces such as Ni,[47] Co[48] and Cu.[49] Accordingly, several supported/unsupported metal nanoparticle-based heterogeneous catalysts and several heterogenised catalysts have been considered in the search for active and recyclable CO_2 hydrogenation catalysts.[39,44,50,51] Gunasekar *et al* [3] heterogenised the [IrCp*(N-N)X]Y complex using gC$_3$-N (1) and HBF (2) supports shown in Figure 1.1. The uniform metalation, as well as the ratio of Ir to Cl (1:2), were confirmed by SEM and EDS respectively. ICP-MS of the catalyst showed 0.86 wt.% Ir in the framework. The catalyst exhibited an initial TOF of 1500 hr^{-1} and TON of 6 400 at 120 ˚C under 8 MPa total pressure. The catalyst was recycled without significant loss in catalytic activity and stability.

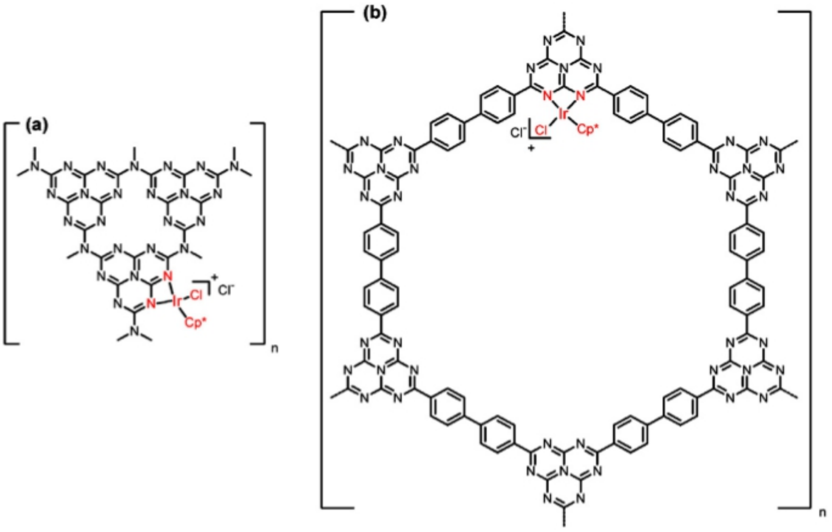

Figure 1.1: Structural representation of HBF heterogenised catalysts 1(a) and 2(b).[3]

Recently, Maru and co-workers developed a ruthenium-grafted hyrotalcite (Ru-HT) as a heterogeneous catalyst for the hydrogenation of CO_2 to formic acid. The hyrotalcite supported Ru(II) based catalyst played a double role, (i) as a base/promoter and (ii) as a catalyst supporter. A maximum TON of 11 389 was obtained for formic acid formation at moderate reaction conditions (60 ˚C and 60 bar (1:1, $_pCO_2/_pH_2$)) using methanol: water (5:1, v/v) as a solvent in 24 hours without using a base. The catalyst was effectively recycled up to 7 times without loss in catalytic activity.[52]

The hydrogenation of CO_2 to formate in the presence of metallic cobalt nanoparticles supported on nitrogen-rich graphitic carbon was reported.[48] The catalyst was highly active for the catalytic hydrogenation of CO_2 to formate in the presence of 1M KOH solution at 120 ˚C. A 1:1 partial pressure of $_pCO_2/_pH_2$ was used to obtain a high TON of 82 265 in 24 hours. Furthermore, the catalyst could be reused for four consecutive cycles without significant loss in catalytic activity.

Based on experimental results and literature findings, the reaction pathway for the formation of formic acid presented in Scheme 1.4 was proposed. At first, hydrogen molecules diffuse to the catalytic sites, and then get activated by cobalt metal centre to engender the hydride bonds and form Co-hydride intermediate. On the other hand, the basic nitrogen atoms present on the support additionally help the heterolytic dissociation of H_2 in aqueous conditions. To this intermediate, hydride attachment takes place directly to a carboxylate carbon atom, which follows a 1st order dependence on CO_2 and also the rate-determining step. The formate intermediate is separated from the active site to give potassium formate and water.

The same mechanism was proposed by Song and coworkers,[56] who investigated the hydrogenation of CO_2 to formic acid over palladium catalysts supported on chitin. Under optimal conditions, 0.25 % Pd/chitin exhibited impressive catalytic activity with turnover frequency of 257 hr^{-1}, under 4 MPa ($_pCO_2$ = $_pH_2$ = 2 MPa) in water at 60 ˚C after 1 hour. The results indicate that the acetamide group in chitin promotes the distribution of Pd particles on the surface, and accelerates the hydrogenation of CO_2 due to its coordinating ability to transition metal and Lewis basic properties.

Heterogeneous catalysts are easily recovered after reaction and are applicable to a continuous reaction system in a large industrial process.[53] However, if the catalysts show low catalytic activity and poor chemoselectivity, corresponding reaction conditions are harsh.[54,55]

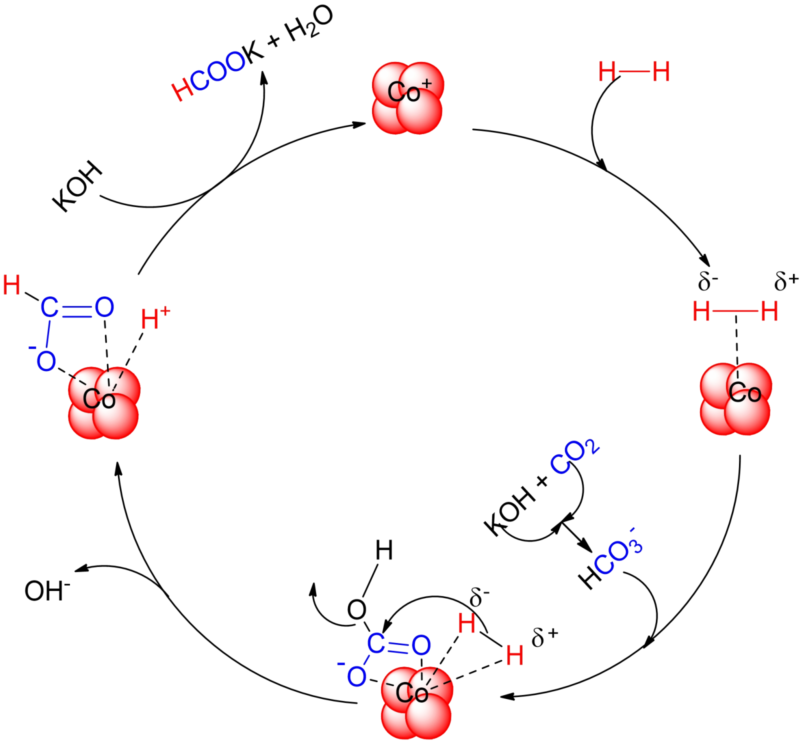

Scheme 1.4: Probable mechanism for the hydrogenation of CO_2 to formate.[48]

Hence a potent catalyst-design strategy that provides a pathway for both enhanced catalytic activity under relatively mild conditions is essential to develop industrially viable recyclable heterogeneous catalysts. Significant efforts are being devoted to developing catalytic materials with high surface area, large adsorption capacity for CO_2, and both high and stable catalytic activity to facilitate the energy-efficient conversion of CO_2. Amongst the potential candidates, metal organic framework (MOFs) have an advantage over other adsorbents or catalysts in CO_2 chemistry in terms of CO_2 capture efficiency with the additional benefit of being able to catalyse CO_2 conversion reactions.[56] The following section, therefore, focuses on recent advances in the field of MOFs, not only as CO_2 capture materials but also as efficient catalysts for the conversion of CO_2 to high-value chemicals.

1.3 Metal Organic Frameworks (MOFs)

1.3.1 The design and synthesis of MOFs

MOFs are a special group of coordination polymers that are currently attracting a tremendous amount of interest due to their unique properties, such as high surface area, tuneable pore size distribution, and uniform-structured cavities which makes them promising candidates for diverse applications in gas storage,[57] separation, [58] catalysis,[59] and sensing.[60–62] Their structure is defined by metal ions or clusters containing metals acting as lattice nodes that are held in place by bi-and multinodal rigid organic linkers as illustrated in Scheme 1.5. [63,64]

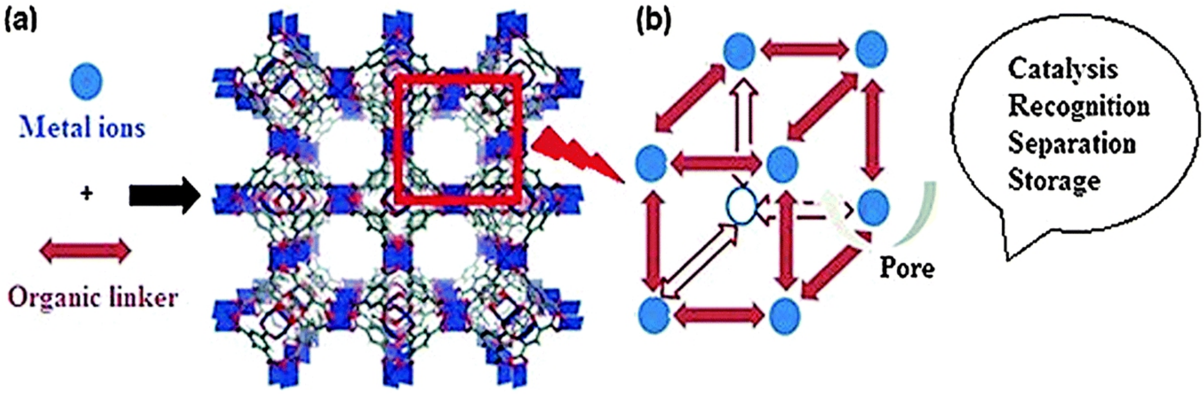

Scheme 1.5: a) Schematic representation of MOF synthesis b) MOF applications. Adapted from ref 64 with permission from the Royal Society of Chemistry.

The linkers are often organic molecules with specific functional groups such as carboxylate or nitrogen donor moieties, which interact strongly with metal nodes (metal ions or clusters) via covalent or coordination bonds.[65] Desired architectural, chemical and physical properties of MOFs depend on the chemical structure of the ligand and the properties of the connecting metal. The directionality of the metal-ligand coordination bonds is responsible for the creation of empty spaces and voids in the lattice, while the stability of the framework depends on the strength of these coordination bonds that have intermediate energy between covalent bonds and weak intermolecular forces.[66] A wide range of network topologies is designed by aggregating molecular building blocks to achieve a specific structure and objective. Depending on different coordination numbers and environment, metal connectors can form many possible geometry centres such as linear, angled, triangle, square planar, tetrahedral, square pyramidal and octahedral centres. The so mentioned motif extends the structure into one-, two- and three-dimensional (1D, 2D, 3D) frameworks with structural flexibility and/or robustness. However, the establishment of permanent porosities is crucial for their function and provides these materials with high surface areas.

With many kinds of metal centres, ligands and synthetic methods, a large number of MOF structures were produced. Yaghi *et al.*[67] demonstrated the systematic design and synthesis of the IRMOF series (IR stands for isoreticular) depicted in Figure 1.2. By reacting dicarboxylate type ligands of different length and functional groups with zinc nitrate, they successfully synthesised a series of isostructures with different pore sizes and functionalities. Ferey group[68] used aluminium nitrate or chromium nitrate and 1,4-benzenedicarboxylic acid to obtain MIL-53 (MIL = Matériaux de l'Institut Lavoisier). Besides the carboxylate ligand MOF series, new series of imidazolate ligand MOFs, ZIFs (zeolitic imidazolate frameworks) were also developed.[69]

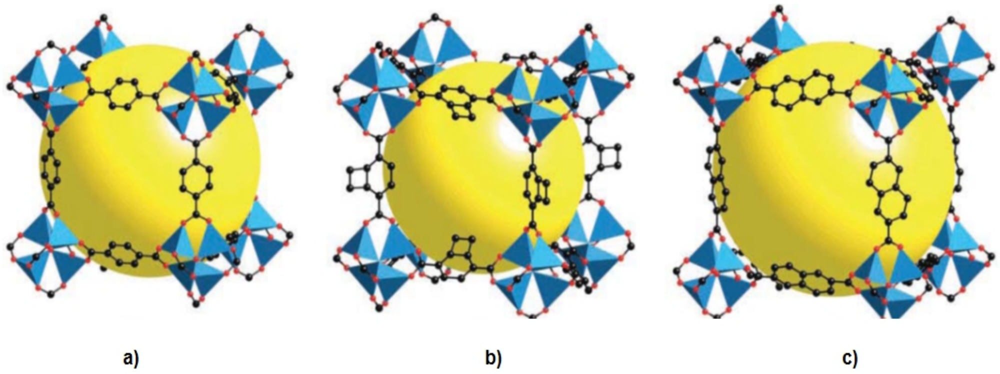

Figure 1.2: Structures of a) IRMOF-1 b) IRMOF-6 c) IRMOF-8.[67]

1.3.2 Gas sorption behaviour in MOFs

Over the last two decades, MOFs have been extensively studied for gas adsorption and separation, where they have been shown to outperform other materials, such as zeolites, silica and metal oxides, in terms of adsorption capacities for CO_2 as reviewed in several articles.[70–72] The high adsorption capacities are attributed to high porosity, large surface area, tuneable functionalities as well as chemical interaction between CO_2 molecules with metal centres or organic ligands within MOFs.

Adsorption in MOFs is mostly characterised by the phenomenon of physisorption whereas chemisorption takes place if the MOF features reactive functional groups,[73] or coordinatively unsaturated metal sites[74] and reactive adsorptive such CO, CO_2, NO are used. Physisorption is assumed to rely on non-specific interactions and happens whenever a gas gets in contact with the solid surface. If the adsorbate is a nonpolar gas like CO_2, and /or the adsorbate features a polar surface, like in many MOFs, specific interactions are very important and predominant the sorption process.[75] Nevertheless, the process is still regarded as physisorption if no chemical bonding takes place.

Gas sorption properties can be determined with various techniques, including the accommodation of sorption isotherms, either via volumetric or gravimetric methods. Adsorbate uptake is monitored at a constant temperature depending on the final pressure or pressure range. Based on these measurements, various properties such as specific surface area, pore volume, pore size and pore distribution can be derived. More so, general information about the nature of the material can be extracted.

Adsorption isotherms are classified by International Union of Pure and Applied Chemistry (IUPAC) into six different types, shown in Figure 1.3, which allows a direct classification of the studied material based on the shape of the isotherm[76]. The Langumuir adsorption isotherms are characteristics of adsorbents that are microporous (type I), nonporous and macroporous (types II, III and IV) and mesoporous (types IV and V). The differences between types II and III and types IV and V arise from the relative strength of gas-solid and gas-gas attractive interactions. When the gas-solid attractive interaction is stronger than that of gas-gas, the adsorption isotherm should be types II and IV, and opposite situation leads to types III and V.[76–78]

MOFs are almost exclusively microporous, but mesoporous MOFs and even microporous-mesoporous MOFs have been reported recently. In terms of commercial and industrial applications in gas storage and separation, microporous materials are promising. The surface area is commonly derived from the data of physisorption isotherms (usually nitrogen isotherms recorded at 77K) by applying the BET method, developed by S. Brunauer, P. H. Emmett and E. Teller in 1938.[79]

Millward and Yaghi[80] investigated room temperature adsorption equilibrium data for CO_2 in a large variety of MOFs shown in Figure 1.4. The list represents frameworks of various characteristics such as square planar (MOF-2), packed cylindrical channels (MOF-505 and $Cu_3(BTC)_2$)), pores with open metal sites (MOF-74), interpenetration (IRMOF-11), alkyl and amino functionalised pore (IRMOF-3 and 6) and ultrahigh porous framework (IRMOF-1 and MOF-177). Amongst them, the 3D MOF-177, synthesised from a solvothermal reaction of 1,3,5-benzenetribenzoate (BTB) and $Zn(NO_3)_2.6H_2O$, gave the highest surface area, with Brunauer-Emmet-Teller (BET) surface area of 4508 m^2g^{-1}.[80, 81] The CO_2 adsorption isotherms of the selected MOFs are shown in Figure 1.5. The volumetric space enclosed by MOF-177 resulted in a CO_2 capacity of 33.5 $mmolg^{-1}$.

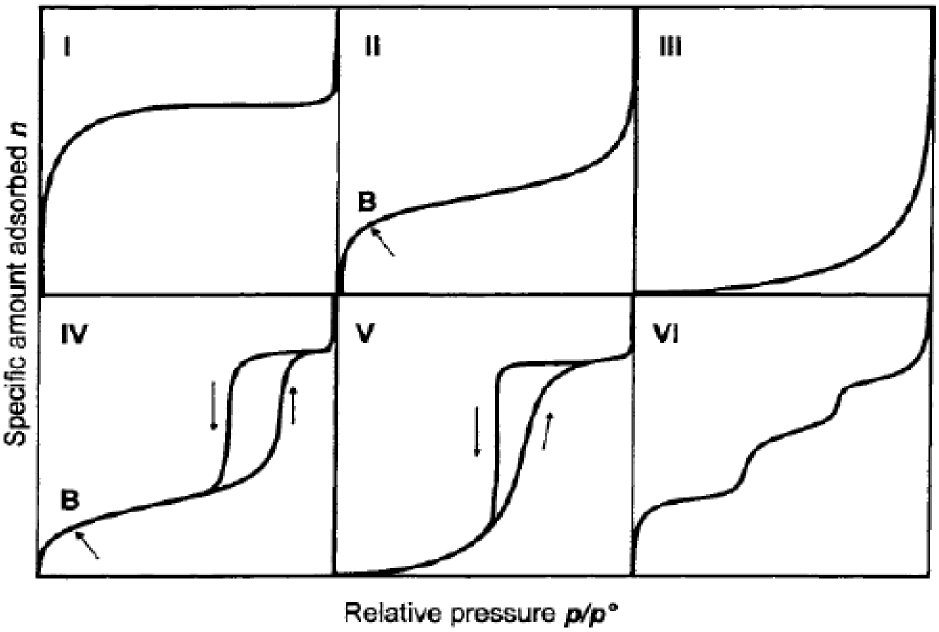

Figure 1.3: IUPAC classification of adsorption isotherms[76]

A comparison in Figure 1.6, was also made between MOF-177 and the benchmark commercial materials at that time such as zeolite 13X and MAXSORB (a type of activated carbon). Zeolites are among the earliest highly successful porous materials for industrial applications. The highest reported gravimetric CO_2 capacity for zeolite 13X at 25 °C was 7.4 $mmolg^{-1}$ (at 32 bar). On the other hand, MAXSORB showed uptake of 25 mmolg^{-1} (at 35 bar) whist MOF-177 had a gravimetric uptake of 33.5 mmolg^{-1} at 25 °C and 42 bar, exceeding that of the benchmark materials. Interestingly, a container filled with MOF-177 could absorb twice the amount of CO_2 than a container filled with the benchmark materials and nine times the amount of CO_2 than a container without adsorbent. [80]

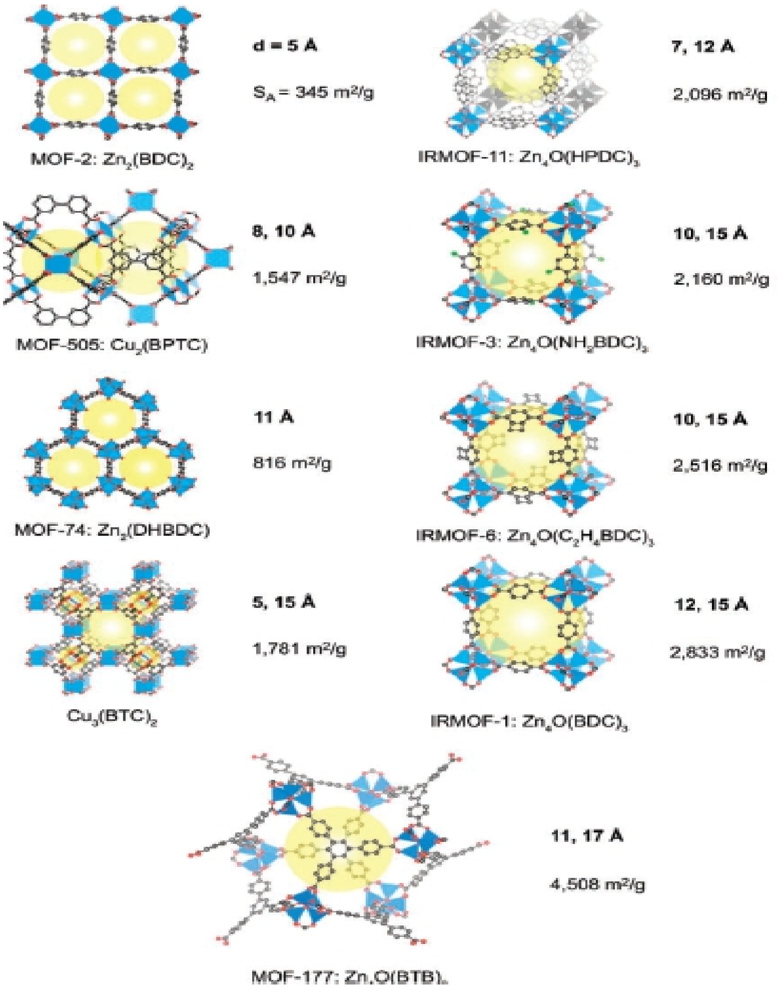

Figure 1.4: Structures of MOFs examined for CO_2 storage capacity at room temperature. The formula, surface area and pore size are given for each framework. Voids are shown as yellow spheres. Reprinted with permission from ref 80. Copyright (2005) American Chemical Society.

1.3.3 Strategies to enhance adsorption of CO_2 and H_2 in MOFs

To improve the gas adsorption capacity (e.g. H_2, CO_2, CH_4,) and separation (e.g. CO_2/N_2, CO_2/CH_4), current efforts are devoted to enhancing the gas binding affinity in MOFs. Strategies reported include increasing the pore size, retention of porosity after guest removal, incorporation of open metal sites, grafting of amines into the frameworks and introduction of nitrogen-rich organic linkers.[82–84]

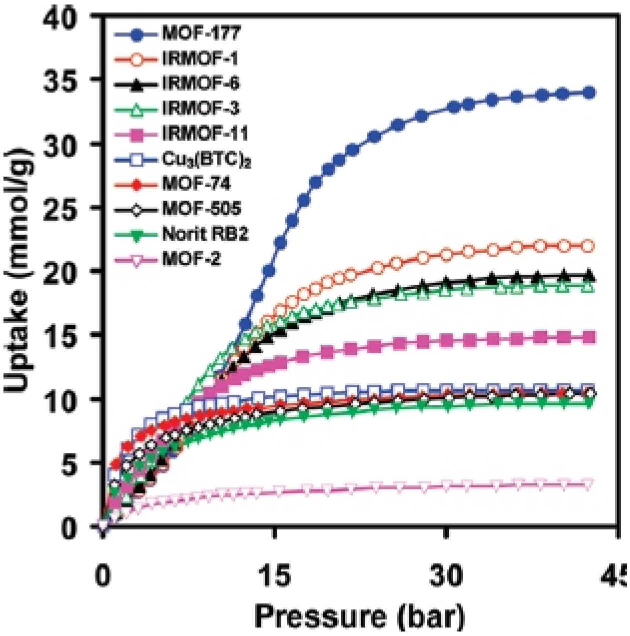

Figure 1.5: Comparisons of gravimetric CO_2 capacities for the MOFs (and activated carbon as a reference) determined at ambient temperature and pressures up to 42 bars. Reprinted with permission from ref 80. Copyright (2005) American Chemical Society.

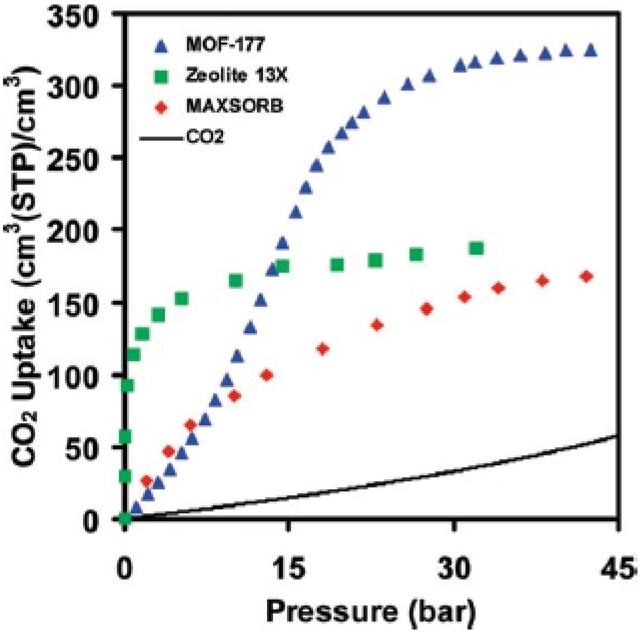

Figure 1.6: A comparison of volumetric CO_2 capacity of MOF-177 relative to zeolite 13X, MAXSORB carbon powder and pressurised CO_2. Reprinted with permission from ref 80. Copyright (2005) American Chemical Society.

In the first approach, both theoretical and experimental investigations focused on the construction of MOFs with large potential solvent-accessible volumes. A common strategy involves the use of elongated ligands to construct the MOFs. For example, a series of non-interpenetrating flexible MOFs formulated as $\{[Cd(tdm)(L_{pillar})_4].x\text{solvent}\}_n$ $\{H_8tdm$ = tetrakis-[(3,5-dicarboxyphenoxy)methyl]methane; L_{pillar} = 4,4'-bipyridine (bipy), 4,4'-azopyridine (azpy) and etbipy} have been prepared based on pillaring strategy.[85] As shown in Scheme 1.6, the binuclear $\{Cd_2(\mu\text{-}O)_2O_6N_4\}$ units are linked by tdm^{8-} to give rise to neutral 2D sheets with square windows of 10 x 10 Å^2 in the *ab* plane, which are further pillared by various secondary pyridyl ligands (L_{pillar}) along *c* axis giving rise to **nbo**-networks. With the increase in pillar length, eg., from bipy to etbipy, the openings of the network cavities changed from 11.7 to 14.0 Å and pore volume ratio of these frameworks vary from 59 to 62.6 % accordingly.

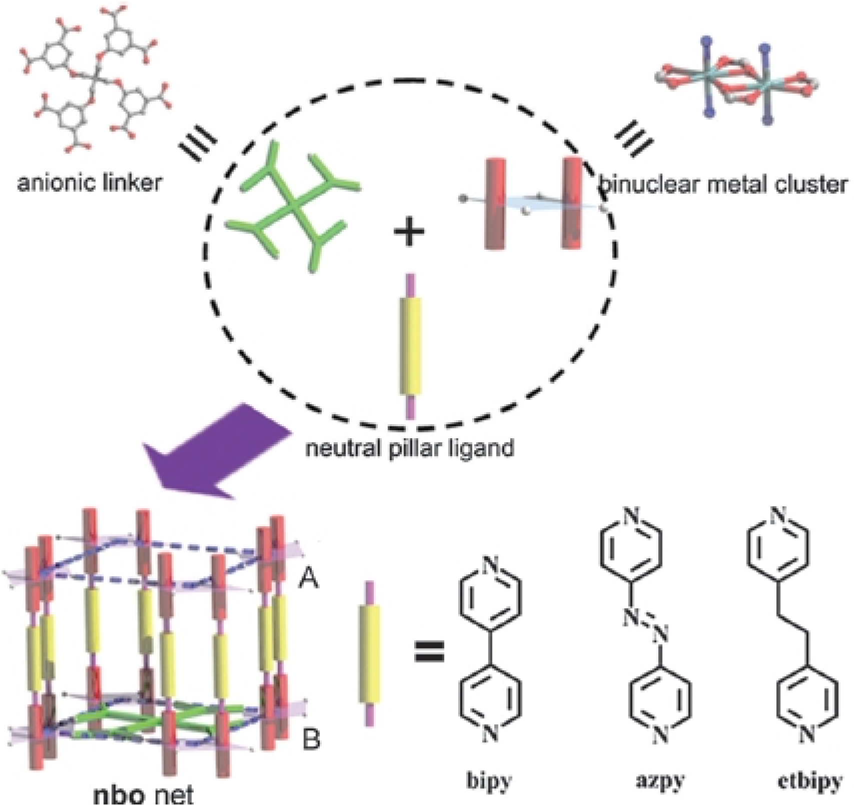

Scheme 1.6: Representation of the pillaring strategy for the synthesis of $\{[Cd(tdm)(L_{pillar})_4].xsolvent\}_n$. Adapted from ref 85 with permission from the Royal Society of Chemistry.

In principle, the use of longer ligands risks bringing in framework interpenetration, which reduces solvent-accessible void volume and leads to less porous structures. While interpenetration reduces pore size, it is not necessarily a disadvantage. The structure may still exhibit useful properties such as an increase in stability, due to an increase in the amount of supramolecular interaction per framework. [86]

Secondly, it is necessary to retain MOF porosity after removal of guest solvent molecules for their application in gas adsorption and separation. An effective strategy to implement permanent porosity on MOFs is to employ mild activation methods to minimise the collapse of the framework. Liang and co-workers synthesised a flexible MOF based on H_4dbip ligand formulated as $\{[Cu_2(dbip).(H_2O)_2.$ *x*solvent$\}_n$ {dbip = 5-(3,5-dicarboxybenzyloxy)isophthalic acid}.[87] The framework had a potential void volume of 67.2 %. The activated sample, prepared by the solvent exchange at 65 °C, shows a BET surface area of 1773 m^2g^{-1}, high CO_2 uptake of 170

cm^3g^{-1} (at 273 K and 0.95 bar) as well as high selectivity of CO_2/N_2 (20.6 at 273 K). However, activation *via* directly heating the fresh sample at 100 ^oC, yielded a BET surface area of only 232 m^2g^{-1}.

Britt and co-workers[88] reported that a MOF with open metal sites, Mg-MOF-74 (Scheme 1.7) showed excellent selectivity, facile regeneration among the highest dynamic capacities reported for CO_2 in porous materials. Specifically, when Mg-MOF-74 was subjected to a gas stream containing 20% CO_2 in CH_4, a percentage in the range relevant to industrial separations, it captured only CO_2. The pores retained 89 g of CO_2 per kilogram of the material before the breakthrough, a value that rivals the highest capacities in zeolites. Interestingly, 87% of the captured CO_2 could be liberated at room temperature and the remaining under mild heating (80 °C). Based on these results, we ascertain that MOFs with open metal sites represent a competitive class of materials for CO_2 capture, notwithstanding the great opportunities available for functionalisation of such MOFs for improved performance.

Because of the dipole-quadruple interactions between polarisable CO_2 molecule and the accessible nitrogen site, theoretical investigations have shown that the incorporation of accessible nitrogen-donor groups, such as pyridine, amine, imidazole, and tetrazole dramatically enhances the gas binding affinity in MOFs. Demessence *et al*. grafted ethylenediamine (en) onto the exposed Cu^{II} sites on the surface of a water-stable triazole-bridged framework, CuBTTri as shown in Figure 1.7.[89]

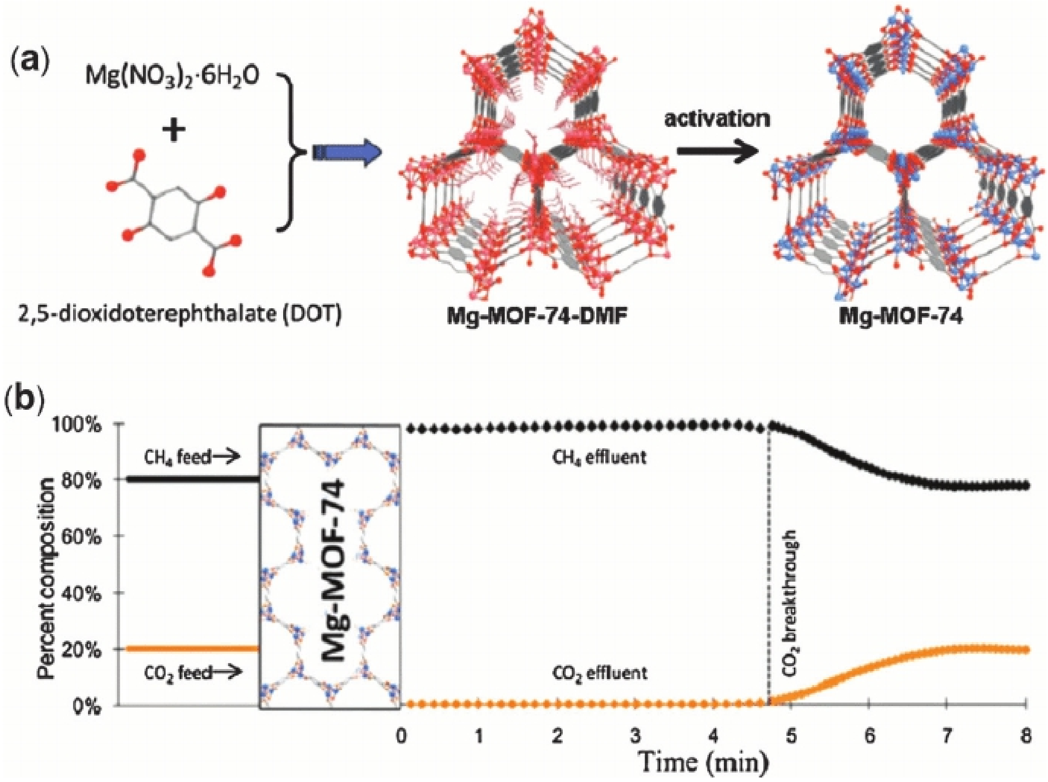

Scheme 1.7: a) Crystal structure of Mg-MOF-74 synthesised through the reaction of DOT linker and $Mg(NO_3)_2·6H_2O$ b) A 20% of CO_2 in CH_4 is fed into a bed of Mg-MOF-74. Effluent concentration is shown, indicating complete retention of CO_2 until saturation. A breakthrough occurs at the dashed line.[88]

The resulting en-CuBTTri exhibited an increased uptake of CO_2 at 298 K under the pressure of up to 0.1 bar, as well as higher CO_2/N_2 selectivity at low pressure than the pristine MOF. For example, en-CuBTTri took up a higher amount of CO_2 (0.36 mmolg^{-1}, 1.6 wt.%) as compared to pristine CuBTTri (0.277 mmolg^{-1}, 0.92 wt.%) at 0.06 bar. Thus the introduction of nitrogen-rich groups in MOFs either during or after their fabrication along with intrinsic porous properties of MOFs, such as high porosity and large pore volume, endow the nitrogen-rich MOFs a high capacity of CO_2 capture.

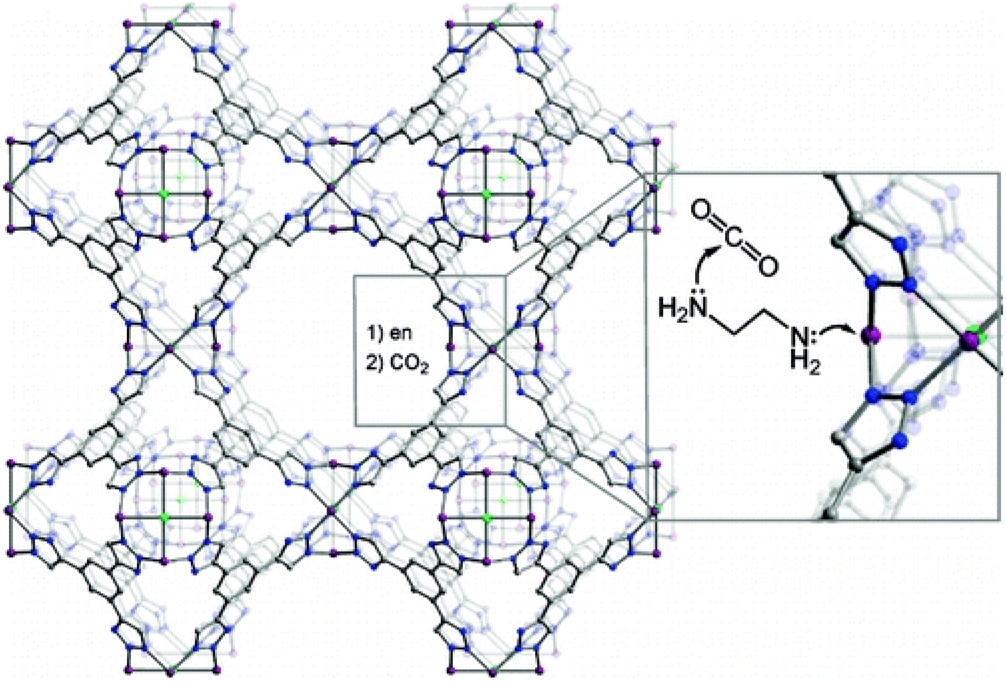

Figure 1.7: A portion of the structure of Cu-BTTri frameworks showing functionalisation of a coordinatively unsaturated Cu^{II} site with ethylenediamine, followed by the attack of an amino group on CO_2. Adapted with permission from ref 89. Copyright (2009) American Chemical Society.

1.3.4 Designing MOFs for heterogeneous catalysis

One of the most recognisable areas of MOF's research is heterogeneous catalysis.[56,62–73] In contrast to other crystalline porous solids, the high versatility of MOF design provides clear advantages for catalysis because of the possibility in rational and precise design of the active site as well as the environment of MOFs.[101] The catalytic function of MOFs can be incorporated at the organic[33] or inorganic[59] component through the direct synthesis of the envisaged scaffold or post-synthetic modification (PSM).[98] Thus, the capacity to insert functional groups into porous MOFs and the presence of well-defined channels make these materials attractive candidates for heterogeneous catalysis.[31] Two different strategies, illustrated in Scheme 1.8, have been utilised to synthesise catalytically active MOFs.[102] In the first approach, (a), the metal-connecting points with unsaturated coordination environments are utilised as catalytically active sites. These metal nodes typically have coordinated solvent molecules that can be easily removed without distorting the MOF structure. Such accessible, coordinatively unsaturated metal centres can then be used to catalyse the organic reactions.

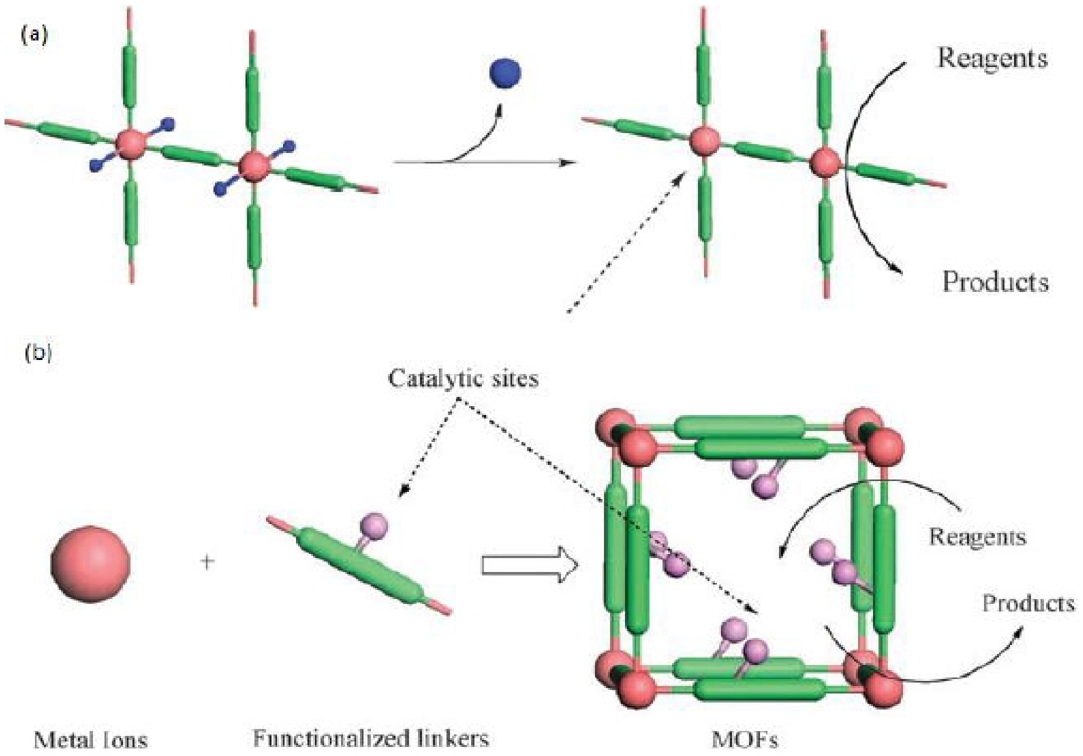

Scheme 1.8: (a) Coordinatively unsaturated metal centres as active catalytic sites. (b) Incorporation of active catalytic sites into the bridging ligands of MOFs. Reproduced from ref 102 with permission from The Royal Society of Chemistry.

In the second approach, (b), catalytic sites are incorporated directly into the bridging ligands used to construct the MOFs. Although more synthetically demanding, the second approach is much more versatile and allows for the incorporation of a wide variety of catalysts. Thus a good MOF catalyst should have: (i) coordinatively unsaturated metal sites, (ii) functionalised organic linkers to activate the reactions; and (iii) the potential to incorporate metal complexes into the organic linker and pores.[64] The linkers can be functionalised with different chemical groups to enhance gas adsorption [103–105] or to mimic ligands in organometallic complexes, thereby stabilising homogeneous organometallic complex catalysts in a solid matrix.[106,107]

Lin and co-workers[108] assembled $Zn(NO_3)_2$ with the tripodal ligand H_3TCPB (1,3,5-tri (4-carboxyphenoxy) benzene) to afford two porous isoreticular MOFs $[Zn_3(TCPB)_2.2DEF].3DEF$ and $[Zn_3(TCPB)_2.2H_2O].2H_2O.4DMF$. Upon the removal of solvent molecules, the MOFs exhibited a highly selective adsorption behaviour towards H_2/N_2, CO_2/N_2, CO_2/CH_4. The coordinatively unsaturated Zn^{2+} sites in the framework could serve as Lewis acid catalytic sites for carbonyl cyanosilylation and Henry reaction with high conversions. Both catalytic systems were dependant on the size of the substrates. The MOFs could be recovered and maintained good activities in catalytic subsequent runs.

Incorporating catalytically active moieties into the organic linkers was experimentally demonstrated by Luan *et al.*[109] who utilised a Zr-based MOF with bipyridine units (UiO-67) for the immobilisation of catalytically active iron species via a post-synthetic metalation method, as depicted in Equation 1.1. FT-IR, XPS and EDX elemental mapping suggested that $FeCl_3$ was coordinatively bonded to the UiO-67 bipyridine framework. The synthesised UiO-67-$FeCl_3$ could catalyse the aerobic oxidation of alcohols and benzylic compounds to corresponding ketones and phenomes (phenolic entities in a cell, tissue, organ, organisms and species) with high yields respectively. In addition, the UiO-67-$FeCl_3$ catalyst could be reused as a heterogeneous catalyst without compromising its activity and selectivity.

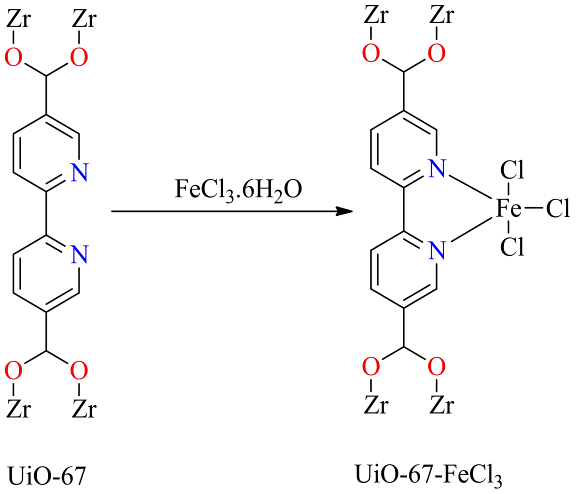

Equation 1.1: An illustration of the synthesis of UiO-67-$FeCl_3$. [109]

1.3.5 MOF supported catalysts for Photo catalytic Reduction of CO_2

MOF materials have generated interest as visible light active photocatalytic materials in the degradation of organic compounds, chemical synthesis and in the reduction of CO_2.[100–112] By judicious selection of metal ions and organic linkers, photocatalytic properties of MOFs can be modulated.[113] The first MOF-based heterogeneous catalytic system was developed by Zhang and Lin. by doping different molecular complexes into UiO-67(Zr) for water oxidation, photocatalytic reduction of CO_2, and organic transformations driven by visible light.[114] The organic ligands may serve as antennae to harvest light and generate electrons, which are then transferred to the metal centres *via* a linker to a metal cluster (LMCT). Some studies have shown that photoinduced electron transfer takes place from a photoexcited terephthalate linker to a metal-oxo cluster within Yaghi's MOF-5. The role of the linker in this process is to absorb light and sensitise the metal-oxo cluster dot. In this regard, MOFs serve as an interesting platform to design and study artificial photosynthetic systems.[114,115] Recent papers have demonstrated that MOFs can be used to achieve light-harvesting and to drive the photocatalytic reduction of CO_2 into small organic molecules, like HCOOH, CH_3OH, and so on.[114] Reference is made to a review by Dhakshinamoorthy and co-workers for an extensive photocatalytic reduction of CO_2 to value-added chemicals.[116]

Fu and co-workers investigated MIL-125(Ti) MOF and its functionalised derivative, NH_2-MIL-125(Ti), for photocatalytic conversion of CO_2 under visible light irradiation. The NH_2-MIL-125(Ti) exhibited an enhanced catalytic activity towards CO_2 reduction to formate in acetonitrile (MeCN), with triethanolamine (TEOA) as a sacrificial agent (electron donor) as compared to MIL-125(Ti) without the amine functionality.[117] The accumulated $HCOO^-$ content, over 10 hour period was 8.14 μmol, while no $HCOO^-$ ions were formed in the absence of amine functionality. The proposed mechanism for the reduction of CO_2 in NH_2-MIL 125 is illustrated in Scheme 1.9.

Upon light absorption in the LMCT band, a long-lived excited charge separation state occurs by transferring an electron from an organic linker to Ti^{4+} clusters, reducing them to Ti^{3+}, whereas TEOA acts as an electron donor. The excess electrons are subsequently transferred to the CO_2 molecule. The valence transition between Ti^{4+}

and Ti^{3+} was witnessed by the observed colour change from light yellow to green upon excitation with visible light, signifying the reduction of Ti^{4+} to Ti^{3+} (Scheme 1.10).

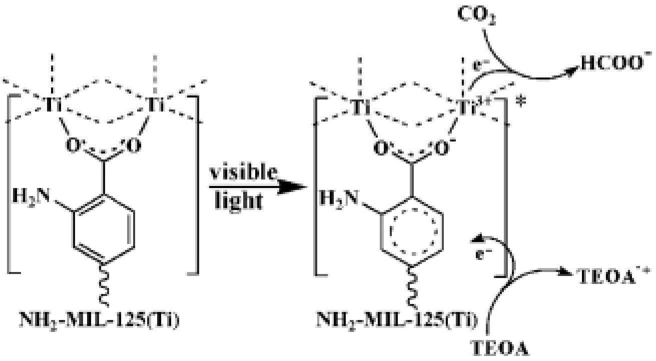

Scheme 1.9: Proposed mechanism for the photocatalytic CO_2 reduction over NH_2-MIL-125(Ti) under visible light irradiation.[117]

When CO_2 is introduced into the suspension, the reduction of CO_2 by Ti^{3+} to $HCOO^-$ occurs. This explains the observation of a gradual colour change from green to its original bright yellow, as Ti^{3+} was oxidised to Ti^{4+}, upon transfer of electrons to CO_2 molecules. PXRD patterns after the photocatalytic reaction revealed that the diffraction profile of the parent MOF was preserved, suggesting crystal structure of the MOF was not compromised during photocatalytic reactions.

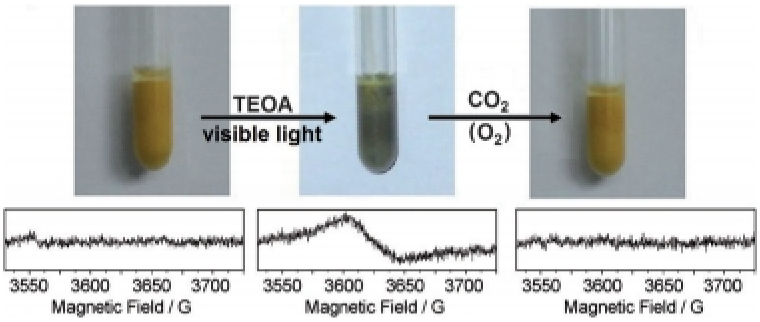

Scheme 1.10: Photos and corresponding ESR spectra of NH_2-MIL-125(Ti) under different conditions: i) fresh NH_2-MIL-125(Ti), ii) TEOA, visible light, and N_2 and iii) after the introduction of CO_2 (or O_2).[117]

Wang and co-workers[118] reported a series of Fe-based MOFs for CO_2 reduction under visible light irradiation in the presence of TEOA as a sacrificial agent. The study compared MIL-101(Fe), MIL-53(Fe) and MIL-88(Fe) and their amine functionalised derivative. Unlike the Ti-O clusters, the Fe-O clusters in the Fe-based MOFs exhibited visible light activity towards the conversion of CO_2 to formic acid, even in the absence of amine functionality, with the yield of 59, 29.7 and 9 μmol for MIL-101(Fe), MIL-53(Fe) and MIL-88(Fe), respectively after 8-hour reaction duration. MIL-101(Fe) exhibited the best photocatalytic activity towards the conversion of CO_2 among the non-functionalised MOFs due to the existence of coordinatively unsaturated Fe sites in the structure. Amine functionality on these Fe-based MOFs was found to significantly enhance the photocatalytic activity, leading to 178, 46.5 and 30 μmol for MIL-101(Fe), MIL-53(Fe) and MIL-88(Fe) respectively over the same reaction time. This was due to the synergetic effect of dual excitation pathways: i.e., exciting NH_2 functionality followed by an electron transfer from the excited organic linker to the Fe centre and the direct excitation of Fe−O clusters (Scheme 1.11).[118] The crystal structure chemical composition and porosity were also preserved as confirmed by PXRD, IR, TGA analysis and N_2 adsorption of the crystals after the reaction matched those of fresh samples.

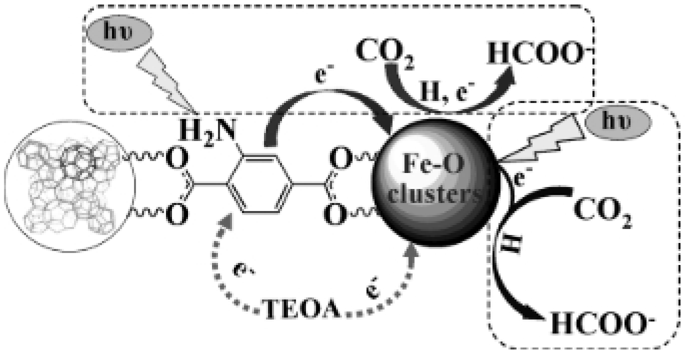

Scheme 1.11: Dual Excitation pathways over amino-functionalised Fe-based MOFs. Reprinted with permission from ref 118. Copyright (2014) American Chemical Society.

The photocatalytic activity of amino-functionalised NH_2-Uio-66 for CO_2 reduction under visible-light irradiation in the presence of TEOA as a sacrificial agent was demonstrated by Sun *et. al.*[119] The concentration change of $HCOO^-$ with irradiation time showed that the amount of $HCOO^-$ produced reached 13.2 μmol in 10 hours. The parent UiO-66 did not show any activity for catalytic reduction confirming that the visible-light absorption characteristics associated with 2-aminoterephthalate

(ATA) moiety are indispensable for promoting photocatalytic reduction under visible light irradiation. Since pure H_2ATA ligand also did not show any catalytic activity for CO_2 reduction, the photocatalytic performance originates from the interaction between the ligand and the metal clusters. The mechanism was proposed as illustrated in Scheme 1.12. The organic linker, ATA, in NH_2-UiO-66 acted as an antenna to absorb visible light. Once irradiated, the excited ATA could transfer electrons to the Zr oxo clusters and Zr(IV) in the Zr-O clusters reduced to Zr(III) which further reduce CO_2 to $HCOO^-$ with TEOA as the hydrogen source. In this photocatalytic reaction system, TEOA plays the role of both electron donor and providing a basic environment which facilitated the photocatalytic CO_2 reduction. The substitution of ATA with benzyl alcohol, ethylenediaminetetraacetic acid, or methanol as electron donors failed to produce $HCOO^-$.[119] The stability of the as-prepared NH_2-UiO66 during the photocatalytic reaction was confirmed by PXRD, IR and BET studies of NH_2-UiO66 after the photocatalytic reaction.

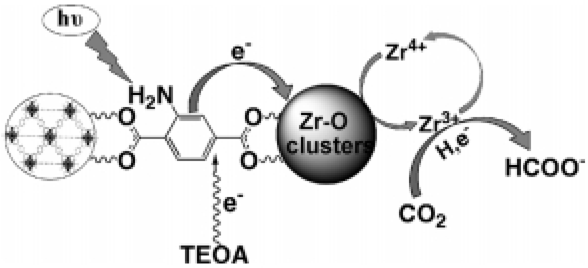

Scheme 1.12: Proposed mechanism for photocatalytic CO_2 reduction over NH_2-UiO-66(Zr) under visible-light irradiation.[119]

Fei *et al.*[120] incorporated a manganese bipyridine complex, Mn(bpydc)$(CO)_3$Br (bpydc = 5,5′-dicarboxylate-2,2′-bipyridine) into a highly robust Zr(IV)-based metal−organic framework (MOF) for use as a CO_2 reduction photocatalyst. In conjunction with $[Ru(dmb)_3]^{2+}$ (dmb = 4,4′-dimethyl-2,2′bipyridine) as a photosensitiser and 1-benzyl-1,4-dihydronicotinamide (BNAH) as a sacrificial reductant, Mn-incorporated MOFs efficiently catalysed CO_2 reduction to formate in DMF/TEOA under visible-light irradiation as shown in Scheme 1.13. The photochemical performance of the Mn-incorporated MOF reached a turnover number of approximately 110 in 18 h, exceeding that of the homogeneous reference catalytic systems. The increased activity of the MOF-incorporated Mn catalyst is ascribed to the struts of the framework providing isolated active sites, which stabilise the catalyst and inhibit dimerisation of the singly reduced Mn complex. The MOF catalyst largely retained its crystallinity throughout prolonged catalysis and was successfully reused over several catalytic runs.

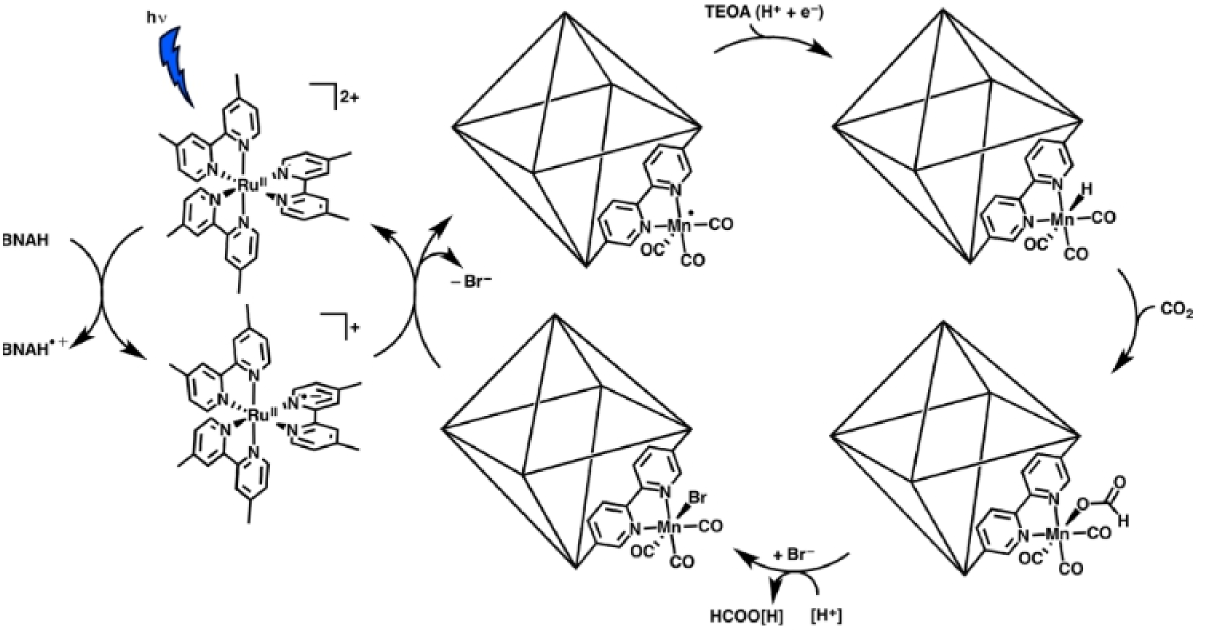

Scheme 1.13: Proposed mechanism for the formation of formate from the photocatalytic reaction with UiO-67-Mn(bpy)$(CO)_3$Br. Adapted with permission from ref 120. Copyright (2015) American Chemical Society.

1.3.6 MOF supported catalysts for Electrocatalytic reduction of CO_2

Electrochemical reduction of CO_2 can proceed through two-, four-, six-, and eight-electro reduction pathways in gaseous, aqueous, and non-aqueous phases at both low and high temperatures.[21] The major reduction products are carbon monoxide, methanol, formic acid or formate, ethylene, ethanol and oxalic acid or oxalate.[125–127] The kinetics of CO_2 electroreduction involve very complicated reaction mechanisms, and the reaction rates are very slow, even in the presence of electrocatalysts. In general, the catalysts currently being employed are still not active enough. Furthermore, in most cases, the product is a mixed product containing several species (for example, C, CO, HCOOH, $H_2C_2O_4$, CH_2O, CH_3OH, CH_4, CH_2CH_2, CH_3CH_2OH and so on). The number of species and the amount of each species present are strongly dependent on the kind and selectivity of the electrocatalyst employed and what electrode potential is applied. In most cases, these catalysts can survive for fewer than 100 hours, which is far below the requirements for practical use and technological commercialisation.[21] Therefore, unsatisfactory catalysis, including low catalytic activity and stability, is the biggest challenge in CO_2 electroreduction.

For a MOF material to be active towards CO_2 conversion, the lowest unoccupied crystal orbital (LUCO) must be above the redox potential of CO_2 reduction half-reaction, which depends on the product formed. For example, the redox potential for the conversion of CO_2 to formic acid is -3.42 eV while for methanol and methane are -3.65 and -3.79 eV respectively.[124] While both bridging metal ions and organic linkers have been shown to have an influence on the electronic properties,[125,126,127] the organic linker has been shown to play the most important role,[124,128,129] and the electronic properties of MOFs can be predicted based on the highest occupied molecular orbital (HOMO) and the lowest unoccupied molecular orbital (LUMO) of the organic linker.[113] The metal clusters should be selected such that the empty orbitals overlap with the LUMO of the linker, to facilitate efficient ligand to metal charge transfer, and long-lived charge separations.[130–132]

Hinogami *et al*. evaluated the electrocatalytic potential of copper rubeanate metal organic framework (CR-MOF), for the electrocatalytic conversion of CO_2. By using the CR-MOF coated on carbon paper to form a working electrode, formic acid was found to be the only product.[133] Under the same conditions, the use of Cu metal as the working electrode in the absence of the MOF led to a mixture of products, including formic acid, methane, ethylene and ethane. Further studies confirmed that the CR-MOF electrode formic acid product amounts were thirteen times greater than that of the Cu-electrode and also exhibited good stability, probably due to the higher CO_2 adsorption within the MOF crystals.

The ability of Cu-containing metal-organic porous materials supported on gas diffusion electrodes to promote the electrocatalytic conversion of CO_2 to alcohols was investigated.[123] Specifically, two MOFs $[Cu_3(\mu_6\text{-}C_9H_3O_6)_2]_n$ (HKUST-1), $[Cu_3(\mu_3\text{-}C_5H_4N_5)_2]_n$ (CuAdeAce), two metal-organic aerogels (MOA), $[Cu(\mu\text{-}C_2H_2N_2S_2)]_n$ (CuDTA) and $[Cu_{0.6}Zn_{0.4}(\mu\text{-}C_2H_2N_2S_2)]n$ (CuZnDTA) were tested. The electrodes showed relatively high surface areas, accessibility (Figure 1.8), and exposure of the Cu catalytic centres as well as favourable electrocatalytic reduction performance, that is, they have high efficiency for the production of methanol and ethanol in the liquid phase. The materials displayed Faradic Efficiencies (FE) of 15.9, 1.2, 6.0, and 9.9% for HKUST-1, CuAdeAce, CuDTA and CuZnDTA, respectively, at a current density of 10 mAcm^{-2}, an electrolyte-flow/area ratio of 3 mLmincm^{-2}, and a gas-flow/area of 20 mLmincm^{-2}. In particular, HKUST-1 and CuZnDTA-based electrodes were the most active electrocatalysts for CO_2 reduction, demonstrating working stability of up to 17 and 12 hours, respectively.

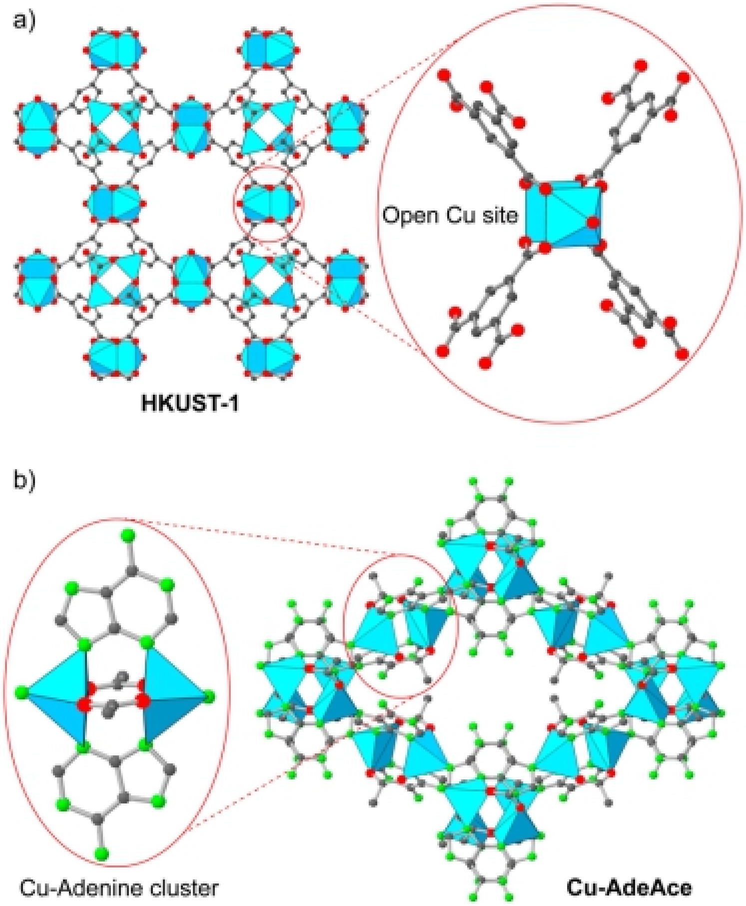

Figure 1.8. Structure of Cu3(BTC) (HKUST-1) a) showing the open metal site (OMS)-based cluster units and b) copper(II)-adeninate-acetate (CuAdeAce) b).[123]

Kornienko *et al.* introduced thin films of nanosized MOFs, $Al_2(OH)_2$TCPP-Co (TCPP-H_2 = 4,4′,4″,4‴-(porphyrin 5,10,15,20-tetrayl)tetra benzoate) on a conductive substrate with a large number of electrochemically active Co-N groups for the efficient and selective reduction of carbon dioxide to carbon monoxide in aqueous electrolytes as shown in Figure 1.9.[121] In addition to Co-N sites, the porphyrin linkers played an important role in CO_2 reduction by acting as electrocatalytic centres and redox hopping-based conduits for charge transfer. The MOF revealed a selectivity for CO production in excess of 76% and stability over 7 h with a per-site turnover number (TON) of 1400. *In situ* spectroelectrochemical measurements revealed that the Co(II) centres are reduced to Co(I) throughout the MOF and subsequently reduce CO_2. This is the first MOF catalyst constructed for the electrocatalytic conversion of aqueous CO_2 to CO, and its high-performance characteristics are encouraging for the further development of this approach.

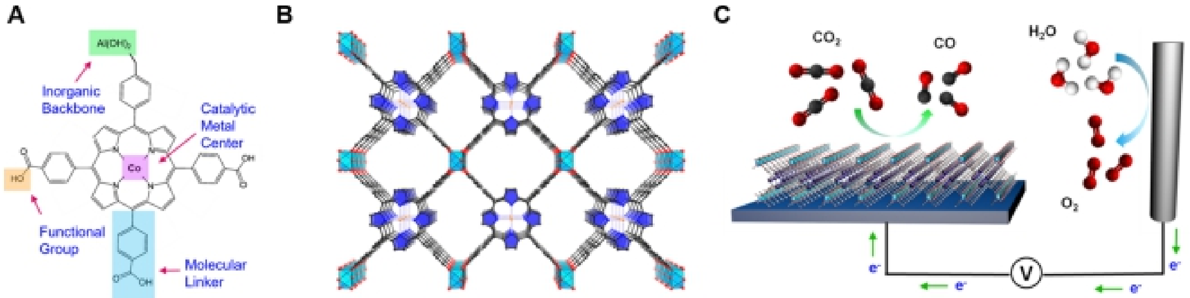

Figure 1.9: MOF catalyst allows for the modulation of metal centres, molecular linkers, and functional groups at the molecular level (A). Structure of the cobalt-metalated TCPP, are assembled into a 3D MOF, $Al_2(OH)_2$TCPP-Co with variable inorganic building blocks (B). Co, orange spheres; O, red spheres; C, black spheres; N, blue spheres; Al, light-blue octahedra; and pyrrole ring, blue. (C) Scheme of functional CO_2 electrochemical reduction system where the MOF is integrated with a conductive substrate as a cathode. Reproduced with permission from ref 121. Copyright (2015) American Chemical Society.

1.3.7 MOF supported catalysts for hydrogenation of CO_2

Several studies have revealed that the incorporation of molecular catalytic moieties into the framework offers the potential to combine CO_2 capture with catalytic hydrogenation of CO_2 in a single material, thereby significantly reducing the overall cost of carbon capture and conversion through process intensification[134–138] The studies mainly focus on UiO-66 because of its exceptional stability and ability to be functionalised. In their study, Ye and Johnson demonstrated that using a novel catalyst, UiO-66-P-BF_2, could capture and also transform CO_2 to formic acid *via* a two-step reaction (yellow arrows) as seen in Scheme 1.14. Functionalisation of UiO-66 with a frustrated Lewis pair moiety resulted in an apparently stable structure with very minor perturbation on the lattice parameters. The functional groups were capable of chemically binding CO_2 and heterolytically dissociating H_2. The major drawback is that CO_2 is bound too strongly to UiO-66-P-BF_2 than H_2, leading to catalyst poisoning by inhibiting the dissociation of H_2. One way to get around this issue would be to expose the material to H_2 first then to CO_2 to avoid competing reaction and catalyst poisoning.[138]

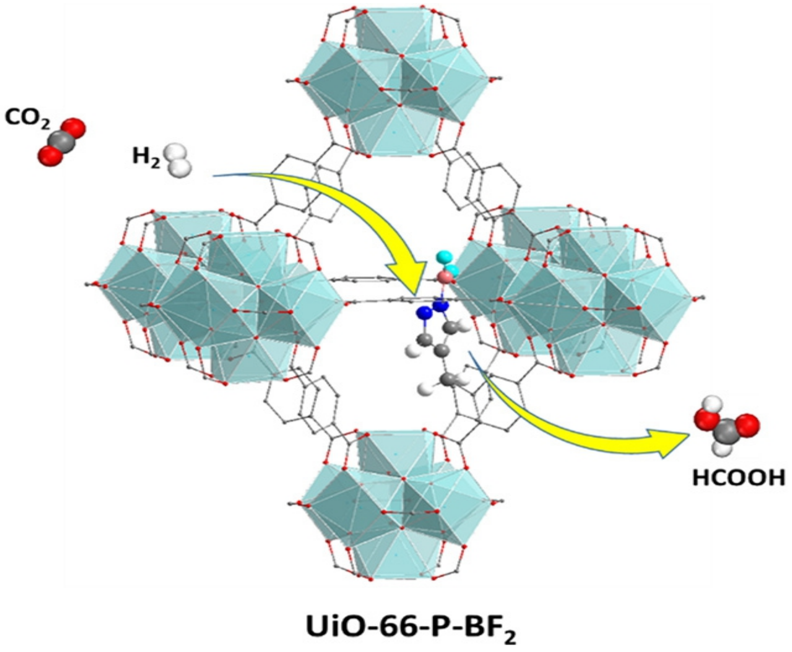

Scheme 1.14: Production of formic acid using Lewis pair functionalised UiO-66. Reprinted with permission from ref 138. Copyright (2015) American Chemical Society.

The same group used density functional theory (DFT) to computationally design a catalyst for the reduction of CO_2 to methanol. They incorporated a catalytically active moiety into the framework of a robust porous UiO-67 that has a significant CO_2 adsorption capacity.[134] The new material, UiO-67-$(NBF_2)_4$ combines the advantages of both homogeneous and heterogeneous catalysts while providing a potential pathway for the design of a single process unit for CO_2 capture and conversion to methanol. Another advantage of UiO-67-$(NBF_2)_4$ over previously reported Lewis pair based catalysts[12,138] is that heterolytic dissociation of H_2 is preferred, over chemisorption of CO_2, avoiding poisoning of catalytic sites with strongly bound CO_2.

In order to get an efficient MOF catalyst for CO_2 reduction, a new method was developed to create dynamic liquid/ gas interfaces to maximise the contact of CO_2, H_2 and H_2O. Lin and co-workers designed a MOF catalyst with the use of a Soxhlet-type reflux-condensing setup shown in Figure 1.10.[107] The incorporated iridium complexes into the UiO-type MOF provides isolated anchoring sites for Ir. After activation, the catalyst exhibited a high activity towards the hydrogenation of CO_2 to formate, with a TON of 6149 and TOF of 410 hr^{-1} under atmospheric pressure at 85 °C.

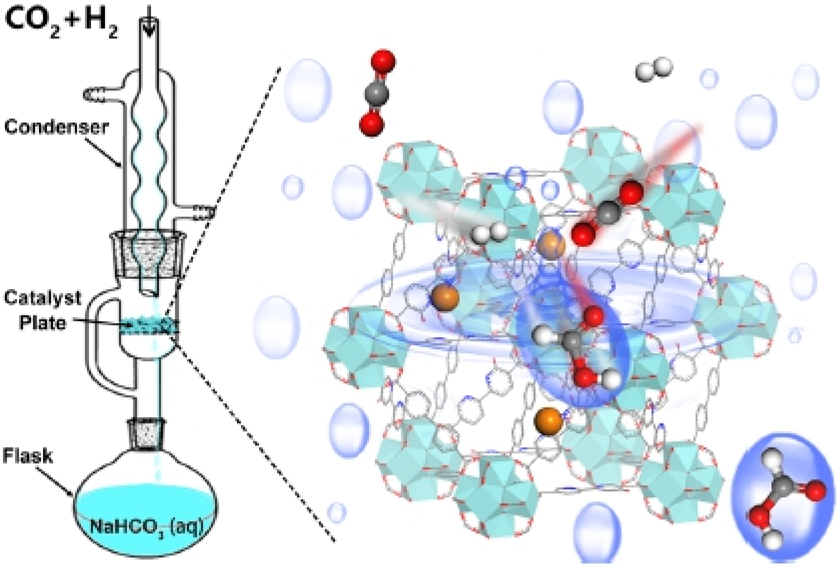

Figure 1.10: Scheme showing a Soxhlet-type reflux-condensing system to place MOF catalysts at a dynamic triphasic interface of CO_2/H_2-H_2O-catalyst for CO_2 hydrogenation to formate. Reprinted with permission from ref 107. Copyright (2017) American Chemical Society.

Scheme 1.15 illustrates the proposed mechanism for the reaction. As the heterolytic splitting of H_2 generates iridium hydride species, formate is produced from CO_2 via hydride transfer step. DFT calculations were done to support the catalytic cycle. The transition states of H_2 heterolysis (A*) and proton hydride transfer (C*) gave activation energies Ea_1 = 0.34 kcal.mol^{-1} and Ea_2 = 16.26 kcal.mol^{-1} respectively, supporting the proton-hydride transfer to be the rate-determining step. The catalytic efficiency of the isolated catalyst was demonstrated over repeated cycles. This work provides opportunities to use MOFs as solid molecular catalysts in designer reactors to enhance the catalytic efficiency.

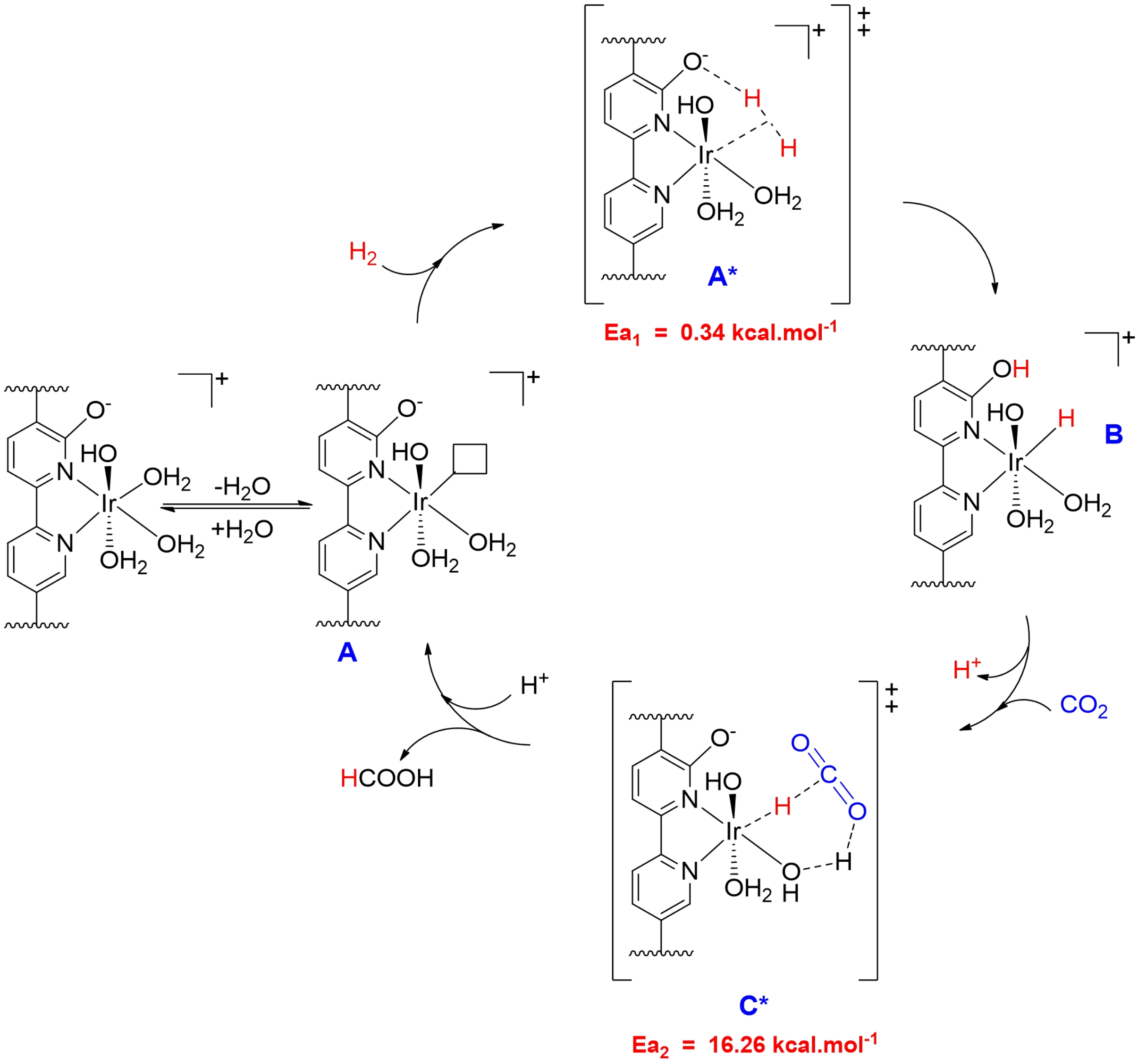

Scheme 1.15: Proposed mechanism for the hydrogenation of CO_2 by mbpyOH-[Ir^{III}]-UiO with activation enthalpies. Reprinted with permission from ref 107. Copyright (2017) American Chemical Society. Scheme 1.15.

Rayder and co-workers developed a new approach to encapsulate a transition metal complex, (^{tBu}PNP)Ru(CO)-HCl, within a MOF, as illustrated in Scheme 1.16, that capitalises on the existence of solvent-dependent, aperture-opening events resulting from dissociative linker exchange reactions in the MOF. ICP-OES confirmed 0.35

wt. % Ru loading in the framework. The resulting encapsulated catalyst, Ru@UiO-66, was very active for the hydrogenation of CO_2 to formate with DBU at 27 °C by applying 1:4 partial pressure of $_{p}CO_2/_{p}H_2$ to obtain a high TON of 350 000 in 30 minutes, which is the highest value reported to date for heterogeneous systems. The catalyst exhibited greater recyclability, slower bimolecular catalyst deactivation and resistance to poisoning compared to its homogeneous counterpart.[136]

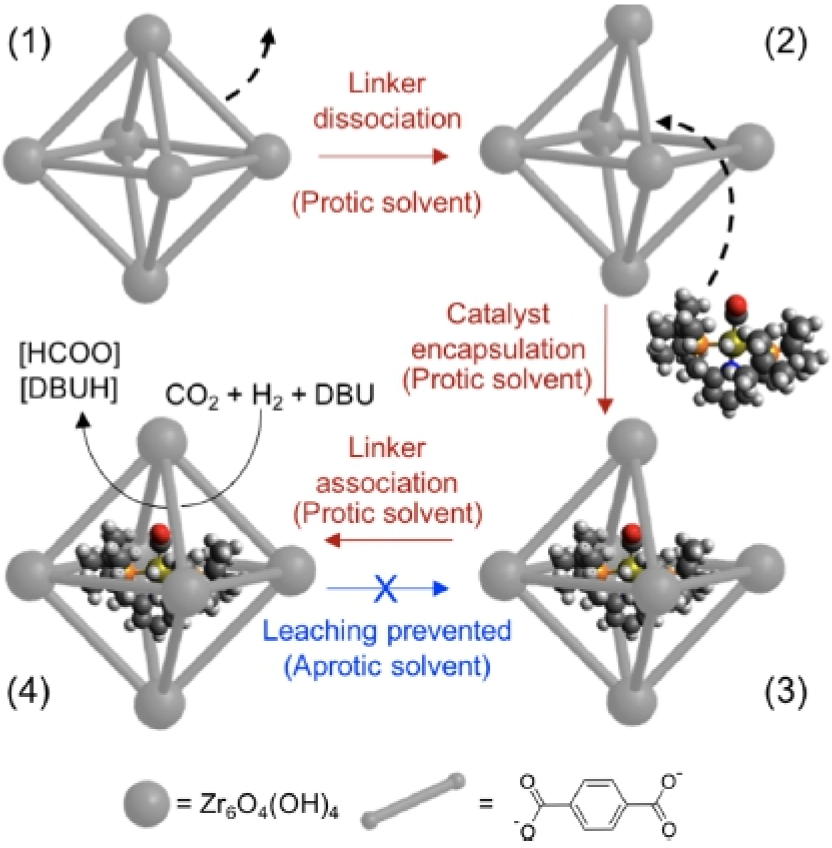

Scheme 1.16: Catalysis in MOF using aperture opening encapsulation. Reprinted with permission from ref 136. Copyright (2018) American Chemical Society.

Recently, Irshad[139] and co-workers reported several ruthenium complexes, namely $RuCl_3$, $[RuCp^*Cl_2]_2$ and $[Ru(C_6Me_6)Cl_2]_2$ immobilised on an azolium based MOF by post-synthetic metalation and subsequently tested these for CO_2 hydrogenation. The designed Ru_3-NHC-MOF catalyst exhibited the highest activity for CO_2 hydrogenation to formic acid because of its stronger electron-donating ability of C_6Me_6 ligand of $[Ru(C_6Me_6)Cl_2]_2$ complex. A high TON value of 3803 was obtained under optimal reaction conditions, 120 ˚C, 8 MPa (CO_2/H_2 = 1) in 2 hours. The MOF showed excellent stability upon recycling.

1.4 Organic linkers

In this project, a bipyridyl carboxylate linker, in particular, 2,2’-bipyridine-4,4’ dicarboxylic acid (H_2bpdc) was used for MOF synthesis. 2,2’-bipyridine 4,4’ dicarboxylic acid comprises of pyridyl and carboxylate moieties. In this work, the choice of the linker was to allow MOF formation through the carboxylate moiety while bipyridyl units have been utilised as anchoring sites for catalytically active metals. Carboxylate ligands are one of the most common types of linkers used in MOF synthesis due to their ability to form strong bonds with the metal ions. The carboxylate groups have been shown to coordinate in a variety of binding modes (eg monodentate and bidentate) and have proven to stabilise the framework.[108,140,141] Furthermore, the aromatic carboxylates are also able to aggregate metal ions into M-O-C clusters, thereby generating secondary building units (SBU) in *situ*. Figure 1.11 shows some of the possible binding modes of H_2bpdc once fully deprotonated.

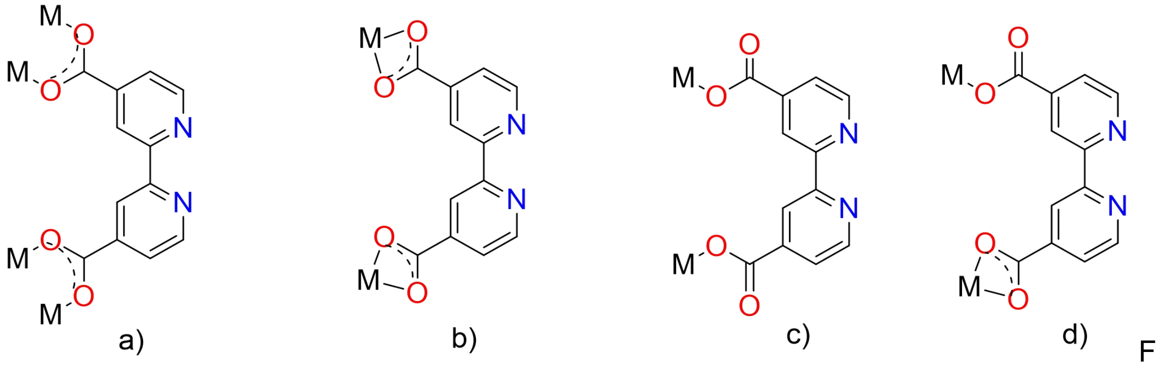

Figure 1.11: The coordination modes of the carboxylate. a) bridging bis-bidentate; b) chelating bis-bidentate; c) bis-monodentate and d) monodentate chelating and bridging fashion

Catalytically active moieties can be anchored onto the pyridyl moiety of the organic linker through metalation[107,118,142, 143] and cyclometalation.[144,145] Some examples of the aforementioned literature papers on post-synthetic metalation have their reaction schemes already illustrated in Equation 1.1 and Scheme 1.15. Before MOF synthesis, the bipyridyl moiety can also be functionalised with catalytically active metals as illustrated in Equation 1.2. The organometallic complex can subsequently be used as a metalloligand for MOF synthesis.

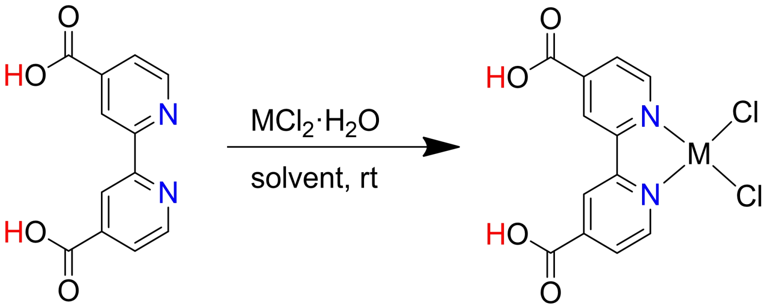

Equation 1.2: Anchoring catalytically active metal centres to the bipyridyl moiety before MOF synthesis.

The bpdc linker can change its conformation during MOF synthesis as illustrated in Scheme 1.17a. Cyclometalated MOFs can then be directly produced via C-H bond deprotonation in the presence of KOAc at room temperature (Scheme 1.17b).

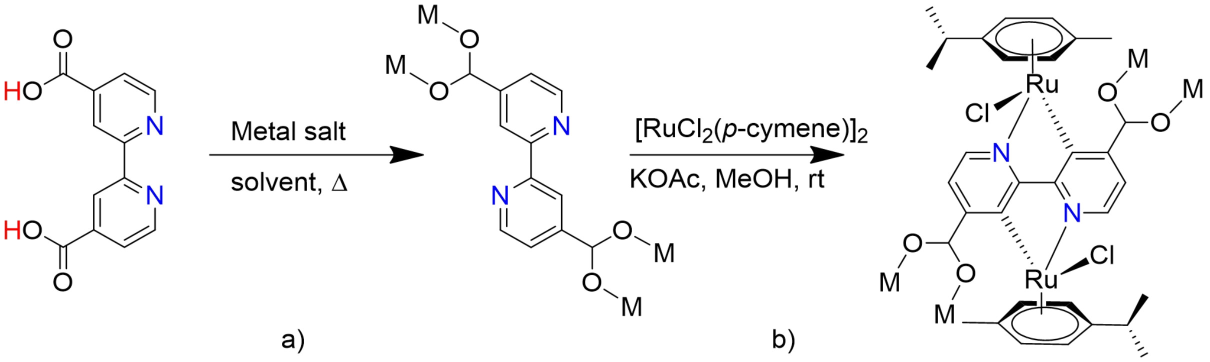

Scheme 1.17. Cyclometalation of a bipyridyl based MOF

Furthermore, because of the dipole-quadruple interactions between polarisable CO_2 molecule and the accessible nitrogen site, it has been reported that the employment of nitrogen-rich organic linkers such as pyridine can dramatically improve CO_2 uptake capacity and selectivity. [82]

1.5 Metal ions

The main choice of metal ions used to bind carboxylate is transition metals, which form a wide variety of coordination geometries affording many different network architectures. There are also numerous examples where carboxylates coordinate to lanthanide metals, generating new unusual network topologies due to their large coordination numbers. In this project, solvothermal reactions of $LaCl_3{\cdot}7H_2O$, $Mg(NO_3)_2{\cdot}6H_2O$, $Mn(Cl)_2{\cdot}4H_2O$, $Cd(NO_3)_2{\cdot}4H_2O$ and $Zn(NO_3)_2{\cdot}4H_2O$ metal salts with 2,2'-bipyridine-4,4'-dicarboxylic acid were used for the preparation of MOFs.

The metal ion that is chosen for a particular MOF is of significant importance as it plays a vital role in the properties of the framework. The oxidation state of the metal usually ranges from +1 to +3, while the coordination number range from 2 to 12, depending on the metal ion used, giving rise to a wide range of geometries such as linear, T-, or Y-shaped, tetrahedral, square-planar, square-pyramidal, trigonal-bipyramidal, octahedral, trigonal-prismatic and pentagonal-bipyramidal. For example, Zn^{II} and Cd^{II} are common metal components used in the preparation of MOFs. They can simultaneously form bonds with different donor atoms. Both metals have been reported with various coordination geometries.[108,141,146,147] This variation arises from two factors: (i) their large ionic radii, which allow flexibility in terms of coordination numbers and (ii) the electronic configuration of the metal ion (d^{10}). According to the ligand field theory, complexes where the metal ion has d^{10} electron configuration experience no ligand field stabilisation and therefore the ligand environment is controlled by steric factors only, permitting a range of diverse geometries.

MOFs based on lanthanides have gained special interest due to their rich coordination geometry, high stability, ability to form coordinated networks and interesting properties.[148,149] Most lanthanide-based MOFs are water stable, and even more stable than their transition metal-based analogues. The use of lanthanide-based building units in the construction of new MOFs is attractive because lanthanide cations typically have a high density of coordinated solvent molecules, which, when removed, can produce unsaturated metal sites that serve as gas binding or Lewis acidic sites which can be used for catalysis.[150] Their large coordination numbers facilitate the removal of solvent molecules without framework collapse.[151]

1.6 Motivation and Objectives of this Study

1.6.1 Motivation

The increasing concern about global warming and a potential energy crisis has prompted the search for new technologies for converting CO_2, a notorious greenhouse gas from fossil fuel burning, back to fuels or other value-added products. Amongst the several chemicals that can be directly prepared from CO_2, formic acid is widely used as a silage agent, dyeing additive, and a precursor for inorganic synthesis.[7] Furthermore, it has recently been considered to be a promising candidate for hydrogen storage.[35] For these reasons, the development of efficient catalysts for the reduction of CO_2 has been extensively investigated, yet it remains a challenge as CO_2 is chemically inert, making it thermodynamically stable.[8,17,18]

Several attempts have been made to achieve the homogeneous hydrogenation of CO_2 to formic acid in aqueous solutions using mainly rhodium and ruthenium catalyst/catalyst precursors.[9,43] Despite the reported homogenous catalysts exhibiting excellent catalytic efficiencies for CO_2 reduction, the industrial realisation of these catalysts still poses difficulty owing to the decomposition of the generated formate into CO_2 and H_2 during the subsequent separation step(s).[44] Therefore the development of effective heterogeneous catalyst, which would be easily separated from the reaction mixture would be highly desirable to overcome such drawbacks.

Heterogeneous hydrogenation of CO_2 can be implemented on metal surfaces such as nickel, cobalt and copper, but these reactions have higher energies than the homogeneous catalysts and hence require higher temperatures.[152] Owing to their high porosity, several studies have revealed that metal-organic frameworks (MOFs) have remarkable H_2 storage and CO_2 capture ability[100,105,137], and also more recently, catalysis.[66] Although some MOFs have been considered as catalysts for CO_2 conversion[153, 154] it is still necessary to construct more effective MOFs for such reaction, especially under mild conditions. Key to this reaction design is the construction of catalytically active MOF systems, including encapsulation of homogeneous catalysts in the MOF during synthesis[136] and functionalisation of linkers with catalytically active species.[106,109] In this thesis, MOFs were rationally designed using bipyridyl dicarboxylate linker which can provide anchoring sites for

Pd^{II} and Ru^{II} complexes. After activation, the MOFs were used in tandem capture of CO_2 and H_2 and subsequent catalytic conversion of the gases to formate. The functionalised MOFs presented in this work bridge the gap between homogeneous and heterogeneous catalysis.

1.6.2 Objectives

The objectives of this study were:

1. Synthesis of metal-organic frameworks based on 2,2'-bipyridine-4,4'-dicarboxylate linker and La^{III}, Mn^{II}, Mg^{II}, Zn^{II} and Cd^{II} metal ions.
2. Characterisation of the MOFs using X-ray diffraction techniques, thermal analysis and spectroscopic techniques.
3. Functionalisation of the prepared MOFs using Ru^{II} and Pd^{II}.
4. Evaluating the efficacy of the MOFs as storage devices of carbon dioxide and hydrogen and catalytic conversion of these gases to formate.

1.7 References

1 S. Saeidi, N. A. S. Amin and M. R. Rahimpour, *Journal of CO_2 Utilization*, 2014, **5**, 66–81.

2 R. M. Cuéllar-Franca and A. Azapagic, *Journal of CO_2 Utilization*, 2015, **9**, 82–102.

3 G. H. Gunasekar, K. Park, K. D. Jung and S. Yoon, *Inorganic Chemistry Frontiers*, 2016, **3**, 882–895.

4 F. Bertini, M. Glatz, N. Gorgas, B. Stöger, M. Peruzzini, L. F. Veiros, K. Kirchner and L. Gonsalvi, *Chemical Science*, 2017, **8**, 5024–5029.

5 Y. Zhang, P. G. Williard and W. H. Bernskoetter, *Organometallics*, 2016, **35**, 860–865.

6 A. Z. Spentzos, C. L. Barnes and W. H. Bernskoetter, *Inorganic Chemistry*, 2016, **55**, 8225–8233.

7 T. Maihom, S. Wannakao, B. Boekfa and J. Limtrakul, *Journal of Physical Chemistry C*, 2013, **117**, 17650–17658.

8 W. Wang, S. P. Wang, X. B. Ma and J. L. Gong, *Chemical Society Reviews*, 2011, **40**, 3703–3727.

9 Y.-N. Li, R. Ma, L.-N. He and Z.-F. Diao, *Catalysis Science and Technology*, 2014, **4**, 1498.

10 M. Mikkelsen, M. Jørgensen and F. C. Krebs, *Energy and Environtal Science*, 2010, **3**, 43–81.

11 P. Silva, S. M. F. Vilela, J. P. C. Tomé and F. A. Almeida Paz, *Chemical Society Reviews*, 2015, **44**, 6774–6803.

12 M.-A. Courtemanche, A. P. Pulis, É. Rochette, M.-A. Légaré, D. W. Stephan and F.-G. Fontaine, *Chemical Communications*, 2015, **51**, 9797–9800.

13 C. Liu, J. H. Xie, G. L. Tian, W. Li and Q. L. Zhou, *Chemical Science*, 2015, **6**, 2928–2931.

14 A. Goeppert, M. Czaun, J. P. Jones, G. K. Surya Prakash and G. A. Olah, *Chemical Society Reviews*, 2014, **43**, 7995–8048.

15 J. Albo, M. Alvarez-Guerra, P. Castaño and a. Irabien, *Green Chemistry*, 2015, **17**, 2304–2324.

16 B. Ugale, S. S. Dhankhar and C. M. Nagaraja, *Crystal Growth and Design*, 2018, **18**, 2432–2440.

17 Y. Suna, Y. Himeda, E. Fujita, J. T. Muckerman and M. Z. Ertem, *ChemSusChem*, 2017, **10**, 4535–4543.

18 A. Dubey, L. Nencini, R. R. Fayzullin, C. Nervi and J. R. Khusnutdinova, *ACS Catalysis*, 2017, **7**, 3864–3868.

19 A. Behr and K. Nowakowski, *Advances in Organic Chemistry*, 2014, **66**, 223-258

20 Q. Zhang, L. Cao, B. Li and L. Chen, *Chemical Science*, 2012, **3**, 2708–2715.

21 J. Qiao, Y. Liu, F. Hong and J. Zhang, *Chemical Society Reviews*, 2014, **43**, 631-675

22 W. Tu, Y. Zhou and Z. Zou, *Advanced Materials*, 2014, **26**, 4607–4626.

23 J. R. Long and O. M. Yaghi, *Chemical Society Reviews*, 2009, **38**, 1213–1214.

24 S. Kar, J. Kothandaraman, A. Goeppert and G. K. S. Prakash, *Journal of CO_2 Utilization*, 2018, **23**, 212–218.

25 S. Kar, A. Goeppert, J. Kothandaraman and G. K. S. Prakash, *ACS Catalysis*, 2017, **7**, 6347–6351.

26 J. Ma, N. Sun, X. Zhang, N. Zhao, F. Xiao, W. Wei and Y. Sun, *Catalysis Today*, 2009, **148**, 221–231.

27 J. Schneidewind, R. Adam, W. Baumann, R. Jackstell and M. Beller, *Angewandte Chemie - International Edition*, 2017, **56**, 1890–1893.

28 S. Wesselbaum, V. Moha, M. Meuresch, S. Brosinski, K. M. Thenert, J. Kothe, T. Vom Stein, U. Englert, M. Hölscher, J. Klankermayer and W. Leitner, *Chemical Science*, 2015, **6**, 693–704.

29 S. Wesselbaum, T. Stein, J. Klankermayer and W. Leitner, *Angewandte Chemie*, 2012, **3**, 1–5.

30 Y. Shen, Y. Zhan, S. Li, F. Ning, Y. Du, Y. Huang, T. He and X. Zhou, *Chemical Science*, 2017, **8**, 7498–7504.

31 W. N. Wang, J. Soulis, Y. Jeffrey Yang and P. Biswas, *Aerosol and Air Quality Research*, 2014, **14**, 533–549.

32 G. A. Filonenko, M. P. Conley, C. Copéret, M. Lutz, E. J. M. Hensen and E. A. Pidko, *ACS Catalysis*, 2013, **3**, 2522–2526.

33 S. Uhm, H. J. Lee and J. Lee, *Physical Chemistry Chemical Physics*, 2009, **11**, 9326–9336.

34 N. Onishi, S. Xu, Y. Manaka, Y. Suna, W. H. Wang, J. T. Muckerman, E. Fujita and Y. Himeda, *Inorganic Chemistry*, 2015, **54**, 5114–5123.

35 W. H. Wang, J. F. Hull, J. T. Muckerman, E. Fujita and Y. Himeda, *Energy and Environmental Science*, 2012, **5**, 7923–7926.

36 A. Boddien and H. Junge, *Nature Nanotechnology*, 2011, **6**, 265–266.

37 K. Tedsree, T. Li, S. Jones, C. W. A. Chan, K. M. K. Yu, P. A. J. Bagot, E. A. Marquis, G. D. W. Smith and S. C. E. Tsang, *Nature Nanotechnology*, 2011, **6**, 302–307.

38 Y. N. Li, L. N. He, A. H. Liu, X. D. Lang, Z. Z. Yang, B. Yu and C. R. Luan, *Green Chemistry*, 2013, **15**, 2825–2829.

39 Y. Li, S. H. Chan and Q. Sun, *Nanoscale*, 2015, **7**, 8663–8683.

40 I. Z, A. V. Hugo, D. Boisgard, D. Friart and F. Garaude, *Chemistry Letters*, 1985, **688**, 317–321.

41 C. A. Huff and M. S. Sanford, *ACS Catalysis*, 2013, **3**, 2412–2416.

42 K. Rohmann, J. Kothe, M. W. Haenel, U. Englert, M. Hölscher and W. Leitner, *Angewandte Chemie - International Edition*, 2016, **55**, 8966–8969.

43 R. Tanaka, M. Yamashita and K. Nozaki, *Journal of American Chemical Society*, 2009, **131**, 14168–14169.

44 G. H. Gunasekar, J. Shin, K. Jung, K. Park and S. Yoon, *ACS Catalysis*, 2018, **8**, 4346–4353.

45 C. Fellay, P. J. Dyson and G. Laurenczy, *Angewandte Chemie - International Edition*, 2008, **47**, 3966–3968.

46 T. Schaub and R. A. Paciello, *Angewandte Chemie - International Edition*, 2011, **50**, 7278–7282.

47 G. Peng, S. J. Sibener, G. C. Schatz, S. T. Ceyer and M. Mavrikakis, *The Journal of Physical Chemistry C*, 2012, **116**, 3001–3006.

48 P. Patel, S. Nandi, M. S. Maru, R. I. Kureshy and N.-U. H. Khan, *Journal of CO_2 Utilization*, 2018, **25**, 310–314.

49 Y. F. Zhao, Y. Yang, C. Mims, C. H. F. Peden, J. Li and D. Mei, *Journal of Catalysis*, 2011, **281**, 199–211.

50 G. H. Gunasekar, K. Park, V. Ganesan, K. Lee, N. K. Kim, K. D. Jung and S. Yoon, *Chemistry of Materials*, 2017, **29**, 6740–6748.

51 G. Gunniya Hariyanandam, D. Hyun, P. Natarajan, K. D. Jung and S. Yoon, *Catalysis Today*, 2016, **265**, 52–55.

52 M. S. Maru, S. Ram, R. S. Shukla and N. H. Khan, *Molecular Catalysis*, 2018, **446**, 23–30.

53 H. Song, N. Zhang, C. Zhong, Z. Liu, M. Xiao and H. Gai, *New Journal of Chemistry*, 2017, **41**, 9170–9177.

54 M. K. Gnanamani, G. Jacobs, H. H. Hamdeh, W. D. Shafer, F. Liu, S. D. Hopps, G. A. Thomas and B. H. Davis, *ACS Catalysis*, 2016, **6**, 913–927.

55 H. Kobayashi, J. M. Taylor, Y. Mitsuka, N. Ogiwara, T. Yamamoto, T. Toriyama, S. Matsumura and H. Kitagawa, *Chemical Science*, 2019, **10**, 3289–3294.

56 A. A. Olajire, *Renewable and Sustainable Energy Reviews*, 2018, **92**, 570–607.

57 Q. Yang, V. Guillerm, F. Ragon, A. D. Wiersum, P. L. Llewellyn, C. Zhong, T. Devic, C. Serre and G. Maurin, *Chemical Communications*, 2012, **48**, 9831–9833.

58 G. Mehlana, G. Ramon and S. A. Bourne, *CrystEngComm*, 2014, **16**, 8160–8168.

59 P. Valvekens, F. Vermoortele and D. De Vos, *Catalysis Science and Technology*, 2013, **3**, 1435–1445.

60 G. Mehlana, C. Wilkinson, G. Ramon and S. A. Bourne, *Polyhedron*, 2015, **98**, 224–229.

61 G. Mehlana, G. Ramon and S. A. Bourne, *Microporous and Mesoporous*

Materials, 2016, **231**, 21–30.

62 G. Mehlana, V. Chitsa and T. Mugadza, *RSC Advances*, 2015, **5**, 88218–88233.

63 A. Dhakshinamoorthy, M. Alvaro and H. Garcia, *Chemical Communications*, 2012, **48**, 11275–11288.

64 A. H. Chughtai, N. Ahmad, H. A. Younus, A. Laypkov and F. Verpoort, *Chemical Society Reviews*, 2015, **44**, 6804–6849.

65 Z. Chi, X. Zhang, B. Xu, X. Zhou, C. Ma, Y. Zhang, S. Liu and J. Xu, *Chemical Society Reviews*, 2012, **41**, 3878–96.

66 A. Dhakshinamoorthy, M. Opanasenko, J. Čejka and H. Garcia, *Catalysis Science and Technology*, 2013, **3**, 2509–2540.

67 M. Eddaoudi, J. Kim, N. Rosi, D. Vodak, J. Wachter, M. O. Keeffe, O. M. Yaghi, J. Kimrn and O. M. Yaghil, *Science*, 2013, **295**, 469–472.

68 G. Férey, M. Latroche, C. Serre, F. Millange, T. Loiseau and A. Percheron-Guegan, *Chemical Communications*, 2003, **13**, 2976–2977.

69 R. Banerjee, A. Phan, B. Wang, C. Knobler, H. Furukawa, M. O'Keeffe and O. M. Yaghi, *Science*, 2008, **319**, 939–943.

70 S. Choi, J. H. Drese and C. W. Jones, *ChemSusChem*, 2009, **2**, 796–854.

71 J. R. Li, Y. Ma, M. C. McCarthy, J. Sculley, J. Yu, H. K. Jeong, P. B. Balbuena and H. C. Zhou, *Coordination Chemistry Reviews*, 2011, **255**, 1791–1823.

72 M. Anbia and V. Hoseini, *Chemical Engineering Journal*, 2012, **191**, 326–330.

73 J. J. Gassensmith, H. Furukawa, R. A. Smaldone, R. S. Forgan, Y. Y. Botros, O. M. Yaghi and J. F. Stoddart, *Journal of American Chemical Society*, 2011, **133**, 15312–15315.

74 P. D. C. Dietzel, V. Besikiotis and R. Blom, *Journal of Materials Chemistry*, 2009, **19**, 7362–7370.

75 F. M. Mulder, B. Assfour, J. Huot, T. J. Dingemans, M. Wagemaker and A. J. Ramirez-Cuesta, *Journal of Physical Chemistry C*, 2010, **114**, 10648–10655.

76 M. Alhamami, H. Doan and C. H. Cheng, *Materials*, 2014, **7**, 3198–3250.

77 A. J. Fletcher, K. M. Thomas and M. J. Rosseinsky, *Journal of Solid State*

Chemistry, 2005, **178**, 2491–2510.

78 A. Schneemann, V. Bon, I. Schwedler, I. Senkovska, S. Kaskel and R. A. Fischer, *Chemical Society Reviews*, 2014, **43**, 6062–6096.

79 S. Brunauer, P. H. Emmett and E. Teller, *Journal of the American Chemical Society*, 1938, **60**, 309–319.

80 A. R. M. and O. M. Yaghi*, *Journal of American Chemical Society*, 2005, **127**, 17998–17999.

81 R. F. Bruinsma, P. G. De Gennes, J. B. Freund and D. Levine, *Nature*, 2004, **427**, 523–527.

82 Z. J. Lin, J. Lü, M. Hong and R. Cao, *Chemical Society Reviews*, 2014, **43**, 5867–5895.

83 L. Wu, W. Wang, R. Liu, G. Wu and H. Chen, *Royal Society Open Science*, 2018, **5**, 1-12.

84 Y. B. Zhang, H. Furukawa, N. Ko, W. Nie, H. J. Park, S. Okajima, K. E. Cordova, H. Deng, J. Kim and O. M. Yaghi, *Journal of the American Chemical Society*, 2015, **137**, 2641–2650.

85 Z. J. Lin, T. F. Liu, B. Xu, L. W. Han, Y. B. Huang and R. Cao, *CrystEngComm*, 2011, **13**, 3321–3324.

86 D. Sun, S. Ma, Y. Ke, D. J. Collins and H. Zhou, *Journal of American Chemical Society*, 2006, **128**, 3896–3897.

87 Z. Liang, J. Du, L. Sun, J. Xu, Y. Mu, Y. Li, J. Yu and R. Xu, *Inorganic Chemistry*, 2013, **52**, 10720–10722.

88 D. Britt, H. Furukawa, B. Wang, T. G. Glover and O. M. Yaghi, *Proceedings of the National Academy of Sciences*, 2009, **106**, 20637–20640.

89 A. Demessence, D. M. D. Alessandro, M. L. Foo and J. R. Long, *Journal of American Chemical Society*, 2009, **131**, 8784–8786.

90 L. Ma, J. M. Falkowski, C. Abney and W. Lin, *Nature Chemistry*, 2010, **2**, 838–846.

91 H.-L. Jiang and Q. Xu, *Chemical Communications*, 2011, **47**, 3351–3370.

92 A. Dhakshinamoorthy and H. Garcia, *Chemical Society Reviews*, 2012, **41**,

5262–5284.

93 M. Zhao, S. Ou and C. De Wu, *Accounts of Chemical Research*, 2014, **47**, 1199–1207.

94 I. Fechete, Y. Wang and J. C. Védrine, *Catalysis Today*, 2012, **189**, 2–27.

95 A. Dhakshinamoorthy, M. Alvaro and H. Garcia, *Catalysis Science and Technology*, 2011, **1**, 856–867.

96 F. X. L. Xamena, O. Casanova, R. G. Tailleur, H. Garcia and A. Corma, *Journal of Catalysis*, 2008, **255**, 220–227.

97 S. Kitagawa, R. Kitaura and S. I. Noro, *Angewandte Chemie - International Edition*, 2004, **43**, 2334–2375.

98 Z. Wang and S. M. Cohen, *Chemical Society Reviews*, 2009, **38**, 1315–1329.

99 N. MacDowell, N. Florin, A. Buchard, J. Hallett, A. Galindo, G. Jackson, C. S. Adjiman, C. K. Williams, N. Shah and P. Fennell, *Energy and Environmental Science*, 2010, **3**, 1645–1669.

100 J. Liu, L. Chen, H. Cui, J. Zhang, L. Zhang and C. Y. Su, *Chemical Society Reviews*, 2014, 43, 6011–6061.

101 M. G. Goesten, F. Kapteijn and J. Gascon, *CrystEngComm*, 2013, **15**, 9249–9257.

102 L. Ma, C. Abney and W. Lin, *Chemical Society Reviews*, 2009, **38**, 1248–1256.

103 W. Li, H. Wang, X. Jiang, J. Zhu, Z. Liu, X. Guo and C. Song, *RSC Advances*, 2018, **8**, 7651–7669.

104 W. Lu, Z. Wei, Z. Y. Gu, T. F. Liu, J. Park, J. Park, J. Tian, M. Zhang, Q. Zhang, T. Gentle, M. Bosch and H. C. Zhou, *Chemical Society Reviews*, 2014, **43**, 5561–5593.

105 M. Almáši, V. Zeleňák, R. Gyepes, S. Bourrelly, M. V Opanasenko, P. L. Llewellyn and J. Čejka, *Inorganic Chemistry*, 2018, **57**, 1774–1786.

106 L. Mino, E. Gallo, G. Agostini, C. Lamberti, E. Borfecchia, U. Olsbye, K. A. Lomachenko, K. P. Lillerud, S. Bordiga, S. Øien and S. Svelle, *Chemistry of Materials*, 2015, **27**, 1042–1056.

107 B. An, L. Zeng, M. Jia, Z. Li, Z. Lin, Y. Song, Y. Zhou, J. Cheng, C. Wang and

W. Lin, *Journal of the American Chemical Society*, 2017, **139**, 17747–17750.

108 X. M. Lin, T. T. Li, Y. W. Wang, L. Zhang and C. Y. Su, *Chemistry - An Asian Journal*, 2012, **7**, 2796–2804.

109 Y. Luan, Y. Jiang, D. Ramella, X. Shu and Y. Yu, *Applied Organometallic Chemistry*, 2017, **31**, 1–8.

110 Y. Horiuchi, T. Toyao, M. Saito, K. Mochizuki, M. Iwata, H. Higashimura, M. Anpo and M. Matsuoka, *Journal of Physical Chemistry C*, 2012, **116**, 20848–20853.

111 C. C. Wang, Y. Q. Zhang, J. Li and P. Wang, *Journal of Molecular Structure*, 2015, **1083**, 127–136.

112 S. Wang and X. Wang, *Small*, 2015, **11**, 3097–3112.

113 J. W. Maina, C. Pozo-Gonzalo, L. Kong, J. Schütz, M. Hill and L. F. Dumée, *Materials Horizons*, 2017, **4**, 345–361.

114 T. Zhang and W. Lin, *Chemical Society Reviews*, 2014, **43**, 5982–5993.

115 J. Bedia, V. Muelas-Ramos, M. Peñas-Garzón, A. Gómez-Avilés, J. J. Rodríguez and C. Belver, *Catalysts*, 2019, **9**, 1–43.

116 A. Dhakshinamoorthy, A. M. Asiri and H. García, *Angewandte Chemie International Edition*, 2016, **55**, 5414–5445.

117 Y. Fu, D. Sun, Y. Chen, R. Huang, Z. Ding, X. Fu and Z. Li, *Angewandte Chemie International Edition*, 2012, **51**, 3364–3367.

118 D. Wang, R. Huang, W. Liu, D. Sun and Z. Li, *ACS Catalysis*, 2014, **4**, 4254–4260.

119 D. Sun, Y. Fu, W. Liu, L. Ye, D. Wang, L. Yang, X. Fu and Z. Li, *Chemistry-A European Journal*, 2013, **19**, 14279–14285.

120 H. Fei, M. D. Sampson, Y. Lee, C. P. Kubiak and S. M. Cohen, *Inorganic Chemistry*, 2015, **54**, 6821–6828.

121 N. Kornienko, Y. Zhao, C. S. Kley, C. Zhu, D. Kim, S. Lin, C. J. Chang, O. M. Yaghi and P. Yang, *Journal of the American Chemical Society*, 2015, **137**, 14129–14135.

122 A. A. Al-Omari, Z. H. Yamani and H. L. Nguyen, *Molecules*, 2018, **23**, 1–12.

123 J. Albo, D. Vallejo, G. Beobide, O. Castillo, P. Castaño and A. Irabien, *ChemSusChem*, 2017, **10**, 1100–1109.

124 S. Hamad, N. C. Hernandez, A. Aziz, A. R. Ruiz-Salvador, S. Calero and R. Grau-Crespo, *Journal of Materials Chemistry A*, 2015, **3**, 23458–23465.

125 C. G. Silva, A. Corma and H. García, *Journal of Materials Chemistry*, 2010, **20**, 3141–3156.

126 R. Grau-Crespo, A. Aziz, A. W. Collins, R. Crespo-Otero, N. C. Hernández, L. M. Rodriguez-Albelo, A. R. Ruiz-Salvador, S. Calero and S. Hamad, *Angewandte Chemie - International Edition*, 2016, **55**, 16012–16016.

127 M. Fuentes-Cabrera, D. M. Nicholson, B. G. Sumpter and M. Widom, *Journal of Chemical Physics*, 2005, 123, 1-5.

128 C. H. Hendon, D. Tiana, M. Fontecave, C. Sanchez, L. D'Arras, C. Sassoye, L. Rozes, C. Mellot-Draznieks and A. Walsh, *Journal of the American Chemical Society*, 2013, **135**, 10942–10945.

129 K. T. Butler, C. H. Hendon and A. Walsh, *ACS Applied Materials and Interfaces*, 2014, **6**, 22044–22050.

130 W. Liang, R. Babarao and D. M. D'Alessandro, *Inorganic Chemistry*, 2013, **52**, 12878–12880.

131 Y. Lee, S. Kim, J. K. Kang and S. M. Cohen, *Chemical Communications*, 2015, **51**, 5735–5738.

132 M. A. Nasalevich, C. H. Hendon, J. G. Santaclara, K. Svane, B. Van Der Linden, S. L. Veber, M. V. Fedin, A. J. Houtepen, M. A. Van Der Veen, F. Kapteijn, A. Walsh and J. Gascon, *Scientific Reports*, 2016, **6**, 1–9.

133 R. Hinogami, S. Yotsuhashi, M. Deguchi, Y. Zenitani, H. Hashiba and Y. Yamada, *ECS Electrochemistry Letters*, 2012, **1**, H17–H19.

134 J. Ye and J. K. Johnson, *Catalysis Science and Technology*, 2016, **6**, 8392–8405.

135 J. Ye, L. Li and J. K. Johnson, *Catalysis Science and Technology*, 2018, **8**, 4609–4617.

136 Z. Li, T. M. Rayder, L. Luo, J. A. Byers and C. Tsung, *Journal of the American*

Chemical Society, 2018, **140**, 8082–8085.

137 B. Ugale, S. S. Dhankhar and C. M. Nagaraja, *Inorganic Chemistry*, 2016, **55**, 9757–9766.

138 J. Ye and J. K. Johnson, *ACS Catalysis*, 2015, **5**, 2921–2928.

139 C. Wu, F. Irshad, M. Luo, Y. Zhao, X. Ma and S. Wang, *ChemCatChem*, 2019, **11**, 1256–1263.

140 O. M. Yaghi, C. E. Davis, G. Li and H. Li, *Journal of American Chemical Society*, 1997, **119**, 2861–2868.

141 J. Xie, *Zeitschrift fur Anorganische und Allgemeine Chemie*, 2009, **635**, 384–388.

142 K. Manna, T. Zhang and W. Lin, *Journal of the American Chemical Society*, 2014, **136**, 6566–6569.

143 S. Zhang, L. Li, S. Zhao, Z. Sun and J. Luo, *Inorganic Chemistry*, 2015, **54**, 8375–8379.

144 B. Li, T. Roisnel, C. Darcel and P. H. Dixneuf, *Dalton Transactions*, 2012, **41**, 10934–10937.

145 S. S. M. Cohen, P. V Dau, M. Kim and S. M. Cohen, *Chemical Science*, 2013, 601–605.

146 J. Ye, P. Zhang, K. Ye, H. Zhang, S. Jiang, L. Ye, G. Yang and Y. Wang, *Journal of Solid State Chemistry*, 2006, **179**, 438–449.

147 B. Ugale, S. S. Dhankhar and C. M. Nagaraja, *Inorganic Chemistry Frontiers*, 2017, **4**, 348–359.

148 Q. Y. Yang, K. Li, J. Luo, M. Pan and C. Y. Su, *Chemical Communications*, 2011, **47**, 4234–4236.

149 D. X. Xue, A. J. Cairns, Y. Belmabkhout, L. Wojtas, Y. Liu, M. H. Alkordi and M. Eddaoudi, *Journal of the American Chemical Society*, 2013, **135**, 7660–7667.

150 H. T. D. Nguyen, Y. B. N. Tran, H. N. Nguyen, T. C. Nguyen, F. Gándara and P. T. K. Nguyen, *Inorganic Chemistry*, 2018, **57**, 13772–13782.

151 C. Pagis, M. Ferbinteanu, G. Rothenberg and S. Tanase, *ACS Catalysis*, 2016, **6**, 6063–6072.

152 C. Federsel, R. Jackstell and M. Beller, *Angewandte Chemie - International Edition*, 2010, **49**, 6254–6257.

153 B. Ugale, S. S. Dhankhar and C. M. Nagaraja, *Crystal Growth and Design*, 2018, **18**, 2432–2440.

154 E. S. Gutterød, S. Øien-ØDegaard, K. Bossers, A. E. Nieuwelink, M. Manzoli, L. Braglia, A. Lazzarini, E. Borfecchia, S. Ahmadigoltapeh, B. Bouchevreau, B. T. Lønstad-Bleken, R. Henry, C. Lamberti, S. Bordiga, B. M. Weckhuysen, K. P. Lillerud and U. Olsbye, *Industrial and Engineering Chemistry Research*, 2017, **56**, 13206–13218.

CHAPTER 2

Experimental

The general synthetic procedures used to prepare MOFs are outlined in this chapter. Various techniques and instruments used for structural elucidation and full characterisation are also presented.

2.1 Starting Materials

The organic ligand 2,2'-bipyridine-4,4'-dicarboxylic acid (98% purity), and metals salts magnesium nitrate hexahydrate ($Mg(NO_3)_2{\cdot}6H_2O$), manganese chloride tetrahydrate ($MnCl_2{\cdot}4H_2O$), lanthanum chloride heptahydrate ($LaCl_2{\cdot}7H_2O$), zinc nitrate hexahydrate ($Zn(NO_3)_2{\cdot}4H_2O$), cadmium nitrate ($Cd(NO_3)_2{\cdot}4H_2O$) were purchased from Sigma-Aldrich and used without further purification unless otherwise mentioned. Compounds potassium hydroxide, sodium hydrogen carbonate, potassium carbonate, sodium acetate, dichlo(p-cymene)ruthenium dimer and triethylamine were of reagent grade purchased from Sigma Aldrich and used as received. $PdCl_2$ was purchased from Heraeus South Africa and used as received. The metal precursor, $PdCl_2(CH_3CN)_2$, was synthesised from $PdCl_2$ following a reported literature method.[1] The solvents N,N dimethyl formamide (99.8 % purity), dimethyl sulphoxide (99.9 % purity),methanol (99.8 %), ethanol (99.5 % purity) and acetone (99.5 %) were also purchased from Sigma Aldrich.

2.2 General synthetic procedure

Single crystals of MOFs were obtained by using the solvothermal technique. The synthesis involved separately dissolving the ligand and the metal salts in DMF before mixing them. The mixed solutions were placed in vials and heated in an oven at a particular temperature, which yielded crystals. Detailed synthetic procedures for the different metal-organic frameworks will be discussed in relevant chapters.

2.3 X-Ray Diffraction

2.3.1 Single Crystal X-Ray Diffraction (SCXRD)

Single Crystal X-ray diffraction is a non-destructive technique which provides detailed information to facilitate the determination of the structure of a material. The information collected includes; crystal symmetry, unit cell dimensions, details of site-ordering, atomic positions and space group. The unit cell parameters can be used to verify if the structure is new or known in the literature by comparing this data with online databases. [2]

Good quality single crystals of suitable dimensions were selected from the mother liquor under a microscope and covered in Paratone N oil [3] to prevent loss of solvent molecules or decomposition. In cases where the single crystals were too big, they were cut to obtain an appropriate size. Simultaneously, the selected single crystal was glued to a nylon loop connected to a rigid mounting at low temperatures. This nylon loop was then mounted on the goniometer head under a cold stream of nitrogen gas.

Single crystal X-ray data collections were performed at low temperature (173 or 150 K) on a Bruker KAPPA APEX II DUO diffractometer equipped with graphite monochromated Mo Kα radiation (λ = 0.71073 Å). Low-temperature measurements ensure that the volatile components such as solvent molecules remain in the crystal throughout the experiment. The strategy is also helpful during the refinement of data for compounds containing disordered molecules by locking them in fixed positions.

Unit cell refinement and data reduction were performed using the program SAINT.[4] Data were corrected for Lorentz polarisation and absorption due to the variation in the path length through the detector faceplate. The crystal system was established from the observed Laue symmetry of the diffraction pattern and the space group were determined from systematic absences in the X-ray intensity data and linking the observed result with the systematic absences of a known space group. The program XPREP[5] was used to confirm the space group of the structures and to prepare input files which were then used for structure solution by direct methods using SHELXS[6] and refined anisotropically on F^2 full-matrix least-squares with SHELXL[6] within the X-SEED[7] interface. Anisotropic thermal parameters were applied to non-hydrogen atoms while all hydrogen atoms were calculated and added at idealised positions.

2.3.2 Powder X-ray diffraction (PXRD)

Powder X-ray diffraction is a rapid analytical technique which is used for characterisation of crystalline materials. The technique is primarily used for phase identification as the powder pattern can be seen as a fingerprint of a specific structure. Powder diffraction measurements were performed on an XPERT-PRO diffractometer using Cu Kα-radiation ($\lambda = 1.5406$ Å) at 298 K. A spatula tip of crystals were removed from the mother liquor and dried on a filter paper before being gently ground into a powder using a motor and pestle. The samples were then placed onto a zero background sample holder and scanned over 2θ range 5 to 40° with a step of 0.017° increments. X-rays were generated with a current flow of 40 mA and voltage of 40 kV. The resultant experimental PXRD patterns recorded were plotted using Excel.

The fully refined single-crystal structure coordinates were input into Mercury program[8] to produce an idealised PXRD pattern (calculated pattern) of the structure. The calculated pattern was compared with the experimental PXRD pattern to determine whether the single crystal is representing the bulk of the material. PXRD was also used to conclude whether any bulk material obtained in subsequent experiments is that of the desired compound. By comparing the PXRD pattern of the MOF catalyst before and after catalysis, we could also determine whether the integrity of the MOF catalyst was maintained.

2.3.3 Topological Analysis

Network topology of the MOFs was obtained using the free software programs SYSTRE,[9] TOPOS[10] and checked against the Reticular Chemistry Structural Resource (RCSR).[11]

2.4 Spectroscopic Analysis

2.4.1 Fourier Transform Infrared Spectroscopy (FITR)

FITR analysis of the samples was recorded in the range 400 to 4000 cm^{-1} on Perkin Elmer Fourier Transform Infrared spectrophotometer (FTIR) BX II fitted with an ATR probe. A small amount of sample was finely ground and mounted on the spectrophotometer for data collection. The technique was used to study the changes in the coordination modes of the carboxylate moiety to the metal through the distinguished magnitude of separation between the carboxylate stretches. It was also used to establish the presence of solvent molecules with distinct functional groups.

2.4.2 Nuclear Magnetic Resonance Spectroscopy (NMR)

NMR is a technique used to elucidate the structures of compounds based on chemical shifts of a proton or carbon following the magnetic field surrounding it.[12] It was applied to the ligand, complex and functionalised MOFs to determine the structure of the synthesised compounds. A few milligrams of the compounds were dissolved in suitable NMR solvents and transferred to 5 mm NMR glass tubes which were then mounted to a Bruker Ultrashield 400 MHz (^{1}H: 400 MHz; ^{13}C: 100 Hz) spectrometer. All chemical shifts were recorded in ppm. ^{1}H NMR was also used to confirm catalysis products.

2.5 Elemental Analysis

Elemental analysis was used to elucidate the empirical formula of the MOFs structures. Two different techniques have been employed to determine the complex formation of theses MOFs, the organic component by CHN analysis and the metal content by ICP.

2.5.1 Inductively Couple Plasma Optical Emission (ICP-OES)

Inductively Couple Plasma Optical Emission analysis was performed on a Spectro Arcros instrument calibrated using standards. Samples were microwave digested in aqua regia (4 mL HNO_3, 1mL HCl) and analysed directly. The technique was used for the detection and quantitative determination of trace metal elements in the MOF catalyst, as well as for testing whether metal species have been leached from the solid catalyst to the solution during the reaction.

2.5.2 CHN-Analysis

CHN analysis experiments were performed on a Scientific FLASH 2000 CHNS-O Analyser to determine the percentage amounts of carbon, hydrogen, and nitrogen in a sample. The results were then compared to the percentages calculated from compound compositions determined from single-crystal X-ray diffraction.

2.6 Thermogravimetric Analysis (TGA)

Thermogravimetric analysis was used to model the number of solvent molecules per asymmetric unit by measuring the mass loss as a function of temperature. It was also used to determine the decomposition temperature, relating to the stability of the framework. Before analysis, samples were surface dried on a filter paper. Approximately 2-5 mg samples were then placed in an aluminium pan. TGA experiments were performed using a TA Discovery Instrument TA-Q50 with a heating rate of 10 °C min^{-1} within a temperature range of 25–600 °C under a dry nitrogen purge gas flow of 50 $mLmin^{-1}$.

2.7 Gas Sorption Measurements:

Porosity and surface properties of the samples were analysed using Micromeritics ASAP 2460 surface and porosity analyser. Before analysis, the samples were degassed using nitrogen gas (N_2) at 90 °C for 12 hours, then at 150 °C for 8 hours. Thereafter, the samples were weighed and analysed at 77K using N_2 as a probe gas. H_2 and CO_2 sorption experiments were performed using a Micrometrics 3Flex Surface Analyser. The samples were prepared by using a Micrometrics Flowprep with the flow of nitrogen over the samples for 4 hours whilst heating at 60 ^{o}C. Furthermore, the samples were heated at 150 °C under vacuum for 2 hours before the analysis commenced.

2.8 High-Resolution Transmission Electron Microscopy (HR-TEM) Analysis

The samples were analysed using the Tescan Vega 3LMH scanning electron microscopy. The samples were placed on sticky tape and carbon-coated using an Agar-Turbo carbon sputter.

2.9 Scanning Electron microscopy- Energy Dispersive (SEM EDX) Analysis

The catalysts were analysed using electron microscopes. The morphological studies were performed on a Jeol-Jem 2100F electron transmission electron microscopy operating at a voltage of 200 kV. Before analysis, the catalytic samples were dispersed in methanol and sonicated for 30 minutes. Thereafter, they were placed on a carbon-coated copper grid and dried at room temperature.

2.10 X-ray Photoelectron Spectroscopy

X-ray photoelectron spectroscopy (XPS) analyses were obtained with a Kratos Axis supra spectrometer using an Al K(alpha) source (15mA, 0.15 eV) Survey scan, a high resolution was carried out with analysis area of 300 x 700 microns and a pass energy of 160 eV. The charging effects were corrected by setting a component of carbon 1S transition (adventitious carbon) at 285 eV. The chemical states were identified by using Casa XPS software version 2.3.22.

2.11 Chemical Stability Tests

Activated MOF samples were soaked in different solvents and bases that are normally used for CO_2 hydrogenation for 36 hours. The solids recovered by filtration were washed thoroughly before recording FTIR and PXRD patterns.

2.12 Catalytic Hydrogenation of CO_2 to Formate

The hydrogenation of CO_2 was carried in a Teflon lined stainless-steel reactor equipped with a magnetic stirrer. In a typical run, known amounts of catalyst and 5 mmol KOH in 8mL ethanol were loaded into the reactor. The reactor was sealed and purged three times with CO_2, and then CO_2 and H_2 charged to the desired pressure at room temperature. The catalytic reactions were carried within a temperature range of 90 to 120 ˚C while stirring was maintained at 945 rpm. After the reaction, the reactor was cooled to room temperature and the residual gas carefully released in a fume hood. The supernatant was analysed by ^{1}H NMR spectroscopy using acetone as an internal standard. The solid catalyst was washed several times with ethanol and dried in an oven at 80 ˚C for recycling. All experiments were performed in duplicate and the average recorded.

2.13 References

1 G.K. Anderson, M. Lin, A. Sen, and E. Gretz, Inorganic Synthesis, John Wiley & Sons, Inc, Hobeken, NJ, USA, 2008, 60-63

2. D. A. Fletcher, R. F. McMeeking and D. Parkin, *Journal of Chemical Information and Computer Sciences*, 1996, **36**, 746–749.

3 Paraton N oil (Exxon Chemical Co., Texas, USA)

4 SAINT, version 7, 7.60a, Bruker AXS Inc, Madison, WI, USA, 2006

5 Bruker (2007), Bruker AXS Inc; Madison, Wisconsin USA, 2007, **1**

6 G. M. Sheldrick, *Acta Crystallographica Section C: Structural Chemistry*, 2015, **71**, 3–8.

7 L. J. Barbour, *Journal of Supramolecular Chemistry*, 2001, **1**, 189–191.

8 C. F. Macrae, I. J. Bruno, J. A. Chisholm, P. R. Edgington, P. McCabe, E. Pidcock, L. Rodriguez-Monge, R. Taylor, J. Van De Streek and P. A. Wood, *Journal of Applied Crystallography*, 2008, **41**, 466–470.

9 O. D. Friedrichs, *SYSTERE, 1.1.4beta*, 2019, http:/gavrog.sourceforge.net./

10 M. O. Keeffe, M. a Peskov, S. J. Ramsden and O. M. Yaghi, *Accounts of Chemical Research*, 2008, **41**, 1782–1789.

11 C. Y. Niu, X. F. Zheng, Y. He, Z. Q. Feng and C. H. Kou, *CrystEngComm*, 2010, **12**, 2847–2855.

12 R. M. Silverstein, F. X. Webster and D. J. Kiemle, *Journal of Molecular*

Structure, 2002, **30**, 424–425.

CHAPTER 3:

Hydrogenation of CO_2 to Formate Using Novel Lanthanum(III) Based Metal-Organic Frameworks.

In this chapter, a novel three-dimensional (3D) metal-organic framework, **JMS-1**, with the molecular formula $[La_3(bpdc)_3(DMF)_3]_n$ was prepared using 2,2'-Bipyridine-4,4'-dicarboxylic acid and $LaCl_3{\cdot}7H_2O$ as starting materials. The MOF was characterised using X-ray diffraction studies (SCXRD and PXRD), thermal analysis (TGA), Fourier Transform Infrared Spectroscopy (FTIR) and Elemental analysis. Network analysis of **JMS-1** revealed a new 7-connected topology (**zaz**). The activated phase (**JMS-1a)** was functionalised by cyclometalation of the MOF backbone using the metal precursor $[RuCl_2(p\text{-cymene})]_2$ to give **Ru(II)@JMS-1a**. Successful incorporation of ruthenium into the MOF was confirmed by X-Ray Photoelectron Spectroscopy (XPS), Nuclear Magnetic Resonance Spectroscopy (^1H NMR) and Inductively Coupled Plasma-Optical Emission Spectroscopy (ICP-OES). Surface characterisation of both MOFs was done using Brunauer–Emmett–Teller (BET). The CO_2 and H_2 storage capacity the native and functionalised MOFs was evaluated. Hydrogenation of CO_2 to formate was also evaluated.

3.1 Synthesis of JMS-1 and Ru(II)@JMS-1a

JMS-1 was prepared by dissolving 2,2'-bipyridine-4,4'-dicarboxylic acid (H_2bpdc) (29 mg, 0,113 mmol) in 11 mL of DMF followed by addition of $LaCl_3.7H_2O$ (110 mg, 0,327 mmol). The reaction mixture was stirred for 15 minutes and heated in an oven at 110 ˚C for 48 hours (Equation 3.1). **JMS-1** was obtained as colourless dendrite-like crystals. **JMS-1** was activated by soaking the as-synthesised crystals in methanol for 24 hours to allow for the exchange of DMF with a low boiling point solvent. The soaked crystals were then heated under vacuum for 24 hours at 78 ºC to give the activated phase **JMS-1a**. **Ru(II)@JMS-1a** was prepared by soaking 50 mg of **JMS-1a** was in 10 mL methanolic and sodium acetate solution of $[RuCl_2($*p*-cymene$)]_2$ for 24 hours at room temperature.[1]

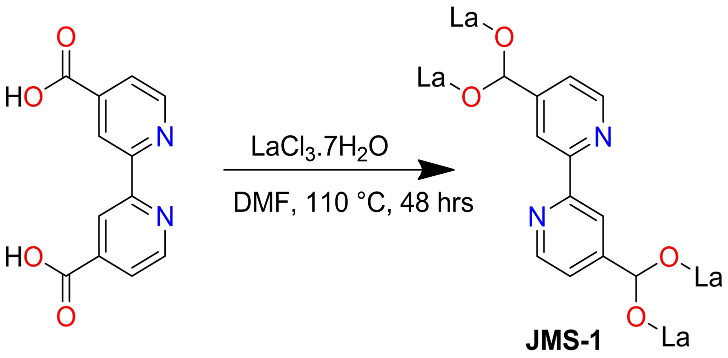

Equation 3.1: Synthesis of JMS-1 illustrating the linker conformation and binding mode of the carboxylate moiety.

3.2 Single Crystal X-ray Diffraction

Single crystal X-ray diffraction (SCXRD) data collection of **JMS-1** was done on a Bruker KAPPA APEX II DUO Diffractometer. All non-hydrogen atoms were located in the difference-electron density maps and were refined anisotropically. Hydrogen atoms were placed with geometric constraints and refined with isotropic temperature factors. Due to high solvent disorder, some atoms of the DMF molecules were refined isotropically. Restraints on bond distances and thermal motion of disordered groups have been applied (DFIX). The crystallographic and refinement parameters of JMS-1 are given in Table 3.1. The structure was deposited at the Cambridge Crystallographic Data Centre and allocated the numbers: CCDC 1851044.

	JMS-1
Empirical formula	$C_{45}H_{39}La_2N_9O_{15}$
Formula weight	1223.67
Temperature/K	293(2)
Crystal system	Orthorhombic
Space group	$Pna2_1$
a/Å	18.0826(12)
b/Å	13.3216(9)
c/Å	21.9623(15)
Volume/Å^3	5290.5(6)
Z	4
ρcalcg/cm^{-3}	1.5361
F(000)	2388
Crystal size(mm)	0.111 x 0.05 x 0.07
Index ranges (*h, k, l max*)	23, 17, 28
Reflections collected	47417
Two theta range	1.788-27.556

Independent reflections	11053
Goodness-of-fit on F^2	1.036
Final R indexes [I>=2σ (I)]	0.0546
Final R indexes [all data]	0.1596
Largest diff. peak/hole / e $Å^{-3}$	1.08/-1.00

Table 3.1: Crystallographic information and refinement parameters of **JMS-1**

3.3 Structural Description

JMS-1 crystallises in the orthorhombic crystal system, space group $Pna2_1$. The asymmetric unit of **JMS-1** consists of two crystallographically independent La^{III} centres, three fully deprotonated 2,2'-bipyridine-4,4'-dicarboxylate (bpdc) linkers and a total of three DMF molecules. The structure of **JMS-1** is made up of $La_2C_3O_6$ secondary building unit (SBU) rods which grow along the *b*-axis as shown in Figure 3.1a. The SBUs are connected by bpdc, linkers which grow along the *a*-axis to give a 3D structure. The presence of the bpdc linkers which connect the SBU along the *b*-*c* plane reduces void space found in **JMS-1**.

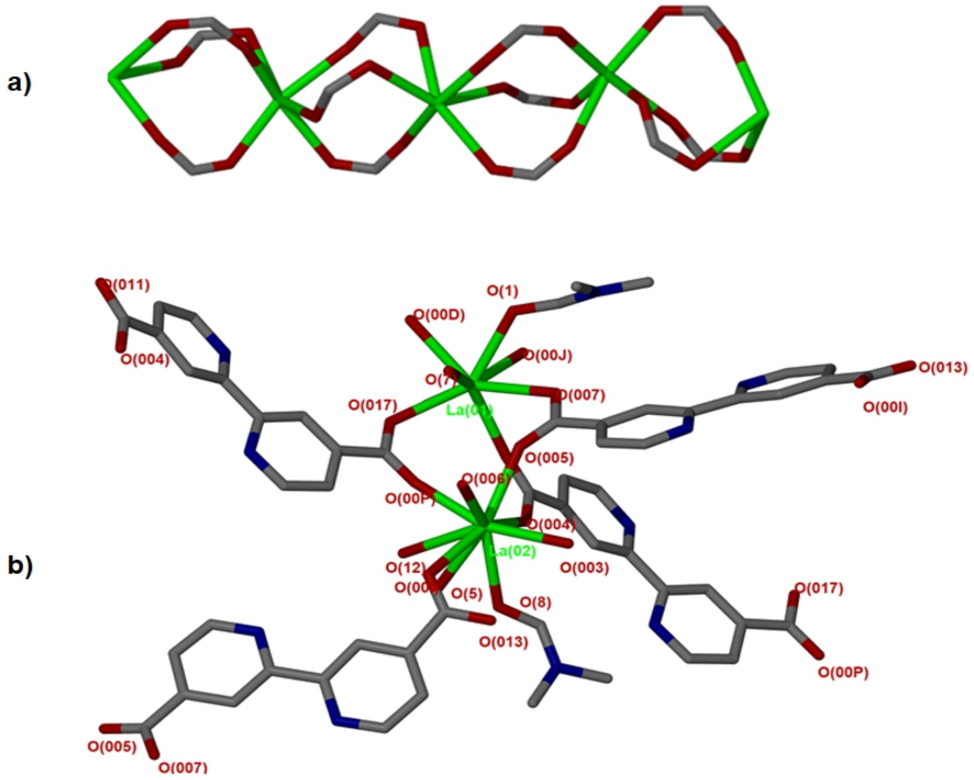

Figure 3.1: a) SBU rod generated *in situ*, b) Coordination environment around the two La^{III} metal centres modelled in the asymmetric unit.

Each La^{III} metal centre is coordinated to two DMF molecules and six oxygen atoms of the bpdc linker to furnish a square antiprismatic geometry as illustrated in Figure 3.1b. One of the coordinated DMF molecules on each La^{III} was found to be disordered over two positions and the atoms were refined isotropically. The other coordinated DMF on each of the metal ions in the asymmetric unit was modelled with 50% site occupancy as suggested by TGA analysis. Due to high-temperature factors, the atoms of these DMF molecules were also refined isotropically. The bpdc linker assumes a bridging bidentate mode connecting two La^{III} metal ions. La-O bond distances range from 2.41(13) to 2.660(4) Å.

The analysis of channels (window dimensions of approximately 6.8 x 5.2 Å) found in **JMS-1** which run along the *b*-axis measured by PLATON[2] shows that they occupy 41 % of the unit cell volume. These channels are occupied by DMF molecules that are coordinated to the La^{III} metal ion. Figure 3.2 illustrates the channels found in **JMS-1.** The analysis of cavities occupied by DMF using the Mercury program[3] shows that they are interconnected as illustrated in Figure 3.3.

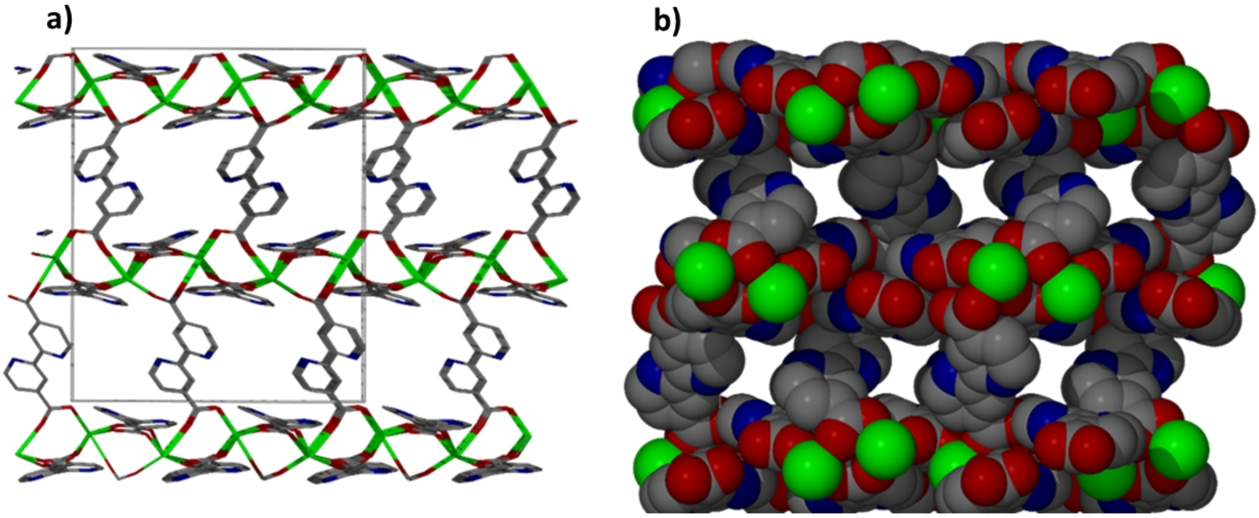

Figure 3.2: a) Packing diagram of **JMS-1** viewed along the *b*-axis drawn in a) stick form and b) van der Waals radii. The guest coordinated DMF and hydrogen atoms have been omitted for clarity.

3.4 Thermal analysis

Thermogravimetric analysis of **JMS-1** (Figure 3.4) shows a 16.5% weight loss between 150 and 250 ˚C, which is ascribed to the loss of three DMF molecules per formula unit modelled in the structure of **JMS-1** (calculated 17.89%). From 320 ˚C, there is a plateau up to 450 ˚C, an indication of high thermal stability. Decomposition of the framework occurs around 460 ˚C. **JMS-1** was activated by soaking the as-made crystals in methanol for 24 hours, followed by heating under vacuum for 24 hours at 78 ˚C to give **JMS-1a**.

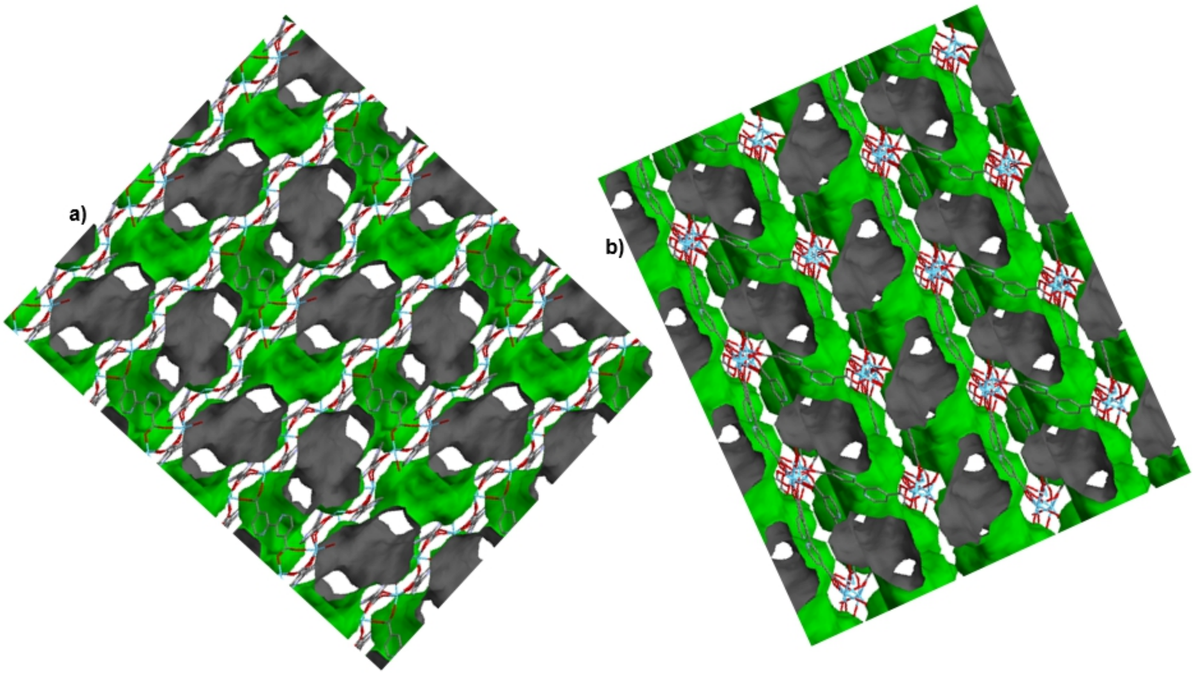

Figure 3.3: Cavities found in **JMS-1** in the absence of DMF viewed along a) b-axis and b) a-axis. The outside and inside surface of the cavities are depicted in green and grey respectively.

Complete removal of the solvent molecules was confirmed by TGA analysis which showed no weight loss until decomposition. Coordinated DMF molecules in MOF **JMS-1** can be removed by guest exchange followed by thermal treatment, making it a suitable candidate for CO_2 capture and catalysis. The removal of coordinated guest molecules has been reported to provide free open metal sites, which enhances the adsorption of hydrogen and carbon dioxide in the pores and catalysis at the metal centres.[4,5] **JMS-1a** and **Ru(II)@JMS-1a** are thermally stable which makes them good candidates for catalysis within the temperature range at which catalysis is carried out.

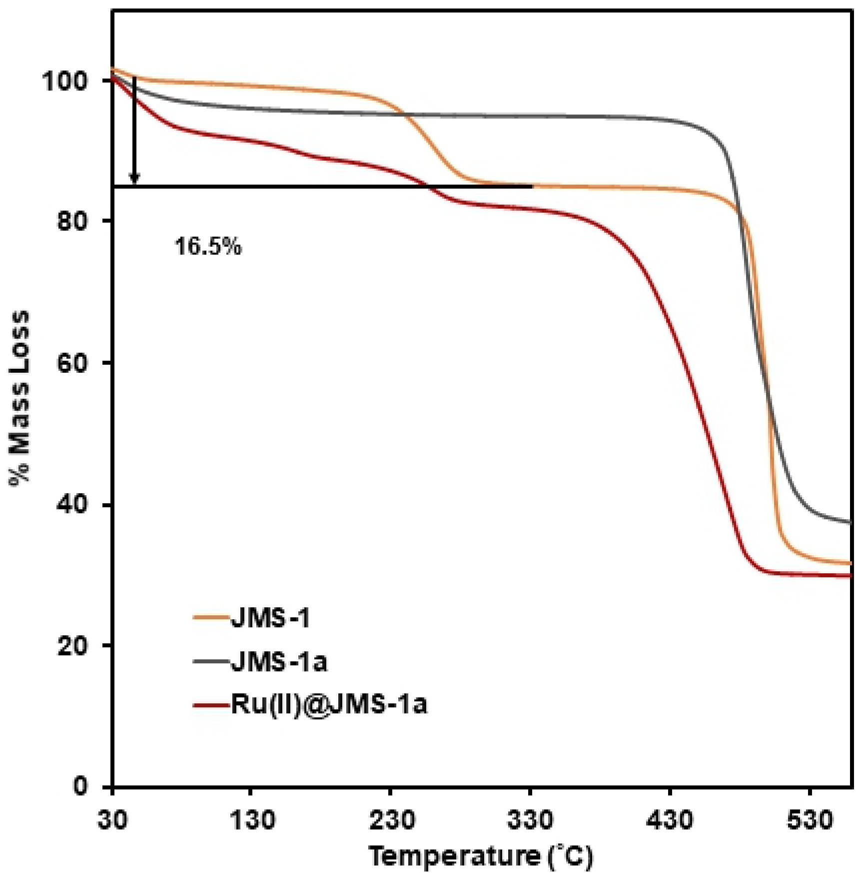

Figure 3.4: TGA traces of **JMS-1**, **JMS-1a** and the $[RuCl_2(p\text{-cymene})]_2$ loaded MOF, **Ru(II)@JMS-1a**.

3.5 FTIR Analysis

Fourier transform infrared (FTIR) spectroscopy analysis provides evidence that the linkers are coordinated to the metal centres and the deprotonation of the carboxylic acid groups (Figure 3.5). This is consistent with what is modelled in the crystal structure. A shift in the absorption bands of the linker from 1739 cm^{-1} to 1578 cm^{-1} in the IR spectrum of the as-synthesised **JMS-1** agrees well with the carboxylate functional groups bound to the La^{III} centre. Successful activation of the MOF is evidenced by the disappearance of the absorption band at 1646 cm^{-1}, which is attributed to coordinated DMF molecules. The asymmetric and symmetric carboxylate stretches in compound **JMS-1** are located at 1578 and 1398 cm^{-1} respectively, and the magnitude of separation was found to be 180 cm^{-1}, suggesting that the carboxylate group is coordinated to two La^{III} ions in a bidentate bridging fashion.[6] The band located at 1539 cm^{-1} is attributed to the C-C of the benzene ring.

The absence of a shoulder on the peak 1605 cm^{-1} (specific to the carboxylic acid hydroxyl) suggests that the linker is fully deprotonated.[7] The FTIR of **JMS-1** and **JMS-1a** retains similar characteristic bands in the carboxylate stretching region confirming that the binding mode of the carboxylate moiety is not affected during the activation process.[8]

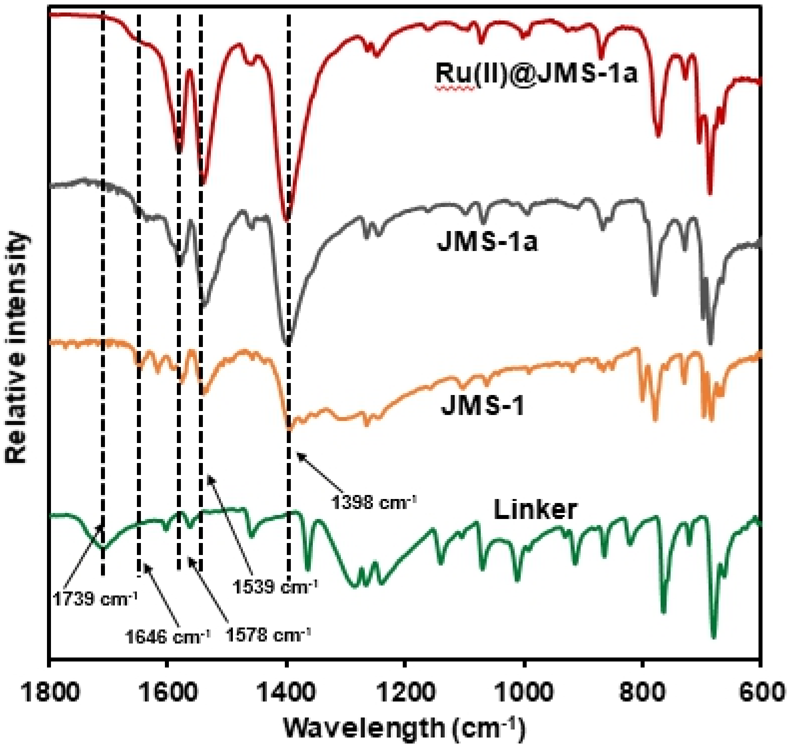

Figure 3.5: IR spectrum of the linker, **JMS-1**, **JMS-1a** and **Ru(II)@JMS-1a**

3.6 PXRD Analysis

The phase purity of **JMS-1** was confirmed by a good match between the experimental and calculated PXRD patterns (Figure 3.6). Comparison of the PXRD patterns of **JMS-1** and **JMS-1a** suggest the formation of a new phase upon activation.

3.7 Topological Analysis

The structural features of MOFs can be analysed based on net topology (structure) composed of nodes (vertices) that have specific geometry and are linked to other nodes *via* linkers (edges).[9, 10] The metal ion (or metal clusters) and organic or inorganic linkers usually serve as secondary building units. The knowledge of topologies can facilitate in not only understanding, description and classification of existing networks, but also the conceiving of new MOFs.[11]

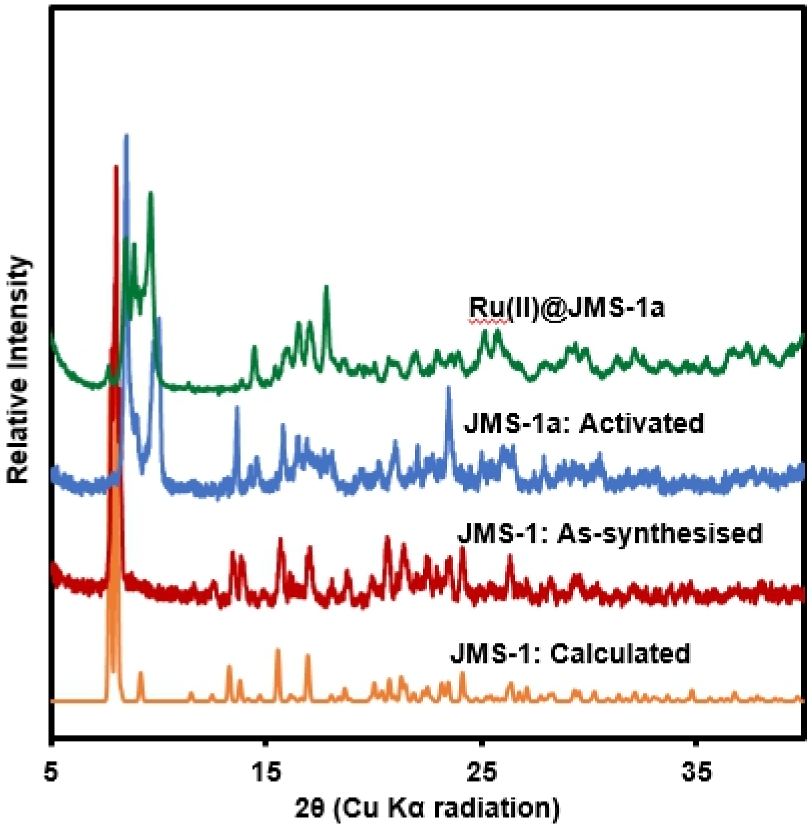

Figure 3.6: PXRD patterns of **JMS-1**: calculated, **JMS-1:** experimental, **JMS-1a**: activated and **Ru(II)@JMS-1a**.

MOFs based on rods, that is when there is a polynuclear coordination entity propagating infinitely in one dimension and connecting to other rods by bridging ligands, (infinite metal SBU:s) has received attention lately.[12,13] One reason is that their topologies do not generally allow for the interpenetration of a second network, and a second is that they often display "breathing" properties (for example of the MIL-53 types), i.e. they may change the volume on uptake or discharge of guest molecules.[14] Compared to the topologies of MOFs based on finite metal SBU:s or single metal nodes that often display one of the high symmetry nets,[15,16] rod-based MOF:s have an intriguing diversity. One recent example is bismuth-based MOF that, although not built of anything more complex than 1,3,5-benzenetricarboxylate (BTC3) ligands and Bi^{3+} ions, has an unprecedented topological complexity with 54 unique nodes and 135 edges, that is the net has transitivity 54 135.[17]

A simple approach considers the La-carboxylate rod in compound **JMS-1** as a featureless rod, except for the links to the bridging ligands. We then consider rod centred nodes at the centroids of the tris-carboxylate binding sites. This gives a five-connected **soe**-net as seen in Figure 3.7.

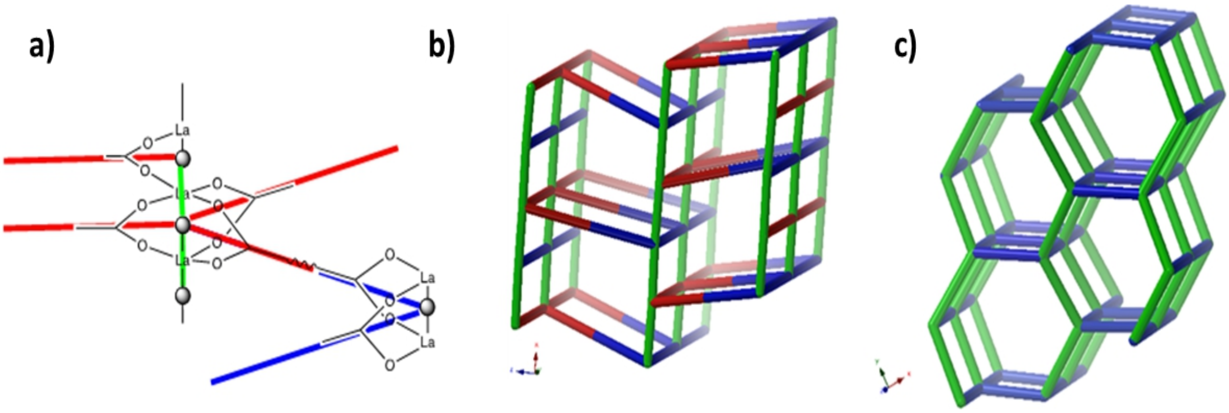

Figure 3.7: a) Node assignment for a simple featureless rod with bridging ligands. b) The resulting **soe**-net in the structure. c) The most symmetric form of the **soe**-net, the edges corresponding to the rod emphasized in green. The **soe**-net has transitivity 1 4 (1 unique node and 4 unique edges). This description disregards the topology of the rod and the relations of the links this enforces and is not the preferred description of the structure.

This conspicuously looks like the same approach that we use with for example paddle-wheel four-connected SBU:s like the $[Cu_2(\text{-}CO_2)_4]$ in for example HKUST-1 with the underlying topology **tbo**.[18] There are two problems, however. The general deconstruction approach where a polynuclear coordination entity is contracted to one point obviously will contract any rod to a single point and thus reduce a 3D net to a 2D net, in this case, the 6-connected **hxl**-net. The other issue is that the divisions we have done on the infinite polynuclear entity are arbitrary and difficult to generalize. In the approach giving the **soe**-net, it is necessary to think of the net as constructed by polygons, triangles, in this case, intersected by the rod. While the triangles are straight forward for this structure, this is not always the situation. This is not necessarily a problem from the analysis point of view, but the relation between these single links, or the triangles as they are in our case, is lost. Also, the relation between the links projecting from the rod is completely determined by the topology of the rod. Thus, important structural information, like the existence of isomers, is potentially lost if this approach is used. In this respect, the problem is similar to the discussion of the "all node" deconstruction approach considering all branch points of the linkers, and the "single-node" method considering only components mixed where the latter also will miss potential isomers.[12]

As suggested by O'Keeffe and coworkers,[19] we instead take the carbonyl carbons as the points of extension and create with them the simplest geometrical forms that describe the features of the rod. Often these descriptions turn out to be ladders, helices or linked polyhedra. In our case, the rod can be described as face-sharing octahedra, see Figure 3.8. As every vertex in an octahedron is four-connected, face sharing the octahedra will mean every vertex is now six-connected, and bridging the rods with the ligands means we will have a seven-connected net. The most regular way of doing this is the **sct**-net, a pleasingly symmetric net where each octahedron have six links protruding from it with 60° angles if projected along the *a*-axis (Figure 3.8).[14]

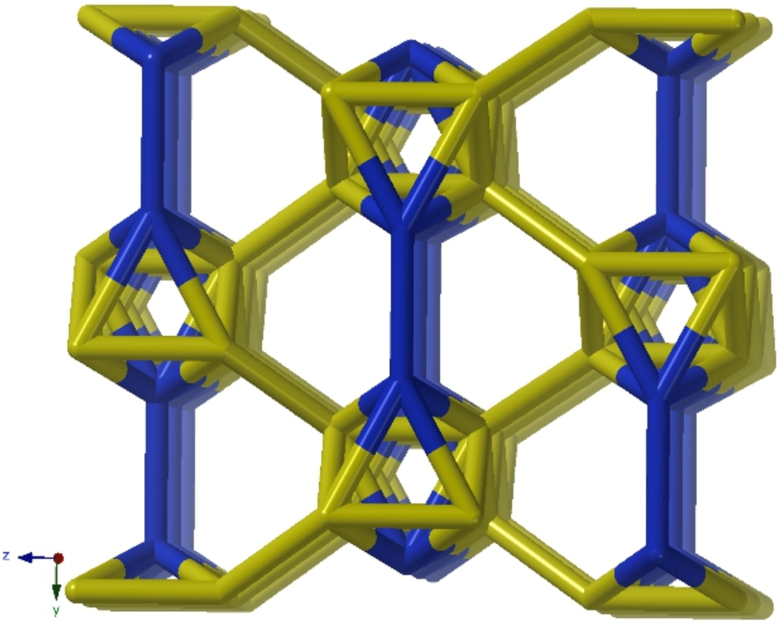

Figure 3.8: The **sct**-net based on face sharing octahedra, note that the number of links going out from the rod in all directions is the same. This net has transitivity 2 8 (2 unique nodes and 8 unique edges).

On the contrary, network analysis of JMS-1 revealed a new 7-connected network topology, **zaz**. (za and z stands South Africa and Zimbabwe respectively). The net (Figure 3.9) has two pairs of two parallel links connecting the rods, resulting in a three-nodal net that is nevertheless symmetric and esthetically attractive.

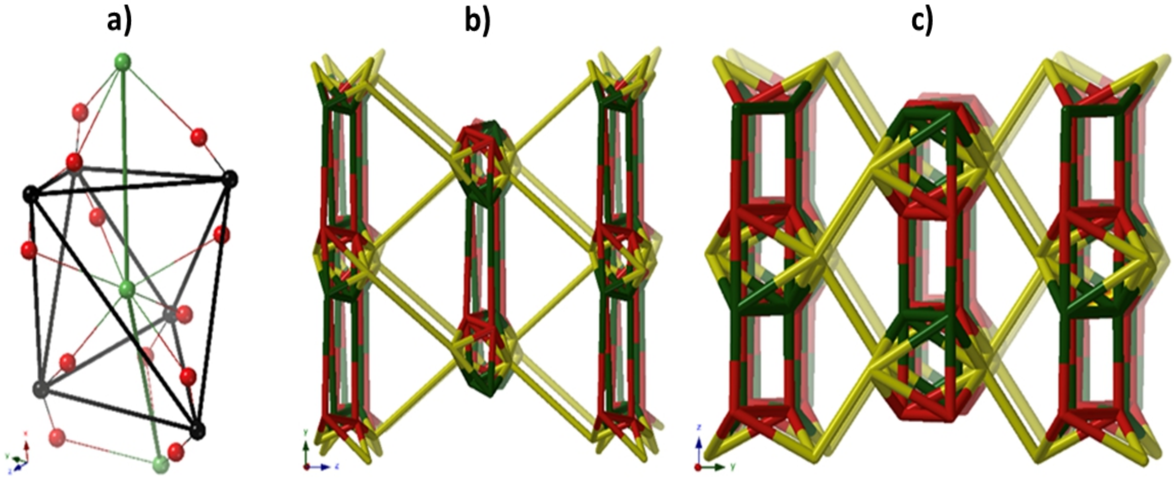

Figure 3.9: a) The face sharing octahedra in the rod of **JMS-1** (emphasised by green links) constructed from the carbonyl carbons (black tick lines) b) The resulting **zaz**-net in the structure. c) The most symmetric form of the **zaz**-net. This net has transitivity 3 12 (3 unique nodes and 12 unique edges).

3.8 Functionalisation of JMS-1a

Ru(II)@JMS-1a was prepared by cyclometalation of the activated phase, **JMS-1a**, according to the method reported in the literature for a homogeneous system.[1] It is a direct method to produce stable cyclometalated ruthenium(II) complexes with $[\mathrm{RuCl_2}(p\text{-cymene})]_2$ metal precursor, *via* the C-H bond deprotonating in the presence of sodium acetate at room temperature in methanol. Successful incorporation of Ru into the MOF was confirmed by XPS and NMR studies.

XPS measurements were conducted to investigate the chemical nature of **JMS-1a** and **Ru@JMS-1a.** The initial state effects or chemical shifts reflect the changes in the electronic structure of the material. During this reaction, we expected the nitrogen and carbon of the linker to bind to the ruthenium(II). Successful coordination of Ru^{II} to nitrogen and carbon was reflected by a decrease in the binding energy of carbon and nitrogen.[20] A shift in the binding energy of C1s from 285.5 eV in **JMS-1a** to 285.3 eV in **Ru(II)@JMS-1a** (Figure 3.10a and b) provides evidence that the Ru^{II} complex is grafted onto the MOF. The species indicated in Figure 3.10a and b is consistent with what is in the structure of **JMS-1a** and **Ru(II)@JMS-1a**. In the case of N1s binding energies (Figure 3.10c and d), one identified peak is correlated to the change in the chemistry of **JMS-1a**. The binding energy of N1s for **JMS-1a** is located at 400.9 eV. Upon cyclometalation, the energy shifted to 400.06 eV, indicating that the nitrogen atom donated electrons to Ru^{II} ion. The observed shifts are consistent with low ruthenium loading content of 0.4% in **Ru@JMS-1a** from ICP-OES analysis.

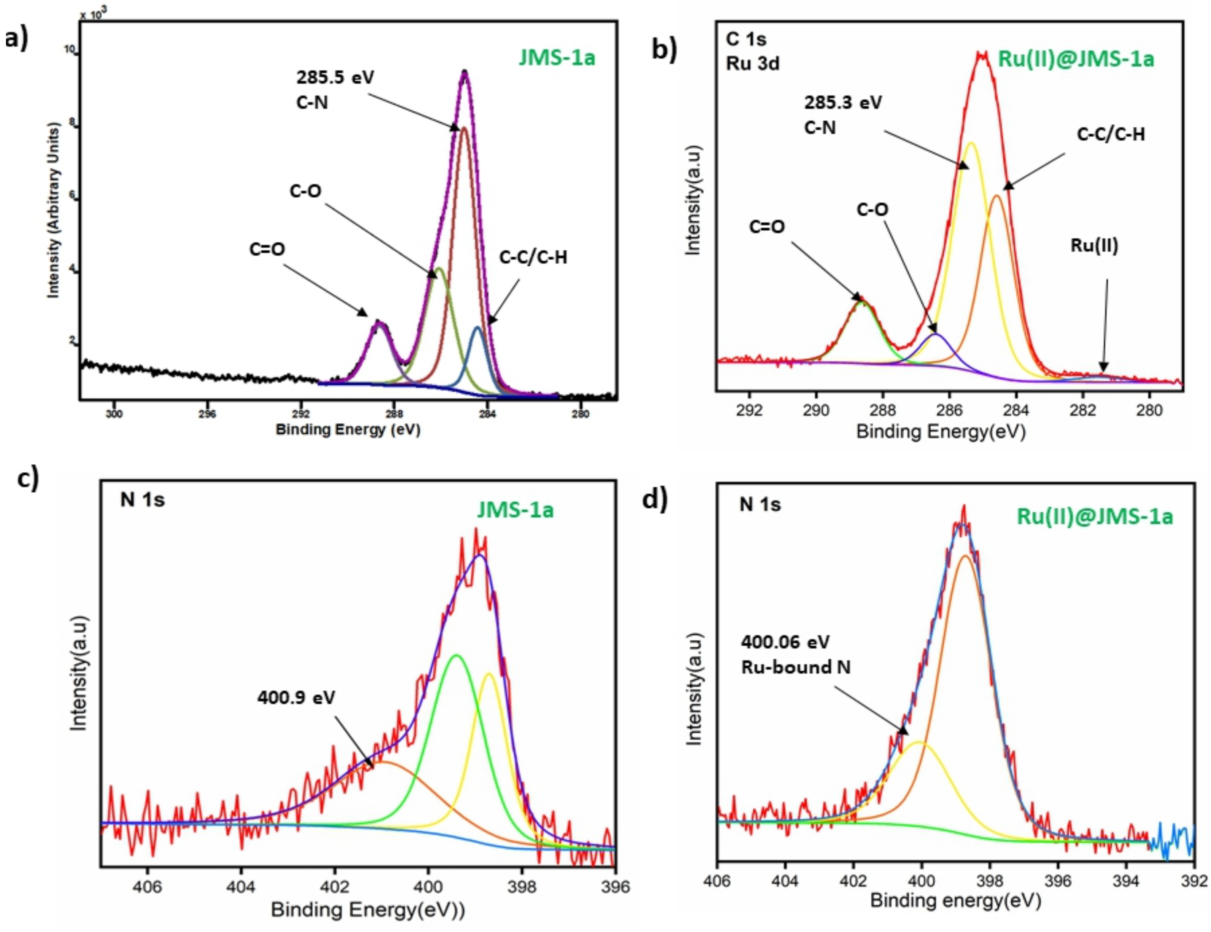

Figure 3.10: XPS spectra (a and b) C 1s (c and d) N1s

The Ru 3p deconvoluted four peaks at 460.3, 464.1, 472.7 and 482.7 eV as illustrated in Figure 3.11. The peak at 482.7 eV corresponds to Ru-N species.

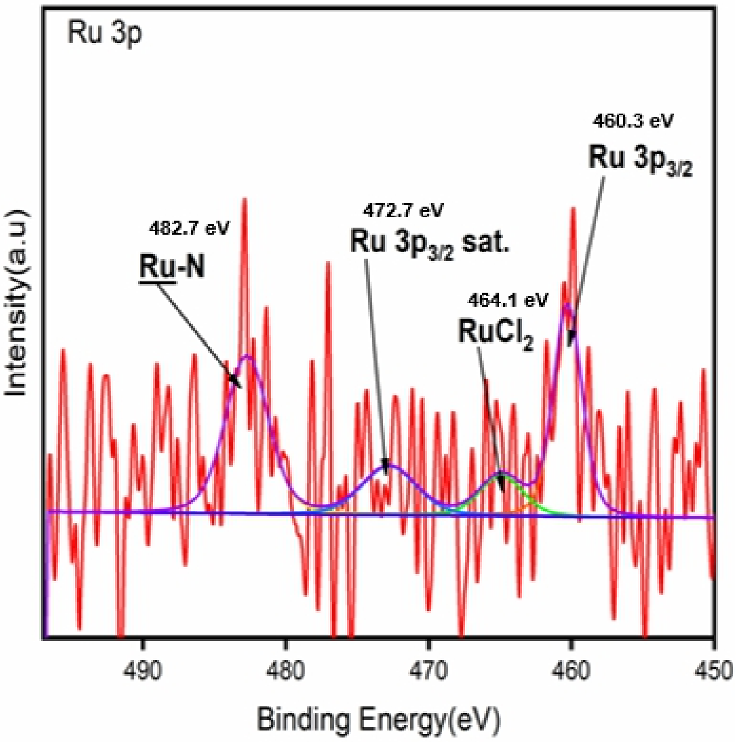

Figure 3.11: XPS spectra of Ru 3p

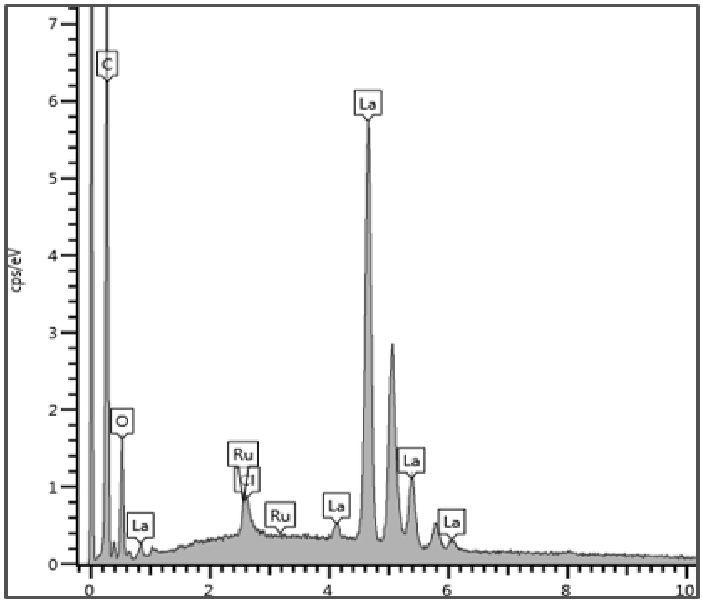

Figure 3.12: SEM-EDX analysis of **Ru(II)@JMS-1a**

Successful incorporation of ruthenium into the MOF was also confirmed SEM-EDS analysis as illustrated in Figure 3.12, which shows the presence of ruthenium and chlorine atoms.

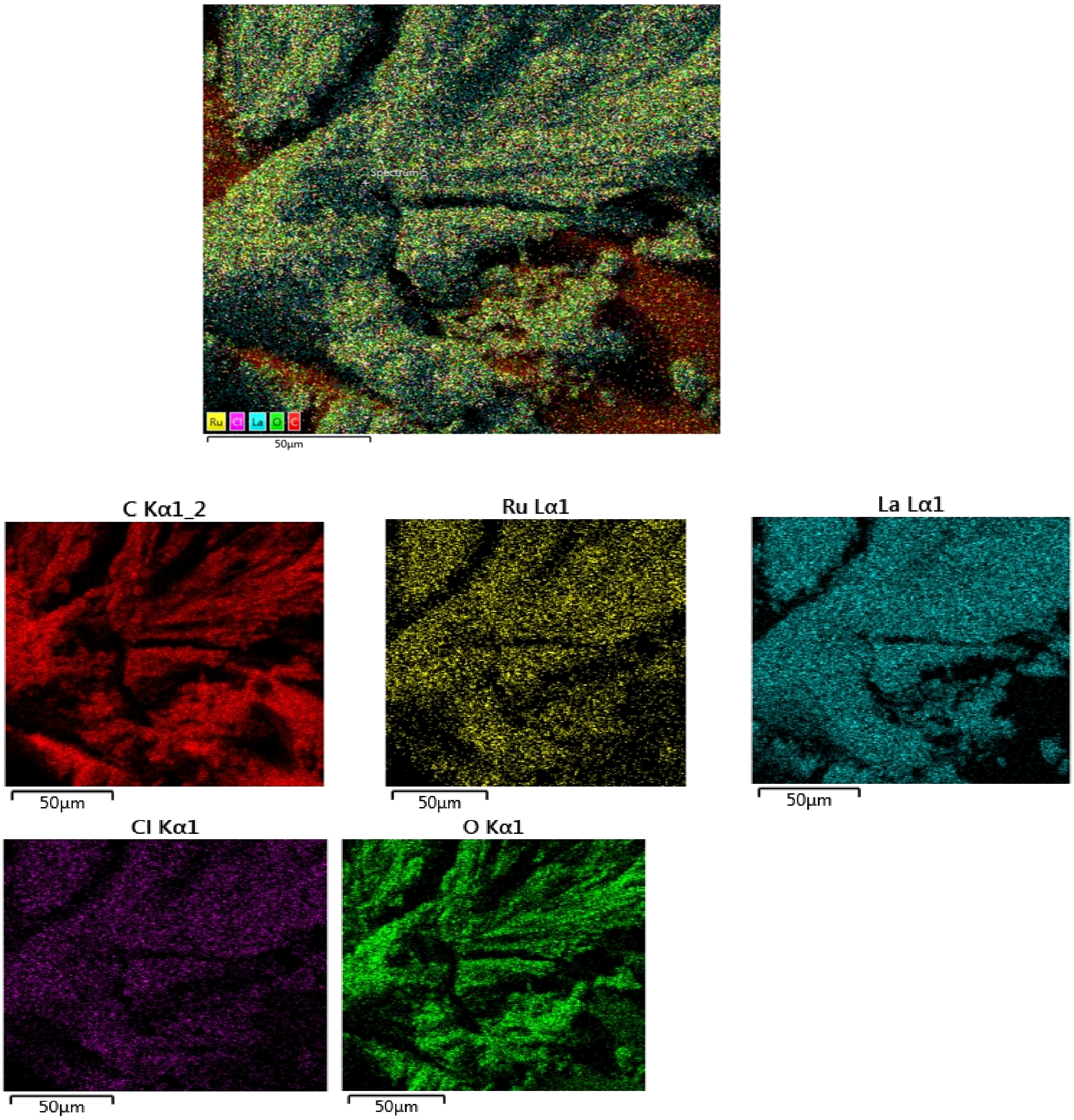

Figure 3.13: a) SEM images and b) elemental mapping of **Ru(II)@JMS-1a**

An element map is an image showing the spatial distribution of elements in a sample. Because it is acquired from a polished section, it is a 2D section through the unknown sample. Element maps are extremely useful for displaying element distributions in textural context, particularly for showing compositional zonation. EDX elemental mapping for the individual atoms in Ru(II)@JMS-1a illustrated in Figure 3.13 infers a consistent and even distribution of Ru^{II} throughout the matrix.

Further confirmation that ruthenium is bound to the MOF was shown by ^{1}H NMR spectroscopy (Figure 3.14). Coordination of the Ru^{II} to **JMS-1a** is evidenced by 2 doublets around 5.3 ppm and 5.5 ppm in the dimer which, upon complexation shifted downfield and split into 4 doublets. The methyl protons of the *p*-cymene around 2.8 ppm, 2.1 ppm and 1.2mppm shifted upfield upon coordination of Ru to the MOF backbone. The presence of identical peaks in the aromatic region of the ^{1}H NMR of **Ru(II)@JMS-1a** relative to that of **JMS-1a** (marked with vertical black lines) infers that the MOF is partially cyclometalated. This was further confirmed by ICP-OES results, with low ruthenium loadings in the MOF. The complexity of the NMR might be due to overlapping of the aromatic protons of the linker in JMS-1a and Ru(II)@JMS-1a.

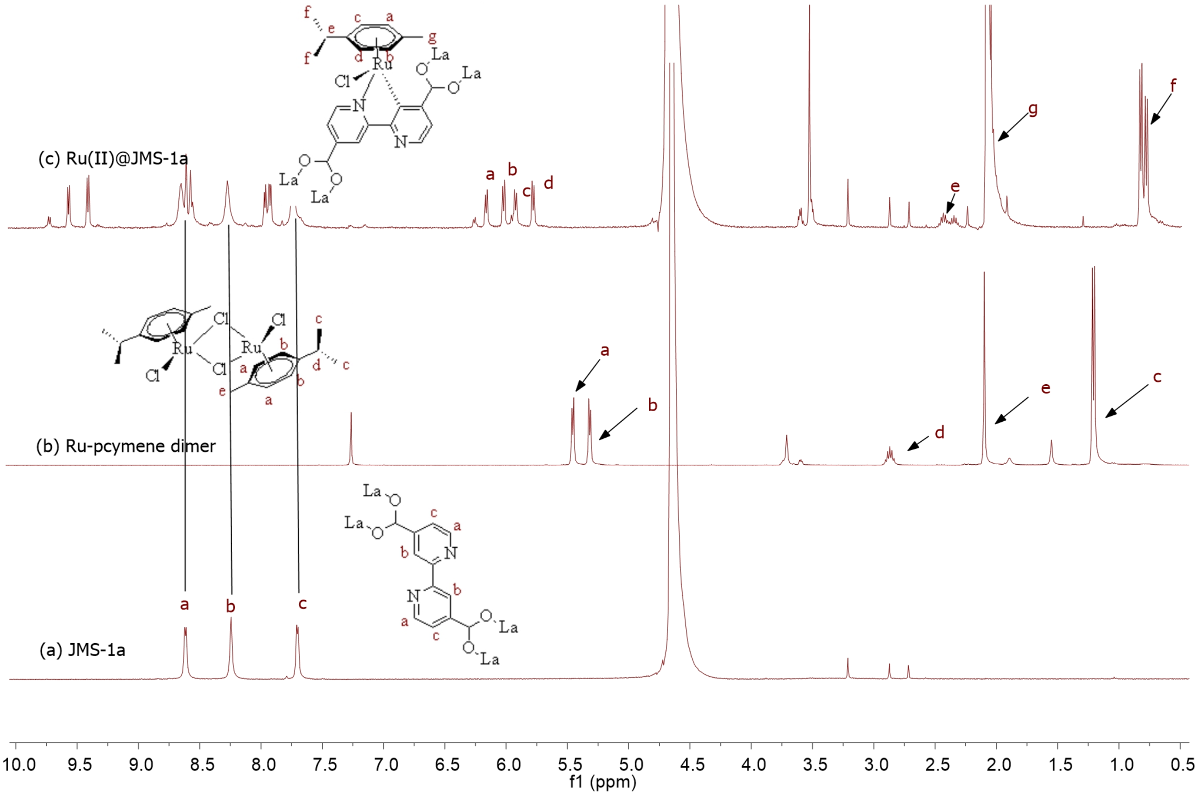

Figure 3.14: ^{1}HNMR of (a) **JMS-1a**, (b) **[RuCl$_2$-*p*cymene]$_2$** and (c) **Ru(II)@JMS-1a**

a) ^{1}H NMR (400 MHz, D_2O): (δ, ppm) 7.71 (d, CH_c, $^3J_{H\text{-}H}$ = 4.0 Hz, 2H), 8.24 (s, CH_b, 2H) and 8.62 (d, CH_a, $^3J_{H\text{-}H}$ = 4 Hz, 2H) **b)** ^{1}H NMR (400 MHz, CD_2Cl_2): (δ, ppm) 1.23 – 1.24 (m, CH_c, 6H), 2.12 (s, CH_e, 3H), 2.84 - 2.91 (m, CH_d, 1H), 5.30 (d, CH_b, $^3J_{H\text{-}H}$ = 8 Hz, 2H) and 5.44 (d, CH_a, $^3J_{H\text{-}H}$ = 8 Hz, 2H). **c)** ^{1}H NMR (400 MHz, D_2O): (δ, ppm) 0.74 – 0.81 (m, CH_c, 6H), 2.01 (s, CH_e, 3H), 2.26 - 2.51 (m, CH_d, 1H), 5.72 (d, CH_b, $^3J_{H\text{-}H}$ = 8 Hz, 1H) and 5.87 (d, CH_b, $^3J_{H\text{-}H}$ = 4 Hz, 1H), 5.96 (d, CH_a, $^3J_{H\text{-}H}$ = 4 Hz, 1H), 6.09 (d, CH_a, $^3J_{H\text{-}H}$ = 8 Hz, 1H) and 7,67 – 9.71 (m, $CH_{aromtic}$)

PXRD patterns showed that upon cyclometalation, a new phase is formed as evidenced by the appearance of new diffraction peaks which are not present in the parent **JMS-1a,** indicating framework flexibility (Figure 3.6). Comparison of the FTIR of **JMS-1a** and **Ru(II)@JMS-1a** in Figure 3.5 shows that the asymmetric and symmetric carboxylate stretches at 1578 and 1398 cm^{-1} did not change upon cyclometalation, suggesting that the binding mode of the carboxylate moiety is retained during cyclometalation. Elemental analysis of **JMS-1a** gave, % Found: 43.15C, 8.45 N, 1.75 H and % Calculated, 43.05 C, 8.37 N, 1.79 H values. **Ru(II)@JMS-1a**, % Found 44.89 C, 7.88 N, 1.98 H. The increase in the percentage carbon content in **Ru(II)@JMS-1a** suggests the presence of *p*-cymene in the functionalised MOF.

3.9 Gas Sorption Measurements:

The textural parameters of **JMS-1a** and **Ru(II)@JMS-1a** illustrated in Figure 3.15a were analysed using Micromeritics ASAP 2460 surface and porosity analyser. Before analysis, the samples were degassed using nitrogen gas (N_2) at 90 °C for 12 hours, then at 150 °C for 8 hours. Thereafter, the samples were weighed and analysed at 77K using N_2 as a probe gas. H_2 and CO_2 sorption experiments were performed using a Micrometrics 3Flex Surface Analyser. The samples were prepared by using a Micrometrics Flowprep with the low of nitrogen over the samples for 4 hours whilst heating at 60 °C. Furthermore, the samples were heated at 150 °C under vacuum for 2 hours before the analysis commenced.

Surface characterisation studies revealed a significant reduction in the BET surface area from 112 m^2/g to 58 m^2/g upon cyclometalation. The observed decrease in the surface area is ascribed to partial blockage of the pores by the Ru(II)*p*-cymene complex,[20] providing further evidence of successful incorporation of Ru(II)*p*-cymene within the pores of **JMS-1a.** The N_2 adsorption isotherms of **JMS-1a** and **Ru(II)@JMS-1a** illustrated in Figure 3.15a show Type I isotherm at very low pressure (< 0.4 P/P_o). Liang and co-workers observed similar behaviour.[21] Hydrogen sorption isotherms of J**MS-1a** and **Ru(II)@JMS-1a** are shown in Figure 3.15b. At 77 K and 800 mmHg, the above-mentioned compounds could store up to 68.17 and 65.34 cm^3 (STP) g^{-1}, corresponding to the sorption of 0.61 and 0.59 wt % respectively. Even though the displayed hysteresis is rare,[22] the H_2 uptake is still comparable to several other MOFs reported in literature.[23–25]

CO_2 adsorption-desorption isotherms of **JMS-1a** and **Ru(II)@JMS-1a** in Figure 3.16 show a typical Type I isotherm with a steep uptake at the low-pressure region, suggesting microporosity nature of these materials. **JMS-1a** has a volumetric uptake of 8.59 and 12.92 cm^3 (STP) g^{-1} (0.384 and 0.576 $mmolg^{-1}$) at 298 and 273K respectively. The presence of Ru(II)*p*-cymene in **Ru(II)@JMS-1a** accounts for its reduced CO_2 uptake of 6.08 and 10.42 cm^3 (STP) g^{-1} (0.274 and 0.465 $mmolg^{-1}$) at 298 and 273K respectively. The amount of CO_2 uptake by these materials is comparable which is consistent with the structural modifications suggested by PXRD studies (Figure 3.6).

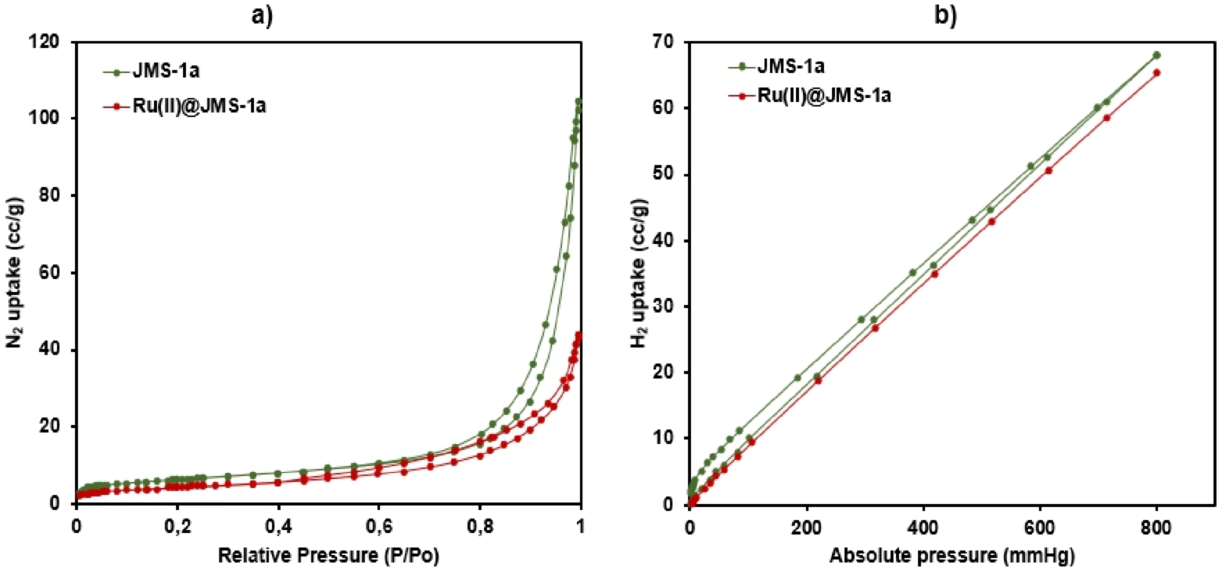

Figure 3.15: a) Nitrogen and b) hydrogen adsorption-desorption studies of **JMS-1a** and **Ru(II)@JMS-1a** at 77K.

Cohen and co-workers found out that upon cyclometalation of the Zr based MOF with Ir complex, the amount of N_2 uptake increased with increase Ir loading relative to the unfunctionalised MOF.[26] This was attributed to the framework flexibility although other mechanisms were not ruled out. At 195 K, the amount of CO_2 uptake increased abruptly at the low-pressure range, with volumetric uptake more than doubling to 36.25 and 32.62 cm^3 (STP) g^{-1} (1.61 and 1.46 $mmolg^{-1}$) at an absolute pressure of 701 mmHg for **JMS-1a** and **Ru(II)@JMS-1a** respectively. This confirms the inherent permanent porosity of both MOFs. The observed CO_2 uptake is comparable to other lanthanide MOFs known for CO_2 capture and conversion. [27, 28]

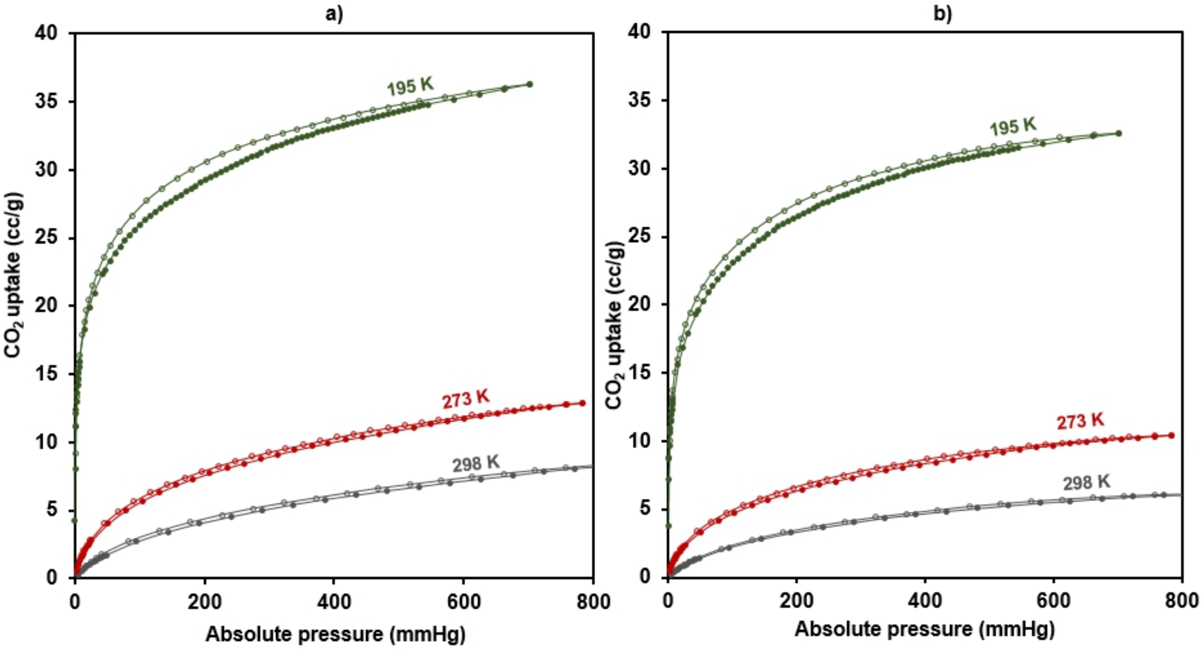

Figure 3.16: CO_2 adsorption-desorption isotherms for **JMS-1a** (a) and **Ru(II)@JMS-1a** (b) (closed circles represent adsorption and open circles desorption).

The adsorption branches of the isotherm carried out at 273 and 298 K were used to obtain isosteric heat of adsorption (Q_{st}) data, [29] illustrated in Figure 3.17 and 3.18. The heat of adsorption represents the energetic interaction strength of the adsorbent with the adsorbate molecules which play a critical role in determining the adsorptive selectivity and the energy required to release CO_2 molecules during regeneration.[30] The estimated values of isosteric heat of adsorption were ranging from 32 to 38 $kJmol^{-1}$ at load values 0.1 to 0.38 $mmolg^{-1}$, indicating moderate to the strong interaction of CO_2 with the MOFs.[22] This was attributed to the quadruple interactions between polarisable CO_2 molecules and the accessible nitrogen sites. Furthermore, theoretical investigations have shown that the removal of guest solvent molecules creates open metal sites which dramatically enhances gas adsorption in MOFs. [24,31,32]

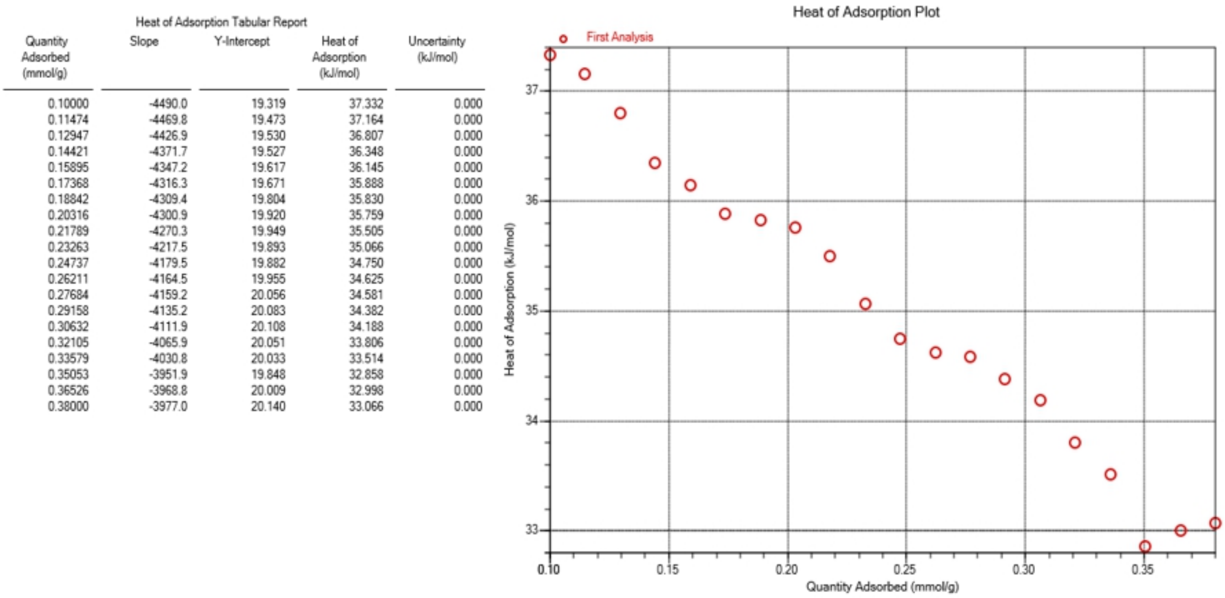

Heat of Adsorption Tabular Report

Quantity Adsorbed (mmol/g)	Slope	Y-Intercept	Heat of Adsorption (kJ/mol)	Uncertainty (kJ/mol)
0.10000	-4490.0	19.319	37.332	0.000
0.11474	-4469.8	19.473	37.164	0.000
0.12947	-4426.9	19.530	36.807	0.000
0.14421	-4371.7	19.527	36.348	0.000
0.15895	-4347.2	19.617	36.145	0.000
0.17368	-4316.3	19.671	35.888	0.000
0.18842	-4309.4	19.804	35.830	0.000
0.20316	-4300.9	19.920	35.759	0.000
0.21789	-4270.3	19.949	35.505	0.000
0.23263	-4217.5	19.893	35.066	0.000
0.24737	-4179.5	19.882	34.750	0.000
0.26211	-4164.5	19.955	34.625	0.000
0.27684	-4159.2	20.056	34.581	0.000
0.29158	-4135.2	20.083	34.382	0.000
0.30632	-4111.9	20.108	34.188	0.000
0.32105	-4065.9	20.051	33.806	0.000
0.33579	-4030.8	20.033	33.514	0.000
0.35053	-3951.9	19.848	32.858	0.000
0.36526	-3968.8	20.009	32.998	0.000
0.38000	-3977.0	20.140	33.066	0.000

Figure 3.17: Isosteric heat of adsorption for **JMS-1a**

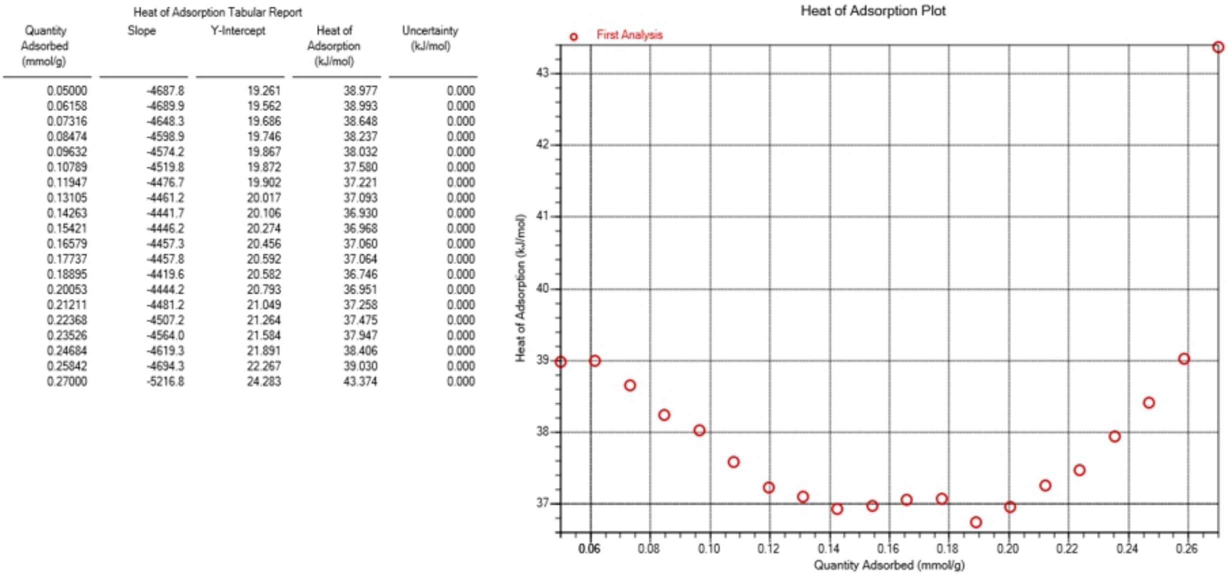

Heat of Adsorption Tabular Report

Quantity Adsorbed (mmol/g)	Slope	Y-Intercept	Heat of Adsorption (kJ/mol)	Uncertainty (kJ/mol)
0.05000	-4687.8	19.261	38.977	0.000
0.06158	-4689.9	19.562	38.993	0.000
0.07316	-4648.3	19.686	38.648	0.000
0.08474	-4598.9	19.746	38.237	0.000
0.09632	-4574.2	19.867	38.032	0.000
0.10789	-4519.8	19.872	37.580	0.000
0.11947	-4476.7	19.902	37.221	0.000
0.13105	-4461.2	20.017	37.093	0.000
0.14263	-4441.7	20.106	36.930	0.000
0.15421	-4446.2	20.274	36.968	0.000
0.16579	-4457.3	20.456	37.060	0.000
0.17737	-4457.8	20.592	37.064	0.000
0.18895	-4419.6	20.582	36.746	0.000
0.20053	-4444.2	20.793	36.951	0.000
0.21211	-4481.2	21.049	37.258	0.000
0.22368	-4507.2	21.264	37.475	0.000
0.23526	-4564.0	21.584	37.947	0.000
0.24684	-4619.3	21.891	38.406	0.000
0.25842	-4694.3	22.267	39.030	0.000
0.27000	-5216.8	24.283	43.374	0.000

Figure 3.18: Isosteric heat of adsorption for **Ru(II)@JMS-1a**

3.10 Catalytic hydrogenation of CO_2 to formate

Equation 3.1 illustrates the reaction for the hydrogenation of CO_2.

$$CO_2 + H_2 \xrightarrow[\text{Solvent, } \Delta \text{, pressure}]{\text{Catalyst, base}} HCOO^- + H^+ \text{base}$$

Equation 3.1: Catalytic reaction for the hydrogenation of CO_2 to formate.

The hydrogenation of CO_2 by the functionalised phase, **Ru(II)@JMS-1a**, was performed systematically under various conditions to establish reaction conditions and the results are summarised in Table 3.2 (Entry 1 to 12). The formate product formed was detected and quantified by ^{1}H NMR spectroscopy with acetone as an internal standard. Figure 3.19 shows the ^{1}H NMR spectra for the results in Table 3.2, Entry 3.

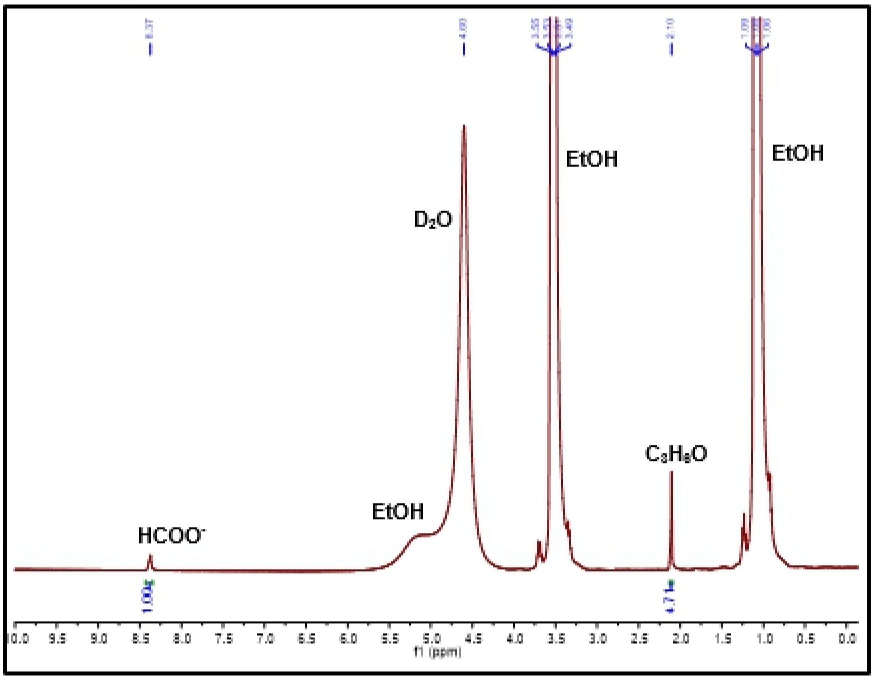

Figure 3.19: ^{1}H NMR of spectra solution sampled after catalysis.

Example showing how the yield of formate was calculated, for ^{1}H NMR in Figure 3.18 and Table 3.2, Entry 3)

Amount sampled for NMR after catalysis = 0.2 mL

NMR solvent, D_2O = 0.3 mL

The total volume of ethanol used for catalysis = 8.0 mL

Moles of Standard = 4.06×10^{-5} calculated from density and the volume of standard used (3μL)

The product potassium formate has 1 proton, so we divide the integral value for formate by 1. Acetone, the internal standard has 6 protons, so divide the integral value for acetone by 6.

Acetone = 4.71/6 = 0.785

Formate = 1/1 = 1

Number of moles of formate = (4.06×10^{-5}) **/** $(0.785/1)$

= 5.170×10^{-5} moles in 0.2 mL sampled

Moles in 8 mL used for catalysis = 2.07×10^{-3} moles

Yield = (moles of formate produced / moles of KOH) × 100 %

= $(2.07 \times 10^{-3}) / (5 \times 10^{-3})$

= 41.4 %

In our first attempt, hydrogenation was tested in different solvents using 15.6 μmol catalyst at 90 ˚C, 40 bars pressure, 24 hours. (Entry 1-3). The reaction does not proceed in THF and toluene. This result was following a previously reported study demonstrating the need for a protic solvent.[33] Based on solvent screening results, the hydrogenation of CO_2 in ethanol was then studied in several bases including KOH, K_2CO_3, $NaHCO_3$ and Et_3N (Entry 3 to 6). CO_2 gets solubilised in basic solution to form bicarbonate/carbonate that is the active ingredient for the formation of formate.[34] When strong inorganic bases were used, (Entry 2 to 5) higher yields of formate were observed, with the strongest base KOH, giving a yield of 41.4 %.

Notably, the weak neutral organic base triethylamine (Entry 6), which has been frequently employed in CO_2 hydrogenation gave inferior results. This is because Et_3N is a bulky molecule and cannot access the metal-hydride site to deprotonate the proton thereby restricting catalysis on the surface of the MOF. This provides further evidence that the ruthenium complex is encapsulated inside the pores of the MOF.

We, therefore, opted to use KOH as our preferred base for further optimisation studies. No reaction occurred in the absence of a base (Entry 7). In most reported catalyst systems, a base is needed to facilitate the hydrogenation of CO_2 to formate because i) the base deprotonates the generated formic acid; thus thermodynamically shifting the equilibrium forward; ii) the base accelerates the heterolysis of H_2 during the catalytic cycle, thereby kinetically promoting the catalytic activity.[8] It is important to note that upon hydrogenation in the absence of a catalyst, Entry 8, the reaction does not proceed, indicating the crucial role of the catalyst in CO_2 reduction. We conducted control experiments in the absence of CO_2 to confirm the role of molecular CO_2. In the absence of CO_2 (Entry 9), no formate was observed which infers that molecular CO_2 played a vital role in the synthesis of formate.

Table 3.2: Catalytic performance of **JMS-1a** and **Ru(II)@JMS-1a**.

Entry	Catalyst	Temp (°C)	Pressure /bars (CO_2/H_2)	Catalyst load (μmol)	Base	Solvent	Formate (mmol)	Yield (%)
1	Ru(II)@JMS-1a	90	40 (1:3)	15.6	KOH	THF	-	0
2	Ru(II)@JMS-1a	90	40 (1:3)	15.6	KOH	Toluene	-	0
3	Ru(II)@JMS-1a	90	40 (1:3)	15.6	KOH	Ethanol	2.07	41.4
4	Ru(II)@JMS-1a	90	40 (1:3)	15.6	K_2CO_3	Ethanol	1.43	26.7
5	Ru(II)@JMS-1a	90	40 (1:3)	15.6	$NaHCO_3$	Ethanol	1.75	35.0
6	Ru(II)@JMS-1a	90	40 (1:3)	15.6	Et_3N	Ethanol	0.27	≈5
7	Ru(II)@JMS-1a	90	40 (1:3)	15.6	No base	Ethanol	-	0
8	No catalyst	90	40 (1:3)	0.00	KOH	Ethanol	-	0
9	Ru(II)@JMS-1a	110	40 (0:4)	15.6	KOH	Ethanol	-	0
10	Ru(II)@JMS-1a	110	10 (1:0)	15.6	KOH	Ethanol	-	0
11	Ru(II)@JMS-1a	110	50 (1:4)	15.6	KOH	Ethanol	4.77	95.4
12	Ru(II)@JMS-1a	110	50 (1:4)	20.8	KOH	Ethanol	4.94	98.8
13	JMS-1a	110	50 (1:4)	15.6	KOH	Ethanol	3.10	62.0
14	$[RuCl_2(p\text{-cymene})]_2$	110	50 (1:4)	15.6	KOH	Ethanol	1.22	24

Conditions: Time 24 hours, 5 mmol base. The yield based on ^1H NMR analysis using acetone as an internal standard. The yield was calculated based on the conversion of 5 mmol added base. (Actual masses in 15.6 μmol catalyst were 31.5, 15.9 and 9.6 mg Ru(II)@JMS-1a, JMS-1a and $[RuCl_2(p\text{-cymene})]_2$.

The activated phase **JMS-1a**'s ability to convert CO_2 was also evaluated, interestingly, ^1H NMR studies showed the formation of formate. However, we noted that under the same conditions, the formate yield obtained using **JMS-1a** (62 %, entry 13) was significantly lower than that of the functionalised material **Ru(II)@JMS-1a** (95.4 %, entry 11). The majority of reports presented in literature use Zr-based MOFs that are functionalised with either Pt[35] or Ir[36] and none of these report on the activity of the Zr centre towards the conversion of CO_2 to formate. However, we were aware of the catalytic activities of lanthanide metals reported in the literature.[29,37] Having this in mind, we soaked our reactors in acid for 24 hours and repeated the experiments several times using **JMS-1a** as the solid catalyst. These repeated experiments gave formate as the catalytic product, confirming that the La^{III} MOF acts as a catalyst for reduction of CO_2. As presented in Table 3.2, encapsulation of [Ru(II)Cl(*p*-cymene)] gave rise to a significant increase in the product yield of formate. The combination of two metals in a single catalyst does not only lower the energetic requirements to speed up the reaction between carbon dioxide and hydrogen but may be altering the reaction pathway, to produce the more desired product.

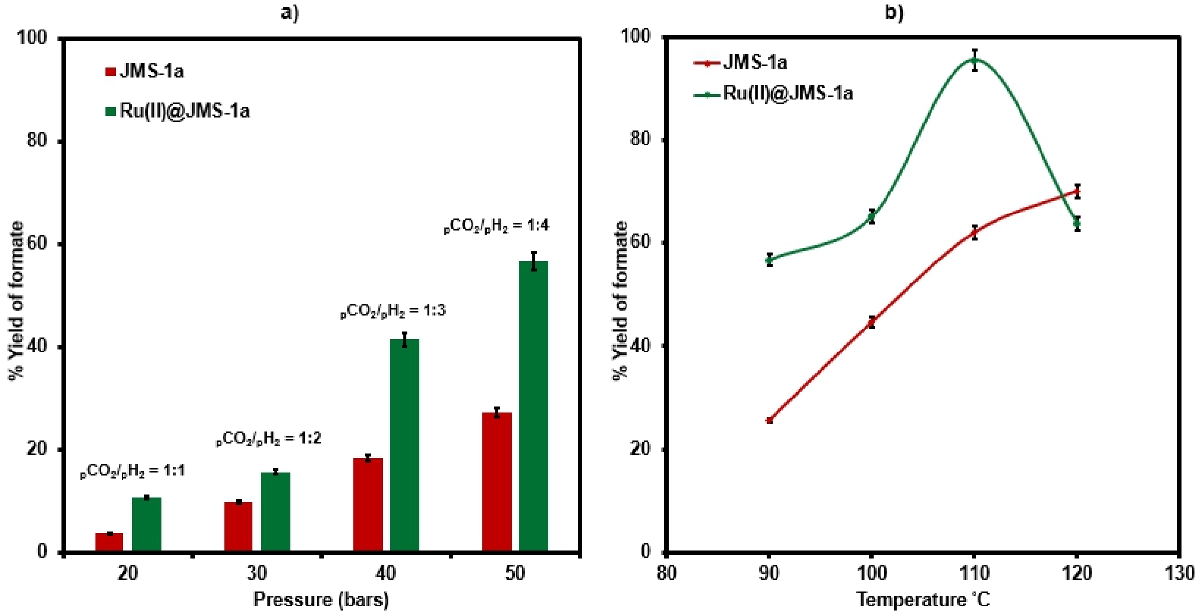

Figure 3.20: a) Effect of changing the partial pressure of H_2. (Conditions: Temperature 90 °C, Time 24 hours, 15.6 µmol catalyst loading, 5 mmol and 8 mL ethanol). b) Effect of changing the temperature. (Conditions: Pressure 50 bar (CO_2/H_2 =1:4), Time 24 hours, 15.6

μmol catalyst loading, 5 mmol KOH and 8 mL ethanol (8 mL).

Pressure variation was determined by changing the partial pressure of H_2 while keeping the pressure of CO_2 constant. As illustrated in Figure 3.20a an increase in the partial pressure of H_2 results in an increase in the yield of formate produced by both **JMS-1a** and **Ru(II)@JMS-1a** catalysts. On increasing the pressure of H_2 to 40 bars while keeping the CO_2 pressure at 10 bars, the yield of formate produced increased up to 56 % and 27.3 % for **Ru(II)@JMS-1a** and **JMS-1a** respectively. This is attributed to the fact that sufficient partial pressure of H_2 is required to generate the hydride and boost CO_2 hydrogenation.

The reaction temperature was carried out between 90 and 120 ˚C with other parameters being kept constant (Figure 3.20b). We observed that, for **Ru(II)@JMS-1a**, the conversion of CO_2 increased gradually with an increase in temperature reaching a yield of 95 % at 110 ˚C. However, a further increase in temperature (120 ˚C) led to a dramatic decrease in the yield of formate produced maybe be due to the decomposition of the formate species or the departure of the *p*-cymene molecule from the MOF backbone. The optimal reaction temperature was 110 ˚C, therefore further experiments were conducted solely at 110 ˚C. Contrary to **Ru(II)@JMS-1a** which shows a dramatic decrease in the yield of formate produced at 120 °C, **JMS-1a** shows a gradual increase in yield of formate as the temperature is increased although the yield of formate produced is lower than that of the functionalised MOF.

Subsequently, the impact of reaction time was monitored as illustrated in Figure 3.21a. The yield increases with an increase in time to reach a yield of 94 % and 62 % for **Ru(II)@JMS-1a** and **JMS-1a** respectively. Finally, catalyst load dependence was examined for both catalysts. In both cases, it was noted that the yield of formate readily increased with increase in catalyst loading as shown in Figure 3.21b, which indicates first-order dependence (d log rate / d log (catalyst amount) = 1 concerning catalyst.[38] When 18.2 μmol of **Ru(II)@JMS-1a** catalyst was used, 4.87 mmol formate which corresponds to 97 % yield was produced. The activated MOF **JMS-1a** produced 4.57 mmol of formate (91 % yield) when 20.8 μmol of catalysts were used. Figure 3.22 illustrates the ^1H NMR of the catalytic solution with **Ru(II)JMS-1a** under optimised conditions. The $[RuCl_2(p\text{-cymene})]_2$ dimer used for the functionalisation of the **JMS-1a** was also used as a catalyst in the hydrogenation of CO_2 under optimised conditions. The dimer afforded a yield of 24.3%, which is significantly lower than that of **JMS-1a** and **Ru(II)@JMS-1a**.

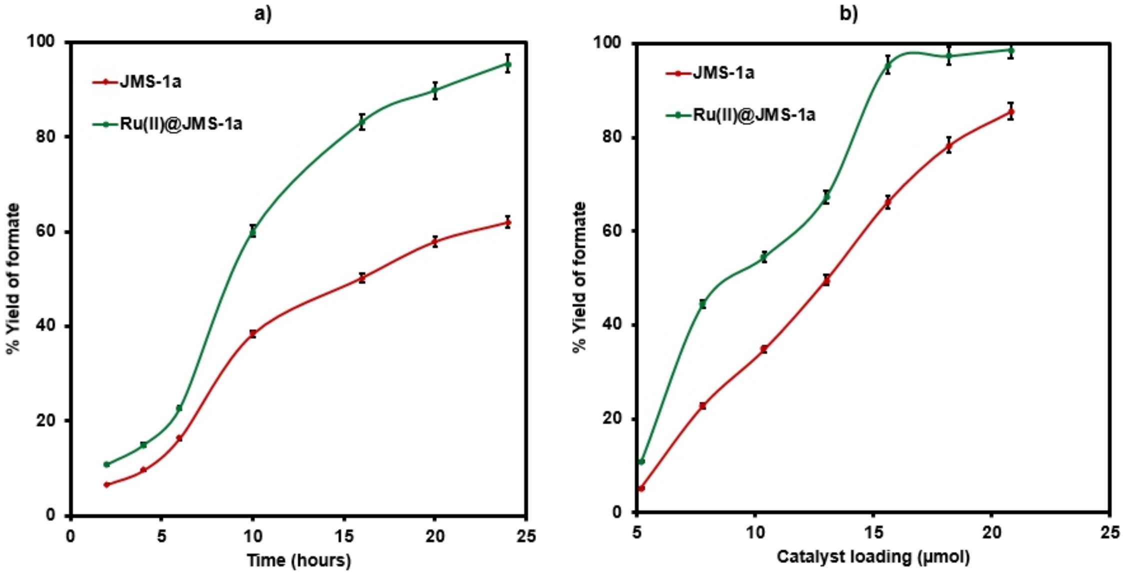

Figure 3.21: Effect of changing a) time, (Conditions: Pressure 50 bar (CO_2/H_2 =1:4), Temp 110 °C, 15 μmol catalyst loading, 5 mmol KOH and 8 mL ethanol) and b) catalyst loading (Conditions: Pressure 50 bar (CO_2/H_2 =1:4), Temperature 110 °C, Time 24 hours, 5 mmol KOH and 8mL ethanol on the yield of formate produced.

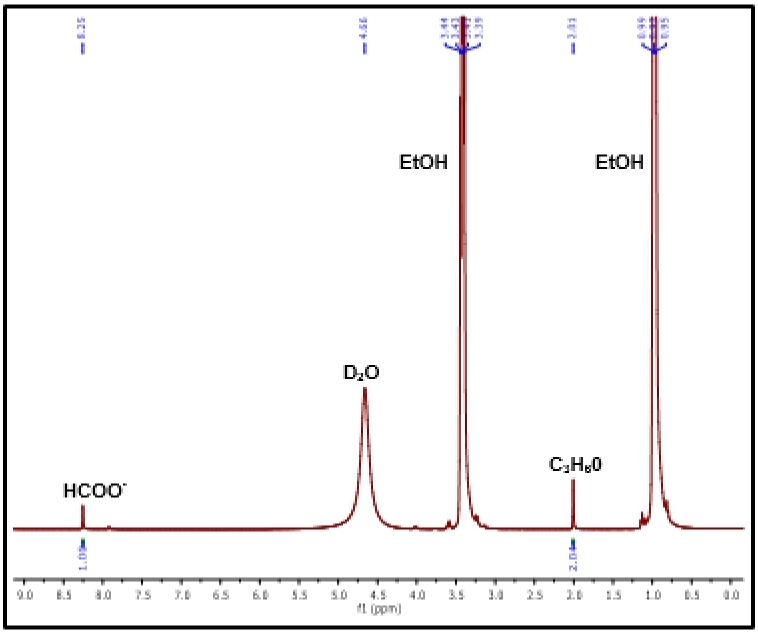

Figure 3.22: ^{1}H NMR of catalysis using Ru(II)@JMS-1a optimised conditions of temperature 110 °C, time 24 hours, 15.6 µmol catalyst loading, 5 mmol KOH base, 8 mL ethanol and pressure 50 bar (CO_2/H_2 =1:4)

Size-selective poisoning studies were used to ascertain that Ru(II)Cl(*p*-cymene)] complex was encapsulated inside the pores of **JMS-1a** rather than being adsorbed on the external surface. The studies were carried out using a wide range of differently sized thiols under optimised conditions {Temperature 110 °C, Time 24 hours, 15.6 µmol catalyst loading, 5 mmol KOH base, 8 mL ethanol and pressure 50 bar (CO_2/H_2 =1:4)}. The results are displayed in Figure 3.23.

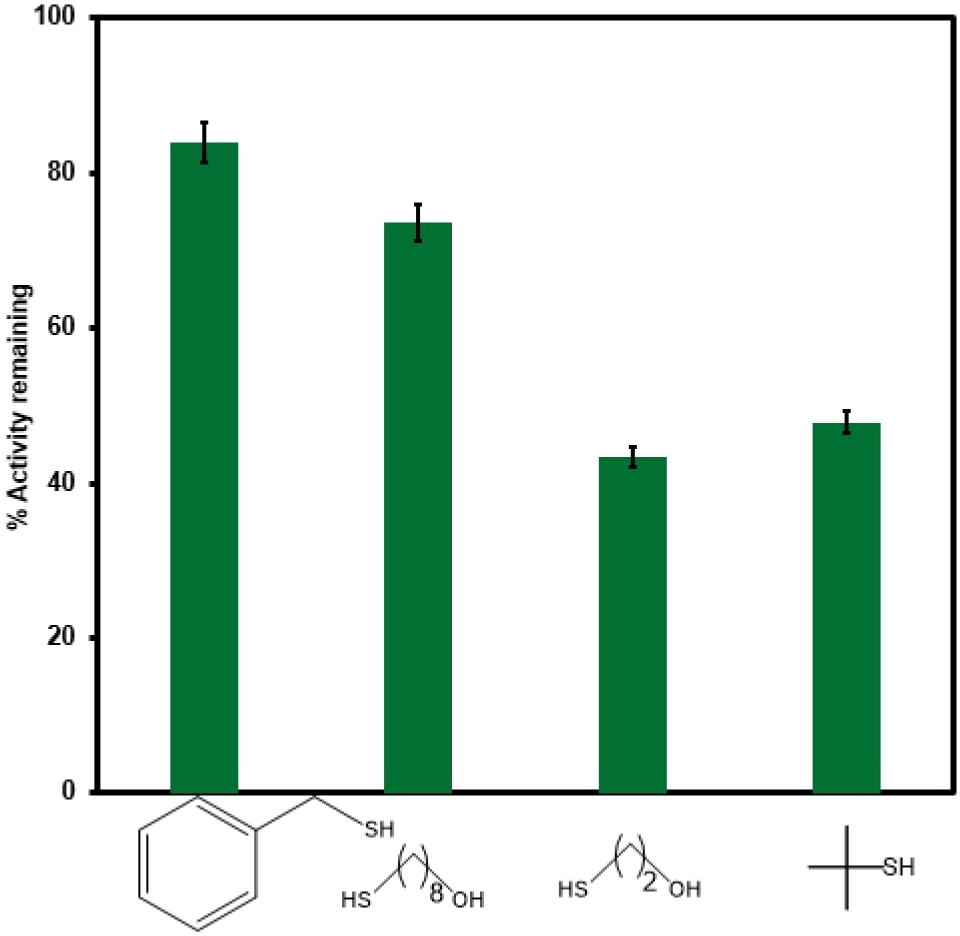

Figure 3.23: Comparison of the catalytic activity of **Ru(II)@JMS-1a** in the presence of different sized thiol poisons.

Thiols are known to poison many transition metal catalysts. When bulky thiols such as benzylmercaptan and 8 mercapto-1-octanol were exposed to **Ru(II)@JMS-1a** the product yield was reduced by 16 % and 24 % respectively. In contrast, when the catalyst was exposed to 2 mercapto-ethanol and 2 methyl-2-propanethiol, the yield was reduced by 56.6 and 52.2 % respectively. Figure 3.24 to 3.27 display the ^{1}H NMR spectra of catalysis in the presence of benzylmercaptan and 2 mercapto-ethanol respectively. The absence of appreciable inhibition in the presence of the bulky thiols suggests that most of the active species is encapsulated in the framework rather than bound to the surface. The most effective poisons were the least sterically demanding thiols (2 mercapto-ethanol and 2 methyl-2-propanethiol). This observation is consistent with the bulk of the catalyst being encapsulated inside the MOF pores because the smaller thiols can easily access the catalytic sites by diffusion through the pores and poison the catalyst. Similar findings were reported by Tsung and co-workers.[39]

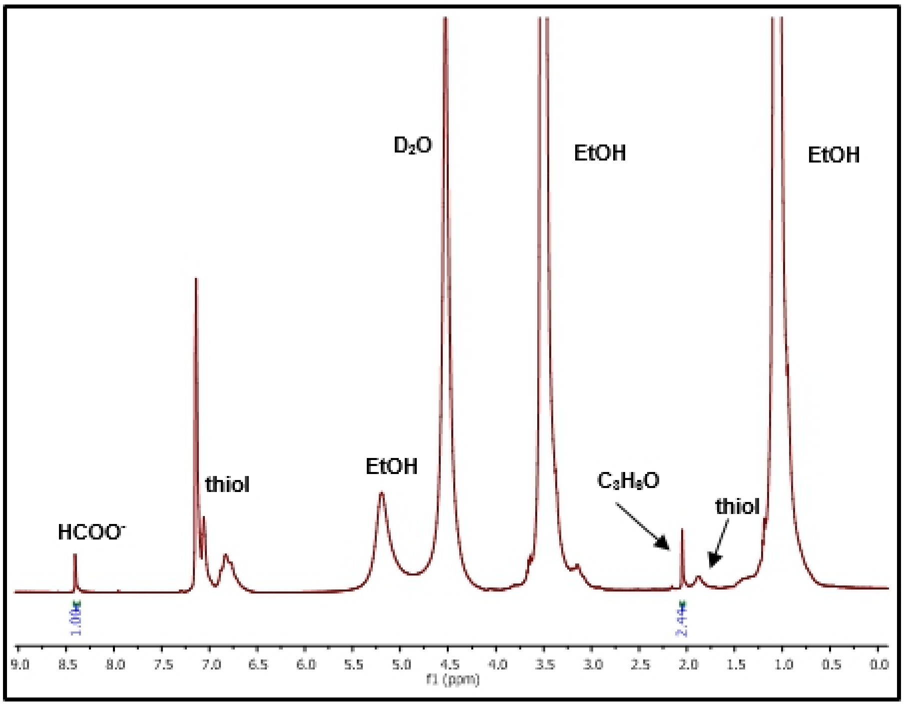

Figure 3.24: ^{1}H NMR spectra when the reaction was carried out in the presence of benzylmercaptan.

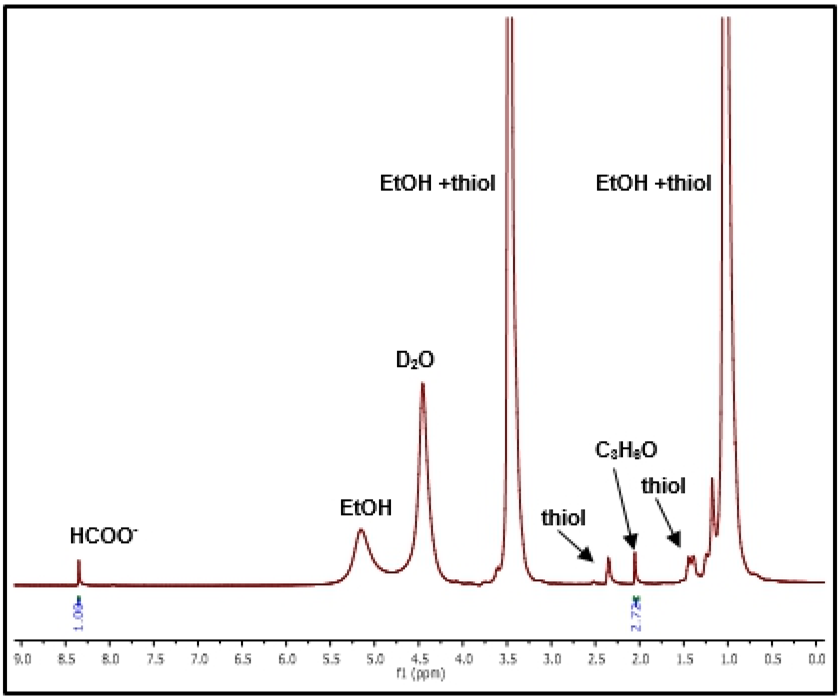

Figure 3.25: ^{1}H NMR spectra obtained when the reaction was carried out in the presence of 8-mecapto-1-octanol

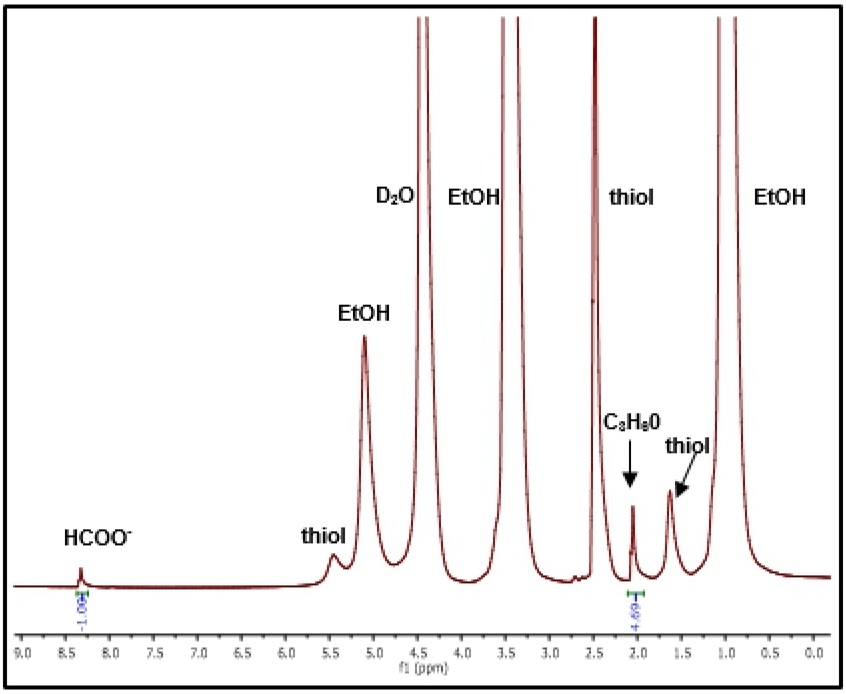

Figure 3.26: ^{1}H NMR of catalysis in the presence of 2 mercapto-ethanol

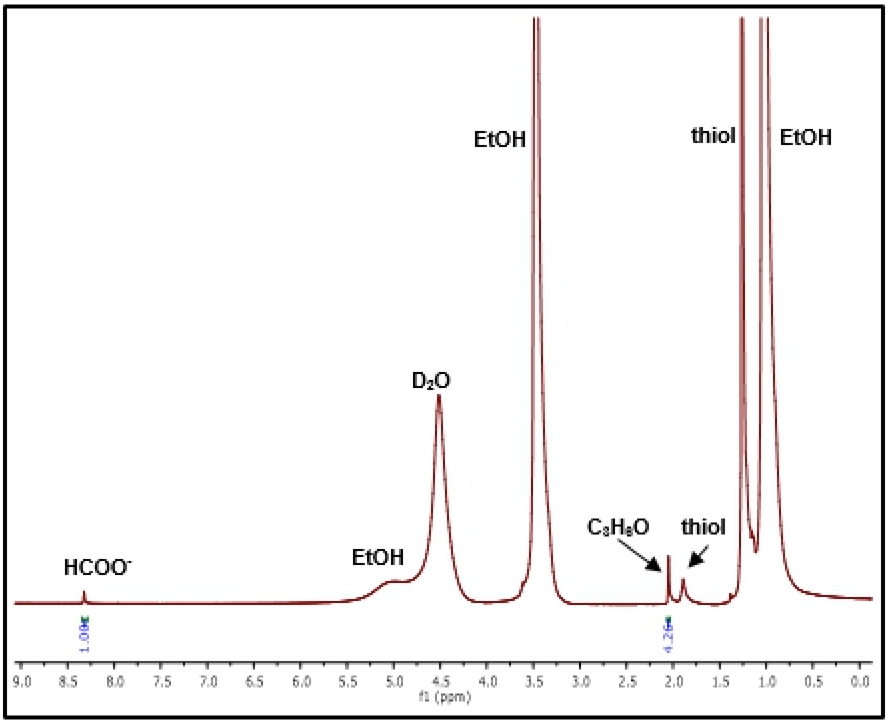

Figure 3.27: ^{1}H NMR of catalysis in the presence of 2 methyl-2-propanethio

3.11 Leaching, Heterogeneity, and Recycling Studies

To check whether the catalysts were working in a heterogeneous manner, the solid catalysts were isolated from the reaction mixture after 6 hours (for which formate (1.14 mmol for **Ru(II)@JMS-1a** and 0.82 mmol for **JMS-1a)** was observed in the filtrate). The supernatant was then used as the catalytic solution for an additional 18 hours. Importantly, a second 18-hour reaction of this solution produced no additional products, whereas the original reaction produced a 4.77 and 3.10 mmol of formate for **Ru(II)@JMS-1a** and **JMS-1a** respectively after 24 hrs. This supports the hypothesis that no leaching of the catalytic species from the framework into the liquid phase occurs, and that the catalysts function as supported molecular catalysts. ICP-OES analysis of the aqueous solution in the reactor showed negligible metal leaching (0.0001 % of La and < 0.0001 % of Ru for **Ru(II)@JMS-1a** and 0.0001 % La for **JMS-1a** respectively).

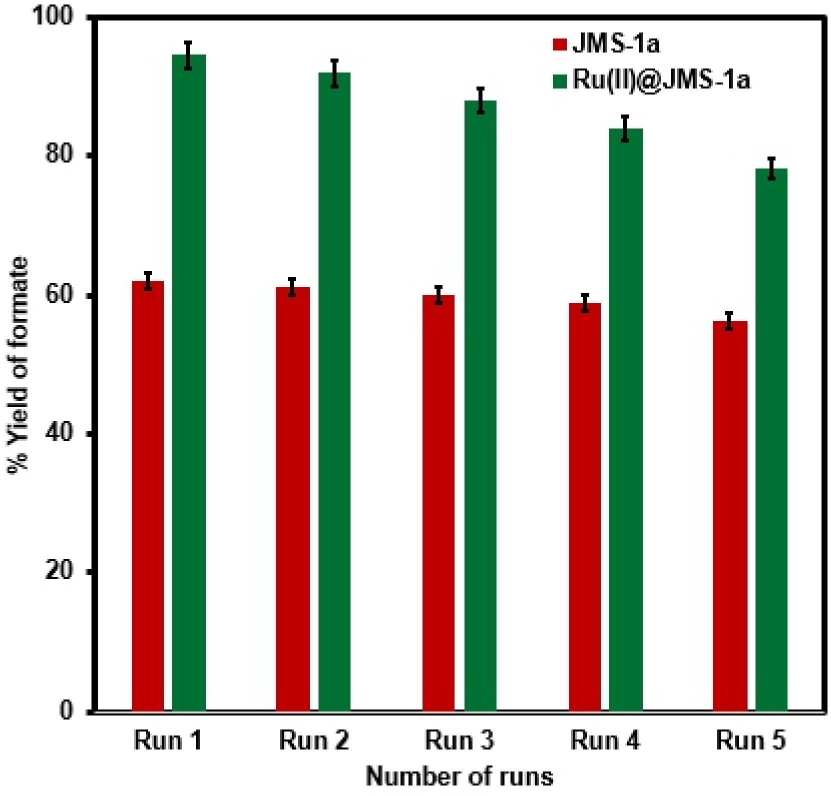

Figure 3.28: A comparison of the performance of catalyst **JMS-1a** and **Ru(II)@JMS-1a** over 5 consecutive cycles,

The reusability of the catalysts was studied over consecutive runs. The solid catalyst was isolated from the reaction mixture by filtration, washed thoroughly with ethanol and vacuum dried. The dried catalysts were directly used for the next run with a fresh ethanolic KOH solution. As shown in Figure 3.28, **JMS-1a** could be recycled up to five times without significant loss in catalytic activity. Contrary to this, **Ru(II)@JMS-1a** showed a 17 % decrease in the yield of formate over five consecutive runs although the yield obtained (78 %) was still higher than that obtained using **JMS-1a.** Remarkably PXRD pattern of recycled **JMS-1a** matches well with that of the parent MOF suggesting retention of the original framework, (Figure 3.29), while that of **Ru(II)@JMS-1a** is slightly changed. The observed change in the PXRD pattern may help explain the significant drop in catalytic activity over the five cycles. The PXRD pattern has been presented up to 40° two-theta positions, and there are no obvious peaks which appear at 29° and 35° two theta positions which correspond to the (110) and (101) planes for RuO_2 and nanoparticles respectively. The (100) plane for Ru normally appears around 36° two theta position. This peak is also absent after catalysis which further proves the absence of nanoparticles.

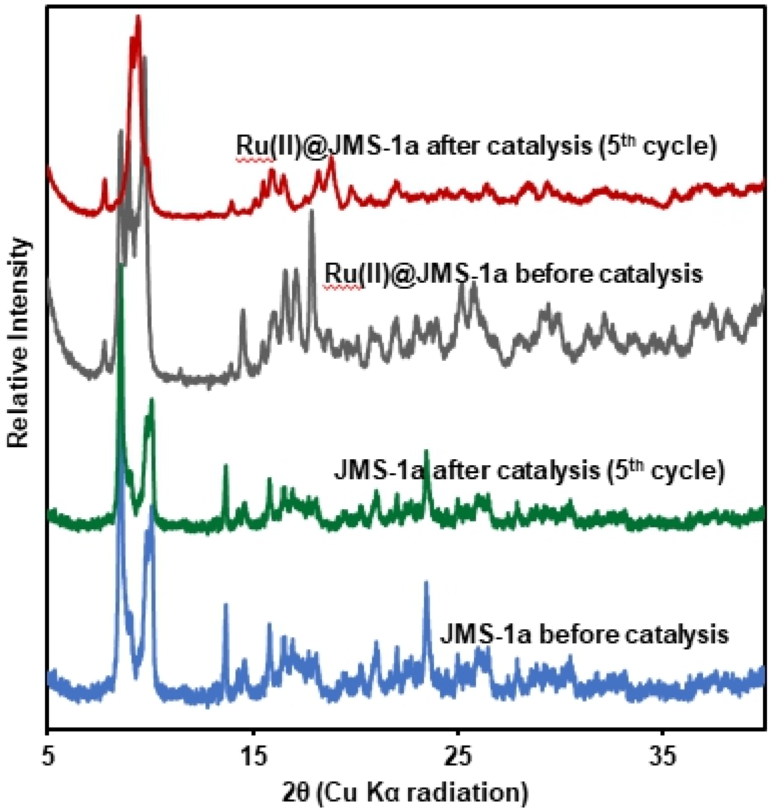

Figure 3.29: PXRD studies of the catalysts before and after catalysis.

Thermal analysis by TGA was used to further probe the structural integrity of the recycled catalysts. As Presented in Figure 3.30, the TGA traces of the used and fresh catalysts are very similar for **JMS-1a**. However, the TGA traces of **Ru(II)@JMS-1a** reveals some subtle differences consistent with the observed change in the PXRD pattern after the 5th cycle. Lastly, FTIR analysis between fresh and used catalysts of J**MS-1a** and **Ru(II)@JMS-1a** presented in Figure 3.31 indicate that the position of asymmetric and symmetric carboxylate stretches located at 1579 and 1398 cm^{-1} respectively are not affected. This suggests that the binding mode of the carboxylate moiety is retained during catalysis.

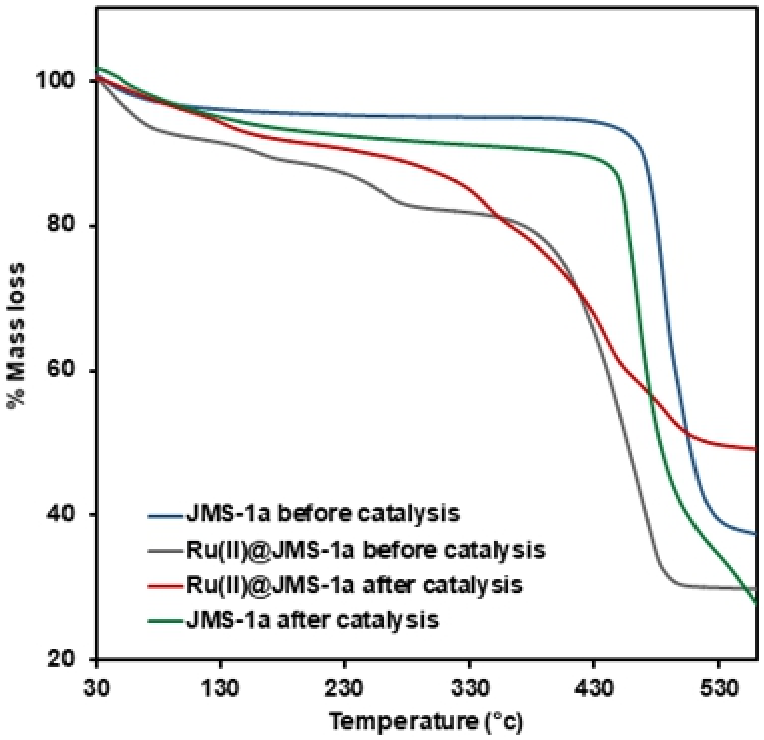

Figure 3.30: TGA analysis of the catalysts before and after catalysis.

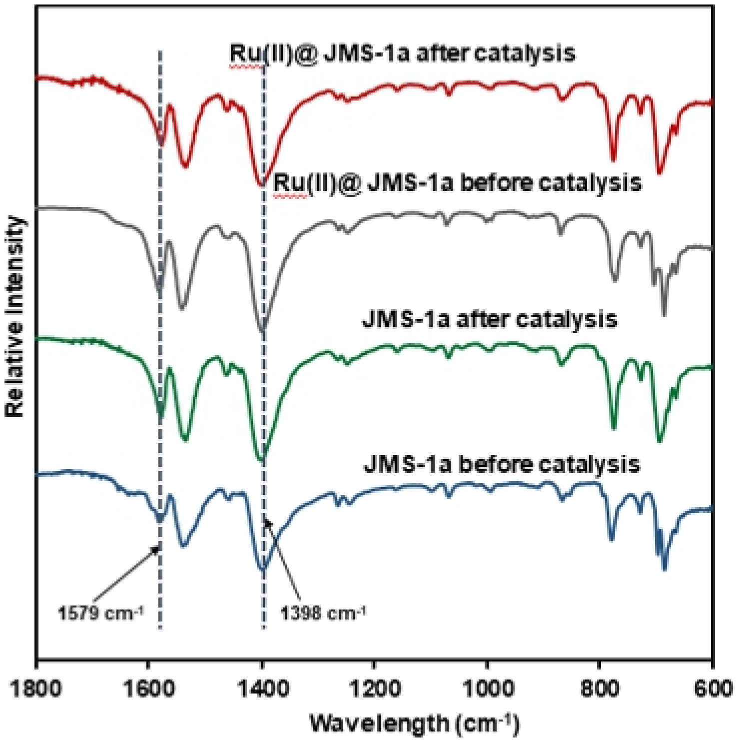

Figure 3.32: a) FTIR analysis of the catalysts before and after catalysis.

3.12 Reaction mechanisms

Based on our experimental results and literature findings [34,36,40–42] both outer sphere,[43] and inner sphere[44] reactions of CO_2/HCO_3^- using **Ru(II)@JMS-1a** catalyst have been proposed. The formation of formate at the Ru^{II} sites is proposed as in Scheme 3.2, where the first step involves reductive elimination of the Cl. This step provides open metal sites for the coordination of H_2 molecules to give a dihydrogen complex [Ru(H_2)(*p*-cymeme)]. The active species, [RuH(*p*-cymene)], is formed upon splitting of the coordinated H_2 molecules with simultaneous elimination HCl. The insertion of CO_2 *via* associative addition into the ruthenium hydride complex generates the formate complex which readily dissociates the formate.

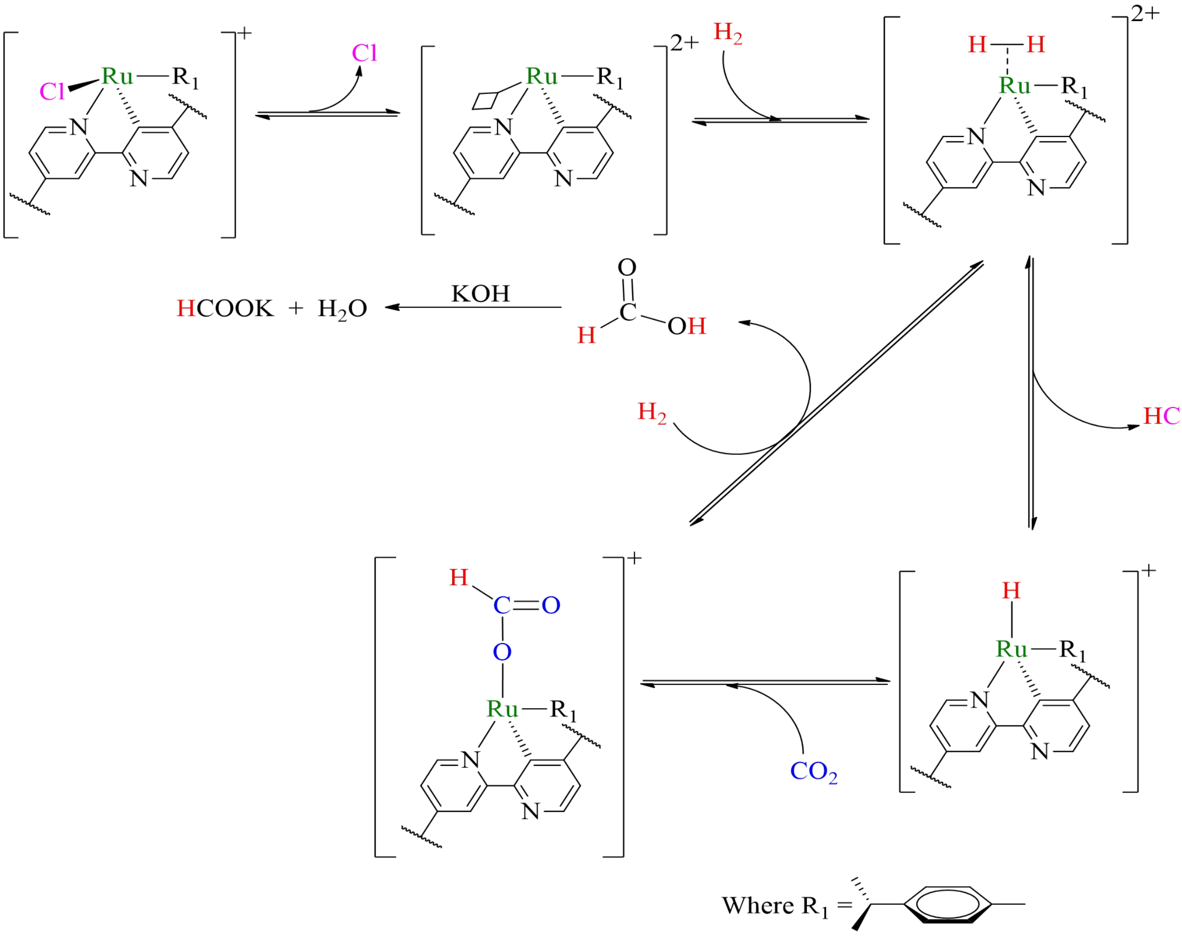

Scheme 3.2: Plausible reaction mechanism for the hydrogenation of CO_2 with Ru(II)@JMS 1a.

3. 13 Summary

Novel lanthanum based MOF (**JMS-1**), with the molecular formula $[La_2(bpdc)_3(DMF)_3]_n$ was synthesised using 2,2'-bipyridine-4,4'-dicarboxylate linker and $LaCl_3.7H_2O$ as starting materials. **JMS-1** crystallises in the orthorhombic crystal system, space group $Pna2_1$. The overall structure of **JMS-1** is a three-dimensional (3D) structure. Network analysis of the MOF revealed a new 7-connected network with a new network topology (**zaz**). The new network was submitted in the Reticular Structural Resource database. The activated phase of **JMS-1**, **JMS-1a**, was functionalised by cyclometalation of the MOF backbone using the metal precursor $[RuCl_2(p\text{-cymene})]_2$ to give **Ru(II)@JMS-1a**. PXRD analysis revealed a phase change induced by the inclusion of the [Ru(II)Cl(*p*-cymene)] in **JMS-1a**. XPS and NMR studies confirmed successful grafting Ru^{II} onto the MOF backbone. Elemental mapping showed that ruthenium was evenly distributed within the MOF matrix. BET studies showed a significant reduction in the surface area of **JMS-1a** upon cyclometalation. This observation was consistent with the pores of the MOF being occupied by the Ru^{II}. The MOFs were evaluated as storage devices of carbon dioxide and hydrogen and catalysts for the hydrogenation of CO_2 to formate. Carbon dioxide sorption studies of **JMS-1a** and **Ru(II)@JMS-1a** showed typical Type I isotherms, which suggests the microporous nature of these materials.

Hydrogenation of CO_2 studies using **JMS-1a** and the functionalised MOF, **Ru(II)@JMS-1a**, revealed that both MOFs were able to convert CO_2 to formate. It was noted that the solvent, base, temperature, pressure and catalyst loading were the factors that affected the yield of formate produced. Our results demonstrate that higher yields of formate require a protic solvent in the presence of a strong base. Contrary to **JMS-1a**, **Ru(II)@JMS-1a** produced higher yields of formate under relatively mild conditions. The unfunctionalised MOF, **JMS-1a** requires higher temperatures and catalyst loading to achieve high yields of formate. The relatively low temperature in the hydrogenation reaction makes the strategy for the incorporation of catalytically active metals in the MOFs attractive.

3.14 REFERENCES

1 B. Li, T. Roisnel, C. Darcel and P. H. Dixneuf, *Dalton Transactions*, 2012, **41**, 10934–10937.

2 A. L. Spek, *Acta Crystallographica. Section D, Biological crystallography*, 2009, **65**, 148–55.

3 C. F. Macrae, I. J. Bruno, J. A. Chisholm, P. R. Edgington, P. McCabe, E. Pidcock, L. Rodriguez-Monge, R. Taylor, J. Van De Streek and P. A. Wood, *Journal of Applied Crystallography*, 2008, **41**, 466–470.

4 P. M. Forster, J. Eckert, B. D. Heiken, J. B. Parise, J. W. Yoon, S. H. Jhung, J.-S. Chang and A. K. Cheetham, *Journal of the American Chemical Society*, 2006, **128**, 16846–50.

5 L. Wen, P. Cheng and W. Lin, *Chemical Science*, 2012, **3**, 2288–2292.

6 V. Zeleňák, Z. Vargová and K. Györyová, *Spectrochimica Acta - Part A: Molecular and Biomolecular Spectroscopy*, 2007, **66**, 262–272.

7 X. L. Wang, J. Li, H. Y. Lin, H. L. Hu, B. K. Chen and B. Mu, *Solid State Sciences*, 2009, **11**, 2118–2124.

8 S. M. Lu, Z. Wang, J. Li, J. Xiao and C. Li, *Green Chemistry*, 2016, **18**, 4553–4558.

9 D. Kim, X. Liu and M. S. Lah, *Inorganic Chemistry Frontiers*, 2015, 2, 336-360.

10 B. Moulton and M. J. Zaworotko, *Chem. Rev*. 2001, **101**, 1629-1658.

11 Y. Zhang and J. Zhang, *Pure Appl. Chem*, 2013, **85**, 405–416.

12 S.-L. Yang, P.-P. Sun, Y.-Y. Yuan, C.-X. Zhang and Q.-L. Wang, *CrystEngComm*, 2018, **20**, 3066–3073.

13 J. Yuan, L. Mu, J. Li, L. Zhang, G. Li, Q. Huo and Y. Liu, *CrystEngComm*, 2018, **20**, 2169–2174.

14 A. Schoedel, M. Li, D. Li, M. O'Keeffe and O. M. Yaghi, *Chemical Reviews*, 2016, **116**, 12466–12535.

15 E. V. Alexandrov, V. A. Blatov, A. V. Kochetkov and D. M. Proserpio,

CrystEngComm, 2011, **13**, 3947–3958.

16 N. W. Ockwig, O. Delgado-Friedrichs, M. O’Keeffe and O. M. Yaghi, *Accounts of chemical research*, 2005, **38**, 176–82.

17 A. K. Inge, M. Köppen, J. Su, M. Feyand, H. Xu, X. Zou, M. O’Keeffe and N. Stock, *Journal of the American Chemical Society*, 2016, **138**, 1970–1976.

18 M. Li, D. Li, M. O. Kee and O. M. Yaghi, *Chem. Rev*, 2014, **114**, 1343–1370.

19 N. L. Rosi, J. Kim, M. Eddaoudi, B. Chen, M. O’Keeffe and O. M. Yaghi, *Journal of the American Chemical Society*, 2005, **127**, 1504–1518.

20 C. Wu, F. Irshad, M. Luo, Y. Zhao, X. Ma and S. Wang, *ChemCatChem*, 2019, **11**, 1256–1263.

21 M. Chen, D. Liu, Y. Deng, W. Fu, H. Zou, Z. Chen, C. Xia and F. Liang, *Inorganic Chemistry Communications*, 2015, **55**, 96–98.

22 N. Chatterjee and C. L. Oliver, *Crystal Growth and Design*, 2018, **18**, 7570–7578.

23 D. C. Zhong, W. X. Zhang, F. L. Cao, L. Jiang and T. B. Lu, *Chemical Communications*, 2011, **47**, 1204–1206.

24 L. Wu, W. Wang, R. Liu, G. Wu and H. Chen, *Royal Society Open Science*, 2018, **5**, 1-12.

25 J. L. C. Rowsell and O. M. Yaghi, *Angewandte Chemie - International Edition*, 2005, **44**, 4670–4679.

26 S. S. M. Cohen, P. V Dau, M. Kim and S. M. Cohen, *Chemical Science*, 2013, **4**, 601–605.

27 B. Ugale, S. S. Dhankhar and C. M. Nagaraja, *Crystal Growth and Design*, 2018, **18**, 2432–2440.

28 H. T. D. Nguyen, Y. B. N. Tran, H. N. Nguyen, T. C. Nguyen, F. Gándara and P. T. K. Nguyen, *Inorganic Chemistry*, 2018, **57**, 13772–13782.

29 B. Ugale, S. S. Dhankhar and C. M. Nagaraja, *Crystal Growth and Design*, 2018, **18**, 2432–2440.

30 J. M. Ngoy and R. Falcon, *Canadian Journal of Chemical Engineering*, 2019, **2019**, 2961–2968.

31 Z. J. Lin, J. Lü, M. Hong and R. Cao, *Chemical Society Reviews*, 2014, **43**, 5867–5895.

32 Y. B. Zhang, H. Furukawa, N. Ko, W. Nie, H. J. Park, S. Okajima, K. E. Cordova, H. Deng, J. Kim and O. M. Yaghi, *Journal of the American Chemical Society*, 2015, **137**, 2641–2650.

33 F. Bertini, N. Gorgas, B. Stöger, M. Peruzzini, L. F. Veiros, K. Kirchner and L. Gonsalvi, *ACS Catalysis*, 2016, **6**, 2889–2893.

34 P. Patel, S. Nandi, M. S. Maru, R. I. Kureshy and N.-U. H. Khan, *Journal of CO_2 Utilization*, 2018, **25**, 310–314.

35 E. S. Gutterød, S. Øien-ØDegaard, K. Bossers, A. E. Nieuwelink, M. Manzoli, L. Braglia, A. Lazzarini, E. Borfecchia, S. Ahmadigoltapeh, B. Bouchevreau, B. T. Lønstad-Bleken, R. Henry, C. Lamberti, S. Bordiga, B. M. Weckhuysen, K. P. Lillerud and U. Olsbye, *Industrial and Engineering Chemistry Research*, 2017, **56**, 13206–13218.

36 B. An, L. Zeng, M. Jia, Z. Li, Z. Lin, Y. Song, Y. Zhou, J. Cheng, C. Wang and W. Lin, *Journal of the American Chemical Society*, 2017, **139**, 17747–17750.

37 C. Pagis, M. Ferbinteanu, G. Rothenberg and S. Tanase, *ACS Catalysis*, 2016, **6**, 6063–6072.

38 Y. Liao, Z. Cheng, W. Zuo, A. Thomas and C. F. J. Faul, *ACS Applied Materials and Interfaces*, 2017, **9**, 38390–38400.

39 Z. Li, T. M. Rayder, L. Luo and C. Tsung, *Journal of American Chemical Society*, 2018, **140**, 8082–8085.

40 M. S. Maru, S. Ram, R. S. Shukla and N. H. Khan, *Molecular Catalysis*, 2018, **446**, 23–30.

41 H. Song, N. Zhang, C. Zhong, Z. Liu, M. Xiao and H. Gai, *New Journal of Chemistry*, 2017, **41**, 9170–9177.

42 A. Behr and K. Nowakowski, *Advances in Inorganic Chemistry*, 2014, **66**, 223-

258.

43 J. E. Heimann, W. H. Bernskoetter and N. Hazari, *Journal of the American Chemical Society*, 2019, **141**, 10520–10529.

44 C. Federsel, R. Jackstell, A. Boddien, G. Laurenczy and M. Beller, *ChemSusChem*, 2010, **3**, 1048–1050.

CHAPTER 4

Palladium(II) Functionalised Metal-Organic Frameworks for Carbon Dioxide Hydrogenation to Formate.

Before MOF synthesis, an organometallic complex, $PdCl_2$bpdc (**C1**), was prepared using $[PdCl_2(CH_3CN)_2]$ and 2,2'-bipyridine-4,4'-dicarboxylate ligand as starting materials. **C1** was subsequently used for the synthesis of 2D isostructural metal-organic frameworks, $Mg(bpdc)(DMF)_2PdCl_2]_n$ (**Pd@Mg:JMS-2**) and $[Mn(bpdc)(DMF)_2PdCl_2]_n$ **(Pd@Mn:JMS-2**). The activated MOFs, **Pd@Mg: JMS-2a** and **Pd@Mn: JMS-2a** were evaluated as heterogeneous catalysts for the hydrogenation of CO_2 to formate. The aforementioned compounds were characterised using Nuclear Magnetic Resonance Spectroscopy (^{1}H NMR and ^{13}C NMR), X-ray diffraction studies (SCXRD and PXRD), Thermogravimetric analysis (TGA), Fourier Transform Infrared spectroscopy (FTIR) and Elemental Analysis, Inductively Coupled Plasma-Optical Emission Spectroscopy (ICP-OES), Brunauer–Emmett–Teller (BET) analysis, X-ray Photoelectron Spectroscopy, High-Resolution Transmission Electron Microscopy (HRTEM) and Scanning Electron microscopy-Energy Dispersive (SEM EDX).

4.1 Synthesis of C1.

The metal precursor, [$PdCl_2(CH_3CN)_2$] was synthesised according to a reported literature method.[1] **C1** was synthesised by reacting the commercially available 2,2'-bipyridine-4,4'-dicarboxylate ligand with [$PdCl_2(CH_3CN)_2$] in DMF for 48 hours as shown Scheme 4.1. The complex was obtained as a yellow powder in good yield, 278 mg (89.3 %).

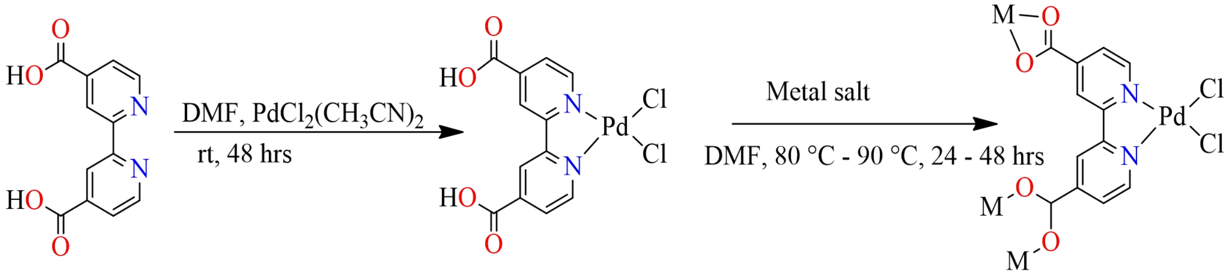

C1 **Pd@Mg:JMS-2 and Pd@Mn:JMS-2**

Scheme 4.1: Synthesis of **C1**, **Pd@Mg: JMS-2** and **Pd@Mn: JMS-2**

4.2: ^{1}H and ^{13}C {H} NMR analysis of C1

Figure 4.1 shows the ^{1}H NMR of 2,2'-bipyridine-4,4'-dicarboxylic acid ligand and **C1**. As expected, the aromatic protons for the ligand appeared as a singlet and two doublets, observed in the region 8.92 ppm to 7.90 ppm. The significant downfield shift in the ^{1}H NMR signals of these protons to the region 9.29 ppm to 8.19 ppm compared to the free ligand was observed confirming successful synthesis of the complex. Two sets of doublets observed at 9.29 ppm and 8.20 ppm for protons H-a and H-b have coupling constants of 4.0 Hz and 8 Hz respectively. ^{1}H NMR (400 MHz, DMSO-d_6): (δ, ppm), 8.20 (d, 2H, CH_{arom}, $^3J_{H\text{-}H}$ = 8.0 Hz), 9.00 (s, 2H, CH_{arom}).9.29 (d, 2H, CH_{arom}, $^3J_{H\text{-}H}$ = 4.0 Hz); ^{13}C NMR (DMSO-d_6) (δ, ppm): 164.55, 156.86, 150.83, 142.49, 126.74, 123.74.

In the ^{13}C {H} NMR spectra of the complex shown in Figure 4.2, the signals for the aromatic carbons are observed in the region 120 ppm to 165 ppm and the number of signals corresponds to the number of carbons present in the complex. The signal for the carboxylate carbon is the most deshielded due to the electron-withdrawing effects of oxygen and is observed further downfield at 164.55 ppm. Elemental analysis for **C1** gave (%) Calculated: 34.20 C, 1.91 H, 6.65 N. Found: 33.86 C, 1.56 H, 6.83 N.

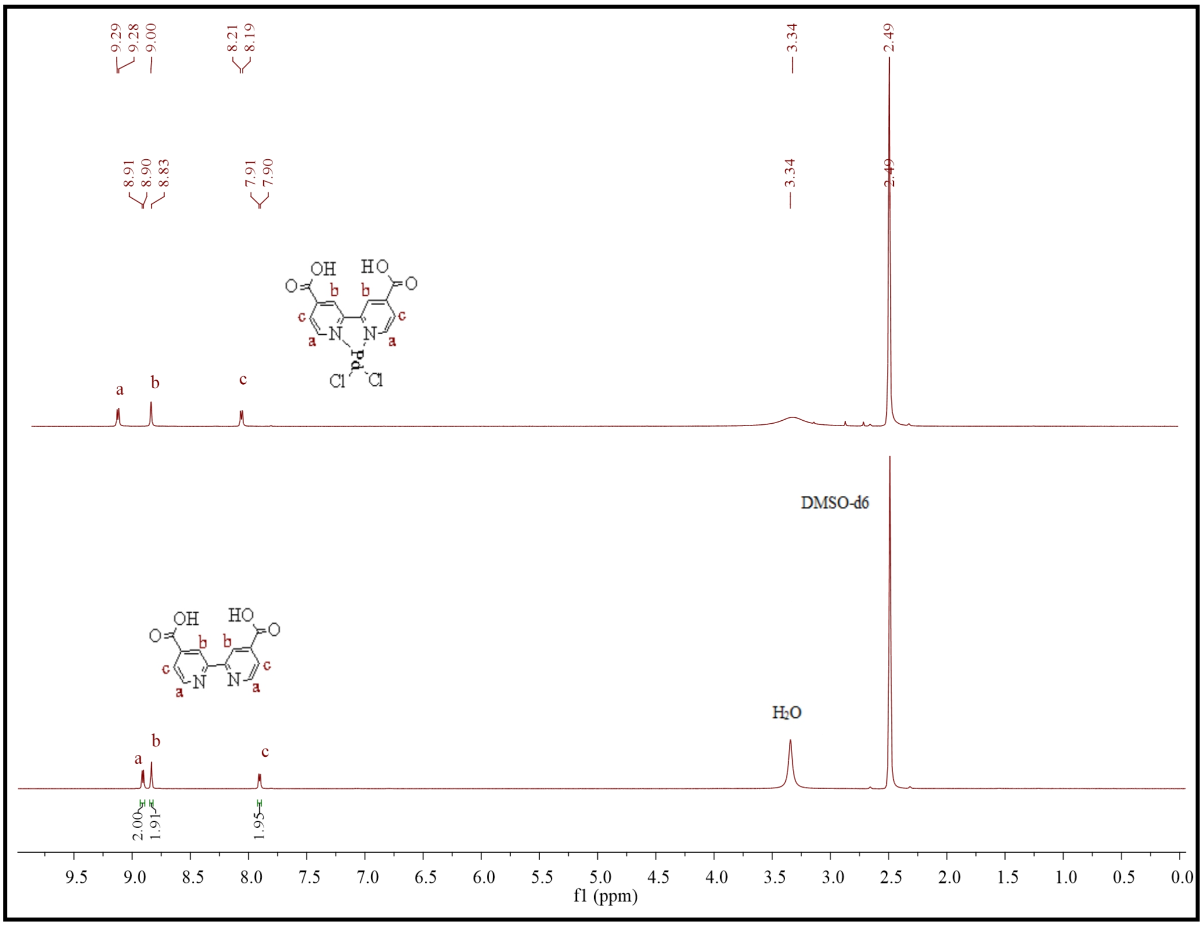

Figure 4.1: ^{1}H NMR spectrum of **bpdc** and **C1** in DMSO-d$_6$ at 30 ˚C

4.3 Synthesis of Pd@Mg: JMS-2 and Pd@Mn: JMS-2

After confirming the identity and purity of **C1**, it was used as a metalloligand for the solvothermal synthesis of **Pd@Mg: JMS-2** and **Pd@Mn: JMS-2.** About 15 mg (0.036 mmol) of **C1** was dissolved in DMF (7 mL) and $Mg(NO_3)_2 \cdot 6H_2O$ (138 mg, 0.537mmol) was added. The mixture was stirred for 10 minutes at room temperature. The resulting homogeneous solution was placed in a tightly sealed vial and heated at 80 ˚C in an oven for 48 hours. Yellowish block-shaped crystals of **Pd@Mg: JMS-2**, suitable for Single-crystal X-ray diffraction data collection were obtained. Following a similar procedure using $MnCl_2 \cdot 4H_2O$ (120 mg, 0,606 mmol), diamond-shaped orange crystals of **Pd@Mn: JMS-2** were obtained after 24 hours at 85 ˚C. Elemental analysis gave (%) Calculated: 34.20 C, 1.91 H, 6.65 N. Found: 33.86 C, 1.56 H, 6.83 N; Calculated: 36.64 C, 3.42 H, 9.50 N. Found: 37.17 C, 3.77 H, 9.11 N and Calculated: 34.83 C, 3.25 H, 9.03 N. Found: 35.07 C, 3.35 H, 8.77 N for C1, **Pd@Mg:JMS-2** and **Pd@Mn:JMS-2** respectively. The Pd loadings determined from the analysis of the digested solids by Inductively Coupled Plasma-Optical Emission Spectroscopy gave 0.58% and 0.67% Pd in **Pd@Mg: JMS-2a** and **Pd@Mn: JMS-2a** respectively.

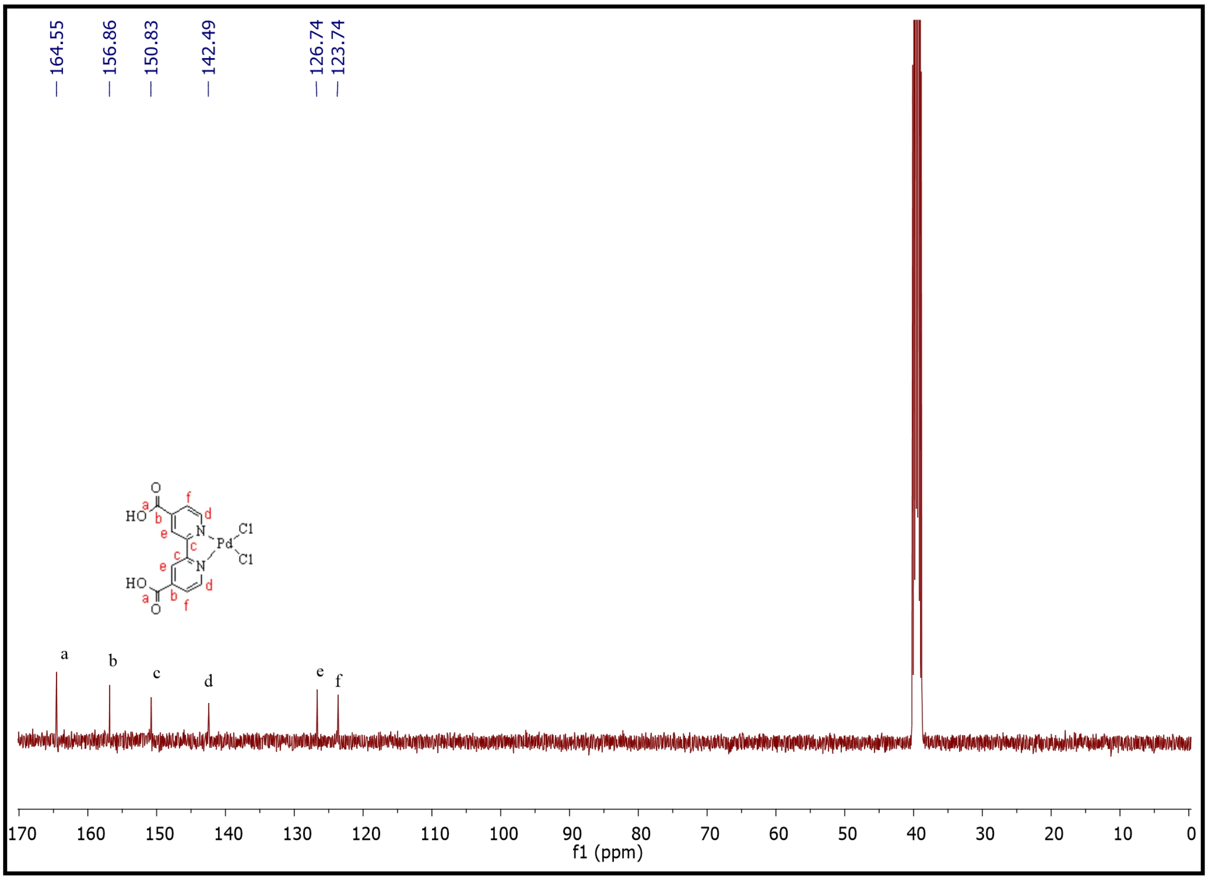

Figure 4.2: ^{13}C NMR spectrum of **C1** in **DMSO-d$_6$**.

4.4 Single Crystal X-ray Diffraction

Single crystal X-ray diffraction (SCXRD) data collections of **Pd@Mg: JMS-2** and **Pd@Mn: JMS-2** were carried at 293 K on a Bruker KAPPA APEX II DUO diffractometer. Anisotropic thermal parameters were applied to all non-hydrogen atoms. The hydrogen atoms were placed in idealised positions using the riding model and assigned temperature factors relative to the parent atom. The crystal data for **Pd@Mg: JMS-2** and **Pd@Mn: JMS-2** is given in Table 4.1. The structures were deposited at the Cambridge Crystallographic Data Centre and allocated the numbers CCDC 1943375 and 1943376 for **Pd@Mg: JMS-2** and **Pd@Mn: JMS-2** respectively.

Table 4.1: Crystal data and structure refinement for **Pd@Mg: JMS-2** and **Pd@Mn: JMS-2**

Empirical formula	$\mathbf{C_{18}H_{20}N_4O_6Mg_1Pd_1Cl_2}$	$\mathbf{C_{18}H_{20}N_4O_6Mn_1Pd_1Cl_2}$
Formula weight (gmol^{-1})	589.99	620.62
Temperature/K	293(2)	293(2)
Crystal system	monoclinic	monoclinic
Space group	C2/c	C2/c
a/Å	27.219(2)	27.534(4)
b/Å	7.7588(6)	7.8567(12)
c/Å	22.3190(17)	22.470(4)
α/°	90	90
β/°	102.764(2)	102.681(4)
γ/°	90	90
Volume/Å^3	4596.8.9(6)	4742.3(13)
Z	8	8
Calculated density (g/cm^3)	1.7048	1.7383
μ(Mo-Kα) /mm^{-1}	1.11	1.55
F(000)	2288	2184
Crystal size/mm^3	0.431 × 0.379 × 0.211	0.18 x 0.15 x 0.12
Radiation	MoKα (λ = 0.71073)	MoKα (λ = 0.71073)
2θ Max/°	52.12	56.63
Index ranges	$-33 \le h \le 33$, $-9 \le k \le 9$, $-27 \le l \le 27$	$-36 \le h \le 36$, $-10 \le k \le 10$, $-27 \le l \le 27$
Reflections collected	37486	60468
No. unique data	4550	5897
The goodness of fit on S	1.071	1.035
Final R indexes [I>=2σ (I)]	0.0359	0.0380
Final wR$_2$ indexes [all data]	0.0882	0.0911
Largest diff. peak/hole / e Å^{-3}	0.63/-0.38	0.42/-0.42

4.5 Structural Description

Single crystal X-ray diffraction revealed that **Pd@Mn: JMS-2** and **Pd@Mg: JMS-2** are isostructural frameworks; therefore the structure of **Pd@Mg: JMS-2** will not be discussed. **Pd@Mn: JMS-2** crystallises in the monoclinic system in the space group C2/c. The asymmetric unit consists of one crystallographically independent Mn^{II}, one Pd^{II}, two Cl atoms, one deprotonated linker and two coordinated DMF molecules. As illustrated in Figure 4.3, each Mn^{II} centre is coordinated to three bpdc linkers, one in a bidentate chelating mode and the other two in a bidentate bridging mode. The overall geometry around the manganese centre is distorted octahedral. The bpdc anion is a bidentate metal linker so in addition to the carboxylate moiety, the two nitrogen atoms are coordinated to one Pd^{II} centre and the geometry around Pd^{II} is square planar. Mn-O, Pd-N, and Pd-Cl bond length range from 2.030 (3) Å to 2.2855(10), and these parameters are given in Table 4.2. The bond angles around Mn^{II} and Pd^{II} centres are in the range 56.20 (6) to 175.22(12)$^{\circ}$. The crystal data for the two isostructural MOFs is given in Table 4.1.

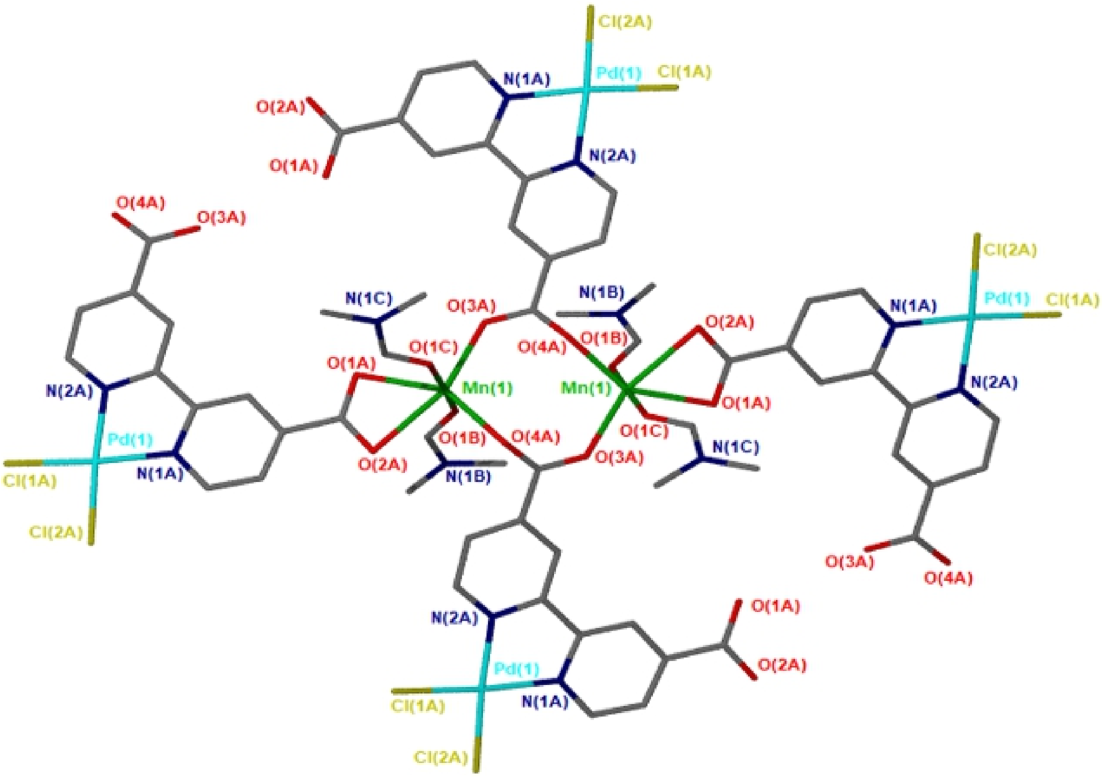

Figure 4.3: Coordination environment around Mn^{II} and Pd^{II} centres in **Pd@Mn: JMS-2**.

(Hydrogen atoms have been omitted for clarity).

Table 4.2: Bond distances around Mg^{II} and Pd^{II} in **Pd@Mn: JMS-2**.

Bond Type	Bond Length (Å)	Bond Type	Bond Length (Å)
Mn1-O4A	2.103(3)	Mn1-O2A	2.425(3)
Mn1-O3A	2.115(2)	Pd1-N2A	2.030(3)
Mn1-O1C	2.155(2)	Pd1-N1A	2.031(3)
Mn1-O1B	2.166(3)	Pd1-Cl2A	2.2852(10)
Mn1-O1A	2.247(2)	Pd1-Cl1A	2.2855(10)

Figure 4.4 illustrates the packing diagram of **Pd@Mn: JMS-2**, with DMF molecules residing in the channels. No classic hydrogen bonding occurs between guest and framework molecules. However, weak intermolecular and intramolecular interactions such as π···π interactions of the aromatic ring are suggested to reinforce the geometry and impart stability to the MOF.

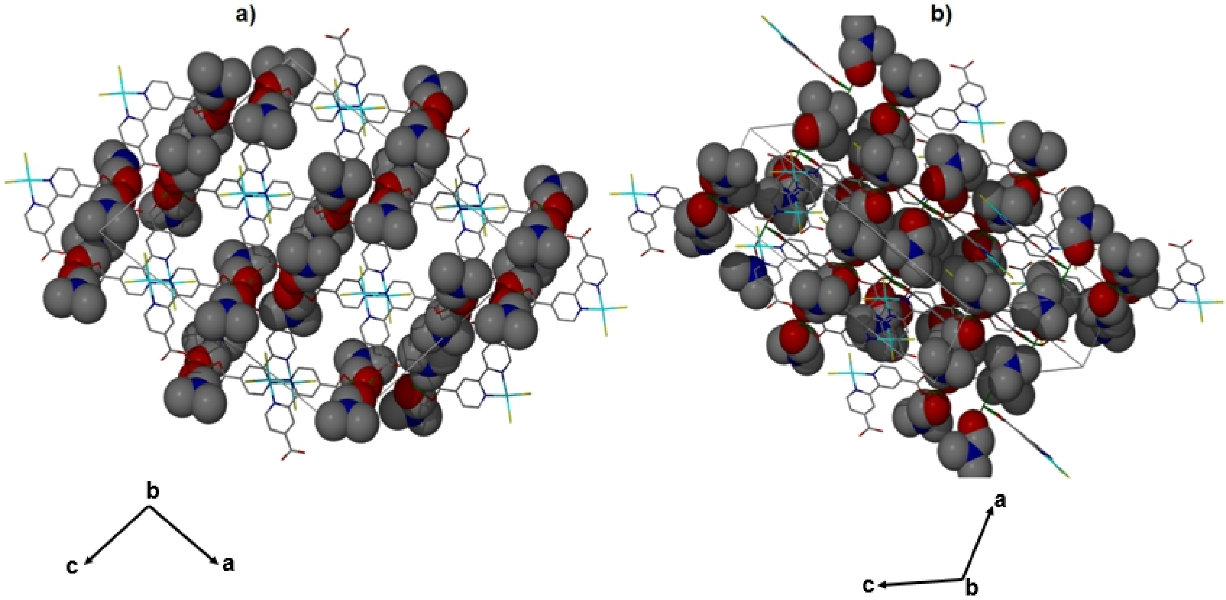

Figure 4.4: Solid-state packing of **Pd@Mn: JMS-2** drawn in stick form with DMF molecules in van der Waals radii confined in the cavities viewed along (a) b axis and (b) c axis. Hydrogen atoms have been omitted for clarity.

The overall structure is a 2D network, with channels running along the *c*-axis as shown in Figure 4.5a. The solvent-accessible volume calculated using PLATON[2] shows 46.6 % and 43.8 % per unit cell in **Pd@Mn: JMS-2** and **Pd@Mg: JMS-2** respectively, after the removal of DMF molecules. Mercury program[3] was used to reveal that the 2D networks contain interconnected cavities as illustrated in Figure 4.5b.

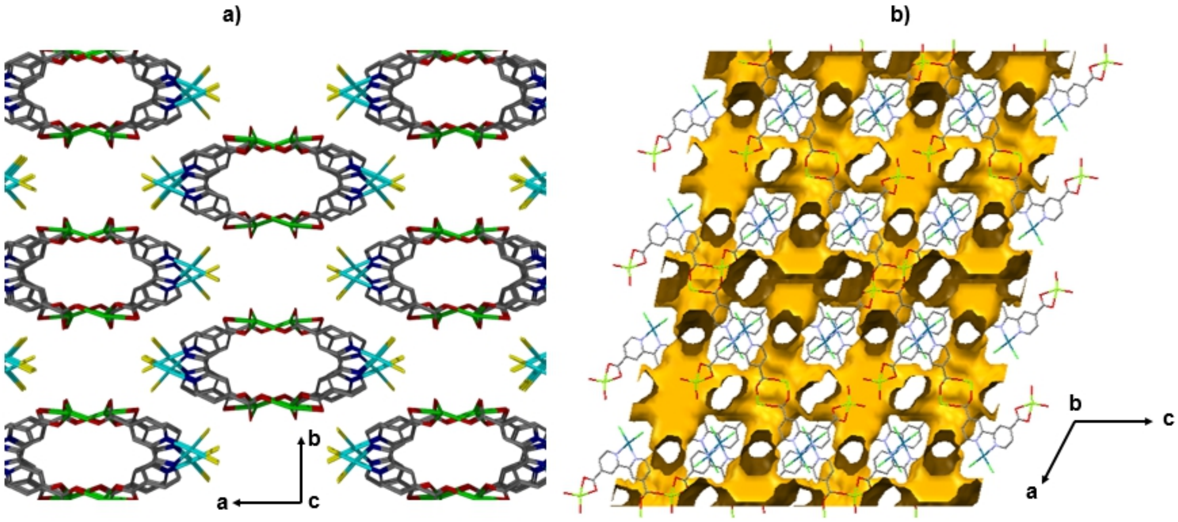

Figure 4.5: a) Packing diagram of **Pd@Mg: JMS-2** viewed along the *c*-axis, DMF molecules have been omitted, b) Channels found in **Pd@Mg: JMS-2** viewed along the *b*-axis.

4.6 FTIR Analysis

Fourier Transform Infrared spectroscopy experiments were performed on **C1**, **Pd@Mg: JMS-2** and **Pd@Mn: JMS-2**. A stretching frequency at 1729 cm^{-1} (COOH) in **C1** shifts to 1600 cm^{-1} for (-COO^{-}) as shown in Figure 4.6 is evidence of coordination between the carboxylate moiety and the metal centre. The results are consistent with single-crystal data. The native **Pd@Mg: JMS-2** and **Pd@Mn: JMS-2** were activated by soaking in methanol at room temperature for 24 hours, during which methanol was refreshed after every 6 hours followed by drying at 80 ˚C under vacuum for 24 hours. Successful activation is evidenced by the disappearance of the FTIR band at 1676 cm^{-1} attributed to coordinated DMF molecules in **Pd@Mg: JMS-2** and **Pd@Mn: JMS-2**. The asymmetric and symmetric stretches of the carboxylate observed at 1600 and 1386 cm^{-1} in both MOFs do not change after activation, suggesting that the binding mode of the carboxylate moiety is not affected.[4] The stretches at 1552 cm^{-1} were assigned to the conjugated C-C of the benzene ring.

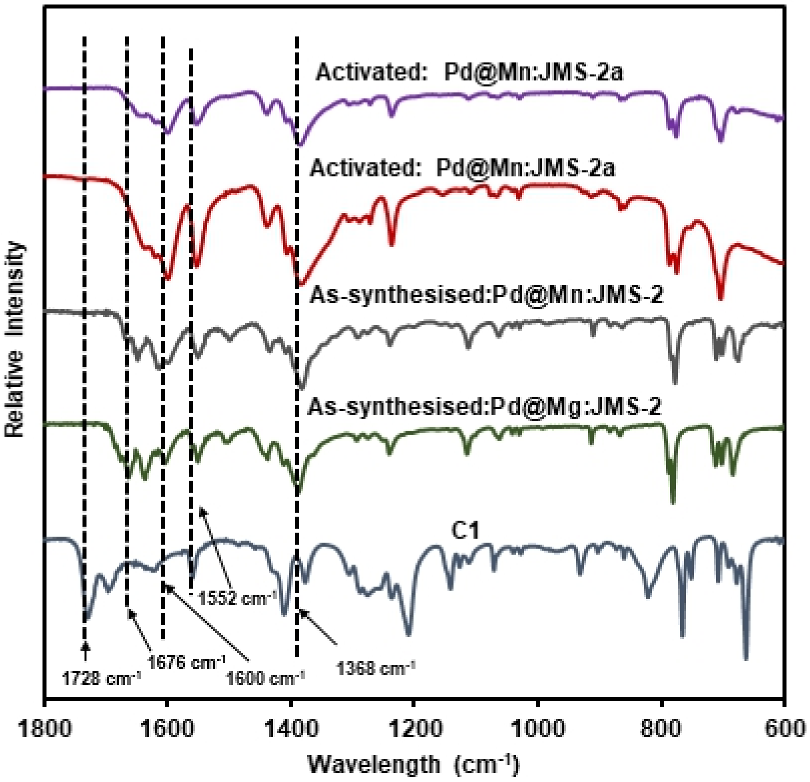

Figure 4.6: IR spectrum of Pd complex, as-synthesised and activated **Pd@Mg: JMS-2** and **Pd@Mn: JMS-2**.

4.7 Thermal Analysis

The thermal behaviour of **Pd@Mg: JMS-2** and **Pd@Mn: JMS-2** were investigated by Thermogravimetric analysis (TGA) and the results are illustrated in Figure 4.7. **Pd@MgJMS-2** shows three stages of weight loss. The initial two-stage weight loss of 24.1 % in the temperature range 50 to 244 ˚C corresponds to desorption of two DMF molecules per formula unit which was modelled as 24.7 % in the asymmetric unit. Decomposition of the framework occurs above 400 ˚C. The TGA of **Pd@Mn: JMS-2** displays the same phenomenon with a total weight loss of 27.4 % between

160 and 305 ˚C, which corresponds to two DMF molecules modelled in the asymmetric unit. Contrary to **Pd@Mg: JMS-2** that exhibit high thermal stability, **Pd@Mn: JMS-2** decomposes around 325 ˚C. The TGA curves of the dissolvated frameworks show only one main weight loss, confirming that guest molecules were completely evacuated. However, due to adsorption of moisture, some weight loss was still observed on the activated sample curve.

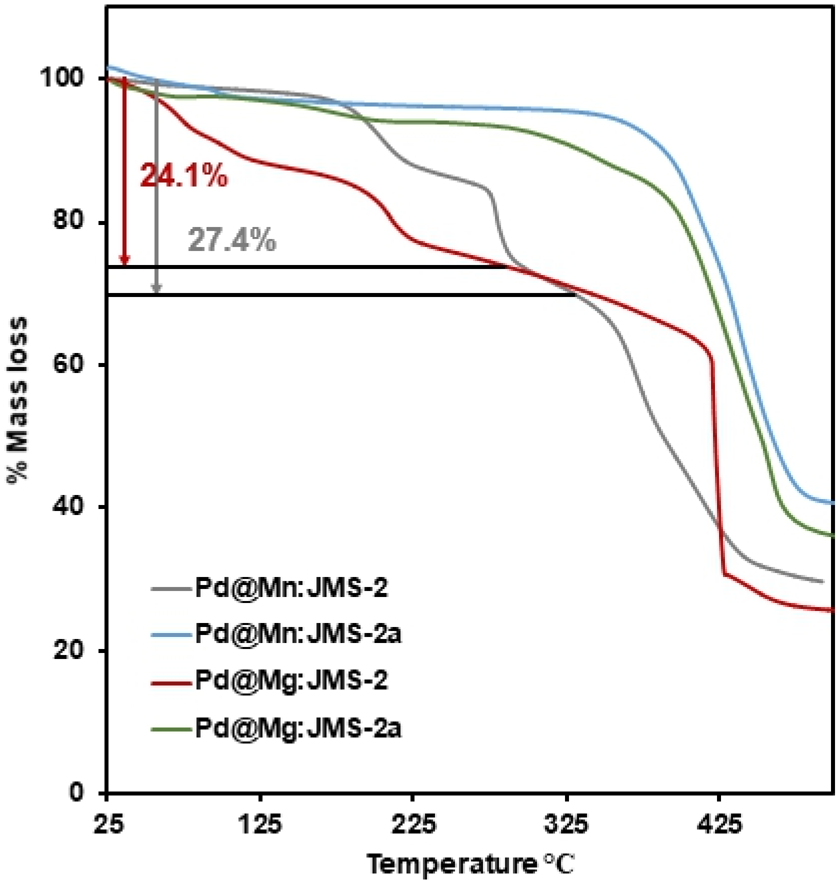

Figure 4.7: TGA traces of the as-synthesised **Pd@Mg: JMS-2** and **Pd@Mn: JMS-2**.

4.8 PXRD Analysis

The calculated and experimental PXRD patterns illustrated in Figure 4.8 are in good agreement, which confirms phase purity of the synthesised compounds. The similarity in the PXRD patterns of the two MOFs also confirms that the two MOFs are indeed isostructural. The structural integrity of the MOF is maintained after activation as evidenced by a good match between as-synthesised and activated phases.

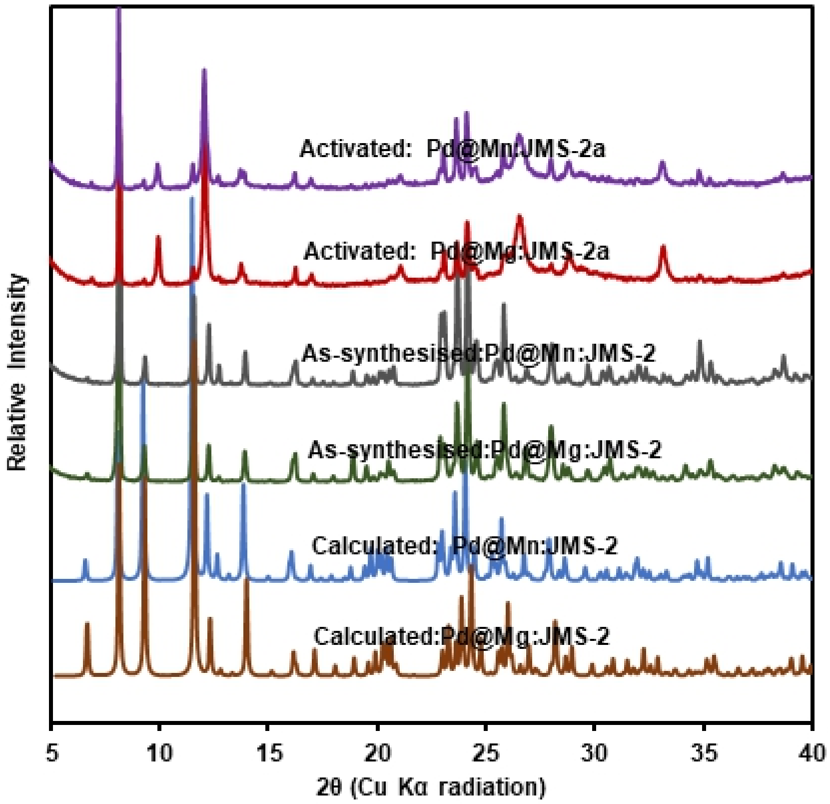

Figure 4.8: PXRD pattern of **Pd@Mg: JMS-2** and **Pd@Mn: JMS-2** calculated, as-synthesised and activated.

4.9 Chemical Stability Tests

A stable MOF structure should have strong coordination bonds to survive the attack by guest molecules. In most MOFs structures, the chemical weak points are the nodes, more specifically the metal linker bonds.[5] It determines the thermodynamic stability of MOFs under different operating environments. The activated phases **Pd@Mg: JMS-2a** and **Pd@Mn: JMS-2a** were thus soaked for 36 hours in different solvents and bases that are normally used for CO_2 hydrogenation. The solids recovered by filtration were washed thoroughly before recording PXRD patterns. Except for crystals soaked in water, the FTIR studies (Figure 4.9) of **Pd@Mg: JMS-2a** soaked in different bases and solvents show that the position of asymmetric and symmetric carboxylate stretches located at 1600 and 1368 cm^{-1} respectively are not affected. This suggests that the binding mode of the carboxylate moiety is retained under different chemical environments.

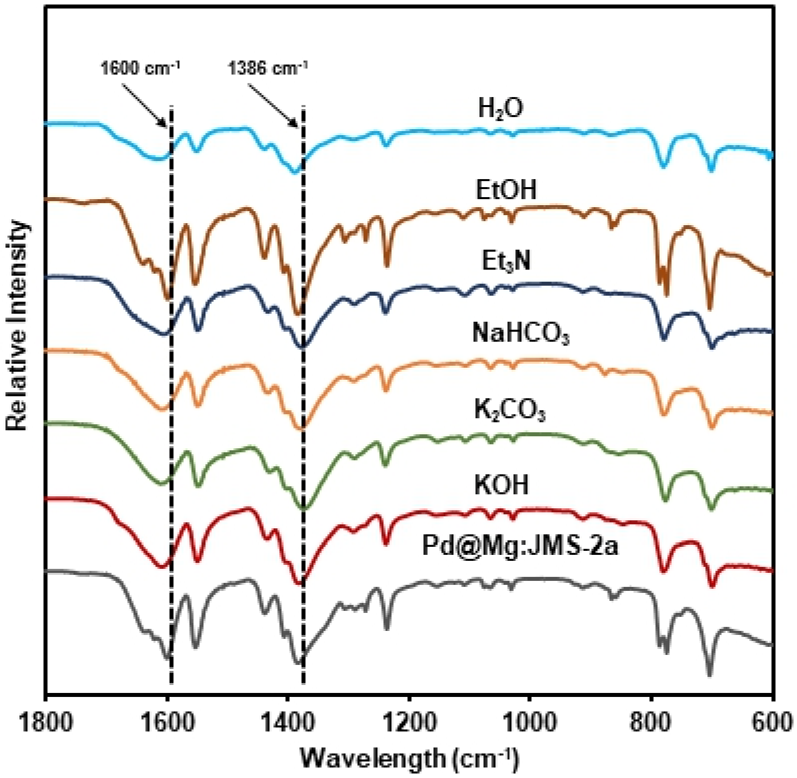

Figure 4.9: FTIR of **Pd@Mg: JMS-2a** soaked in different bases and solvents (Conditions: 0.5 M base, 10 mL solvent, 36 hours at room temperature)

As shown in the PXRD pattern (Figure 4.10), compound **Pd@Mg: JMS-2a** is not stable in water and $NaHCO_3$. The compound is poisoned by water as evidenced by a transformation from crystalline to an amorphous phase. In the presence of $NaHCO_3$, a new phase is obtained. Notably, the 2D framework is maintained in ethanolic solutions of KOH, K_2CO_3 and Et_3N.

Similar chemical stability studies were carried using **Pd@Mn: JMS-2a**. The FTIR studies of the recovered samples in different bases and solvents are presented in Figure 4.11. The bands at 1600 cm^{-1} and 1386 cm^{-1}, assigned to the asymmetric and symmetric stretches of the carboxylate did not change suggesting that the binding mode of the carboxylate moiety to the metal centre is retained under various chemical conditions.

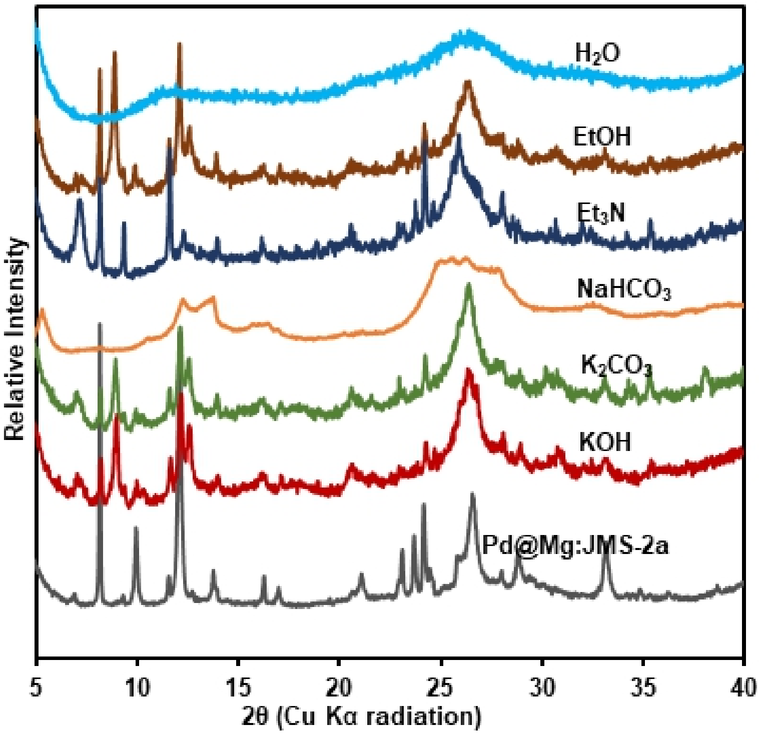

Figure 4.10: PXRD traces of **Pd@Mg: JMS-2a** soaked in different bases and solvents (Conditions: 0.5 M base, 10 mL solvent, 36 hours at room temperature).

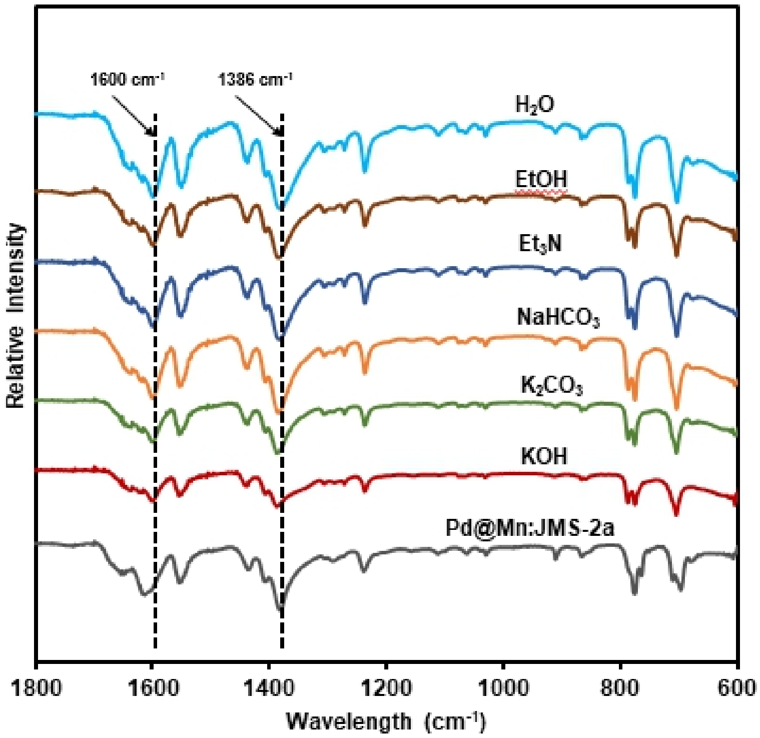

Figure 4.11: FTIR of **Pd@Mn: JMS-2a** soaked in different bases and solvents (Conditions: 0.5 M base, 10 mL solvent, 36 hours at room temperature).

This is in agreement with PXRD patterns (Figure 4.12) which shows that structural integrity is maintained. Notably, **Pd@Mn: JMS-2a** is stable in water as evidenced by a good match between the activated phase and the one obtained after soaking the material in water for 36 hours. The difference observed in the chemical stability of the two MOFs may be attributed to the strength of the metal-oxygen bond.

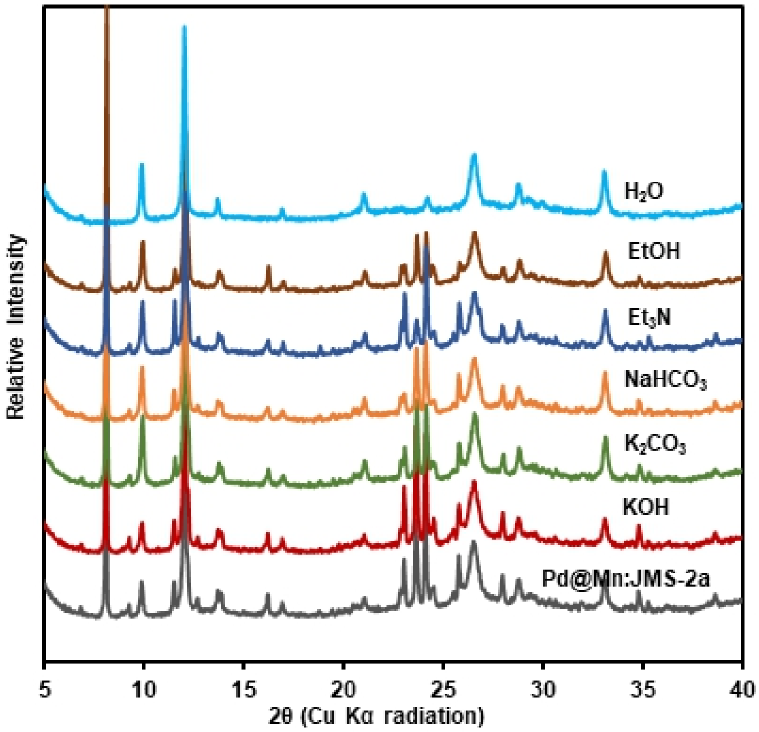

Figure 4.12: PXRD traces of **Pd@Mn: JMS-2a** soaked in different bases and solvents (Conditions: 0.5 M base, 10 mL solvent, 36 hours at room temperature).

4.10 Nitrogen Sorption Studies

Nitrogen isotherms were measured (Figure 4.13) at 77 K for **Pd@Mg: JMS-2a** and **Pd@MnJMS-2a** to assess their porosities and surface areas. The adsorption-desorption isotherm shows a Type IV hysteresis loops (H-1 type) which are indicative of the presence of porous channels, with a Brunauer-Emmet-Teller (BET) surface areas of 0.72 and 5.8 m^2/g and total pore volumes of 0.16 and 5.84 cm^3/g for **Pd@Mg: JMS-2a** and **Pd@MnJMS-2a** respectively. The obtained surface areas and pore volumes are relatively low due to partial occupancy by palladium complexes inside the MOFs.

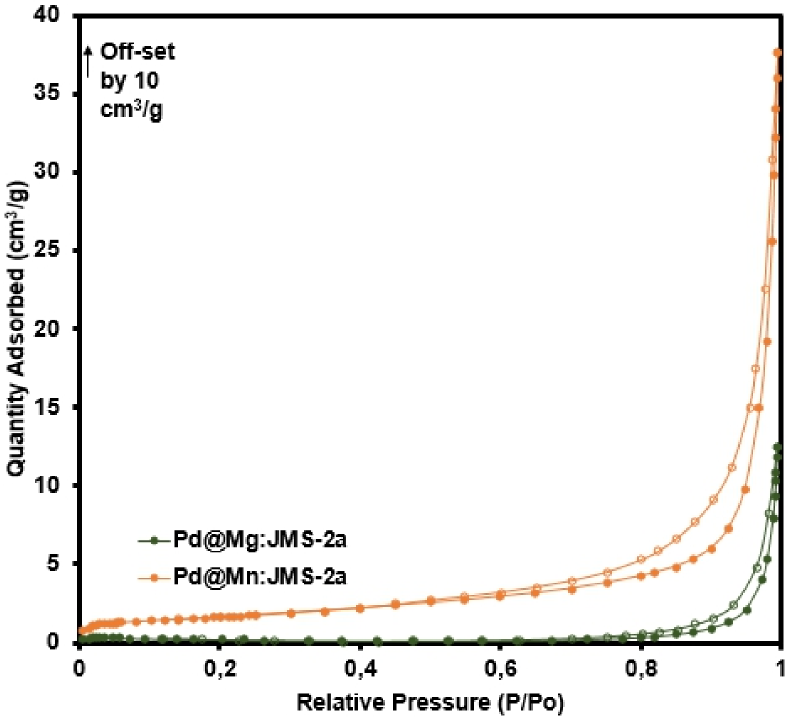

Figure 4.13: Nitrogen adsorption-desorption studies of **Pd@Mg: JMS-2a** and **Pd@Mn: JMS-2a** at 77 K.

4.11 Catalysis Studies

Equation 4.1 illustrates the catalytic reaction for the hydrogenation of CO_2 to formate.

$$CO_2 + H_2 \xrightarrow[\text{Solvent, }\Delta\text{, pressure}]{\text{Catalyst, base}} HCOO^- + H^+\text{base}$$

Equation 4.1: Catalytic reaction for the hydrogenation of CO_2 to formate.

Preliminary catalytic reactions (Table 4.3, entry 1 to 11) were conducted using the more stable **Pd@MnJMS-2a** catalyst, to identify the optimum reaction conditions. The formate produced was detected and quantified by ^{1}H NMR spectroscopy with acetone as an internal standard. An example of how the yield is calculated was presented in Chapter 3, page 79. Several bases including Et_3N, KOH, K_2CO_3 and $NaHCO_3$ were screened (Entry 1 to 4). When strong inorganic bases were used, (Entry 2 to 4) higher yields of formate were observed with KOH reaching 45.7 % formate yield. The weak organic base, triethylamine (pKa =18.8) gave a yield of 22.6 % (Entry 1). Based on base screening results, we opted to use KOH as our preferred base for the reaction in all optimisation studies. In the absence of a base (Entry 5), the system fails to produce any formate. In most reported catalytic systems, a base is needed to facilitate the hydrogenation of CO_2 to formate because i) the base deprotonates the generated formic acid; thus thermodynamically shifting the equilibrium forward; ii) the base has been found to accelerate the heterolysis H_2 during the catalytic cycle, thereby kinetically promoting the catalytic activity.[4]

Table 4.3: Hydrogenation of CO_2 to formate using **Pd@Mg: JMS-2a**, **Pd@Mn: JMS-2a** and **C1**

Entry	**Catalyst**	**Base**	**Temp/ºC**	**Pressure (bars) (CO_2:H_2)**	**Formate (mmol)**	**% Yield**
1	Pd@Mn:JMS-2a	Et_3N	90	40 (1:3)	1.13	22.6
2	Pd@Mn:JMS-2a	KOH	90	40 (1:3)	2.29	45.7
3	Pd@Mn:JMS-2a	$NaHCO_3$	90	40 (1:3)	1.71	34.2
4	Pd@Mn:JMS-2a	K_2CO_3	90	40 (1:3)	1.35	27.0
5	Pd@Mn:JMS-2a	None	90	40 (1:3)	0.00	0.00
6	None	KOH	90	40 (1:3)	0.00	0.00
7	Pd@Mn:JMS-2a	KOH	90	20 (1:1)	0.83	16.5
8	Pd@Mn:JMS-2a	KOH	90	30 (1:2)	1.37	27.3
9	Pd@Mn:JMS-2a	KOH	90	50 (1:4)	3.19	69.8
10	Pd@Mn:JMS-2a	KOH	90	40 (0:4)	0.00	0.0
11	Pd@Mn:JMS-2a	KOH	90	10 (1:0)	0.00	0.0
12	Pd@Mn:JMS-2a	KOH	100	50 (1:4)	4.57	91.5
13	Pd@Mg:JMS-1a	KOH	100	50 (1:4)	2.40	48.0
14	C1	KOH	100	50 (1:4)	1.87	37.5
14*	C1	KOH	100	50 (1:4)	1.48	29.6

Conditions: Time (24 hours), ethanol (8 mL) and base (5 mmol) and TONs are based on Pd (0.46 μmol). The yield based on ^1H NMR analysis using acetone as an internal standard. *In the presence of mercury. The yield was calculated based on the conversion of the base.

It is important to note that upon hydrogenation in the absence of a catalyst, Entry 6, the reaction does not proceed, indicating the crucial role of the catalyst in CO_2 reduction. A yield of 69.8 % (Entry 9) was observed when the pressure of H_2 was raised to 40 bar. This might be because sufficient partial pressure of H_2 is required to generate enough hydride to boost CO_2 hydrogenation.

A complete screening of the effects of temperature, time and catalyst loading on both catalysts was carried out (Figure 4.14 and 4.15). In all cases, the more stable, **Pd@Mn: JMS-2a**, with a large surface, performed better than **Pd@Mg: JMS-2a** under analogous conditions. The catalytic activity tends to increase with increasing BET surface because the reactants can easily access the surface of catalyst.[6] Figure 4.14 illustrates the results of CO_2 reduction conducted at different temperatures (90 to 120 ˚C) with other parameters kept constant. The outcome suggests that for both catalysts, the yield of potassium formate increased with increase in temperature.

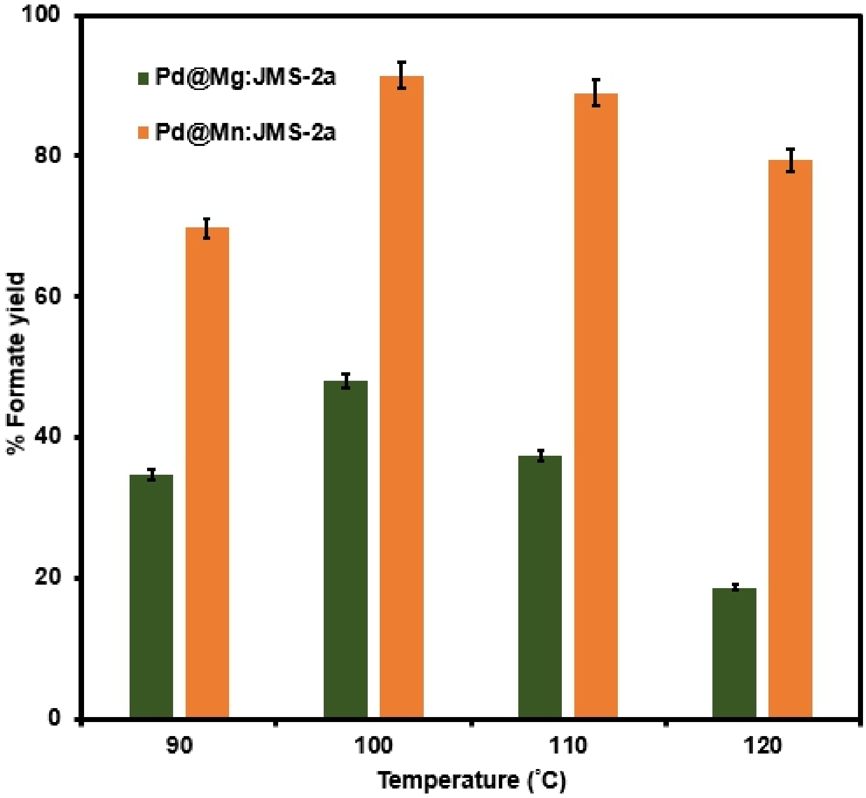

Figure 4.14: Effect of temperature. (**Conditions**: Pressure 50 bar (CO_2/H_2 =1:4), Time 24 hours, Catalyst loading 0.46 µmol based on Pd), 5 mmol KOH and 8 mL ethanol.

Above 100 ˚C, a decrease in formate was observed. High temperatures may result in either the reverse water gas shift reaction or decomposition of the formate.[7] Our results show that 100 ˚C was the most suitable temperature for further studies.

We further studied the effects of other parameters such as the effect of time and catalyst loading on the reaction at 100 ˚C and the results are shown in Figure 4.15. The yield/time profile of the CO_2 hydrogenation to formate (a) was mapped out by performing batch reactions with different times under identical conditions. The results show a progressive increase in the amount of formate produced, with maximum yield being obtained after 24 hours. Catalyst loading based on Pd was varied from 0 to 0.55 µmol keeping all parameters constant (b). In both cases, an increase in catalyst load gave rise to an increase in the yield of formate produced. Further increase in catalyst loading results in no significant increase in the product.

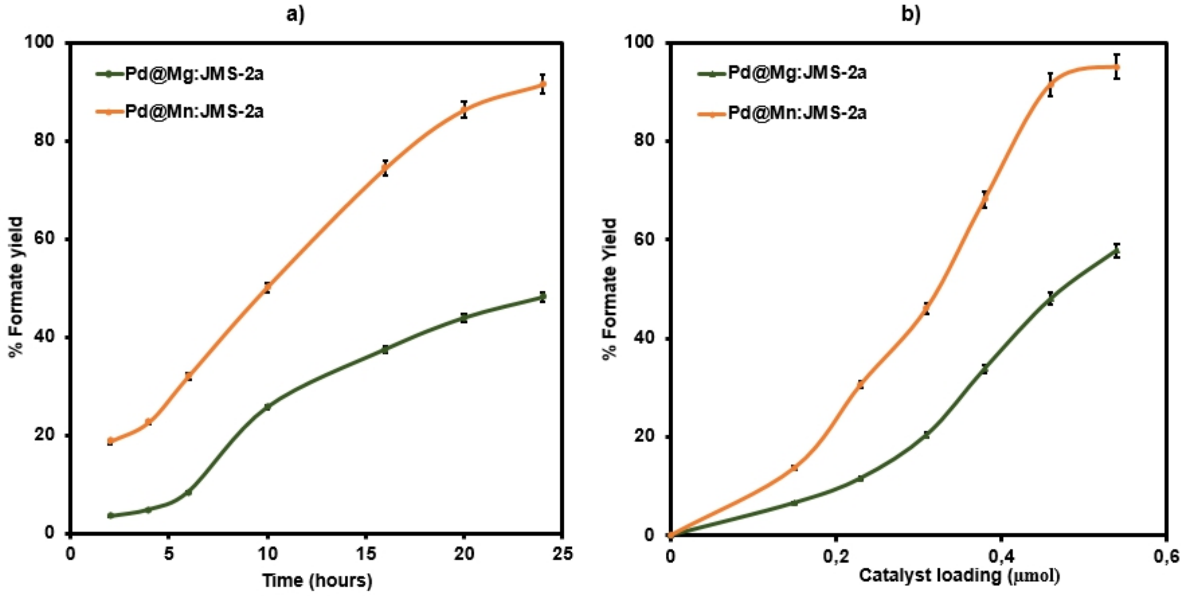

Figure 4.15: a) Effect of time, (**Conditions**: Pressure 50 bar (CO_2/H_2 =1:4), Temp 100 ^{0}C, 0.46 µmol catalyst loading based on Pd, 5 mmol KOH and 8 mL ethanol) and b) Effect of catalyst loading (**Conditions**: Pressure 50 bar (CO_2/H_2 =1:4), Temperature 100 ˚C, Time 24 hours, 5 mmol KOH and 8mL ethanol).

We tested the hydrogenation reaction under optimised conditions (Table 4.2, Entry 12 to 14). Figure 4.16 illustrates the ^{1}H NMR spectra for the reaction solution catalysed by **Pd@Mn: JMS-2a** under optimised conditions. While the homogeneous counterpart, **C1**, shows some activity (yield 37.5 %, Entry 14), in addition to being able to be recycled by simple filtration, the Pd functionalised based MOF catalysts (**Pd@Mg.JMS-1a** and **Pd@Mn.JMS-2a**) show higher catalytic activity (Entry 12 and 13). This might be because heterogeneous catalysts are often more stable and degrade much slower than the homogeneous catalysts. The metals and ligands are strongly bound within the framework to prevent its decomposition in solution.[8,9] In addition to that, after activation, the MOFs contain coordinatively unsaturated metal centres that can display CO_2 and H_2 adsorption[10,11] and conversion at the catalytic centres.[12–14]

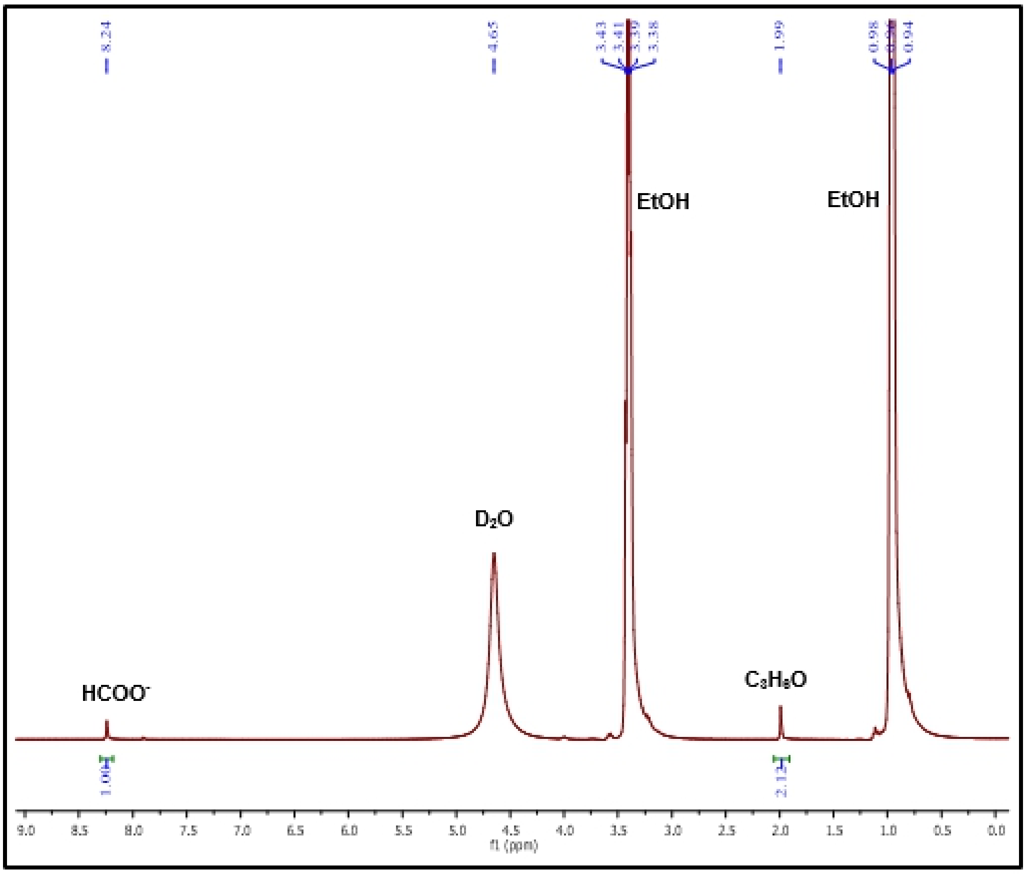

Figure 4.16: ^1H NMR for the reaction solution catalysed by Pd@Mn: JMS-2a under optimised conditions.

The catalytic activity of **Pd@Mg: JMS-2a** and **Pd@Mn: JMS-2a** was compared with similar systems reported in the literature as illustrated in Table 4.4. Remarkably, the reaction conditions employed in this work are milder than some of the previously reported heterogeneous systems for CO_2 hydrogenation to formate. [7,8,12,15–17] Since we were unable to isolate the two isostructural non-palladated MOFs, we did catalysis in the presence of metal salts used in MOF synthesis to ascertain whether catalysis is promoted by Mg^{II} or Mn^{II} or other moieties present in MOF. Though Mn^{II} complexes prepared by Gonsalvi *et al*.[18] were found to be active, the Mn^{II} metal salt is not, indicating the importance of molecular structure in catalysts design.

Table 4.4: Comparative study of the heterogeneous catalytic systems for the hydrogenation of CO_2 to formate.

Catalyst	pH_2/pCO_2 (bars)	Temp/ºC	Time /hr	TON	Ref
MbpyOH-[Ir^{III}]-UiO	1	85	15	6 149	12
Ru@UiO-66	15	27	0.5	32 000	8
IrCp*(HBF-2)Cl_2	80	120	10	6 400	15
Bpy-CTF-Ru(acac)$_2$Cl	80	120	5	21 200	16
IrCp*(N-N)x}y/HBF	40	120	10	6 400	15
Ru-HT	60	60	24	11 389	17
Nitrogen rich g-C CoNPs	62	120	24	82 265	7
$[Mn(bpdc)PdCl_2]_n$	50	100	24	9808	This work
$[Mg(bpdc)PdCl_2]_n$	50	100	24	7272	This work

TON = Turnover number: moles of product formed per moles of active metal centre

4.12 Poisoning Studies

Thiols are known to be incompatible with many transition metal catalysts[8] especially Pd and Pt. Such poisons can be ascribed to the strong and intractable thiol-Pd interactions that effectively seal off the coordination and suppress the bonding lability that is crucial for the catalytic process.[19]To prove that most of the active species responsible for CO_2 hydrogenation is located within the pores rather than being bound to the surface, the hydrogenation reaction was carried in the presence of differently sized thiol poisons using the most active catalyst, in this case, **Pd@Mn:JMS-2a**. Figure 4.17 and 4.18 shows the ^1H NMR spectra of these poisoning studies. As expected, when **Pd@Mn:JMS-2a** was exposed to benzylmercaptan, which does not easily penetrate the host framework, the remaining activity was 72.9 %.

In contrast, when the catalyst was exposed to a least sterically demanding thiol, 2 mercapto-ethanol, the retained activity dropped to 39.4 %. These results are consistent with the bulk of Pd sites being situated inside instead of on the surface of the MOF because more facile diffusion of the smaller thiols through the pores of the MOF is expected, resulting in more poisoning of the catalyst than with larger and more sterically bulky thiol poisons.

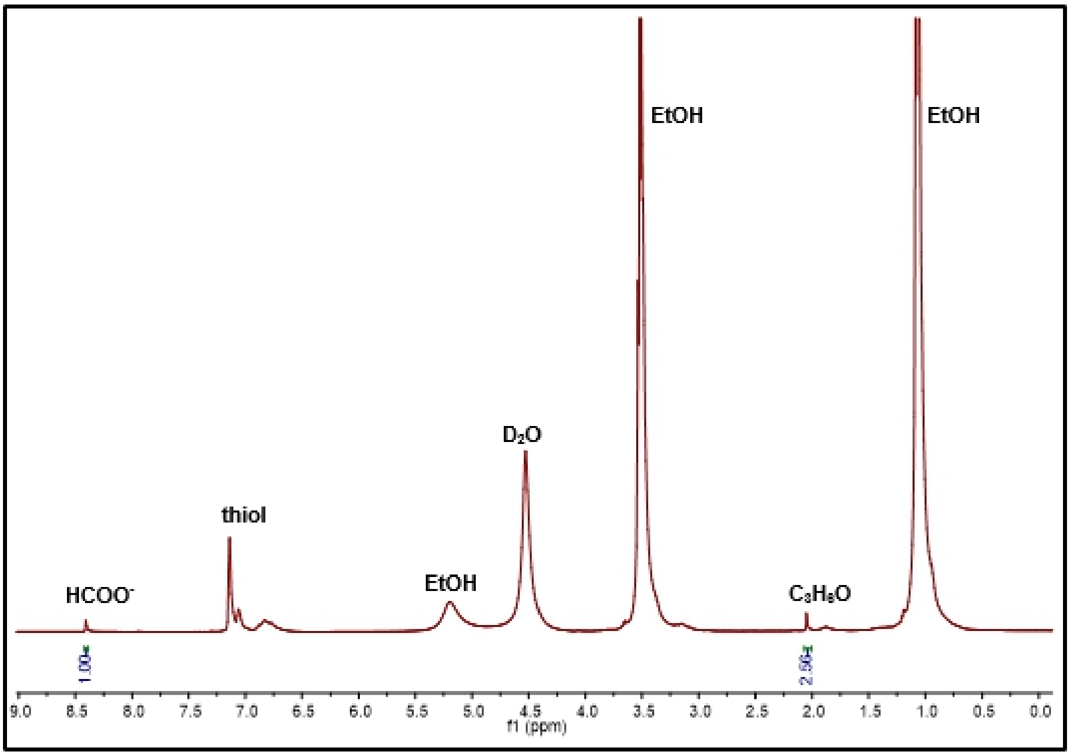

Figure 4.17: ^{1}H NMR spectra obtained when the reaction was carried out in the presence of benzylmercaptan.

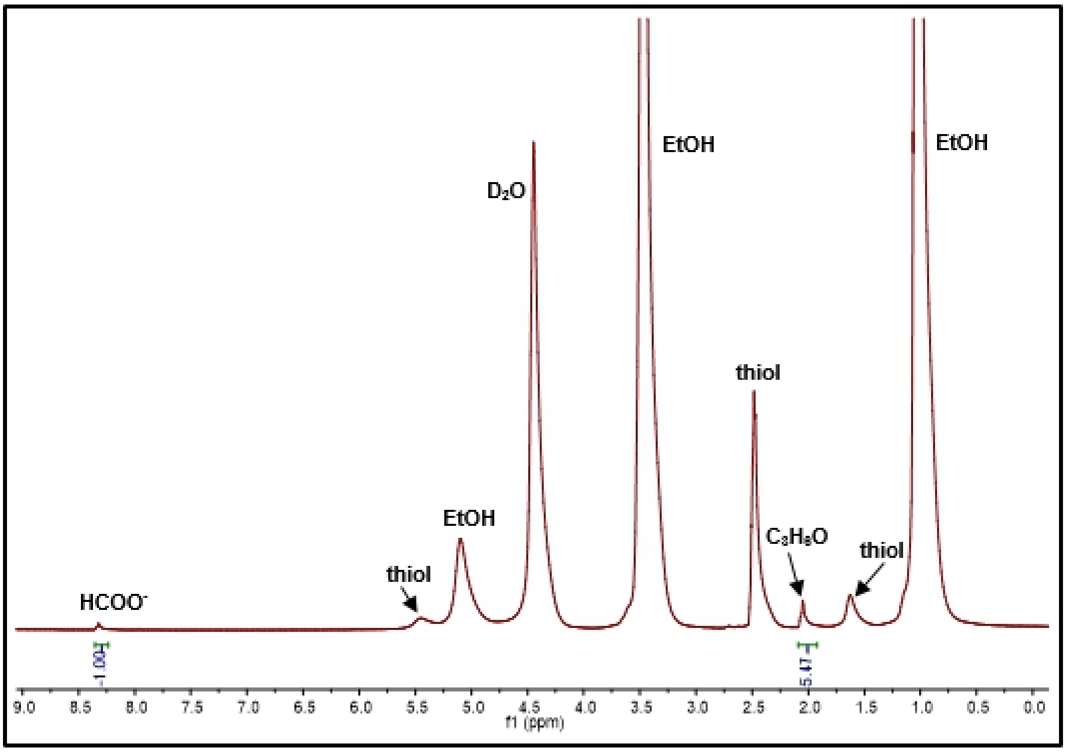

Figure 4.18: ^{1}H NMR spectra obtained when the reaction was carried out in the presence of 2 mercapto-ethanol**.**

4.13 Leaching, Heterogeneity, and Recyclability Studies

Next, to investigate whether Pd^{II} in **Pd@Mg.JMS-1a** and **Pd@Mn.JMS-2a** was working in a heterogeneous manner, the supernatants from the catalysis reaction mixture were reused for catalysis under optimised conditions. No additional formate was detected which approved the heterogeneous nature of the catalytic systems. The ICP-OES analysis of the filtrate from the reactor showed negligible metal leaching (~ 0.0003 % Pd)

To determine the reusability of the catalysts, they were isolated after the reaction by simple filtration followed by washing several times with ethanol and then vacuum dried. The catalysts were recycled and reused for four consecutive cycles (Figure 4.19).

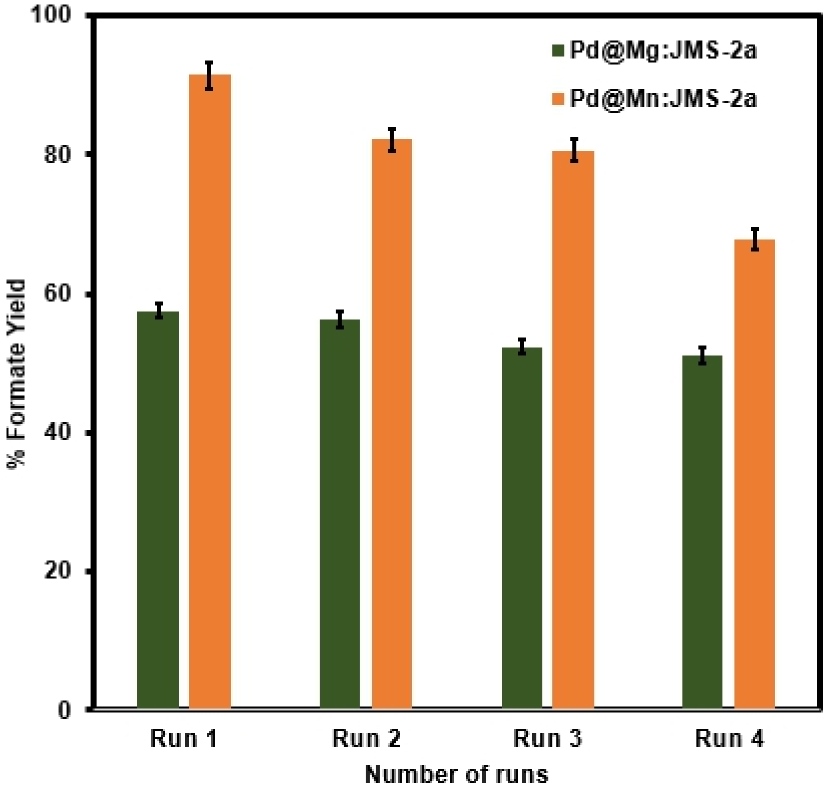

Figure 4.19: Recyclability studies for compound **Pd@Mg.JMS-1a** and **Pd@Mn.JMS-2a**.

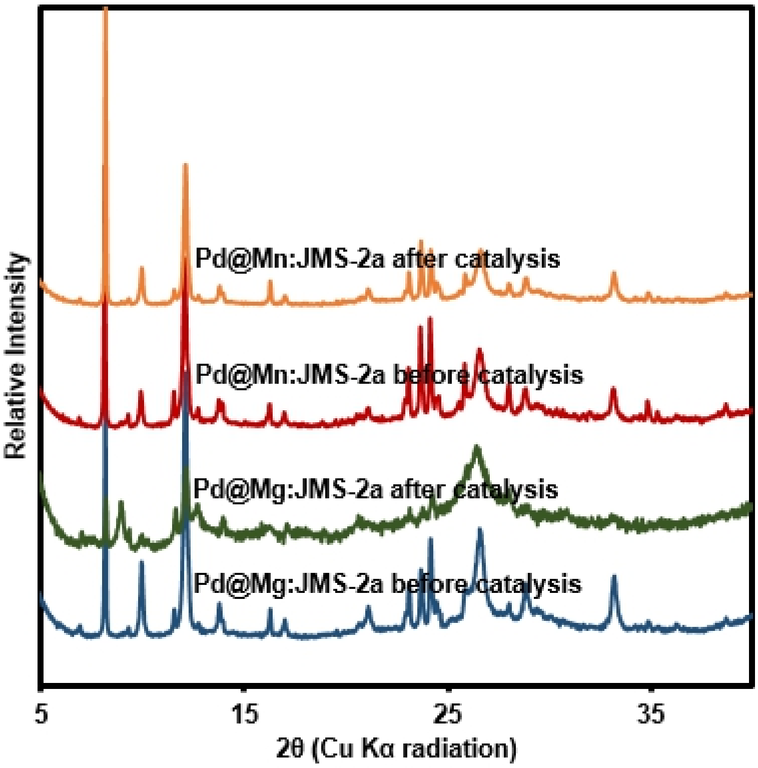

Figure 4.20: PXRD studies of the catalysts before and after catalysis.

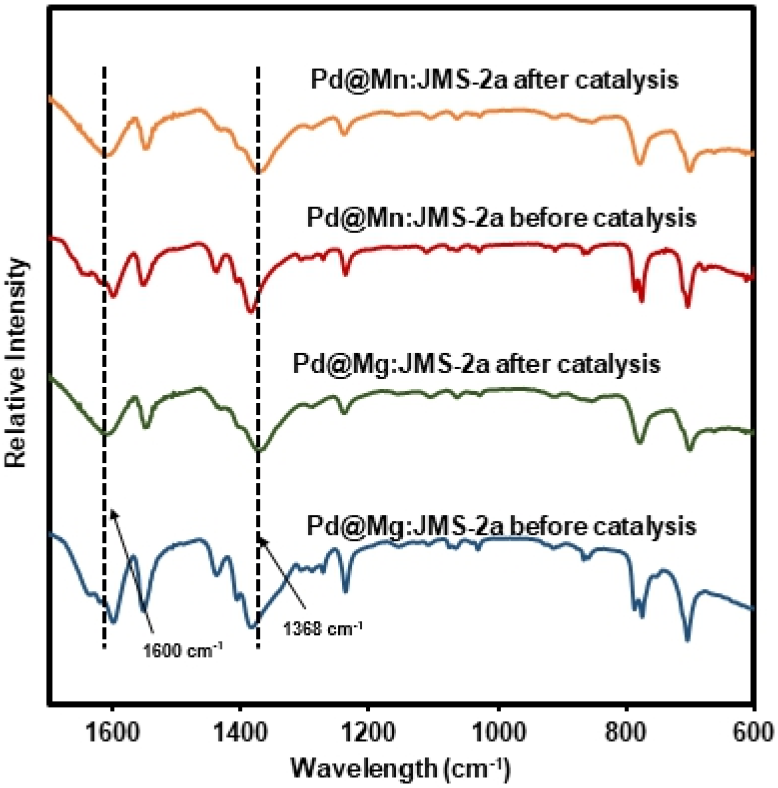

Figure 4.21: FTIR of **Pd@Mg: JMS-2a** and **Pd@Mn: JMS-2a** before and after catalysis.

Remarkably PXRD pattern of recycled catalysts shown in Figure 4.20 matches well with that of the parent compounds suggesting retention of the original framework structure, although peak broadening is observed for **Pd@Mg: JMS-2a.** In addition to the lower void volume estimated using PLATON, the change in the diffraction pattern of **Pd@Mg: JMS-2a** may have resulted in its lower catalytic activity relative to its counterpart **Pd@Mn: JMS-2a**. FTIR studies illustrated in Figure 4.21 indicate that the binding mode of the carboxylate moiety to the metal centre is retained in both MOFs after catalysis.

Scanning Electron Microscopy (SEM) illustrated in Figure 4.22 and 4.23 revealed that the surface morphology of both MOFs is not affected during catalysis. EDX elemental mapping of the recovered **Pd@: JMS-2a** and **Pd@Mg: JMS-2a** presented in Figure 4.24 and 4.25 infers a consistent and even distribution of Pd atoms throughout the MOFs.

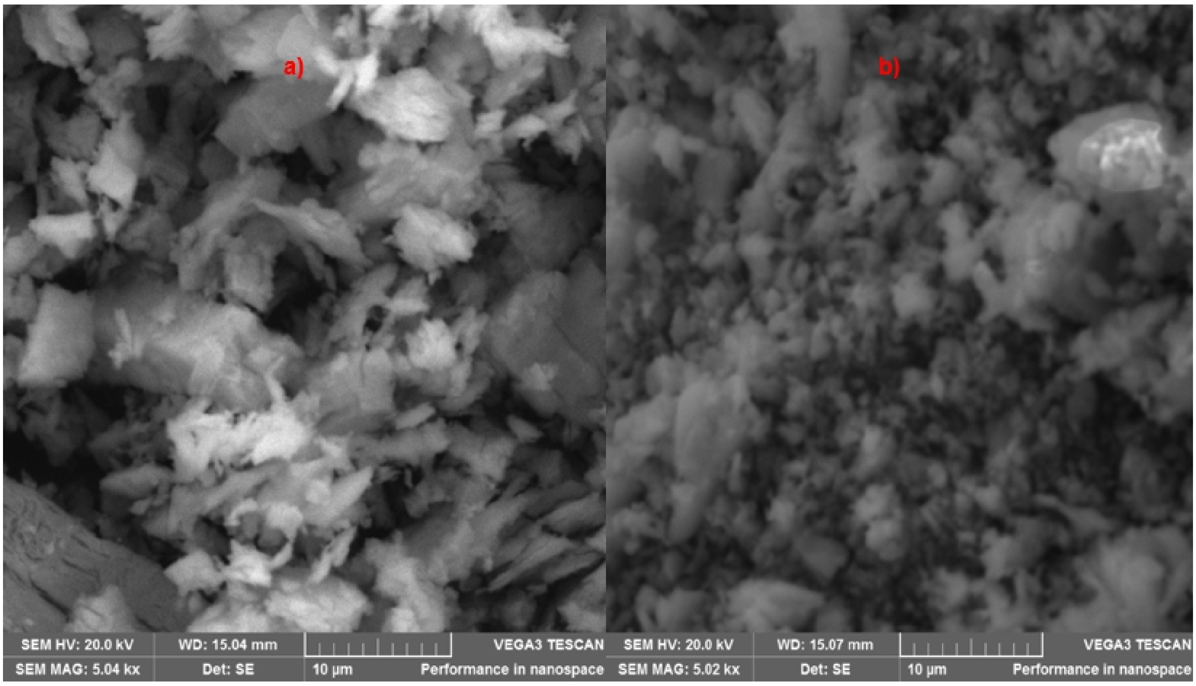

Figure 4.22: SEM images of **Pd@Mn: JMS-2a** a) before and b) after catalysis.

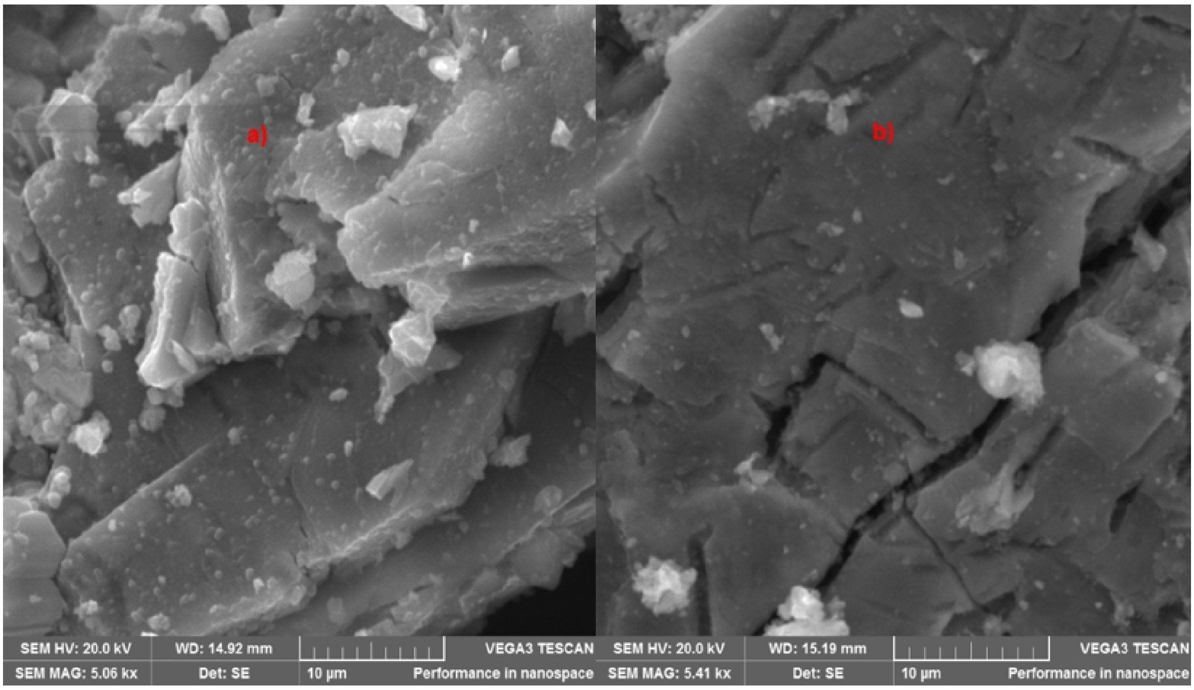

Figure 4.23: SEM images of **Pd@Mg: JMS-2a** a) before and b) after catalysis.

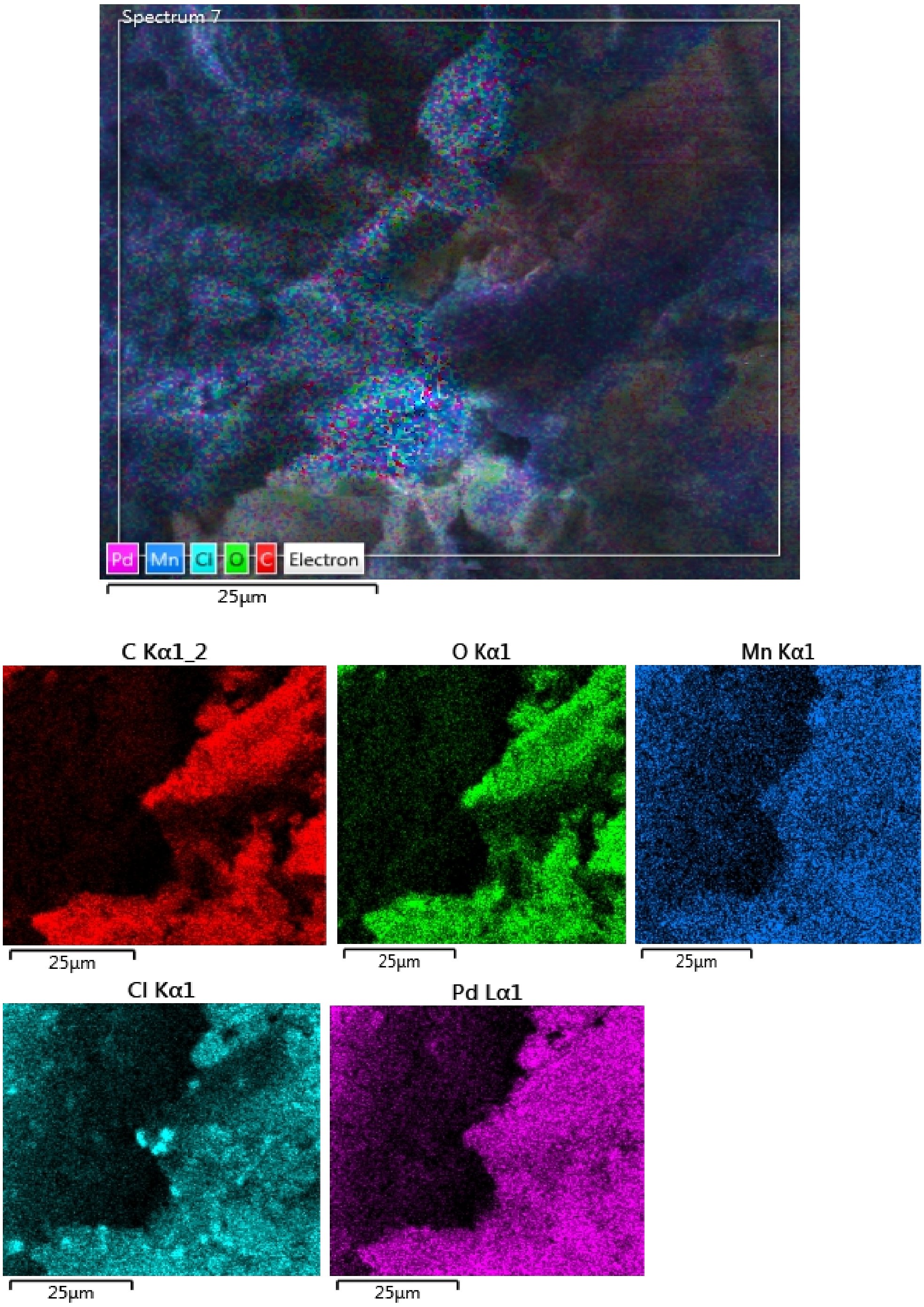

Figure 4.24: EDX elemental mapping images of **Pd@Mn: JMS-2a** after catalysis.

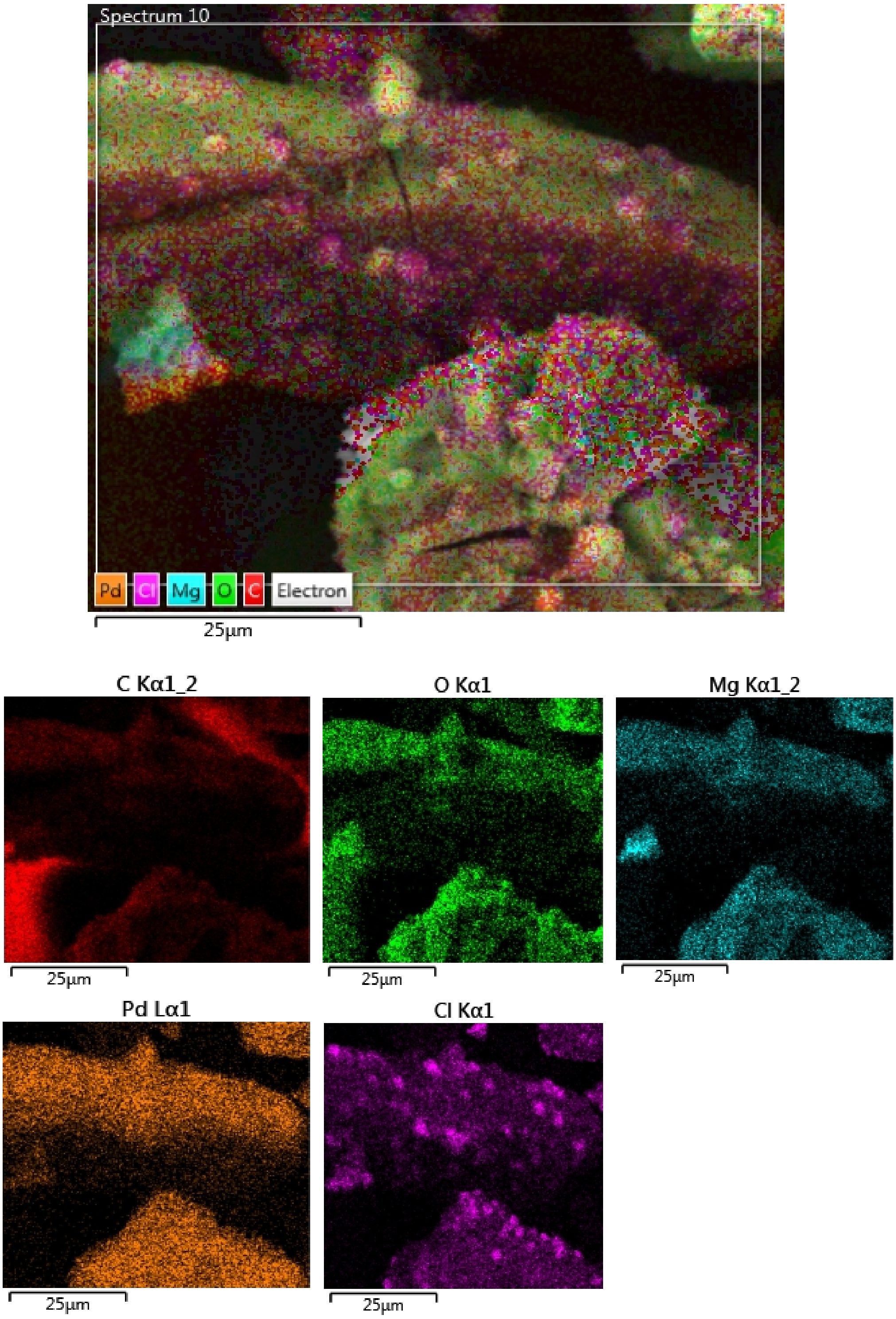

Figure 4.25: EDX elemental mapping images of **Pd@Mg: JMS-2a** after catalysis.

High-Resolution Transmission Electron Microscopy (HR-TEM) images were collected to check for the formation of Pd(0) during catalysis. As illustrated in Figure

4.26, the HR-TEM images of **Pd@Mg: JMS-2a** do not show the significant formation of nanoparticles after catalysis, this may also explain the insignificant drop (6%) in the catalytic activity of this system as presented in Figure 4.19. Contrary to **Pd@Mg: JMS-2a**, **Pd@Mn: JMS-2a** shows the significant formation of nanoparticles which are agglomerated after catalysis. This observation is consistent with a 24 % drop in catalytic activity over the four cycles.

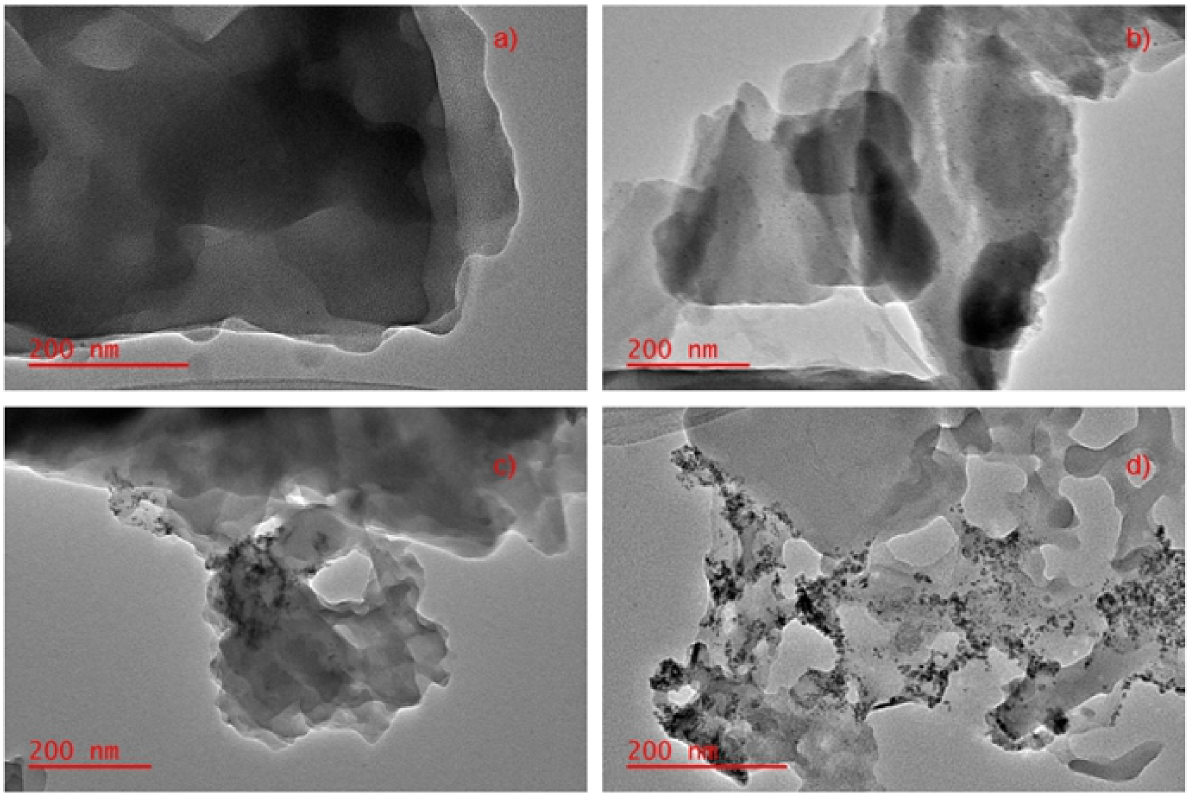

Figure 4.26: HR-TEM images of a) **Pd@Mg: JMS-2a** before catalysis, b) **Pd@Mg: JMS-2a** after catalysis, c) **Pd@Mn: JMS-2a** before catalysis and d) **Pd@Mn: JMS-2a** after catalysis.

The X-ray photoelectron spectroscopy (XPS) measurements of **Pd@Mg: JMS-2a** presented in Figure 4.27 revealed the $3d^{5/2}$ and $3d^{3/2}$ peaks of Pd^{II} species that appear at binding energies of 338.41 and 343.6 eV, respectively, which confirmed the +2 oxidation state of Pd. After catalysis, the XPS spectra of **Pd@Mg: JMS-2a** showed an additional peak at 335.31 eV at 0.96% concentration suggesting negligible formation of Pd(0) nanoparticles.

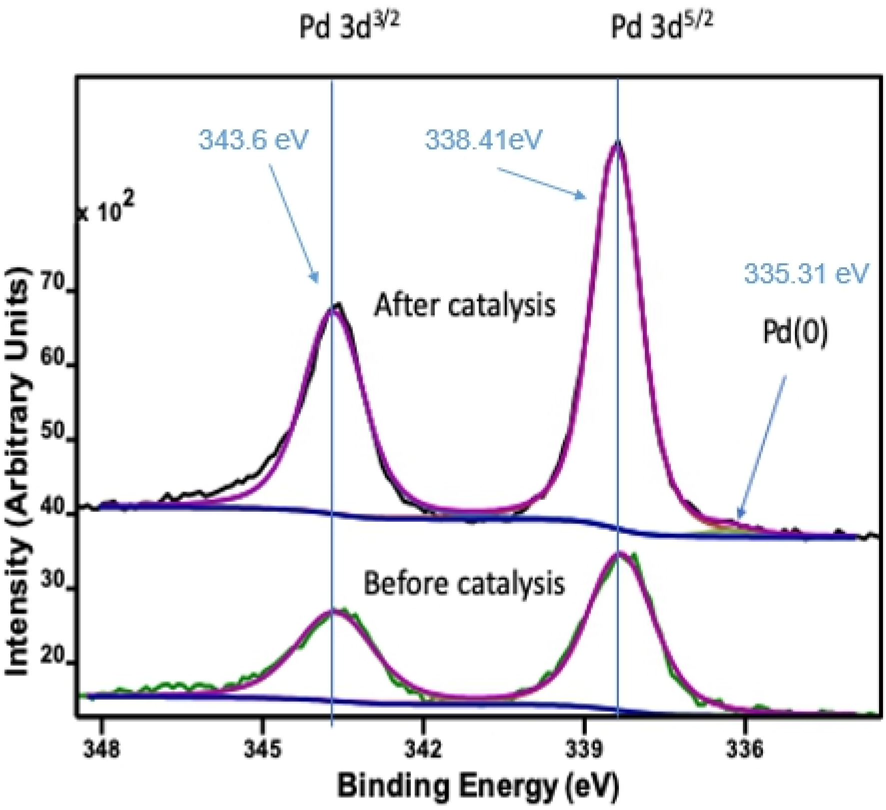

Figure 4.27: XPS spectra of Pd@Mg: JMS-2a before and after the fourth cycle of catalysis.

A mercury drop test was conducted using the homogeneous counterpart **C1** as a model to evaluate the extent to which palladium nanoparticles formed during catalysis are involved in the catalytic reaction. The ^{1}H NMR spectra for the results is presented in Figure 4.28. Hg(0) has been known for quite some time to bind to metal surfaces resulting in poisoning catalytic reactivity for metals in their zero oxidation state.[20] It is not anticipated that Hg(0) will poison metals bound to protective ligands or in higher oxidation states.[21, 22] Thus, the Hg(0), was used to determine if "naked" Pd(0) species were involved in the catalytic cycle. As shown in Table 4.3, entry 14*, in the presence of Hg(0), the yield of formate dropped from 37.5 to 29.6 %. This is an indication that both nanoparticles and molecular catalysts, which have been referred to as “cocktail” of catalysts[23–25] are responsible for the catalytic activity. The added Hg(0) scavenges the Pd(0) through amalgamation or adsorption to the active species thereby inhibiting their catalytic action, whilst residual molecular Pd continue to catalyse the reaction, albeit to a lesser extent as shown by the reduced yield. Several studies have demonstrated that the formation of Pd(0) is a common problem in the applicability of Pd based catalysts in many organic reactions especially in the presence of a strong base at elevated temperatures.[19, 24, 26]

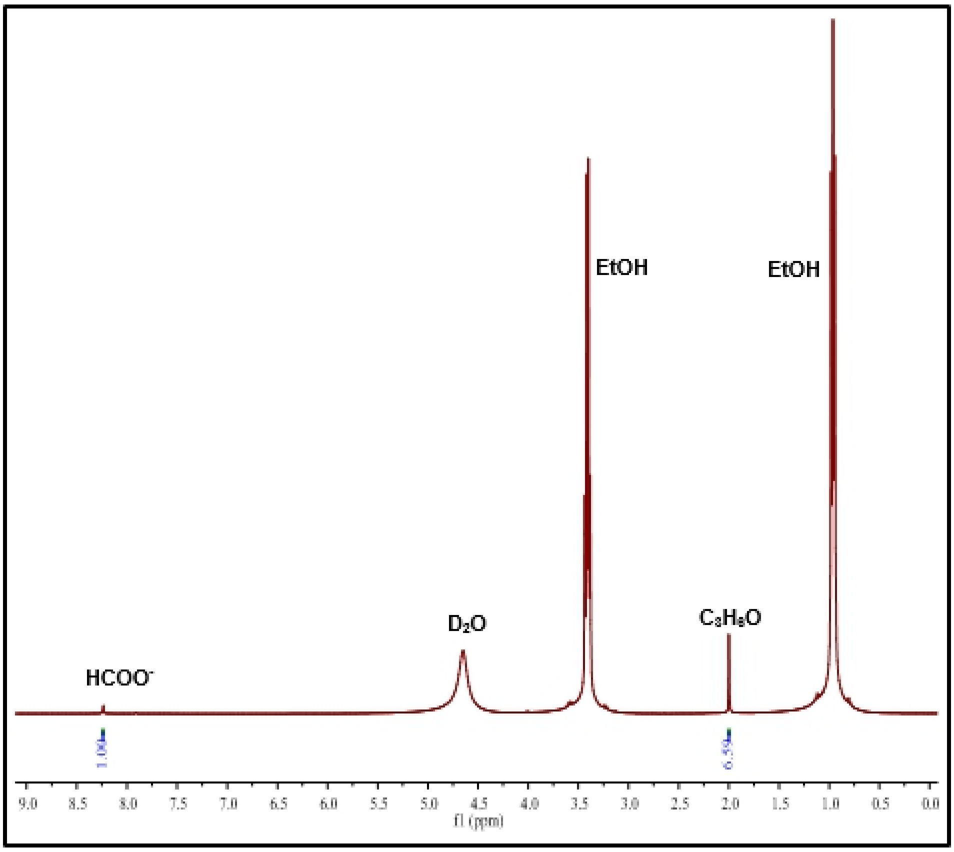

Figure 4.28: Mercury drop test for the hydrogenation of CO_2 to formate.

4.14 Reaction Kinetics

The formate formation follows a pseudo first order kinetics (the rate of reaction is based on the conversion of KOH to HCOOK). Accordingly, the rate of CO_2 conversion is expressed as

$-r[CO_2] = -d[CO_2]/dt = k[CO_2] = d[formate]/dt$ ----------------------------- equation (1)

k represent the rate constant of KOH conversion to HCOOH,

According to the Arrhenius equation,

$\ln k = -(Ea/RT) + \ln A$ -------------------------------- equation (2)

Substituting (1) in (2), we get,

$-\ln (1-x) = kt + C$ -------------------------------- equation (3)

Where KOH is expressed in terms of x, t is the reaction time and C is a constant. The linear relationship of the plot of -ln(1-x) versus time, t, confirms the assumption of pseudo-first-order reaction kinetics for KOH to HCOOK. The rate constant k, at different temperatures, is obtained from the plot in Figure 4.29. Kinetic studies reveal that **Pd@Mn: JMS-2a** has high rate constants within a temperature range of 70 to 100 °C as compared to **Pd@Mg: JMS-2a**. This may explain why the yield of formate in **Pd@Mn: JMS-2a** is higher than that obtained use the **Pd@Mg: JMS-2a** MOF.

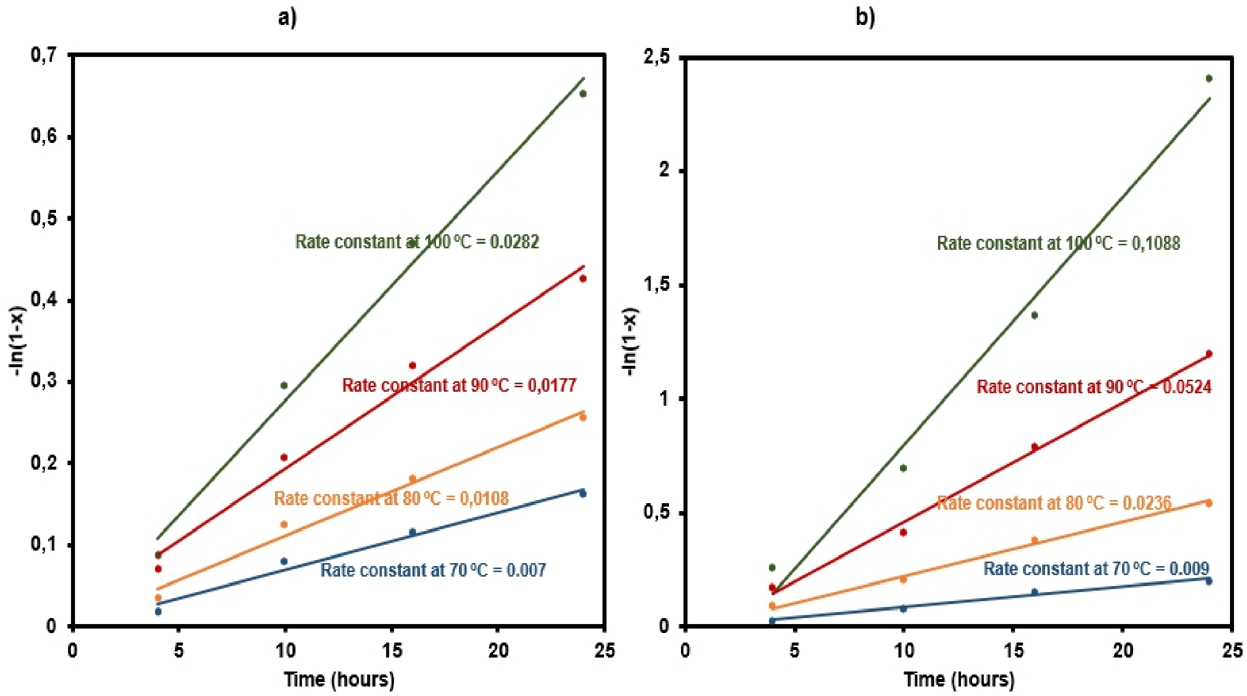

Figure 4.29: Plots of -ln(1-x*) versus* time, t**,** for a) **Pd@Mg:JMS-2a** and b) **Pd@Mn:JMS-2a**.

4.15 Reaction Mechanism

Mechanistic studies using high-pressure NMR tubes were precluded by the insolubility of the complex, **C1**, in several NMR solvents. Herein, we propose the mechanistic pathway for the hydrogenation of CO_2 by **Pd@Mg: JMS-2a** and **Pd@Mn: JMS-2a** based on literature reports for related heterogeneous systems.[7,12,17,27]

Scheme 4.2 illustrates the proposed mechanism for the hydrogenation of CO_2 to formate at the Pd^{II} site. The metal centre activates the reactants H_2 and CO_2, however, because of the lower reactivity of CO_2, H_2 gets activated first to form Pd-dihydride intermediate. Elimination of HCl from the Pd-dihydride complex gives the active species Pd-hydride complex. The insertion of CO_2 *via* associative addition into the Pd-hydride complex generates the formate complex that readily dissociates the formate.

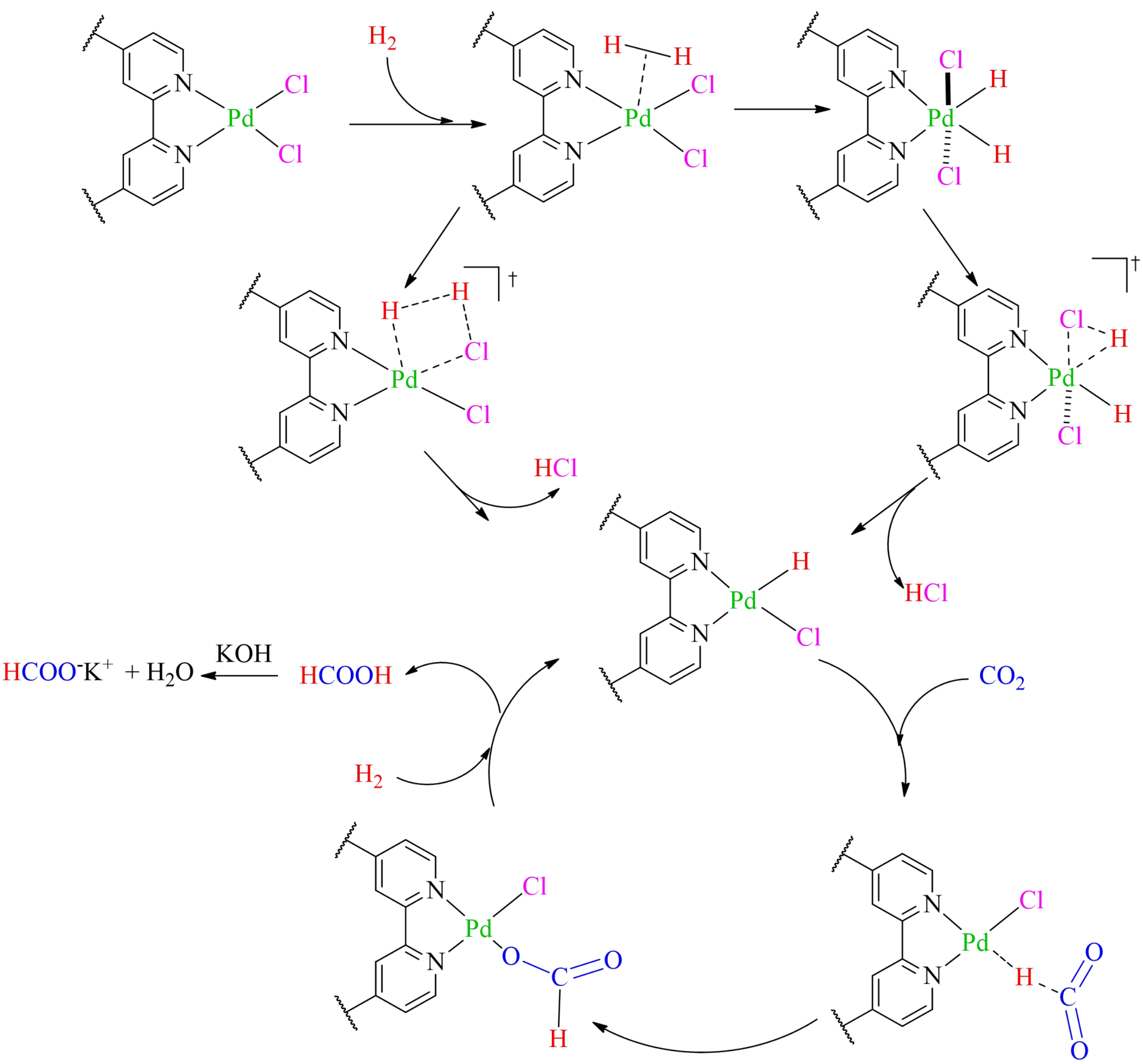

Scheme 4.2: The plausible mechanism for the hydrogenation of CO_2 to formate at the Pd^{II} site.

4.16 Summary

In summary, two novel isostructural 2D Pd containing MOF catalysts, **Pd@Mg: JMS-2** and **Pd@Mn: JMS-2**, with molecular formula $[MgPdCl_2(bpdc)(DMF)_2]_n$ and $[MnPdCl_2(bpdc)(DMF)_2]_n$) were prepared for the hydrogenation of CO_2 to formate. The design strategy involved functionalisation of the bipyridyl dicarboxylate linker with Pd before MOF synthesis. The MOFs crystallise in the monoclinic crystal system, space group C2/c. PXRD studies of the activated MOFs revealed that **Pd@Mg: JMS-2a** is poisoned by water whilst **Pd@Mn: JMS-2a** is stable in all the solvents and bases normally used for CO_2 hydrogenation. Incorporation of palladium into the MOFs has been reported without conclusive single-crystal X-ray structure elucidation, except for the one reported by Wade and co-workers, where the structure was elucidated from synchrotron powder X-ray diffraction data. To the best of my knowledge, this work represents the first example of this type of catalyst being employed in CO_2 hydrogenation. The majority of work reported in the literature on Pd^{II} anchored on MOFs mainly focuses on CO_2 oxidation.

The MOFs demonstrated remarkable catalytic activity in basic media (formate yield of 48 % (2.40 mmol formate) and 91.5 % (4.57 mmol formate)) for **Pd@Mg: JMS-2a** and **Pd@Mn: JMS-2a** in 24 hours respectively. The performance of the catalysts is very much comparable with what is in literature. Reaction conditions employed in this work are milder than some of the previously reported heterogeneous systems for CO_2 hydrogenation to formate. Thiol poisoning studies revealed that most of the active species are within the pores rather than being bound to the surface. From HR-TEM studies we observed that for **Pd@Mn: JMS-2a**, there is the significant formation of nanoparticles which are agglomerated after catalysis, resulting in a significant drop in catalytic activity over the four cycles. A mercury drop test conducted using the homogeneous counterpart C1 as a model indicates that both nanoparticles and molecular catalysts are responsible for the catalytic activity, though the nanoparticles' contribution is minimal. Contrary to **Pd@Mn: JMS-2a**, **Pd@Mg: JMS-2a** does not show the significant formation of nanoparticles after catalysis. The results demonstrate that the catalytic activity of homogeneous systems can be improved by incorporating them in MOFs as organic linkers bearing catalytic sites.

4.17 REFERENCES

1 Anderson, G.K., Lin, M., Sen, A., and Gretz, E., Inorganic Synthesis, John Wiley and Sons, Inc, Hobeken, NJ, USA, 2008, 60-63.

2 A. L. Spek, *Acta Crystallographica. Section D, Biological crystallography*, 2009, **65**, 148–55.

3 C. F. Macrae, I. J. Bruno, J. A. Chisholm, P. R. Edgington, P. McCabe, E. Pidcock, L. Rodriguez-Monge, R. Taylor, J. Van De Streek and P. A. Wood, *Journal of Applied Crystallography*, 2008, **41**, 466–470.

4 S. M. Lu, Z. Wang, J. Li, J. Xiao and C. Li, *Green Chemistry*, 2016, **18**, 4553–4558.

5 S. Yuan, L. Feng, K. Wang, J. Pang, M. Bosch, C. Lollar, Y. Sun, J. Qin, X. Yang, P. Zhang, Q. Wang, L. Zou, Y. Zhang, L. Zhang, Y. Fang, J. Li and H. C. Zhou, *Advanced Materials*, 2018, **30**, 1–35.

6 H. Kobayashi, J. M. Taylor, Y. Mitsuka, N. Ogiwara, T. Yamamoto, T. Toriyama, S. Matsumura and H. Kitagawa, *Chemical Science*, 2019, **10**, 3289–3294.

7 P. Patel, S. Nandi, M. S. Maru, R. I. Kureshy and N.-U. H. Khan, *Journal of CO_2 Utilization*, 2018, **25**, 310–314.

8 Z. Li, T. M. Rayder, L. Luo, J. A. Byers and C. Tsung, *Journal of the American Chemical Society*, 2018, **140**, 8082–8085.

9 X. M. Lin, T. T. Li, Y. W. Wang, L. Zhang and C. Y. Su, *Chemistry - An Asian Journal*, 2012, **7**, 2796–2804.

10 Z. Liang, J. Du, L. Sun, J. Xu, Y. Mu, Y. Li, J. Yu and R. Xu, *Inorganic Chemistry*, 2013, **52**, 10720–10722.

11 D. Britt, H. Furukawa, B. Wang, T. G. Glover and O. M. Yaghi, *Proceedings of the National Academy of Sciences*, 2009, **106**, 20637–20640.

12 B. An, L. Zeng, M. Jia, Z. Li, Z. Lin, Y. Song, Y. Zhou, J. Cheng, C. Wang and W. Lin, *Journal of the American Chemical Society*, 2017, **139**, 17747–17750.

13 A. H. Chughtai, N. Ahmad, H. A. Younus, A. Laypkov and F. Verpoort, *Chemical Society Reviews*, 2015, 44, 6804–6849.

14 R. Poloni, K. Lee, R. F. Berger, B. Smit and J. B. Neaton, *Journal of Physical Chemistry Letters*, 2014, **5**, 861–865.

15 G. Gunniya Hariyanandam, D. Hyun, P. Natarajan, K. D. Jung and S. Yoon, *Catalysis Today*, 2016, **265**, 52–55.

16 G. H. Gunasekar, J. Shin, K. Jung, K. Park and S. Yoon, *ACS Catalysis*, 2018, **8**, 4346–4353.

17 M. S. Maru, S. Ram, R. S. Shukla and N. H. Khan, *Molecular Catalysis*, 2018, **446**, 23–30.

18 F. Bertini, M. Glatz, N. Gorgas, B. Stöger, M. Peruzzini, L. F. Veiros, K. Kirchner and L. Gonsalvi, *Chemical Science*, 2017, **8**, 5024–5029.

19 B. Gui, K. K. Yee, Y. L. Wong, S. M. Yiu, M. Zeller, C. Wang and Z. Xu, *Chemical Communications*, 2015, **51**, 6917–6920.

20 C. S. Consorti, F. R. Flores and J. Dupont, *Journal of the American Chemical Society*, 2005, **127**, 12054–12065.

21 O. N. Gorunova, I. M. Novitskiy, Y. K. Grishin, I. P. Gloriozov, V. A. Roznyatovsky, V. N. Khrustalev, K. A. Kochetkov and V. V. Dunina, *Organometallics*, 2018, **37**, 2842–2858.

22 K. Yu, W. Sommer, J. M. Richardson, M. Weck and C. W. Jones, *Advanced Synthesis and Catalysis*, 2005, **347**, 161–171.

23 D. B. Eremin and V. P. Ananikov, *Coordination Chemistry Reviews*, 2017, **346**, 2–19.

24 A. S. Kashin and V. P. Ananikov, *Journal of Organic Chemistry*, 2013, **78**, 11117–11125.

25 G. Amenuvor, B. C. E. Makhubela and J. Darkwa, *ACS Sustainable Chemistry and Engineering*, 2016, **4**, 6010–6018.

26 H. Baier, A. Kelling, U. Schilde and H. J. Holdt, *Zeitschrift fur Anorganische und Allgemeine Chemie*, 2016, **642**, 140–147.

27 H. Song, N. Zhang, C. Zhong, Z. Liu, M. Xiao and H. Gai, *New Journal of Chemistry*, 2017, **41**, 9170–9177.

CHAPTER 5

Synthesis of Cd, Zn and Mg-based Metal-Organic Frameworks for CO_2 and H_2 adsorption

In this chapter, three novel MOFs **JMS-3**, **JMS-4** and **JMS-5** having the molecular formula, $[Cd_2(bpdc)_2(DMF)_2\cdot 2DMF]_n$, $[Zn(bpdc)(DMF)\cdot DMF]_n$ and $[Mg_1(bpdc)(DMF)_2]_n$ respectively were successfully synthesised using 2,2'-bipyridine-4,4'-dicarboxylate (bpdc) linker, $Cd(NO_3)_2\cdot 4H_2O$, $Zn(NO_3)_2\cdot 6H_2O$ and $Mg(NO_3)_2\cdot 6H_2O$ as starting materials. The compounds were characterised using X-ray diffraction studies (SCXRD and PXRD), Thermogravimetric analysis (TGA) and Fourier Transform Infrared spectroscopy (FTIR). The CO_2 and H_2 storage capacities of the dissolvated phases of **JMS-3a** and **JMS-4a** were evaluated.

5.1 Synthesis of JMS-3, JMS-4 and JMS-5

Scheme 5.1 gives the experimental conditions that led to the isolation of **JMS-3**, **JMS-4** and **JMS-5**. About 25 mg (0.098 mmol) 2,2’-bipyridine-4,4’-dicarboxylic acid was pre-dissolved in DMF (10 mL) and $Cd(NO_3)_2\cdot 4H_2O$ (117mg, 0.38 mmol) was added. The reaction mixture was stirred for 10 minutes at room temperature and sealed in a Teflon lined autoclave. The solution was then heated at 115 ˚C for 8 hours to yield colourless block-shaped crystals of **JMS-3** suitable for single-crystal X-ray diffraction data collection. The reaction of 2,2'-bipyridine-4,4'-dicarboxylic acid (27 mg, 0.105 mmol) in DMF (10 mL) with $Zn(NO_3)_2\cdot 6H_2O$ (112 mg, 0.377 mmol) afforded **JMS-4**. A reaction mixture of $Mg(NO_3)_2\cdot 6H_2O$ (104 mg, 0.405 mmol), 2,2’-bipyridine-4,4’-dicarboxylic acid (25 mg, 0.098 mmol) and DMF (8 mL) gave diamond-shaped crystals of **JMS-5**.

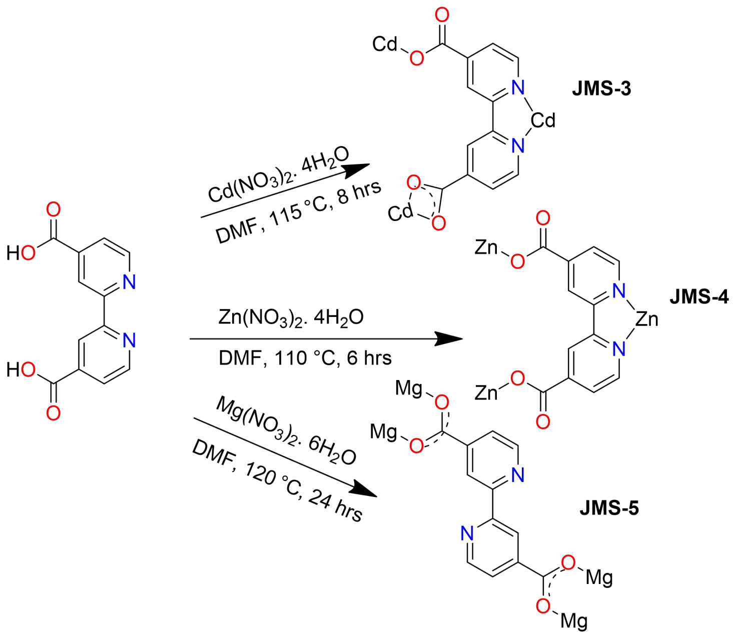

Scheme 5.1: Synthesis of **JMS-3**, **JMS-4** and **JMS-5** illustrating the binding modes of the carboxylate moiety in the three MOFs

5.2 Single Crystal X-ray Diffraction

Single crystal X-ray diffraction data collections of **JMS-3**, **JMS-4** and **JMS-5** were performed on a Bruker KAPPA APEX II DUO diffractometer equipped with graphite monochromated Mo Kα radiation (λ = 0.71073 Å). Unit cell refinement and data reduction were performed using the SAINT program. Data were corrected for Lorentz polarisation and absorption due to the variation in the path length through the detector faceplate. The structures of the two compounds were solved by direct methods (program SHELXS)[1] and refined anisotropically on F^2 full-matrix least-squares with SHELXL[1] within the X-SEED[2] interface. The crystal data for **JMS-3**, **JMS-4** and **JMS-5** is given in Table 5.1. Anisotropic thermal parameters were applied to all non-hydrogen atoms. The hydrogen atoms were placed in idealised positions using the riding model and assigned temperature factors relative to the parent atom. The structures were deposited at the Cambridge Crystallographic Data Centre and allocated the number CCDC numbers 2010232, 2010231 and 1851045 for **JMS-3**, **JMS-4** and **JMS-5** respectively.

5.3 Structural Description of JMS-3

Single crystal X-ray diffraction revealed that J**MS-3** crystallises in the monoclinic crystal system and space group $P2_1/c$. The asymmetric unit of **JMS-3** consists of two crystallographic independent Cd^{II} centres, two deprotonated bpdc linkers, two coordinated DMF molecules and two uncoordinated DMFs. The crystallographic data for **JMS-3** is given in Table 5.1. As illustrated in Figure 5.1, each Cd^{II} centre is coordinated to three bpdc linkers, one in a bidentate chelating mode and the other in a monodentate bridging mode. Two nitrogen atoms of the third linker are coordinated to Cd^{II} in a bidentate chelating mode. A DMF molecule is also bound to each of the Cd centres in a monodentate fashion. The Cd–N bond length around Cd^{II} ranges from 2.318(2) to 2.366 (3) while Cd-O ranges from 2.239 (2) to 2.588(2) Å (see Table 5.2).The coordination geometry around the metal centres, concerning bond length, are different, resulting in two crystallographically independent metal centres. The Cd^{II} metal centre assumes a distorted octahedral geometry with bond angles ranging from 54.19(8) to 152.57(9) and 84.89(8) to 154.73(8)° for Cd1 and Cd2 respectively.

Table 5.1: Crystal data and structure refinement for **JMS-3**, **JMS-4** and **JMS-5**

	JMS-3	**JMS-4**	**JMS-5**
Empirical formula	$C_{36}H_{40}N_8Cd_2O_{12}$	$C_{18}H_{20}N_4Zn_1O_6$	$C_{18}H_{20}N_4Mg_1O_6$
Formula weight (gmol^{-1})	1001.58	453.75	412.69
Temperature/K	293(2)	150(2)	150(2)
Crystal system	monoclinic	monoclinic	monoclinic
Space group	P2(1)/c	P2(1)/n	P2(1)/n
a/Å	18.4447(13)	9.3824(6)	9.0631(5)
b/Å	15.0567(11)	14.7232(9)	8.8240(5)
c/Å	16.0209(11)	14.7089(9)	23.8835(13)
α/°	90	90	90
β/°	113.878(1)	101.203(2)	93.859(2)
γ/°	90	90	90
Volume/Å^3	4068.4(5)	1993.2(2)	1905.70(18)
Z	4	4	4
Calculated density (g/cm^3)	1.635	1.5119	1.4082
μ(Mo-Kα) /mm^{-1}	1.12	1.27	0.14
F(000)	2016	936	864
Crystal size/mm^3	0.38 × 0.36 × 0.21	0.26 × 0.20 × 0.17	0.641× 0.419 × 0.21
Radiation	MoKα (λ= 0.71073)	MoKα (λ = 0.71073)	MoKα (λ = 0.71073)
2θ Max/°	56.82	52.94	53.07
Reflections collected	95569	54023	55684
No. unique data	10205	4105	3924
The goodness of fit on S	1.021	1.085	1.062
Final R indexes [I>=2σ (I)]	0.0638	0.0546	0.0619
Final wR$_2$ indexes [all data]	0.0829	0.1052	0.1052
Largest diff. peak/hole / e Å^{-3}	0.69/-0.57	1.15/-0.80	0.53/-0.24

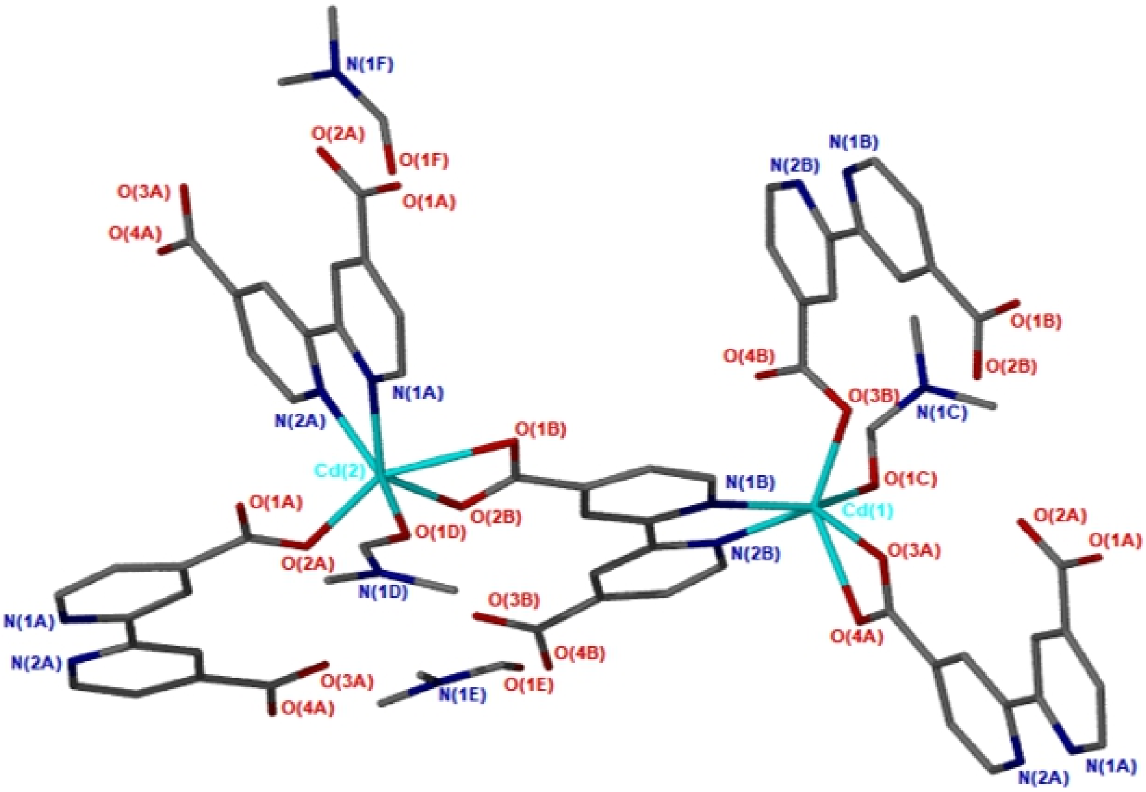

Figure 5.1: Coordination environment of Cd^{II} in **JMS-3**. Hydrogen atoms have been omitted for clarity.

Table 5.2: Bond distances around Cd^{II} in **JMS-3**.

Bond Type	**Bond Length (Å)**	**Bond Type**	**Bond Length (Å)**
Cd1-O3B	2.239(2)	Cd2-O2A	2.252(2)
Cd1-O1C	2.299(2)	Cd2-O2B	2.275(2)
Cd1-N2B	2.318(2)	Cd2-O1D	2.281(2)
Cd1-O3A	2.322(3)	Cd2-N1A	2.327(2)

Cd1-N1B	2.335(3)	Cd2-N2A	2.366(2)
Cd1-O4A	2.458(3)	Cd2-O1B	2.588(2)

The packing diagram of **JMS-3** displays 2D networks that are interdigited (Figure 5.2a). The DMF guest molecules are trapped in the rectangular channels as illustrated in Figure 5.2b. No classic hydrogen bonding occurs between DMF molecules and the framework. However, weak intermolecular and intramolecular interactions (C-H···O bonding) present are suggested to reinforce the geometry and impart stability in the MOF. Guest molecules occupy 53.8% of the unit cell, as estimated in PLATON.[3]

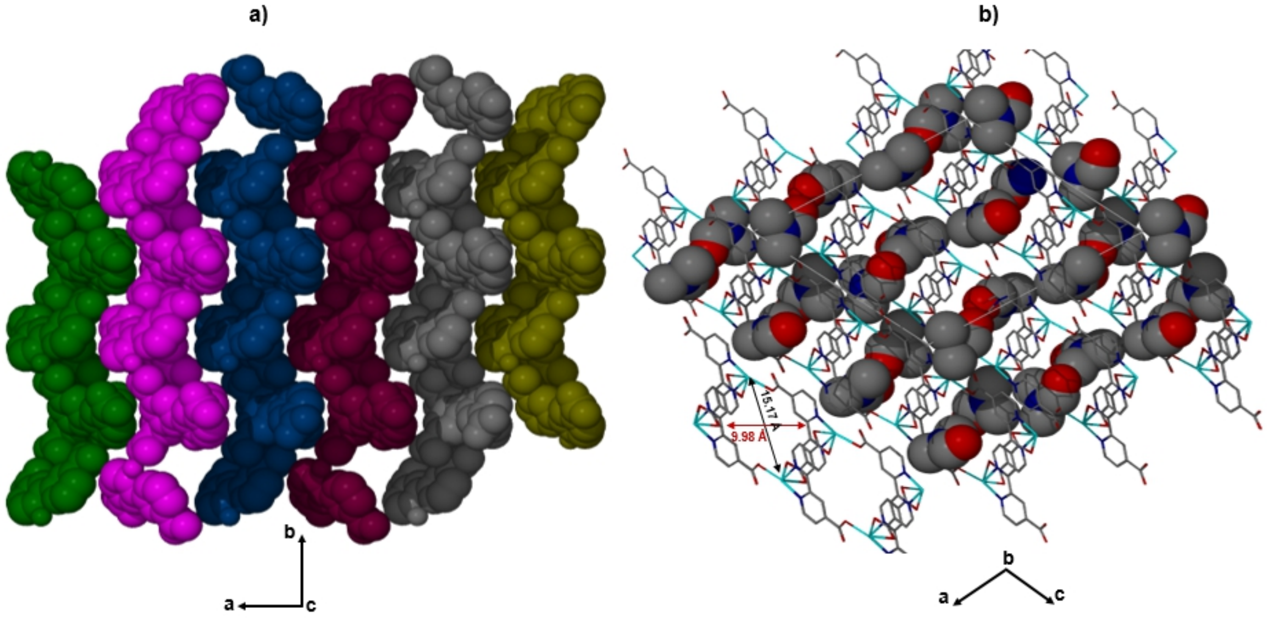

Figure 5.2: a) Solid-state structure of JMS-3 displaying interdigited channels, viewed along *c*-axis. b) The 2D network drawn in stick form and guest molecules, drawn with van der Waals radii are residing in the cavities. Hydrogen atoms have been omitted for clarity.

Thermal analysis of **JMS-3** by TGA illustrated in Figure 5.3 exhibits an initial weight loss of 28.6 % in the temperature range of 100−150 °C, which corresponds to the loss of 4 DMF molecules that were modelled in the asymmetric unit (calculated

29.2 %). The dehydrated framework is found to be stable up to 370 ˚C, suggesting high thermal stability.

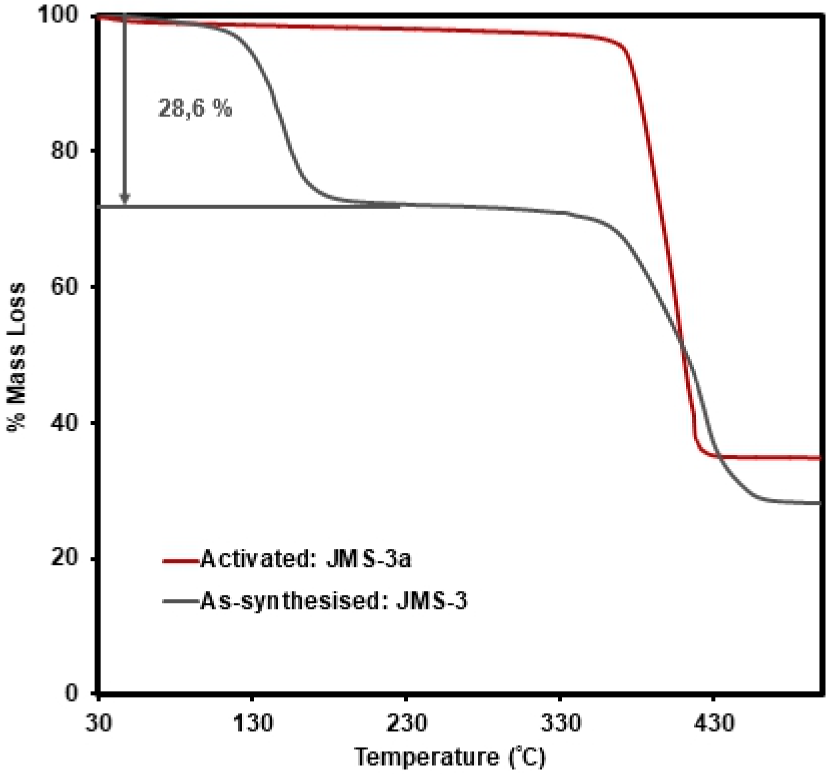

Figure 5.3: TGA traces of experimental and activated **JMS-3**.

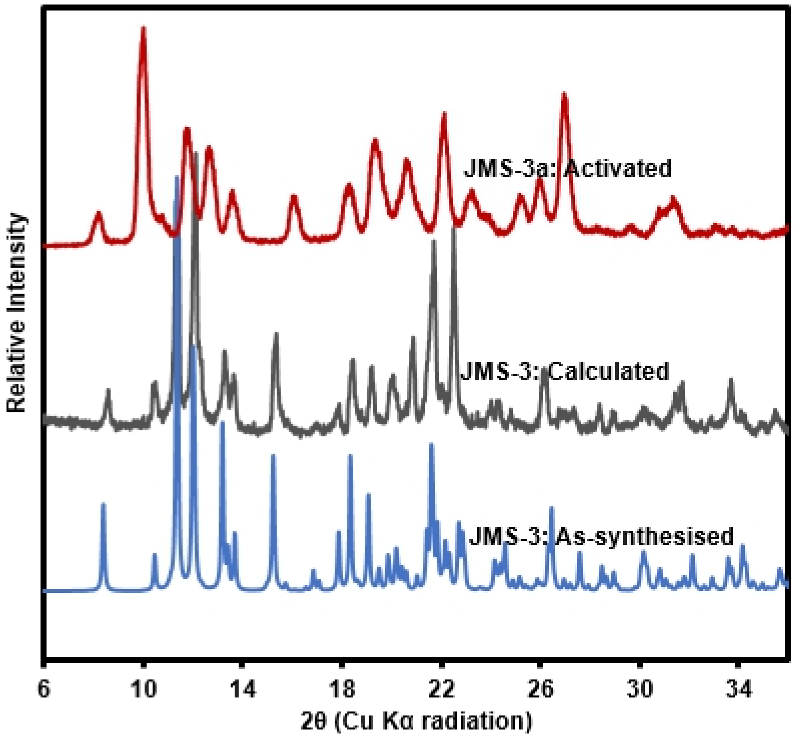

Figure 5.4: PXRD patterns of calculated, as-synthesised and activated **JMS-3**.

A comparison of the PXRD of **JMS-3** with the simulated pattern derived from the single-crystal XRD is shown in Figure 5.4. A good match between the simulated and experimentally measured patterns was found, which confirms the phase purity of the as-synthesised compound. Upon removal of the guest DMF molecules, **JMS-3** undergoes a structural transformation as evidenced by the appearance of new diffraction peaks around 10°, 16° and 27° two-theta positions. The peak at around 15 two theta position has disappeared. FTIR results in Figure 5.5 suggests that a stretching frequency at 1708 cm^{-1} (COOH) in the linker shifts to 1604 cm^{-1} in **JMS-3**, which is evidence that the carboxylate moiety is coordinated to the Cd centre. These results are consistent with single-crystal X-ray data. Successful activation of the MOF is evidenced by the disappearance of the FTIR band at 1641 cm^{-1}, which is attributed to coordinated DMF molecules. The band at 1550 cm^{-1} is attributed to the C-C of the benzene ring. The carboxylate asymmetric and symmetric carboxylate stretches were observed at 1604 and 1365 cm^{-1} respectively, and the wavelength difference was found to be 239 cm^{-1}. This position does not change after activation suggesting that the binding mode of the carboxylate moiety is retained.[4]

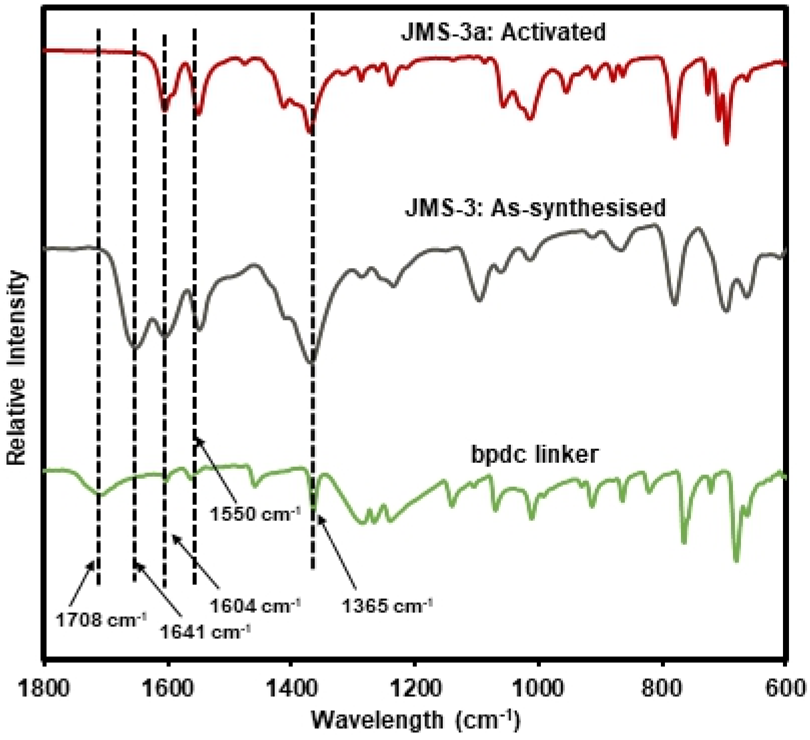

Figure 5.5: IR spectra of the linker, as synthesised and activated **JMS-3**

5.4 Topological Analysis of JMS-3

Topological analysis of **JMS-3** was performed using Systre[5] and Topos[6] computer program. Concerning Figure 5.6a, the compound was reduced to a simple net by considering each metal centre as a 4 connected node. Each cadmium centre is connected to the other cadimium centre by the linear bpdc bridges to produce a square-lattice (**sql**) topology.[7] The point symbol was established as $4_4.6_2$ and extended point symbol as $4.4.4.4.6_2.6_2$, while the vertex symbol was determined as [4.4.4.4*.*] [8,9] The packing in Figure 5.6b, is a zig-zag 2D layered network.

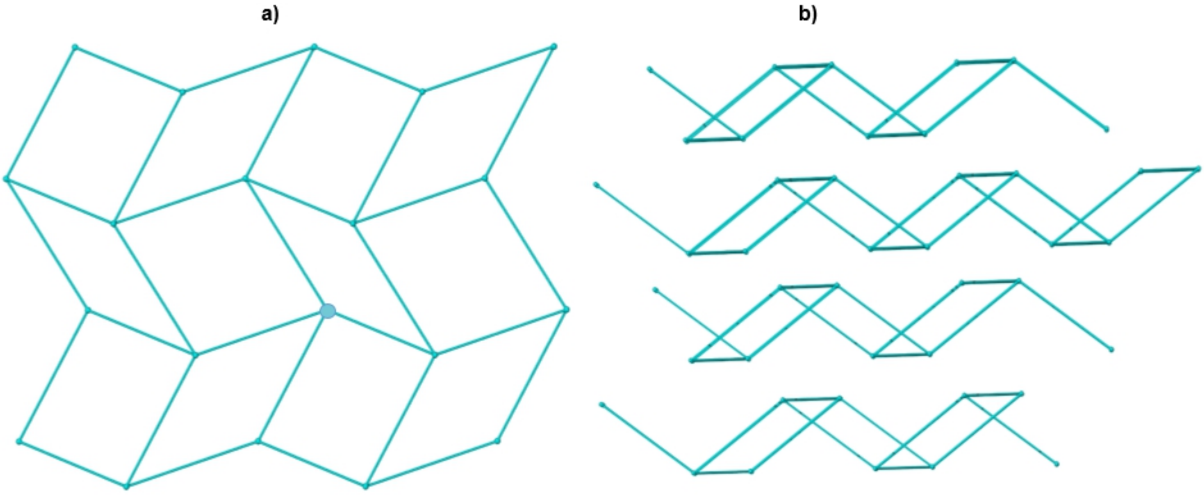

Figure 5.6: a) 4-connected 2D net of **JMS-3** and b) Zig-zag packing in **JMS-3**

5.5 Structural Description of JMS-4

JMS-4 crystallises in the monoclinic crystal system and space group $P2_1$. The asymmetric unit consists of one crystallographically independent Zn^{II} metal centre and one deprotonated bpdc linker and two DMF molecules. As illustrated in Figure 5.7, the Zn^{II} centre is coordinated to one bpdc linker through two unidentate Zn^{II}-O of the carboxylate moiety, two bipyridyl nitrogens in a chelating fashion. One DMF molecule is ligated to the Zn atom and directed into the empty channels. This gives rise to trigonal bipyramidal coordination. The Zn–N and Zn-O bond length ranges from 2.1019(2) to 2.177(3) and 1.976(2) to 2.104(2) Å respectively. These bond lengths are given in Table 5.3. The bond angles around the Zn^{II} metal centres range from 76.40(10) to 159.71(10)°.

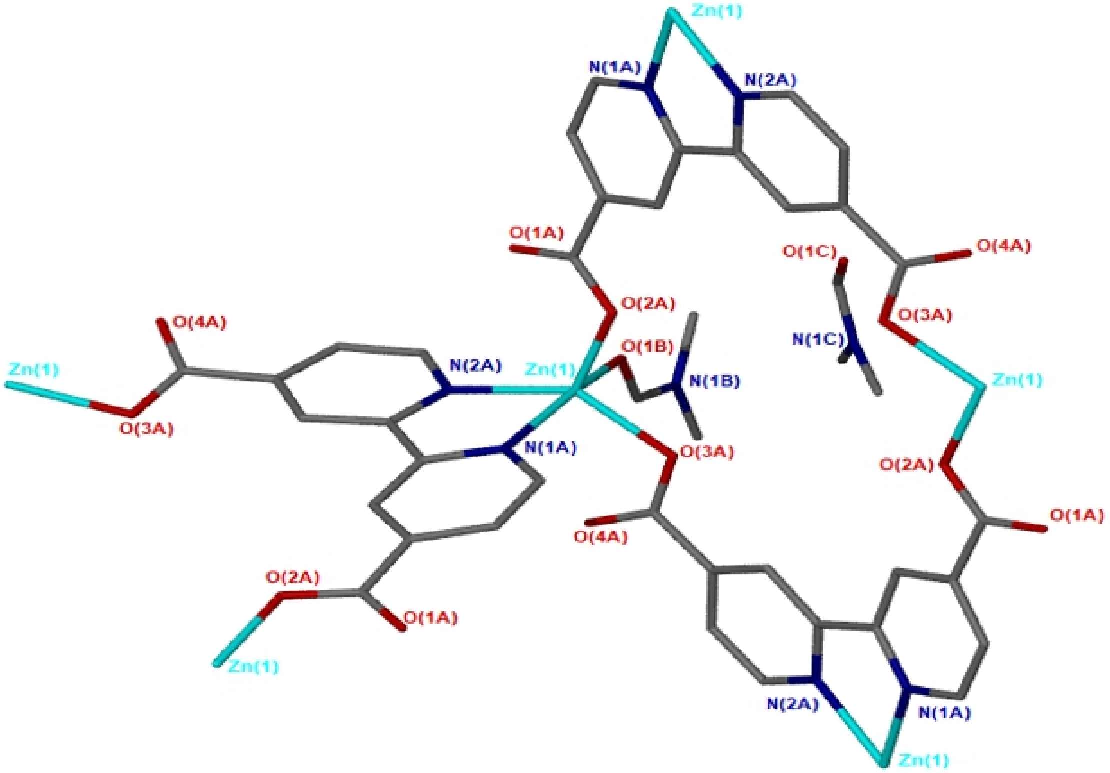

Figure 5.7: Coordination environment of Zn^{II} in **JMS-4**. Hydrogen atoms have been omitted for clarity.

Table 5.3: Bond distances around Zn^{II} in **JMS-4**.

Bond Type	Bond Length (Å)	Bond Type	Bond Length (Å)
Zn1-O2A	1.976(2)	Zn1-N2A	2.101(2)
Zn1-O3A	2.022(2)	Zn1-N1A	2.177(3)
Zn1-O1B	2.104(2)		

In the guest free packing diagram of **JMS-4**, illustrated in Figure 5.8, the 2D layers pack similarly to that of **JMS-3**. The rectangular-shaped channels (10.342 × 9.036 Å) running along *b*-axis are occupied by both coordinated and uncoordinated DMF molecules. The analysis of interactions between the guest and framework shows that there are no noticeable interactions between the two. However, the structure is stabilised by weak intermolecular hydrogen bonding between the 3D layers and π…π interactions of the aromatic rings. PLATON[3] was used to estimate that the volume occupied by DMF molecules accounts for 52.3 % of the unit cell volume.

An initial weight loss of 32.5 % observed in the TGA of **JMS-4** in Figure 5.9 corresponds to the loss of four DMF molecules per formula unit which was modelled in the structure (calculated 32.2 %). From 150 ˚C, there is a plateau up to 350 ˚C above which there is a slow decomposition of the framework. No significant weight loss occurs below 350 ˚C on the TGA curve of the activated framework, **JMS-4a**, indicating solvent molecules have been completely removed, although due to humidity, about 4 % loss was still observed on the activated sample curve.

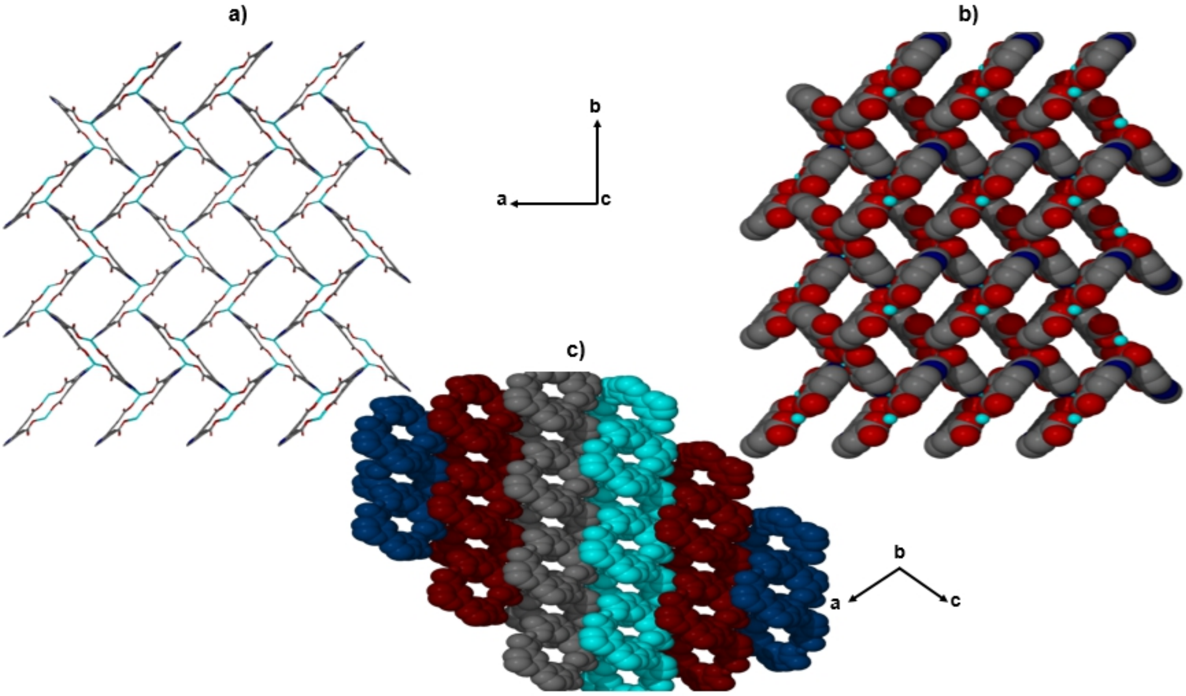

Figure 5.8. Channels of **JMS-4** a) stick form, b) space-filling viewed along the c axis and c) Packing diagram is drawn in Van der waals radii displaying the interdigited layers. Solvent molecules and hydrogen atoms have been omitted for clarity.

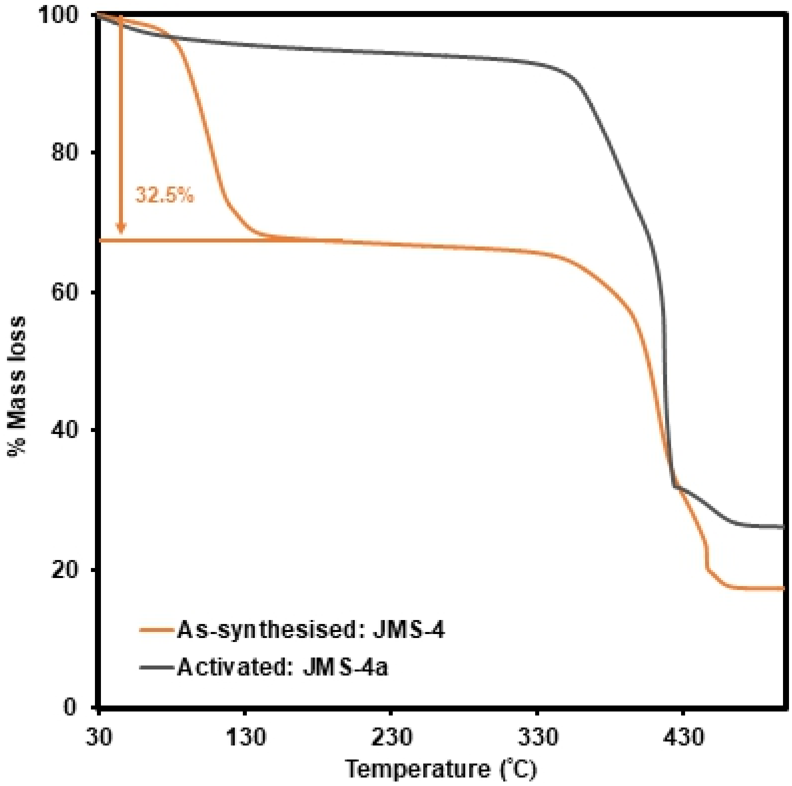

Figure 5.9: TGA traces of experimental and activated **JMS-4**.

The phase purity of the bulk of the material was confirmed by PXRD studies, as the observed pattern matches that simulated from the crystal structure (Figure 5.10). Dissolvated sample shows broadening of most diffraction peaks, accompanied by a crystalline to crystalline transformation.

The IR spectrum of as-synthesized **JMS-4** (Figure 5.11) displays a band at 1648 cm^{-1} which is assigned to carbonyl stretch of DMF molecules. This band disappears upon activation. The bands at 1590 and 1378 cm^{-1} are assigned to the asymmetric and symmetric stretches of the carboxylate group respectively, with a magnitude of separation of 212 cm^{-1}. Upon activation, the afore-mentioned band position did not change suggesting that the binding mode of the carboxylate is not altered.[4]

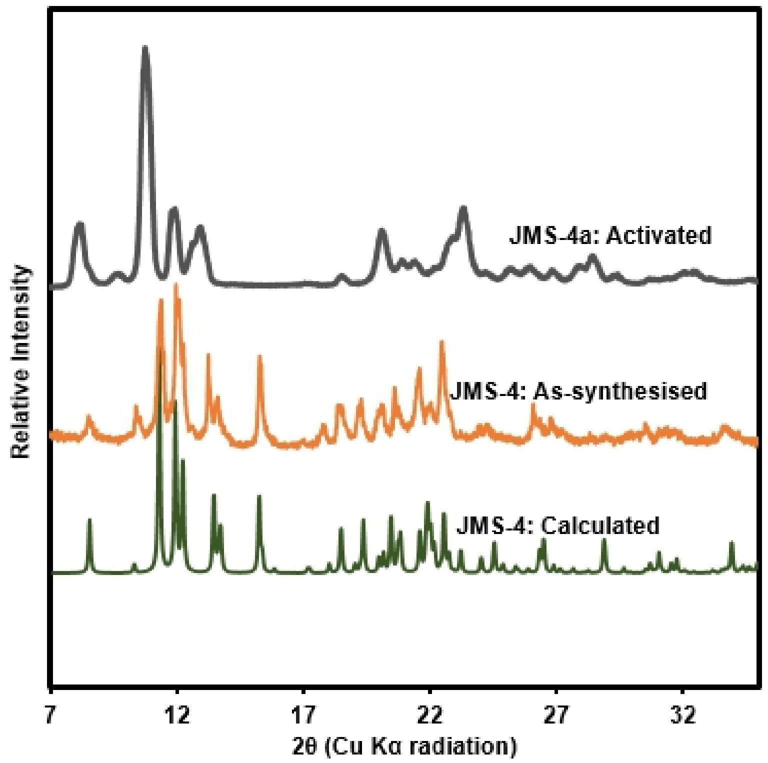

Figure 5.10: PXRD patterns of calculated, experimental and activated **JMS-4**

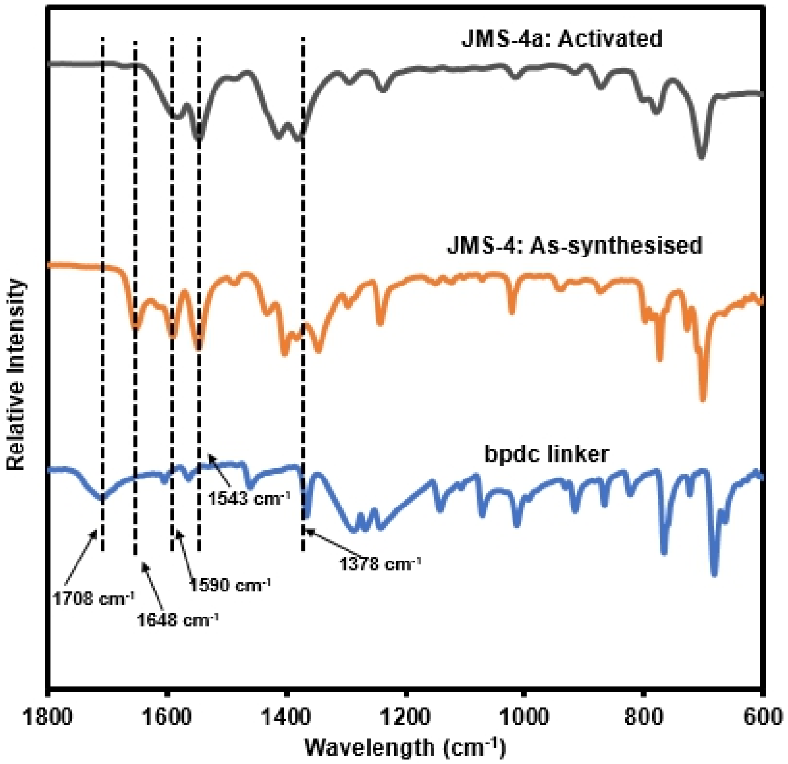

Figure 5.11: IR spectrum of the linker, as-synthesized and activated **JMS-4**

5.6 Topological Analysis of JMS-4

Topological analysis of **JMS-4** by Systre[5] and Topos[6] illustrated in Figure 5.12 revealed that it is similar to that of **JMS-3**. Each node, placed on zinc metal, is 4-connected to other metal centres by the bpdc linker to give an **sql** network topology.[7]

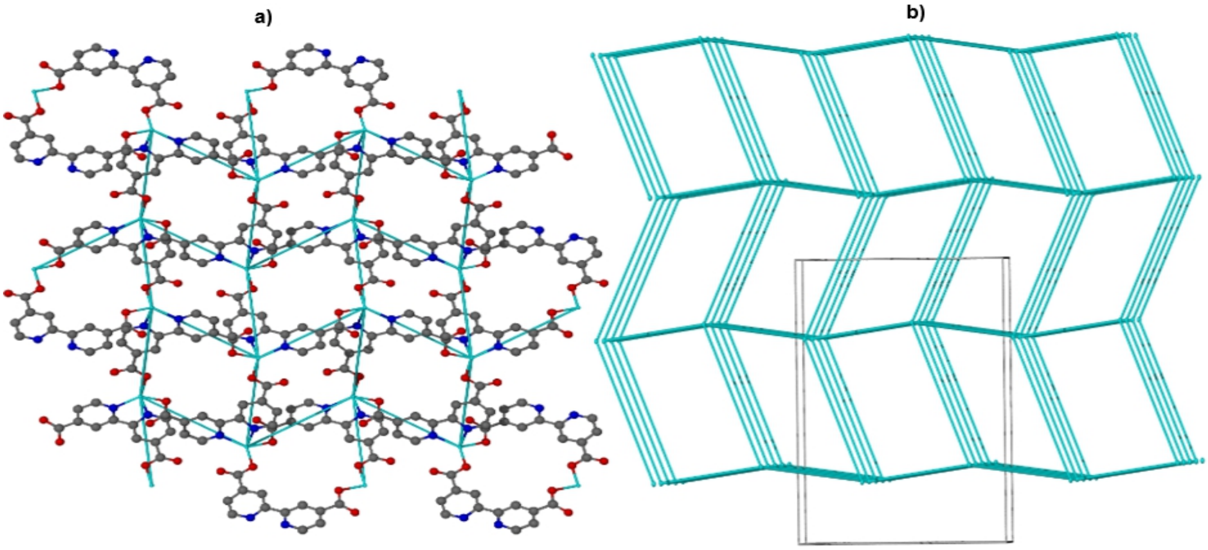

Figure 5.12: a) 4-connected 2D net and b)Packing of topological representation of **JMS-4**

5.7 Structural Description of JMS-5

JMS-5 crystallises in a monoclinic crystal system and space group $P2_{1/}n$. In the asymmetric unit of **JMS-5**, one Mg^{II} ion, one bpdc linker and two DMF molecules were modelled. The structure of **JMS-5** comprises $Mg_2C_2O_4$ binuclear secondary building unit (SBU) illustrated in Figure 5.13a which grows along the *a*-axis. The SBUs are connected by the bpdc linker to give a non-interpenetrated 3D structure. As shown in Figure 5.13b, the Mg^{II} is coordinated to two DMF molecules and four oxygen atoms of the bpdc linker to furnish a distorted octahedral geometry. As in compound **JMS-1**, the carboxylate moiety assumes a bidentate bridging mode. The Mg-O bond length ranges from 2.0361(14) to 2.1100(14)Å. These are given in Table 5.4. The bond angles around the Mg^{II} centres are in the range from 83.67(6) to 178. 18(6)°.

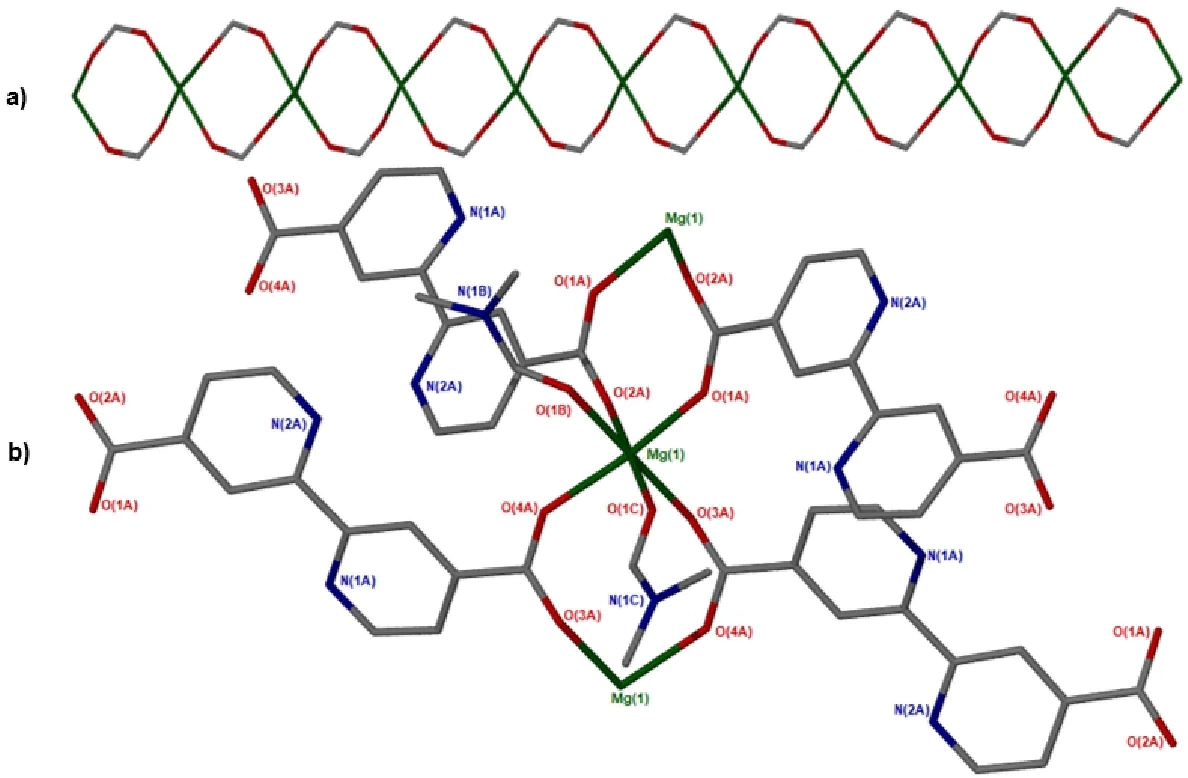

Figure 5.13: a) Binuclear $Mg_2C_2O_4$ generated in situ, b) coordination environment of Mg(II). Hydrogen atoms have been omitted for clarity.

Table 5.4: Bond distances around Mg^{II} in **JMS-5**.

Bond Type	Bond Length (Å)	Bond Type	Bond Length (Å)
Mg1-O2A	2.0361(14)	Mg1-O1C	2.0890(15)
Mg1-O4A	2.0374(14)	Mg1-O1B	2.1039(15)
Mg1-O1A	2.0515(14)	Mg1-O3A	2.1100(14)

JMS-5 possesses channels which run along the *a*-axis as revealed by the packing diagram in Figure 5.14. These channels which are occupied by coordinated DMF molecules, constitute 47% of the unit cell volume as estimated using PLATON.[3] Weak intermolecular hydrogen bonding exists within the framework of **JMS-5.**

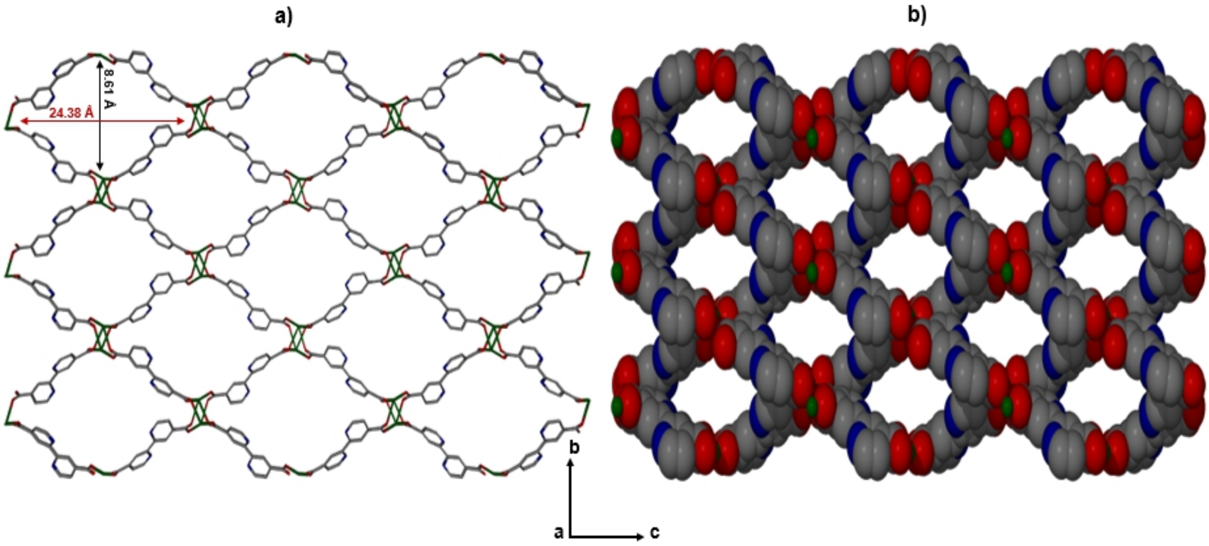

Figure 5.14: Channels found in **JMS-5** viewed along the *b*-axis, a) drawn in stick form, b) van der Waals radii. The guest DMF molecules which occupy these channels have been omitted.

The thermal analysis of **JMS-5** in Figure 5.15 shows an initial weight loss of 34.8 % between 60-355 ˚C which corresponds to the extrusion of two DMF molecules per formula unit modelled in the structure (calculated 35.2%). The slope of the TGA curve gives an indication of the amount of energy that is required to desorb the guest molecules. It can be noted that the DMF loss occurs over a wide temperature range, which suggests that a lot of energy is required to desorb the guest molecules. This is in agreement with the crystal structure, in which the DMF guests are coordinated to the Mg^{II}, resulting in a higher temperature range of weight loss. From 350 ˚C, there is a plateau up to 430 ˚C above which there is a slow decomposition of the framework. **JMS-5** was activated by soaking the as-made crystals in methanol for 24 hours to allow for the exchange of DMF with a low boiling solvent. The soaked crystals were then heated under a vacuum for 24 hours at 100 ˚C. Complete removal of the solvent molecules was confirmed by TGA analysis which showed weight loss until decomposition.

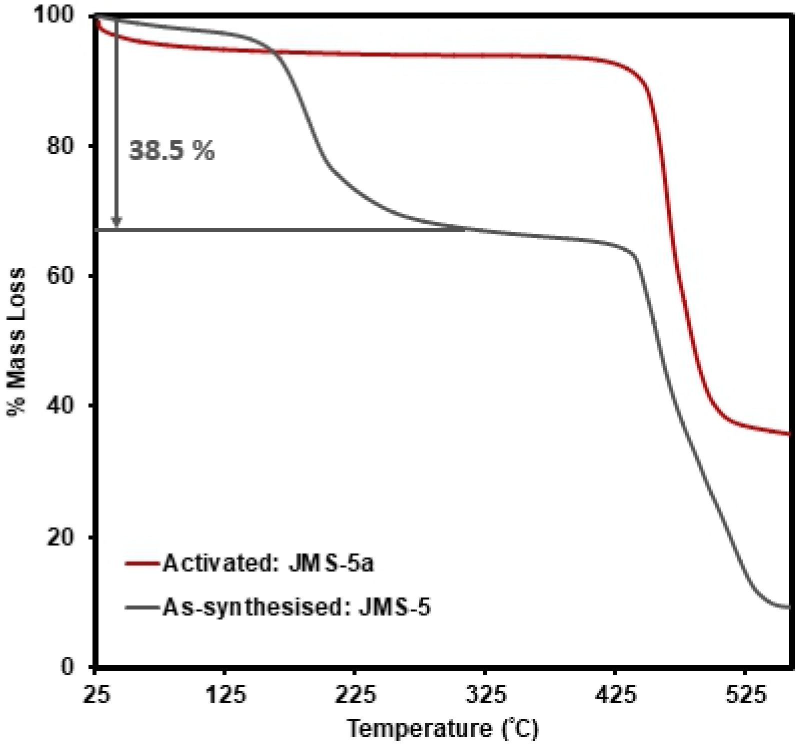

Figure 5.15: TGA traces of experimental and activated **JMS-5**.

PXRD studies shown in Figure 5.16 show an agreement between the calculated and experimental pattern. This confirms the phase purity of the prepared crystals. The structural integrity of the framework is maintained upon the evacuation of the guest molecules.

In the IR spectrum of **JMS-5**, the band at 1666 cm^{-1}, which disappears upon activation is assigned to the carbonyl stretch of DMF molecules. The asymmetric and symmetric carboxylate stretches in JMS-5 are located at 1612 cm^{-1} and 1381cm^{-1} respectively and the magnitude of separation was found to be 231 cm^{-1}, suggesting that the carboxylate moiety is coordinated to two Mg^{II} ions in a bidentate bridging mode.[10] The band located at 1550 cm^{-1} is attributed to the C-C of the benzene ring. The FTIR of **JMS-5** and **JMS-5a** (Figure 5.17) retains similar characteristic bands in the carboxylate stretching region confirming that the binding mode of the carboxylate moiety is retained upon the activation process.[4]

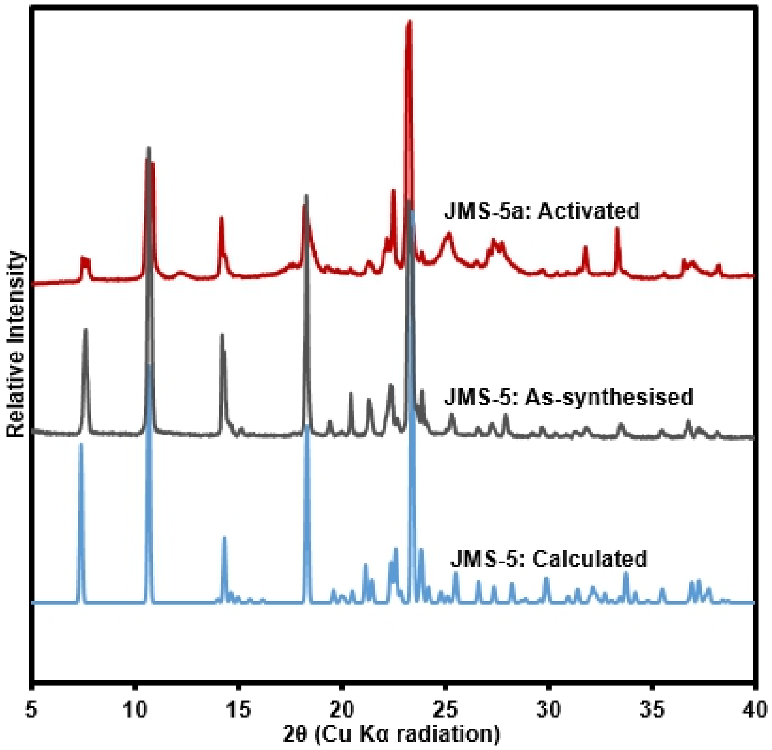

Figure 5.16: PXRD patterns of calculated, experimental and activated J**MS-5**

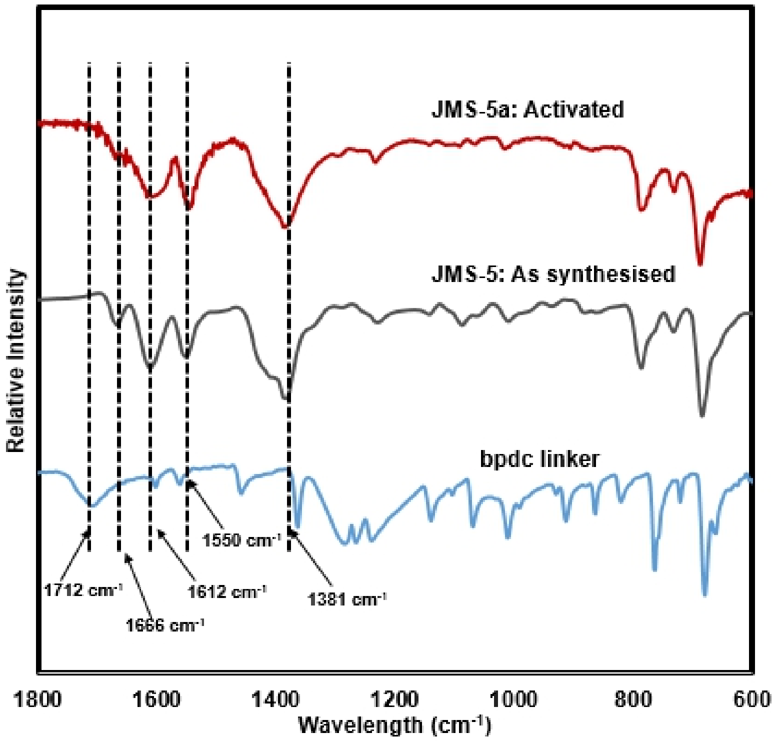

Figure 5.17: IR spectrum of the linker, as-synthesized and activated **JMS-5**

5.8 Topological Analysis of JMS-5

A similar simple approach as for **JMS-1** was used (see Chapter 3, page 67), just connecting the links to a featureless rod, in this case, gives two links intersecting at the same point. Connecting up and down the rod then yields a four-connected net with **cds** topology shown in Figure 5.18.

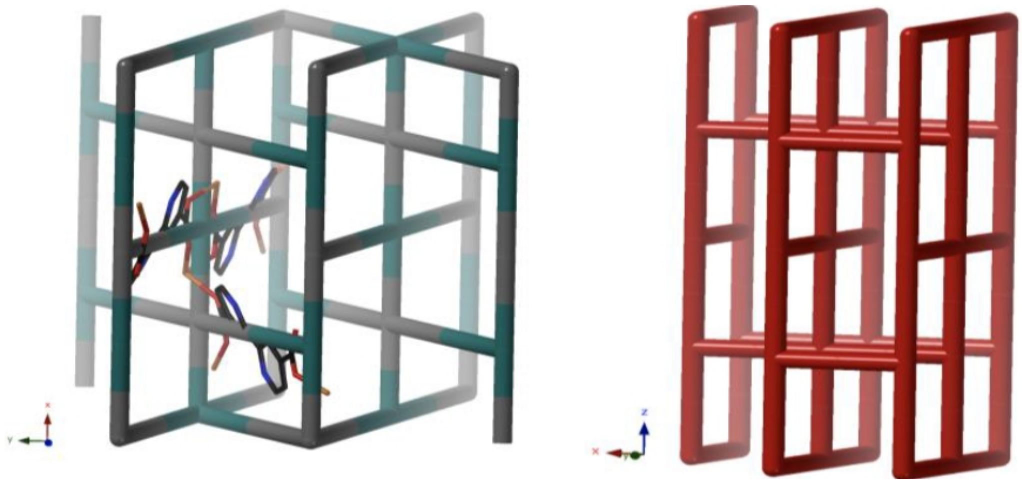

Figure 5.18: Left: The **cds**-net in **JMS-5** based on a simple connection of the linkers to the rod. Right: the most symmetric form of the **cds**-net where the angles between the square units are exactly 90° as opposed to 140°/40° in **JMS-5**. This net has transitivity 1 2 (1 unique node and 2 unique edges. Again, this assumes a featureless rod.

Arguably the **cds**-net is not a bad description of **JMS-5**, as this topology has a unique axis along the rods, therefore to some extent it mirrors the rod-like structure. However, again the topology of the rod is ignored. Taking the O'Keeffe approach to this by constructing the simplest geometrical forms that can define the rod one arrives at a distorted ladder and the resulting net is **irl**, (Figure 5.19). (In principle, one could also consider the rods to be constructed by edge-sharing tetrahedra, but this just adds complexity without giving a better description of the structure. For the record: this description yields the six-connected binodal **snp**-net also with transitivity 1 3.)

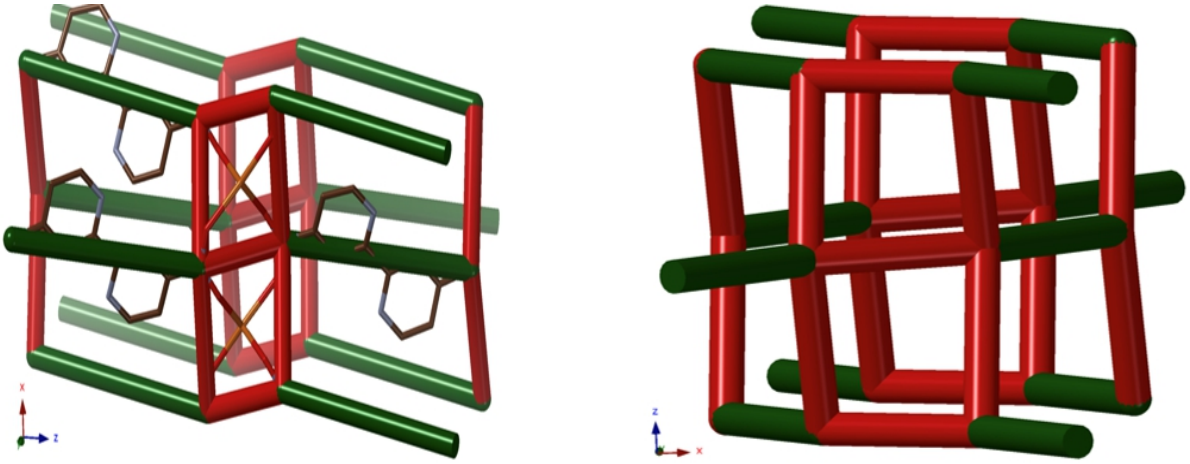

Figure 5.19: Left: The ladders in the rod of **JMS-5** (emphasised by red links) constructed from the carbonyl carbons and the resulting **irl**-net. Three linking ligands and two magnesium ions are also shown. Right: The most symmetric form of the **irl**-net, with transitivity 1 3 (1 unique node and 3 unique edges).

5.9 Chemical Stability Studies

Due to the potential degradation of MOF catalysts during catalytic reactions, detailed characterisation before catalysis is necessary.[11,12] The bond between the metal ion and the organic linker is the weakest point in the structure, since the MOF crystals may be degraded *via* hydrolysis or displacement of the organic linker with solvent molecules.[13] Depending on the properties of metal centres such as coordination number and hydrophobicity or chemical structure of the organic linker, MOF materials can exhibit the properties of metal centres with different levels of stability in the presence of solvents.[14] Metals with high coordination numbers exhibit higher stability because they can coordinate multiple bonds, which can hold the structure together after cleavage of some bonds.[15] In addition, the strength of the metal-ligand bond varies depending on the nature of metal ions.

The chemical stability of MOFs is often judged by comparing the PXRD pattern of a MOF before and after soaking in a given aqueous solution.[13,15] PXRD analysis after the exposure to these reaction conditions may reveal details about the integrity of the crystal structure. FTIR analysis, on the other hand, could shed light on any change in the coordination mode of the linker following the reactions. To test the chemical stability, the activated MOFs, **JMS-3a**, **JMS-4a** and **JMS-5a** were thus soaked in different organic solvents (ranging from high protic to aprotic) for 36 hours. The solids recovered by filtration were washed thoroughly before recording the PXRD pattern.

As shown in the PXRD pattern of the recovered samples (Figure 5.20), **JMS-3a** is not stable under different chemical environments. A new phase, which is uniform throughout is obtained. Peaks at two theta positions around 8°, 12°, 13°, 14°, 18°, 19° and 22° disappear. At two theta positions 12° and 17° there are new peaks.

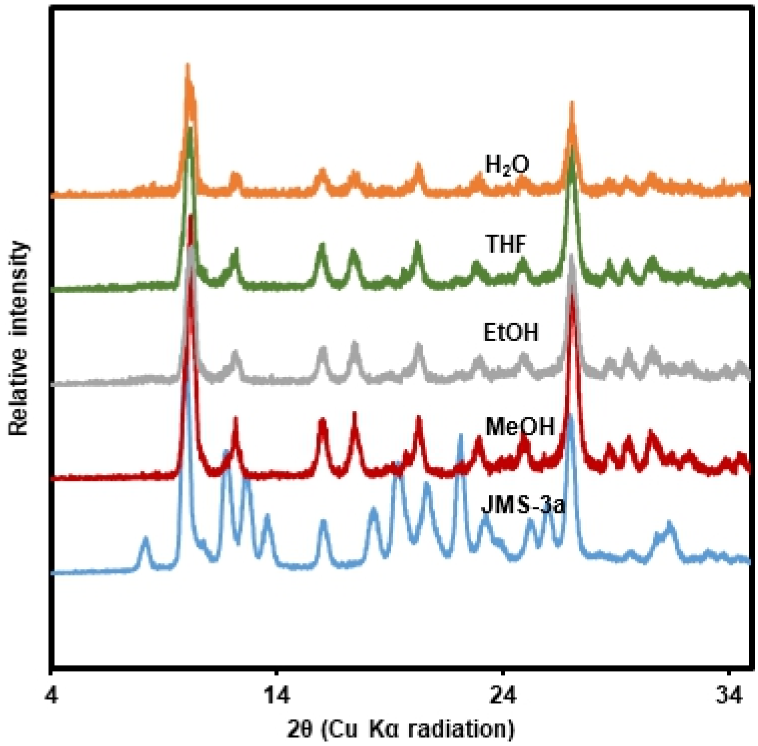

Figure 5.20: PXRD of **JMS-3a** soaked in different solvents.

The FTIR studies of **JMS-3a** soaked in different solvents, illustrated in Figure 5.21, show that the position of the asymmetric and symmetric carboxylate located at 1604 and 1365 cm^{-1} respectively are not affected. This suggests that the binding mode of the carboxylate moiety is retained in different solvents.

Contrary to **JMS-3a,** the structural integrity of **JMS-4a** is maintained as shown by a good match between the PXRD patterns of the activated phase and the ones obtained after soaking the materials in different solvents for 36 hours (Figure 5.22).

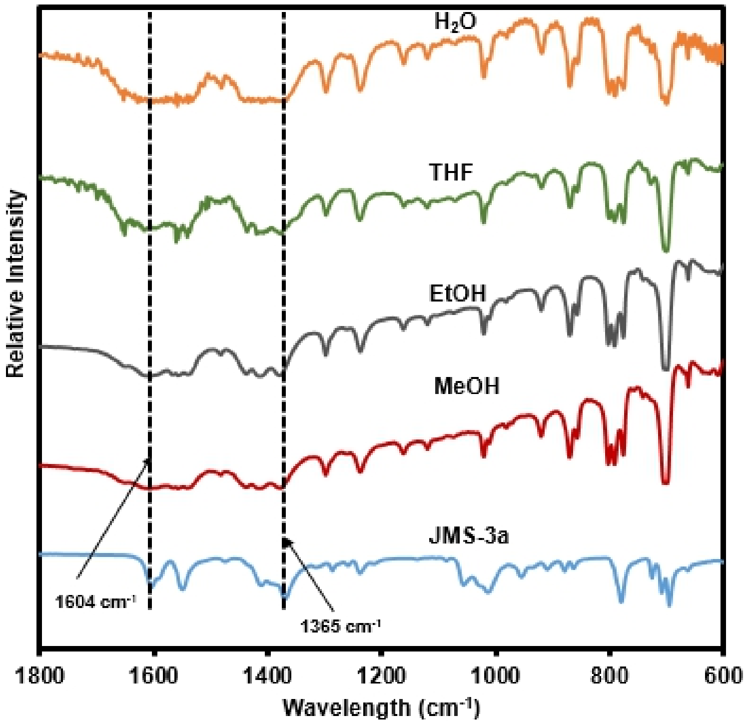

Figure 5.21: FTIR of **JMS-3a** soaked in different solvent.

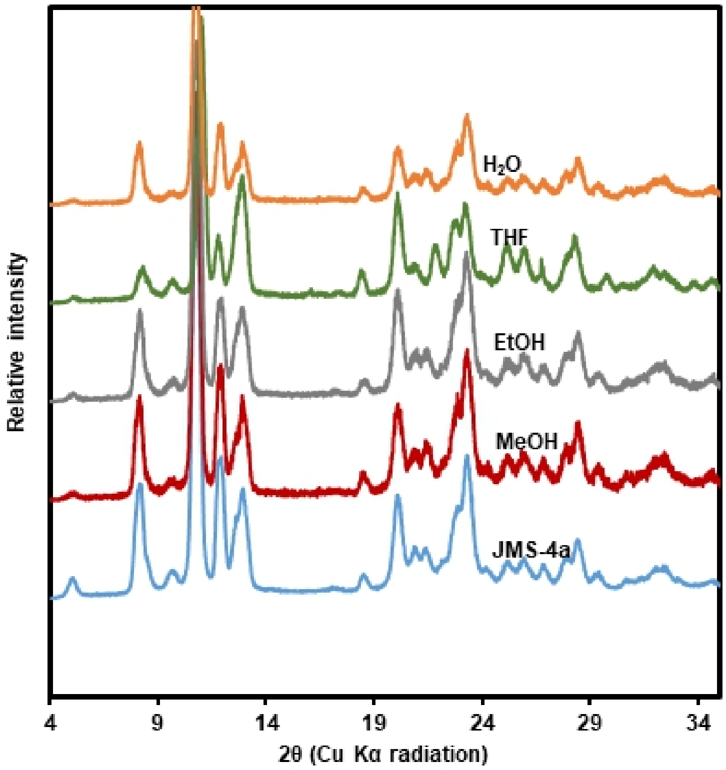

Figure 5.22: PXRD of **JMS-3a** soaked in different solvents.

In the IR spectrum of **JMS-4a**, the asymmetric and symmetric stretches of the carboxylate observed at 1590 and 1378 cm^{-1} (Figure 5.23) do not change after soaking in different solvents, suggesting that the binding mode of the carboxylate moiety is not affected. This is in agreement with the PXRD pattern in Figure 5.22, which shows that the structural integrity of the activated MOF is maintained.

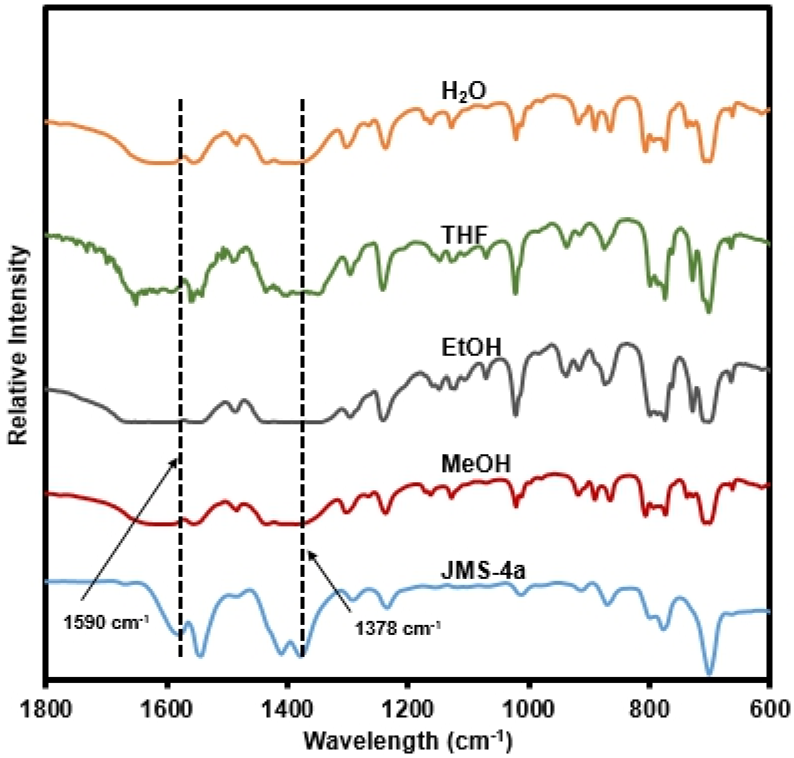

Figure 5.23: FTIR of **JMS-4a** soaked in different solvents.

As illustrated in Figure 5.24, **JMS-5a** is not stable. The MOF is poisoned by water as evidenced by the transformation from crystalline to an amorphous phase. The observed difference in the chemical stability of the three MOFs may be attributed to the strength of the metal-oxygen bond.[13] In the presence of methanol, ethanol and tetrahydrofuran, a new is a phase formed. The peaks at two theta positions around 8° and 24° disappear. The FTIR studies (Figure 5.25), of the recovered samples, shows that the position of the asymmetric and symmetric stretches at 1612 cm^{-1} and 1381 cm^{-1} did not change confirming that the binding mode of the carboxylate moiety to the metal is retained under various chemical conditions.

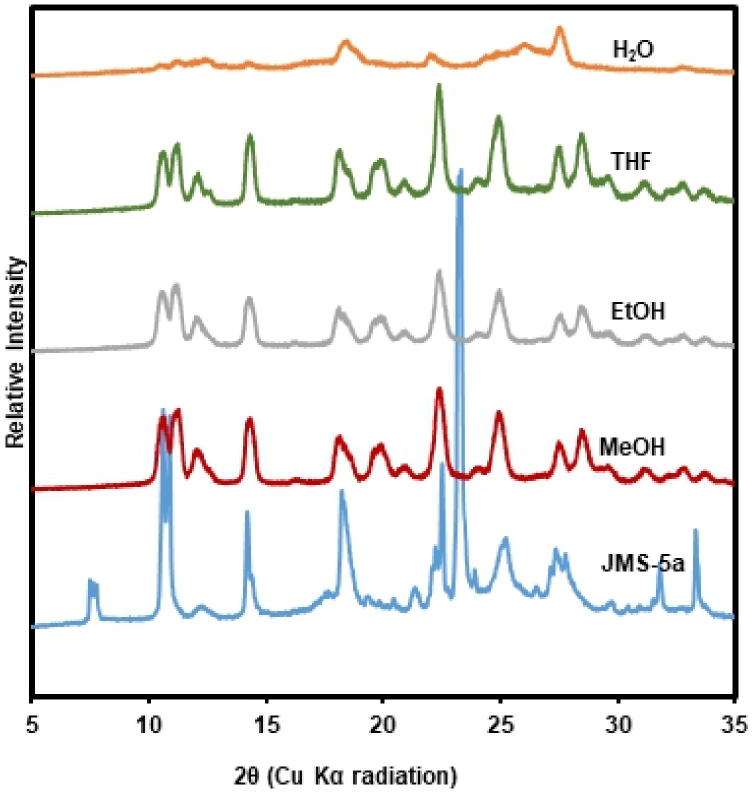

Figure 5.24: PXRD of JMS-5a soaked in different solvents.

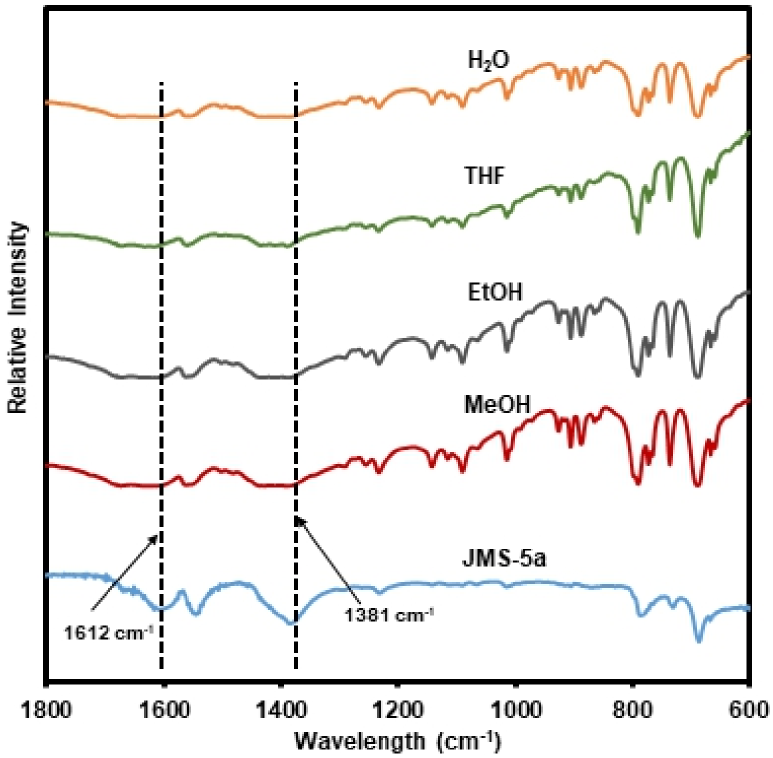

Figure 5.25: FTIR of JMS-5a soaked in different solvents.

5.10 Gas Sorpton Studies

Prior to adsorption measurements, the as-synthesised samples were activated by evacuating at an elevated temperature of 150 ˚C under vacuum to generate a solvent-free framework. The removal of guest molecules has been reported to provide open metal sites which enhance adsorption of H_2 and CO_2.[16] The CO_2 adsorption measurements at various temperatures illustrated in Figure 5.26 revealed a Type-1 isotherm according to IUPAC classification, which is typical of microporous materials.[17] **JMS-3a** gave volumetric uptakes of 26.50 and 30.89 cm^3 (STP) g^{-1} (1.18 and 1.39 $mmolg^{-1}$) whist **JMS-4a** gave 10.96 and 16.08 cm^3 (STP) g^{-1} (0.49 and 0.71 $mmolg^{-1}$) at 298 and 273 K respectively.

At 195 K, both MOFs show a steep uptake of CO_2 at low-pressure range with volumetric uptake of 34.66 and 38.84 cm^3 (STP)g^{-1} (1.52 and 1.74 $mmolg^{-1}$) for **JMS-3a** and **JMS-4a** respectively, confirming inherent permanent porosity of the MOFs. In the absence of N_2 sorption, CO_2 sorption at 273 K reveals a modest surface area of 151 and 36 m^2g^{-1} for **JMS-3a** and **JMS-4a**. Although the use of CO_2 sorption for BET calculation is controversial, Bae and coworkers demonstrated that it may be used for ultramicroporous materials at 273 K.[18] **JMS-3a** perform exceptionally well for CO_2 capture at 273 and 298 K, probably due to its high surface area compared to **JMS-4a**. Furthermore, upon activation, the PXRD pattern of **JMS-3a** (Figure 5.4) shows that structural transformation is not much as compared to **JMS-4a** (Figure 5.10).

The hysteresis nature of the isotherms can be attributed to the stronger interaction of the CO_2 with the framework, which is further supported by the isosteric heat of adsorption (Q_{st}) studies. The heat of adsorption is an important parameter for CO_2 storage through physical adsorption. It represents the energetic interaction strength of the adsorbent with the adsorbate molecules that play a critical role in determining the adsorptive selectivity and the energy required to release CO_2 molecules during regeneration. If the heat of adsorption is too high, the regeneration cost will increase because the material binds strongly, therefore a large quantity of energy will be required to break the framework-CO_2 interaction. On the other hand, very low heat of adsorption is also not preferable although the regeneration energy will be lower, however, the purity of the captured CO_2 will be lowered due to lower adsorption selectivity and the required volume of the adsorbent bed will be larger due to lower density of the adsorbed CO_2.[19]

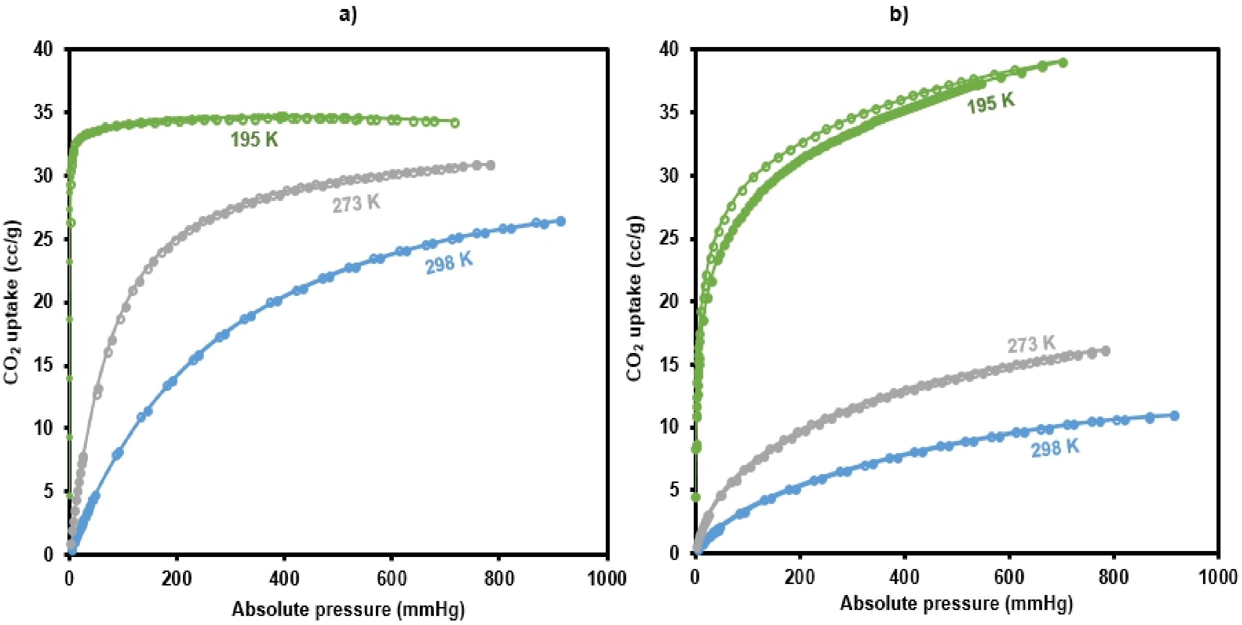

Figure 5.26: CO_2 adsorption-desorption isotherms for **JMS-3a** (a) and **JMS-4a** (b) (closed circles represent adsorption and open circles desorption).

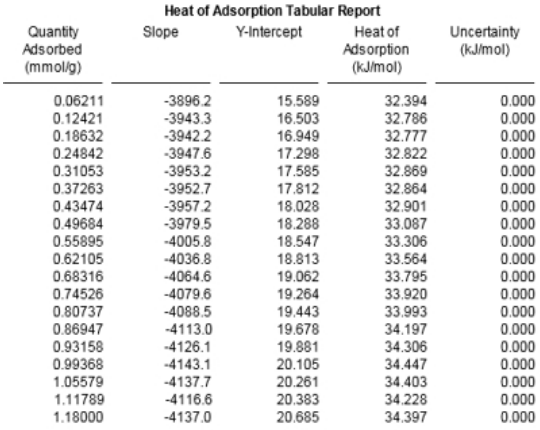

Heat of Adsorption Tabular Report

Quantity Adsorbed (mmol/g)	Slope	Y-Intercept	Heat of Adsorption (kJ/mol)	Uncertainty (kJ/mol)
0.06211	-3896.2	15.589	32.394	0.000
0.12421	-3943.3	16.503	32.786	0.000
0.18632	-3942.2	16.949	32.777	0.000
0.24842	-3947.6	17.298	32.822	0.000
0.31053	-3953.2	17.585	32.869	0.000
0.37263	-3952.7	17.812	32.864	0.000
0.43474	-3957.2	18.028	32.901	0.000
0.49684	-3979.5	18.288	33.087	0.000
0.55895	-4005.8	18.547	33.306	0.000
0.62105	-4036.8	18.813	33.564	0.000
0.68316	-4064.6	19.062	33.795	0.000
0.74526	-4079.6	19.264	33.920	0.000
0.80737	-4088.5	19.443	33.993	0.000
0.86947	-4113.0	19.678	34.197	0.000
0.93158	-4126.1	19.881	34.306	0.000
0.99368	-4143.1	20.105	34.447	0.000
1.05579	-4137.7	20.261	34.403	0.000
1.11789	-4116.6	20.383	34.228	0.000
1.18000	-4137.0	20.685	34.397	0.000

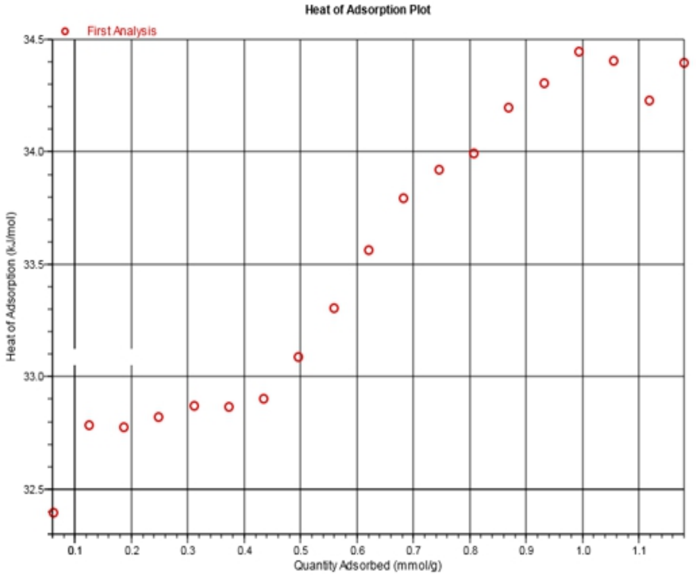

Figure 5.27: Isosteric heat of adsorption for **JMS-3a**

The adsorption branches of the isotherm carried out at 273 and 298 K were used to obtain a precise prediction over the quantity of CO_2 adsorbed at the saturation point.[20] The estimated values of isosteric heat of adsorption for **JMS-3a** were found to be 33 to 34 $kJmol^{-1}$ at load values ranging from 0.12 to 0.99 $mmolg^{-1}$(Figure 5.27). CO_2 isotherms for **JMS-4a** revealed isosteric heats of adsorption values of 29 to 31 $kJmol^{-1}$ at load values of 0.32 to 0.45 $mmolg^{-1}$ (Figure 5.28). The observed CO_2

uptake indicates moderate to the strong interaction of CO_2 with the MOFs and the results are comparable to other MOFs reported in the literature as illustrated in Table 5.5.

Table 5.5. A comparison of CO_2 adsorption capacity for various Cd and Zn based MOFs at 1atm.

MOF material	**Temp (K)**	**CO_2 uptake ($mmolg^{-1}$)**	**Qst ($kJmol^{-1}$)**	**Ref**
$[\{Cd_2(L\text{-}glu)_2(bpe)\}]_n$	273	0.92	40.8	[21]
	298	0.64		
$[Cd_2(Tzc)_2]n$	195	2.45	-	[22]
$[Zn(TCPB)_2]_n$	195	6.29	-	[23]
	273	2.89		
$[Zn(hfipbb)(bpt)]_n$	195	1.71	35.8	[24]
	273	0.96		
	298	0.62		
$[Cd_2(bpdc)_2]_n$	195	1.52	34.4	This work
	273	1.39		
	298	1.18		
$[Zn(bpdc)]_n$	195	1.74	30.7	This work
	273	0.71		
	298	0.49		

L-glu = L-glutamate dianion, bpe = 1.2-bis(4-pyridyl)ethylene, Tzc = tetraazolate-5-carboxylate, TCPB = 1,3,5-tri(4-carboxyphenoxy)benzene, hfipbb = 4,4’-(hexafluoroisooropylidene)bis (benzoate) and bpt = 4-amino-3,5-bis(4-pyridyl)-1,2,4-triazole. Reports in this table include adsorption capacities in $mmolg^{-1}$. (Some have been converted to these units from the originally reported units).

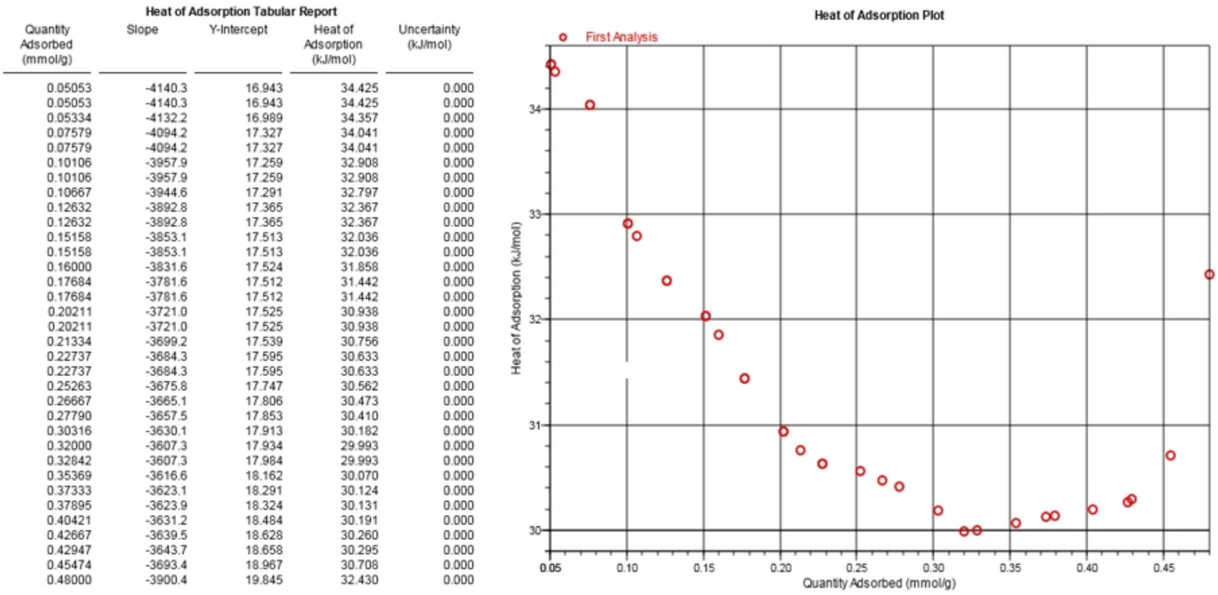

Heat of Adsorption Tabular Report

Quantity Adsorbed (mmol/g)	Slope	Y-Intercept	Heat of Adsorption (kJ/mol)	Uncertainty (kJ/mol)
0.05053	-4140.3	16.943	34.425	0.000
0.05053	-4140.3	16.943	34.425	0.000
0.05334	-4132.2	16.989	34.357	0.000
0.07579	-4094.2	17.327	34.041	0.000
0.07579	-4094.2	17.327	34.041	0.000
0.10106	-3957.9	17.259	32.908	0.000
0.10106	-3957.9	17.259	32.908	0.000
0.10667	-3944.6	17.291	32.797	0.000
0.12632	-3892.8	17.365	32.367	0.000
0.12632	-3892.8	17.365	32.367	0.000
0.15158	-3853.1	17.513	32.036	0.000
0.15158	-3853.1	17.513	32.036	0.000
0.16000	-3831.6	17.524	31.858	0.000
0.17684	-3781.6	17.512	31.442	0.000
0.17684	-3781.6	17.512	31.442	0.000
0.20211	-3721.0	17.525	30.938	0.000
0.20211	-3721.0	17.525	30.938	0.000
0.21334	-3699.2	17.539	30.756	0.000
0.22737	-3684.3	17.595	30.633	0.000
0.22737	-3684.3	17.595	30.633	0.000
0.25263	-3675.8	17.747	30.562	0.000
0.26667	-3665.1	17.806	30.473	0.000
0.27790	-3657.5	17.853	30.410	0.000
0.30316	-3630.1	17.913	30.182	0.000
0.32000	-3607.3	17.934	29.993	0.000
0.32842	-3607.3	17.984	29.993	0.000
0.35369	-3616.6	18.162	30.070	0.000
0.37333	-3623.1	18.291	30.124	0.000
0.37895	-3623.9	18.324	30.131	0.000
0.40421	-3631.2	18.484	30.191	0.000
0.42667	-3639.5	18.628	30.260	0.000
0.42947	-3643.7	18.658	30.295	0.000
0.45474	-3693.4	18.967	30.708	0.000
0.48000	-3900.4	19.845	32.430	0.000

Figure 5.28: Isosteric heat of adsorption for **JMS-4a**

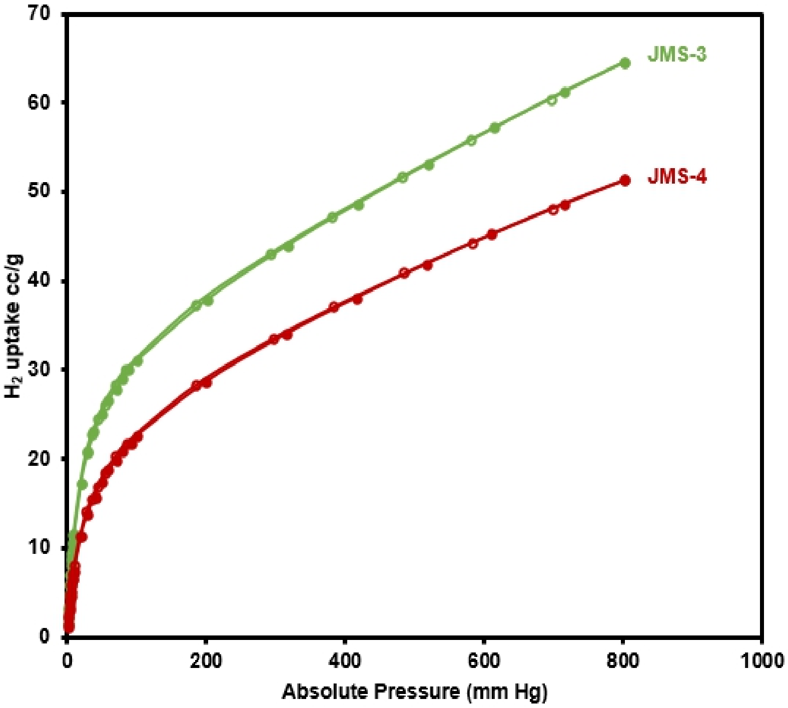

Figure 5.29: Hydrogen adsorption and desorption isotherms of **JMS-3a** and **JMS-4a** at 77 K

For H_2, the sorption isotherms in Figure 5.29 reveal a storage capacity of up to 65 and 51 cm^3g^{-1} for **JMS-3a** and **JMS-4a** at 800 mmHg and 77 K, corresponding to the sorption of 0.58 and 0.46 wt.% (2.88 and 2.29 $mmolg^{-1}$). The hydrogen adsorption values are comparable to that of $[Cd_2(Tzc)_2]_n$ (0.55 wt.%) [22] and $[Zn(hfipbb)(bpt)]_n$ (0.44 wt.%) [24] but less than that of $[Zn(TCPB)_2]_n$ (0.80 wt.%) [23] under similar conditions.

5.11 Summary

In the present study, three novel MOFs, **JMS-3**, **JMS-4** and **JMS-5**, with molecular formula $[Cd_2(bpdc)_2(DMF)_2{\cdot}2DMF]_n$, $[Zn(bpdc)(DMF){\cdot}DMF]_n$ and $[Mg_1(bpdc)(DMF)_2]_n$ respectively, were successfully synthesised using 2,2'-bipyridine-4,4'-dicarboxylate (bpdc) linker. The MOFs crystallises in the monoclinic system and space group $P2_1/c$, $P2_1/n$ and $P2_1/n$ respectively. Topology reveals that **JMS-3** and **JMS-4** MOFs possess 2D interdigited rectangular layers with a 4-connected **sql** network topology. **JMS-5** possess a 3D net with an **irl** topology. Our PXRD results indicate that upon activation, **JMS-3a** and **JMS-4a** undergo a structural transformation. The stability tests reveal that the binding mode of the carboxylate moiety is retained in different chemical environments.

The three MOFs were not evaluated for the hydrogenation of CO_2 to formate as **JMS-3** and **JMS-4** did not have anchoring sites for the catalysts. This was because, during MOF formation, the nitrogen sites were used for coordination by both Zn and Cd. Cyclometalation of **JMS-5** was not successful. The native forms of the three MOFs could not produce any formate even under harsh conditions. The evacuated frameworks of **JMS-3** and **JMS-4** were evaluated for H_2 and CO_2 capture. The MOFs showed appreciable carbon dioxide sorption at 195 K and hydrogen at 77 K. Insufficient material for **JMS-5a** precluded gas sorption studies.

5.12 REFERENCES

1 G. M. Sheldrick, *Acta Crystallographica Section C: Structural Chemistry*, 2015, **71**, 3–8.

2 L. J. Barbour, *Journal of Supramolecular Chemistry*, 2001, **1**, 189–191.

3 A. L. Spek, *Acta Crystallographica. Section D, Biological crystallography*, 2009, **65**, 148–55.

4 S. M. Lu, Z. Wang, J. Li, J. Xiao and C. Li, *Green Chemistry*, 2016, **18**, 4553–4558.

5 O. D. Friedrichs, *SYSTERE, 1.1.4beta*, 2019, http:/gavrog.sourceforge.net./

6 M. O. Keeffe, M. a Peskov, S. J. Ramsden and O. M. Yaghi, *Accounts of Chemical Research*, 2008, **41**, 1782–1789.

7 G. Mehlana, C. Wilkinson, C. N. T. Dzesse, G. Ramon and S. A. Bourne, *Crystal Growth and Design*, 2017, **17**, 6445–6454.

8 G. Mehlana, S. A. Bourne, G. Ramon and L. Öhrström, *Crystal Growth and Design*, 2013, **13**, 633–644.

9 L. Öhrström, *Crystals*, 2015, **5**, 154–162.

10 V. Zeleňák, Z. Vargová and K. Györyová, *Spectrochimica Acta - Part A: Molecular and Biomolecular Spectroscopy*, 2007, **66**, 262–272.

11 J. B. Decoste, G. W. Peterson, H. Jasuja, T. G. Glover, Y. G. Huang and K. S. Walton, *Journal of Materials Chemistry A*, 2013, **1**, 5642–5650.

12 N. C. Burtch, H. Jasuja and K. S. Walton, *Chemical Reviews*, 2014, **114**, 10575–10612.

13 J. W. Maina, C. Pozo-Gonzalo, L. Kong, J. Schütz, M. Hill and L. F. Dumée, *Materials Horizons*, 2017, **4**, 345–361.

14 D. J. Tranchemontagne, J. L. Mendoza-Cortés, M. O'Keeffe and O. M. Yaghi, *Chemical Society Reviews*, 2009, **38**, 1257–1283.

15 A. J. Howarth, Y. Liu, P. Li, Z. Li, T. C. Wang, J. T. Hupp and O. K. Farha, *Nature Reviews Materials*, 2016, **1**, 1–15.

16 D. Britt, H. Furukawa, B. Wang, T. G. Glover and O. M. Yaghi, *Proceedings of*

the National Academy of Sciences, 2009, **106**, 20637–20640.

17 M. Alhamami, H. Doan and C. H. Cheng, *Materials*, 2014, **7**, 3198–3250.

18 K. C. Kim, T. U. Yoon and Y. S. Bae, *Microporous and Mesoporous Materials*, 2016, **224**, 294–301.

19 J. M. Ngoy and R. Falcon, *Canadian Journal of Chemical Engineering*, 2019, **2019**, 2961–2968.

20 B. Ugale, S. S. Dhankhar and C. M. Nagaraja, *Crystal Growth and Design*, 2018, **18**, 2432–2440.

21 B. Ugale, S. S. Dhankhar and C. M. Nagaraja, *Inorganic Chemistry Frontiers*, 2017, **4**, 348–359.

22 D. C. Zhong, W. X. Zhang, F. L. Cao, L. Jiang and T. B. Lu, *Chemical Communications*, 2011, **47**, 1204–1206.

23 X. M. Lin, T. T. Li, Y. W. Wang, L. Zhang and C. Y. Su, *Chemistry - An Asian Journal*, 2012, **7**, 2796–2804.

24 N. Chatterjee and C. L. Oliver, *Crystal Growth and Design*, 2018, **18**, 7570–7578.

CHAPTER 6

Conclusion

6.1 Summary

Catalytic hydrogenation is considered to be one of the most promising ways to convert carbon dioxide (CO_2), a greenhouse gas and major contributor to global warming to value-added products.[1,2,3] For these reasons, the development of efficient catalysts for the reduction of CO_2 is highly desirable. Several studies have revealed that metal-organic frameworks (MOFs) have remarkable H_2 storage and CO_2 capture ability[4], and also more recently, catalysis.[5] Although some MOFs have been considered as catalysts for CO_2 conversion[6,7] it is still necessary to construct more effective MOFs for such reactions, especially under mild conditions. Key to this reaction design is the construction of catalytically active MOF systems, including encapsulation of homogeneous catalysts in the MOF during synthesis and functionalisation of linkers with catalytically active species.[8,9] The work presented in this thesis focused on the preparation and characterisation of MOFs using bipyridyl dicarboxylate linker, 2,2'-bipyridine-4,4'-dicarboxylate. The choice of the linker was to allow MOF formation through the carboxylate moiety while bipyridyl units provide anchoring sites for Pd^{II} and Ru^{II} complexes. After activation, the efficacy of the MOFs as storage devices of carbon dioxide and hydrogen and catalytic conversion of these gases to formate was evaluated.

The MOFs were characterised using Fourier Transform Infrared Spectroscopy, Thermogravimetric analysis, Scanning Electron Microscopy-Energy Dispersive, High-Resolution Transmission Electron Microscopy and X-ray Photoelectron Spectroscopy Structural elucidation were performed by single-crystal X-ray diffraction and powder X-ray diffraction studies were used to check the phase purity and phase transition of the prepared materials. Topological analysis of the crystal structures was performed using the TOPOS computer program to gain a better understanding of the underlying network of the structures. Nuclear Magnetic Resonance Spectroscopy was used to elucidate the structures of compounds based on chemical shifts of a proton or carbon in accordance to the magnetic field surrounding it.[9] ^1H NMR was also used to confirm catalysis products. Inductively Couple Plasma Optical Emission was used for the detection and quantitative determination of trace metal elements in the MOF catalyst, as well as for testing whether metal species have been leached from the solid catalyst to the solution during the reaction.

6.1.1: Hydrogenation of Carbon Dioxide to Formate Using Novel Lanthanum(III) Based Metal-Organic Frameworks.

A novel 3D metal-organic framework, **JMS-1**, with the molecular formula $[La_3(bpdc)_3(DMF)_3]_n$ was obtained under solvothermal conditions using 2,2'-bipyridine-4,4'-dicarboxylic acid and $LaCl_3 \cdot 7H_2O$ at 110 ˚C. The MOF crystallises in the orthorhombic crystal system, space group *Pna2₁*. The structure of **JMS-1** is made up of $La_2C_3O_6$ secondary building unit (SBU) rods which grow along *b*-axis. Network analysis of the MOF revealed a new 7-connected network with a new network topology (**zaz**). Analysis of the channels using PLATON[10] shows that they occupy 41 % of the unit cell volume. Thermogravimetric analysis of **JMS-1** revealed a 16.5 % weight loss which corresponds to the loss of three DMF molecules per formula unit modelled in the structure of **JMS-1** (calculated 17.89%). The framework decomposes around 460 ˚C.

JMS-1 was activated by soaking the as-made crystals in methanol for 24 hours, followed by heating under vacuum for 24 hours at 78 ˚C to give the activated phase, **JMS-1a**. The activated phase was functionalised by cyclometalation of the MOF backbone using the metal precursor, $[RuCl_2(p\text{-cymene})]_2$, to give **Ru(II)@JMS-1a**. Successful incorporation of Ru into the MOF was confirmed by XPS and NMR studies. A shift in the binding energy of C1s from 285.5 eV in **JMS-1a** to 285.3 eV in **Ru(II)@JMS-1a** provides evidence that the Ru(II) complex is grafted onto the MOF. The binding energy of N1s for **JMS-1a**, located at 400.9 eV, shifted to 400.06 eV upon cylcometalation, indicating that the nitrogen atom donated electrons to Ru^{II} ion. Further confirmation that ruthenium is bound to the MOF was studied using ^1H NMR spectroscopy. Coordination of Ru^{II} to **JMS-1a** is evidenced by two doublets around 5.3 ppm and 5.5 ppm in the dimer which, upon complexation shifted downfield and are split into four doublets. The observed shifts in both XPS and ^1H NMR revealed that the MOF is partially cyclometalated, which is consistent with low ruthenium loading content of 0.4% in **Ru(II)@JMS-1a** from ICP-OES analysis. EDX elemental mapping for the individual atoms in **Ru(II)@JMS-1a** infers a consistent and even distribution of Ru(II) throughout the matrix. PXRD analysis revealed that upon cyclometalation of **JMS-1a**, a new phase is induced. A comparison of the FTIR of **JMS-1a** and **Ru(II)@JMS-1a** shows that the asymmetric and symmetric carboxylate stretches at 1578 and 1398 cm^{-1} did not change upon cyclometalation, suggesting that the binding mode of the carboxylate moiety to the metal centre is retained during cyclometalation.

Gas sorption experiments were performed on **JMS-1a** and **Ru(II)@JMS-1a** using nitrogen, carbon dioxide and hydrogen. A significant decrease in BET surface area from 112 to 58 m^2/g was observed upon cyclometalation. The decrease is ascribed to partial blockage of the pores by the Ru(II)*p*-cymene complex.[11] At 77 K and 800 mmHg **JMS-1a** and **Ru(II)@JMS-1a** could store up to 68.17 and 65.34 cm^3 (STP) g^{-1}, corresponding to the sorption of 0.61 and 0.59 wt.% hydrogen respectively. CO_2 adsorption-desorption isotherms of **JMS-1a** and **Ru(II)@JMS-1a** show a typical Type I isotherm, with a steep uptake at the low-pressure region, suggesting microporosity nature of these materials. **JMS-1a** has a CO_2 volumetric uptake of 8.59 and 12.92 cm^3 (STP) g^{-1} (0.384 and 0.576 $mmolg^{-1}$) at 298 and 273K respectively. Upon cyclometalation, the uptake reduced to 6.08 and 10.42 cm^3 (STP) g^{-1} (0.274 and 0.465 $mmolg^{-1}$) at 298 and 273K respectively. At 195 K, the amount of CO_2 uptake increased abruptly at the low-pressure range, with volumetric uptake more than doubling to 36.25 and 32.62 cm^3 (STP) g^{-1} (1.61 and 1.46 $mmolg^{-1}$) at an absolute pressure of 701 mmHg for J**MS-1a** and **Ru(II)@JMS-1a** respectively. This confirms inherent permanent porosity of both MOFs.[12] The estimated values of isosteric heat of adsorption (Q_{st}) were ranging from 32 to 38 $kJmol^{-1}$ at load values 0.1 to 0.38 $mmolg^{-1}$, indicating moderate to the strong interaction of CO_2 with the MOFs.[13] The observed H_2 and CO_2 uptake is are comparable to several MOFs known for CO_2 capture and conversion.[14,15]

Hydrogenation of CO_2 studies using **JMS-1a** and the functionalised MOF, **Ru(II)@JMS-1a**, revealed that both MOFs were able to convert CO_2 to formate. The formate product formed was detected and quantified by ^1H NMR spectroscopy, with acetone as an internal standard. The formate yield obtained using **JMS-1a** was significantly lower (62 %) than that of the functionalised material, **Ru(II)@JMS-1a** (95.4 %) under similar conditions (temperature 110 °C, pressure $_pH_2/_pCO_2$ of 1:3, time 24 hours, and 15.6 μmol catalyst loading in ethanol and KOH). The non-functionalised MOF, **JMS-1a** requires higher temperatures and catalyst loading to achieve high yields of formate. Under optimised conditions, the **[RuCl$_2$(*p*-cymene)]$_2$** dimer afforded a yield of 24.3%, which is significantly lower than that of **JMS-1a** and **Ru(II)@JMS-1a**.The relatively low temperature in the hydrogenation reaction of **Ru(II)@JMS-1a** makes the strategy for the incorporation of catalytically active metals in the MOFs attractive.

Size-selective thiol poisoning studies were used to ascertain that Ru(II)Cl(*p*-cymene)] complex was encapsulated inside the pores of **JMS-1a** rather than being adsorbed on the external surface. When bulky thiols such as benzylmercaptan were exposed to **Ru(II)@JMS-1a**, the product yield was reduced by 16 %. In contrast, when the catalyst was exposed to 2 mercapto-ethanol, which can easily access the catalytic sites by diffusion through the pores and poison the catalyst, the yield was reduced by 56.6%. This confirms that most of the active species is encapsulated in the framework rather than bound to the surface.

The reusability of the catalysts was studied over consecutive runs. **JMS-1a** could be recycled up to five times without significant loss in catalytic activity. Contrary to this, **Ru(II)@JMS-1a** showed a significant decrease in the yield of formate (17 %) over five consecutive runs although the yield obtained was still higher (78 %) than that obtained using **JMS-1a.** Remarkably PXRD pattern of recycled **JMS-1a** matches well with that of the parent MOF suggesting retention of the original framework, while that of **Ru(II)@JMS-1a** is slightly changed. TGA and FTIR analysis showed no significant difference between fresh and used catalysts. ICP-OES analysis of the aqueous solution in the reactor showed negligible metal leaching of the metals into solution.

Based on our experimental results and literature findings,[16–18] the reaction mechanism of CO_2/HCO_3^- using **Ru(II)@JMS-1a** catalyst was proposed. The first step involves reductive elimination of the Cl, providing open metal sites for the coordination of H_2 molecules to give a dihydrogen complex [Ru(H_2)(*p*-cymeme)]. The active species, RuH(*p*-cymene), is formed upon splitting of the coordinated H_2 molecules with simultaneous elimination HCl. The insertion of CO_2 *via* associative addition into the ruthenium hydride complex generates the formate complex which readily dissociates the formate.

6.1.2: Palladium(II) Functionalised Metal-Organic Frameworks for Carbon Dioxide Hydrogenation to Formate

Prior to MOF synthesis, the bipyridyl units were functionalised with palladium to give an organometallic complex, [$PdCl_2$bpdc] (**C1**), using [$PdCl_2(CH_3CN)_2$] and 2,2' bipyridine 4,4'dicarboxylate ligand as starting materials. As expected, a significant downfield shift in the ^{1}H NMR signals of aromatic protons of the linker, observed in the region 8.92 ppm to 7.90 ppm to the region 9.29 ppm to 8.19 ppm confirmed the successful synthesis of the complex. The subsequent solvothermal reaction of **C1** with $Mg(NO_3)_2{\cdot}6H_2O$ or $MnCl_2{\cdot}4H_2O$ afforded two novel isostructural 2D Pd containing MOF catalysts, **Pd@Mg: JMS-2** and **Pd@Mn: JMS-2**, with molecular formula [$MgPdCl_2$(bpdc)$(DMF)_2$]$_n$ and [$MnPdCl_2$(bpdc)$(DMF)_2$]$_n$). The MOFs crystallise in the monoclinic system, space group C2/c. The solvent-accessible volume calculated using PLATON[10] shows 46.6 % and 43.8 % per unit cell in **Pd@Mn: JMS-2** and **Pd@Mg: JMS-2** respectively. Mercury program[19] was used to reveal that the 2D networks contain interconnected cavities.

The native **Pd@Mg: JMS-2** and **Pd@Mn: JMS-2** were activated by soaking in methanol at room temperature for 24 hours, followed by drying at 80 ˚C under vacuum for 24 hours. Successful activation is evidenced by the disappearance of the FTIR band at 1676 cm^{-1} attributed to coordinated DMF molecules in **Pd@Mg: JMS-2** and **Pd@Mn: JMS-2**. The asymmetric and symmetric stretches of the carboxylate observed at 1600 and 1386 cm^{-1} in both MOFs do not change after activation, suggesting that the binding mode of the carboxylate moiety is retained.[20]

Thermogravimetric analysis showed an initial two-stage weight loss of 24.1 % and 27.4 % for **Pd@Mg: JMS-2** and **Pd@Mn: JMS-2** respectively, which corresponds to desorption of two DMF molecules per formula unit. Decomposition of the frameworks occurs above 400 ˚C and 325 ˚C respectively. The TGA curves of the dissolvated frameworks show only one main weight loss, confirming that guest molecules were completely evacuated. The structural integrity of the MOFs were maintained after activation as evidenced by a good match between as-synthesised and activated phases PXRD patterns.

To test the chemical stability, the activated MOFs, **Pd@Mg: JMS-2a** and **Pd@Mn: JMS-2a** were soaked for 36 hours in different organic solvents and bases normally used for CO_2 hydrogenation. PXRD studies after exposure to these reaction conditions revealed that **Pd@Mg: JMS-2a** is poisoned by water whilst **Pd@Mn: JMS-2a** is stable in all the solvents and bases tested. Nitrogen adsorption-desorption isotherm, measured at 77 K, shows Type IV hysteresis loops which are indicative of the presence of porous channels. The BET surface areas were found to be 0.72 and 5.8 m^2/g with a total pore volume of 0.16 and 5.84 cm^3/g for **Pd@Mg: JMS-2a** and **Pd@MnJMS-2a** respectively. The obtained low surface areas and pore volumes are attributed to partial occupancy by palladium complexes inside the MOFs.

The MOFs demonstrated remarkable catalytic activity in basic media (formate yield of 48 % (2.40 mmol formate) and 91.5 % (4.97 mmol formate)) for **Pd@Mg: JMS-2a** and **Pd@Mn: JMS-2a** in 24 hours respectively. The more stable, **Pd@Mn: JMS-2a**, with a large surface, performed better than **Pd@Mg: JMS-2a** under analogous conditions. The catalytic activity tends to increase with increasing BET surface because the reactants can easily access the surface of the catalyst.[21] Furthermore, kinetic studies reveal that **Pd@Mn: JMS-2a** has high rate constants within a temperature range of 70 to 100 ˚C as compared to **Pd@Mg: JMS-2a**. This may also explain why the yield of formate in **Pd@Mn: JMS-2a** is higher than that obtained use the **Pd@Mg: JMS-2a** MOF. Under optimised conditions, the homogeneous counterpart, **C1**, shows less catalytic activity (yield 37.5 %). The catalytic activity of **Pd@Mg: JMS-2a** and **Pd@Mn: JMS-2a** was compared with similar systems reported in the literature. It was found that the reaction conditions employed in this work are milder than some of the previously reported heterogeneous systems for CO_2 hydrogenation to formate. [16–18,22–24]

Thiol poisoning studies were used to reveal that most of the active species is within the pores rather than being bound to the surface. The hydrogenation reaction was carried in the presence of differently sized thiol poisons using the most active catalyst, **Pd@Mn: JMS-2a**. When the catalyst was exposed to the bulky benzylmercaptan, the remaining activity was found to be 72.9 %. In contrast, on exposure to a least sterically demanding thiol, 2 mercapto-ethanol, the retained activity dropped to 39.4 %. These results are consistent with the bulk of Pd sites being situated inside instead of on the surface of the MOF catalyst.

Scanning Electron Microscopy revealed that the surface morphology of both MOFs is not affected during catalysis. EDX elemental mapping of recovered **Pd@Mn: JMS-2a** and **Pd@Mg: JMS-2a** infers a consistent and even distribution of Pd atoms throughout the matrix. High-Resolution Transmission Electron Microscopy images of **Pd@Mg: JMS-2a** do not show the significant formation of nanoparticles after catalysis, explaining the insignificant drop (6%) in the catalytic activity of the system. Contrary to **Pd@Mg: JMS-2a**, **Pd@Mn: JMS-2a** shows the significant formation of nanoparticles which are agglomerated after catalysis, resulting in a significant drop in catalytic activity (24 %) over the four cycles. A mercury drop test conducted using the homogeneous counterpart, **C1**, as a model indicates that both nanoparticles and molecular catalysts are responsible for the catalytic activity, though the nanoparticles' contribution is minimal.

The reaction mechanism was proposed based on literature findings for related heterogeneous systems.[16,17,18] H_2 gets activated on the Pd^{II} sites to form Pd-dihydride intermediate. The elimination of HCl from the Pd-dihydride complex gives the active species Pd-hydride complex. This is followed by the insertion of CO_2 *via* associative addition into the Pd-hydride complex, generating the formate complex that readily dissociates the formate.

6.1.3: Synthesis of Cd, Zn and Mg Based Metal-Organic Frameworks for CO_2 and H_2 Adsorption

The solvothermal reaction of 2,2'-bipyridine-4,4'-dicarboxylate linker with $Cd(NO_3)_2 \cdot 4H_2O$, $Zn(NO_3)_2 \cdot 6H_2O$ or $Mg(NO_3)_2 \cdot 6H_2O$ in DMF at 115, 110 and 120 ˚C afforded three novel MOFs, $[Cd_2(bpdc)_2(DMF)_2.2DMF]_n$ **(JMS-3)**, $[Zn(bpdc)(DMF).DMF]_n$ (**JMS-4)** and $[Mg_1(bpdc)(DMF)_2]_n$ **(JMS-5).** J**MS-3** crystallizes in the monoclinic system and space group $P2_1/c$. The packing diagram of **JMS-3** displays 2D networks that are interdigited, with a 4-connected **sql** network topology. DMF molecules occupy 53.8% of the unit cell, as estimated by PLATON.[10] Thermal analysis of **JMS-3 shows** an initial weight loss of 28.6 % which corresponds to the loss of 4 DMF molecules modelled in the asymmetric unit (calculated 29.2 %). The dehydrated framework is found to be stable up to 370 ˚C. PXRD of the dissolvated sample (**JMS-3a**), indicates structural transformability.

JMS-4 crystallises in the monoclinic crystal system and space group $P2_1/n$. The guest free network shows that chains are interconnected through the bpdc linkers to generate a 2D network with elongated rectangular-shaped channels running along *b*-axis. PLATON[10] estimates that the volume occupied by DMF molecules accounts for 52.3 % of the unit cell volume. Topological analysis of **JMS-4 r**evealed 4-connected network connectivity with a **sql** network topology. Thermogravimetric analysis of **JMS-4** revealed an initial weight loss of 32.5 %, corresponding to the loss of four DMF molecules per formula unit which was modelled in the structure (calculated 32.2 %). The MOF decomposes at 350 ˚C. Dissolvated framework, **JMS-4a**, remains crystalline with PXRD patterns resembling patterns of the single crystal, only showing a slight broadening of some diffraction peaks, suggesting the framework is robust upon removal of guest materials. The position of the asymmetric and symmetric stretches of the carboxylate group in the IR spectrum of **JMS-1a** did not change upon activation, suggesting that the binding mode of the carboxylate is not altered.[20]

JMS-5 crystallises in a monoclinic crystal system and space group $P2_1/n$. The structure of **JMS-5** comprises $Mg_2C_2O_4$ binuclear SBU which grows along the *a*-axis. The SBUs are connected by the bpdc linker to give a non-interpenetrated 3D structure. The channels in **JMS-5**, constitute 47% of the unit cell volume as estimated by PLATON.[10] Topological analysis of JMS-5 yields an **irl** net topology. The thermal analysis of **JMS-5** shows an initial weight loss of 34.8 % which corresponds to the extrusion of two DMF molecules per formula unit modelled in the structure (calculated 35.2%). The framework decomposes at 430 ˚C. PXRD analysis revealed that the structural integrity of the framework is maintained upon the evacuation of the guest molecules.

To test the chemical stability, the activated MOFs, **JMS-3a**, **JMS-4a** and **JMS-5a** were soaked in different organic solvents for 36 hours. The PXRD patterns of recovered samples indicate that **JMS-4a** retains the original framework suggesting high chemical and water stability. **JMS-3a** shows a slight broadening of some diffraction peaks. **JMS-5a** is not stable in any solvent. The compound is poisoned by water as evidenced by a transformation from crystalline to an amorphous phase. In the presence of other solvents, a new phase is obtained. FTIR studies indicate that the binding mode of the carboxylate moiety is retained in **JMS-3a** and **JMS-4a** under different chemical environments.

CO_2 sorption at 273 K reveals surface areas of 151 and 36 m^2g^{-1} for **JMS-3a** and **JMS-4a** respectively. The adsorption measurements at various temperatures revealed a Type-1 isotherm, which is typical of microporous materials.[25] **JMS-3a** gave volumetric uptakes of 26.50 and 30.89 cm^3 (STP) g^{-1} (1.18 and 1.39 $mmolg^{-1}$) whist **JMS-4a** gave 10.96 and 16.08 cm^3 (STP) g^{-1} (0.49 and 0.71 $mmolg^{-1}$) at 298 and 273 K respectively. At 195 K, the MOFs show a steep uptake of CO_2 at low-pressure range with volumetric uptake of 34.66 and 38.84 cm^3 (STP)g^{-1} (1.52 and 1.74 $mmolg^{-1}$) for **JMS-3a** and **JMS-4a** respectively, confirming inherent permant porosity of the MOFs. The estimated values of isosteric heat of adsorption were found to be 33 to 34 $kJmol^{-1}$ at load values ranging from 0.12 to 0.99 $mmolg^{-1}$ and 29 to 31 $kJmol^{-1}$ at load values of 0.32 to 0.45 $mmolg^{-1}$ for **JMS-3a** and **JMS-4a** respectively. The observed CO_2 uptake indicates moderate to the strong interaction of CO_2 with the MOFs. Hydrogen sorption reveals a storage capacity of up to 65 and 51 cm^3g^{-1} for **JMS-3a** and **JMS-4a** at 77 K, corresponding to the sorption of 0.58 and 0.46 wt.% (2.88 and 2.29 $mmolg^{-1}$). The observed CO_2 and H_2 uptake are comparable to other MOFs reported in the literature under similar conditions. [13,26–28]

The hydrogenation of CO_2 using **JMS-3a** and **JMS-4a** was not evaluated since both MOFs did not have anchoring sites for catalytically active metal centres. Functionalisation of **JMS-5a** was not successful. The native forms did not yield any product even under harsh conditions.

6.2: Final remarks and future work

The objectives of the work presented in this thesis (Section 1.6.2) were successfully achieved. Novel metal-organic frameworks based on La^{III}, Mg^{II}, Mn^{II}, Cd^{II} and Zn^{II} metal ions were prepared under solvothermal conditions using 2,2'-bipyridine-4,4'-dicarboxylate linker. Gas sorption experiments showed that **JMS-1a**, **Ru(II)@JMS-1a**, **JMS-3a** and **JMS-5a** can be used as storage devices for H_2 and CO_2. The functionalised MOFs, **Ru(II)@JMS-1a**, **Pd@Mn: JMS-2a**, **Pd@Mg: JMS-2a** displayed excellent catalytic hydrogenation of CO_2 to formate under relatively mild conditions. Our results demonstrate the need for a protic solvent in the presence of a strong base. Temperature, pressure and catalyst loading played a significant role in the yield of formate obtained. The native MOF, **JMS-1a**, requires harsh conditions to achieve high yields of formate. The relatively low temperature in the hydrogenation reaction makes the strategy for the incorporation of catalytically active metals in MOFs attractive.

Future work should focus on the preparation of lanthanide-based metal-organic frameworks. Such MOFs, with high coordination numbers, exhibit higher stability because they can coordinate multiple bonds, which can hold the structure together after cleavage of some bonds. It would also be interesting to investigate the preparation of MOFs anchored using iridium complexes. Iridium functionalised MOFs are expected to have superior catalytic activities. Suggestions for future work for **JMS-3a**, **JMS-4a** and **JMS-5a** would involve encapsulating transition metal complexes within the MOFs. The resulting encapsulated MOF catalyst can then be used for CO_2 hydrogenation.

6.3 REFERENCES

1 W. Li, H. Wang, X. Jiang, J. Zhu, Z. Liu, X. Guo and C. Song, *RSC Advances*, 2018, **8**, 7651–7669.

2 M. S. Jeletic, M. T. Mock, A. M. Appel and J. C. Linehan, *Journal of the American Chemical Soceity*, 2013, **135**, 11533–11536.

3 W. H. Wang, J. F. Hull, J. T. Muckerman, E. Fujita and Y. Himeda, *Energy and Environmental Science*, 2012, **5**, 7923–7926.

4 B. Ugale, S. S. Dhankhar and C. M. Nagaraja, *Inorganic Chemistry*, 2016, **55**, 9757–9766.

5 A. Dhakshinamoorthy, M. Opanasenko, J. Cejka and H. Garcia, *Catalysis Science & Technology*, 2013, **3**, 2509–2540.

6 B. Ugale, S. S. Dhankhar and C. M. Nagaraja, *Crystal Growth and Design*, 2018, **18**, 2432–2440.

7 E. S. Gutterød, S. Øien-ØDegaard, K. Bossers, A. E. Nieuwelink, M. Manzoli, L. Braglia, A. Lazzarini, E. Borfecchia, S. Ahmadigoltapeh, B. Bouchevreau, B. T. Lønstad-Bleken, R. Henry, C. Lamberti, S. Bordiga, B. M. Weckhuysen, K. P. Lillerud and U. Olsbye, *Industrial and Engineering Chemistry Research*, 2017, **56**, 13206–13218.

8 L. Mino, E. Gallo, G. Agostini, C. Lamberti, E. Borfecchia, U. Olsbye, K. A. Lomachenko, K. P. Lillerud, S. Bordiga, S. Øien and S. Svelle, *Chemistry of Materials*, 2015, **27**, 1042–1056.

9 Y. Luan, Y. Jiang, D. Ramella, X. Shu and Y. Yu, *Applied Organometallic Chemistry*, 2017, **31**, 1–8.

10 A. L. Spek, *Acta crystallographica. Section D, Biological crystallography*, 2009, **65**, 148–55.

11 C. Wu, F. Irshad, M. Luo, Y. Zhao, X. Ma and S. Wang, *ChemCatChem*, 2019, **11**, 1256–1263.

12 J. M. Ngoy and R. Falcon, *Canadian Journal of Chemical Engineering*, 2019, **2019**, 2961–2968.

13 N. Chatterjee and C. L. Oliver, *Crystal Growth and Design*, 2018, **18**, 7570–

7578.

14 B. Ugale, S. S. Dhankhar and C. M. Nagaraja, *Crystal Growth and Design*, 2018, **18**, 2432–2440.

15 H. T. D. Nguyen, Y. B. N. Tran, H. N. Nguyen, T. C. Nguyen, F. Gándara and P. T. K. Nguyen, *Inorganic Chemistry*, 2018, **57**, 13772–13782.

16 P. Patel, S. Nandi, M. S. Maru, R. I. Kureshy and N.-U. H. Khan, *Journal of CO2 Utilization*, 2018, **25**, 310–314.

17 B. An, L. Zeng, M. Jia, Z. Li, Z. Lin, Y. Song, Y. Zhou, J. Cheng, C. Wang and W. Lin, *Journal of the American Chemical Society*, 2017, **139**, 17747–17750.

18 M. S. Maru, S. Ram, R. S. Shukla and N. H. Khan, *Molecular Catalysis*, 2018, **446**, 23–30.

19 C. F. Macrae, I. J. Bruno, J. A. Chisholm, P. R. Edgington, P. McCabe, E. Pidcock, L. Rodriguez-Monge, R. Taylor, J. Van De Streek and P. A. Wood, *Journal of Applied Crystallography*, 2008, **41**, 466–470.

20 S. M. Lu, Z. Wang, J. Li, J. Xiao and C. Li, *Green Chemistry*, 2016, **18**, 4553–4558.

21 H. Kobayashi, J. M. Taylor, Y. Mitsuka, N. Ogiwara, T. Yamamoto, T. Toriyama, S. Matsumura and H. Kitagawa, *Chemical Science*, 2019, **10**, 3289–3294.

22 Z. Li, T. M. Rayder, L. Luo, J. A. Byers and C. Tsung, *Journal of the American Chemical Society*, 2018, **140**, 8082–8085.

23 G. Gunniya Hariyanandam, D. Hyun, P. Natarajan, K. D. Jung and S. Yoon, *Catalysis Today*, 2016, **265**, 52–55.

24 G. H. Gunasekar, J. Shin, K. Jung, K. Park and S. Yoon, *ACS Catalysis*, 2018, **8**, 4346–4353.

25 M. Alhamami, H. Doan and C. H. Cheng, *Materials*, 2014, **7**, 3198–3250.

26 B. Ugale, S. S. Dhankhar and C. M. Nagaraja, *Inorganic Chemistry Frontiers*, 2017, **4**, 348–359.

27 D. C. Zhong, W. X. Zhang, F. L. Cao, L. Jiang and T. B. Lu, *Chemical Communications*, 2011, **47**, 1204–1206.

28 X. M. Lin, T. T. Li, Y. W. Wang, L. Zhang and C. Y. Su, *Chemistry - An Asian Journal*, 2012, **7**, 2796–2804.

APPENDICES

Appendices

The disc enclosed contains hkl and res files for the following crystal structures;

Structure	CCDC number
JMS-1	1851044
JMS-3	2010232
JMS-4	2010231
JMS-5	1851045
Pd@Mg:JMS-2	1943375
Pd@Mn:JMS-2	1943376